UNITED NATIONS
UNIVERSITY
GEOTHERMAL TRAINING PROGRAMME

ORKUSTOFNUN

Gunnuhver hot spring at Reykjanes geothermal field

Charles Muturia Lichoro

# MULTI-DIMENSIONAL INTERPRETATION OF ELECTROMAGNETIC DATA FROM SILALI GEOTHERMAL FIELD IN KENYA: COMPARISON 1-D, 2-D AND 3-D MT INVERSION

Report 4
November 2013

UNITED NATIONS
UNIVERSITY
GEOTHERMAL TRAINING PROGRAMME
Orkustofnun, Grensásvegur 9,
IS-108 Reykjavík, Iceland

Reports 2013
Number 4

# MULTI-DIMENSIONAL INTERPRETATION OF ELECTROMAGNETIC DATA FROM SILALI GEOTHERMAL FIELD IN KENYA: COMPARISON OF 1-D, 2-D AND 3-D MT INVERSION

**MSc thesis**
School of Engineering and Natural Sciences
Faculty of Earth Sciences
University of Iceland

by

**Charles Muturia Lichoro**
Geothermal Development Co., Ltd. (GDC)
Generation House, Nakuru
P.O. Box 17700
Nakuru, KENYA
*cmuturia@gdc.co.ke / cmuturia@gmail.com*

United Nations University
Geothermal Training Programme
Reykjavík, Iceland
Published in November 2013

ISBN 978-9979-68-335-3
ISSN 1670-7427

This MSc thesis has also been published in April 2013 by the
Faculty of Earth Sciences
School of Engineering and Natural Sciences
University of Iceland

# INTRODUCTION

The Geothermal Training Programme of the United Nations University (UNU) has operated in Iceland since 1979 with six month annual courses for professionals from developing countries. The aim is to assist developing countries with significant geothermal potential to build up groups of specialists that cover most aspects of geothermal exploration and development. During 1979-2013, 554 scientists and engineers from 53 developing countries have completed the six month courses, or similar. They have come from Asia (39%), Africa (34%), Central America (15%), Central and Eastern Europe (11%), and Oceania (1%) There is a steady flow of requests from all over the world for the six month training and we can only meet a portion of the requests. Most of the trainees are awarded UNU Fellowships financed by the Government of Iceland.

Candidates for the six month specialized training must have at least a BSc degree and a minimum of one year practical experience in geothermal work in their home countries prior to the training. Many of our trainees have already completed their MSc or PhD degrees when they come to Iceland, but several excellent students who have only BSc degrees have made requests to come again to Iceland for a higher academic degree. From 1999 UNU Fellows have also been given the chance to continue their studies and study for MSc degrees in geothermal science or engineering in co-operation with the University of Iceland. An agreement to this effect was signed with the University of Iceland. The six month studies at the UNU Geothermal Training Programme form a part of the graduate programme.

It is a pleasure to introduce the 35th UNU Fellow to complete the MSc studies at the University of Iceland under the co-operation agreement. Charles Muturia Lichoro, BSc in Electronics from GDC - the Geothermal Development Co., Ltd., completed the six month specialized training in Geothermal Utilization at the UNU Geothermal Training Programme in October 2009. His research report was entitled: “Joint 1-D inversion of TEM and MT data from Olkaria Domes geothermal area, Kenya.”. After two years of geothermal research work in Kenya, he came back to Iceland for MSc studies at the Faculty of Earth Sciences in September 2011. In April 2013, he defended his MSc thesis presented here, entitled “Multi-dimensional interpretation of electromagnetic data from Silali geothermal field in Kenya: comparison of 1-D, 2-D and 3-D MT inversion”. His studies in Iceland were financed by the Government of Iceland through a UNU-GTP Fellowship from the UNU Geothermal Training Programme. We congratulate him on his achievements and wish him all the best for the future. We thank the Faculty of Earth Sciences at the School of Engineering and Natural Sciences of the University of Iceland for the co-operation, and his supervisors for the dedication.

Finally, I would like to mention that Charles’ MSc thesis with the figures in colour is available for downloading on our website *www.unugtp.is,* under publications.

With warmest greetings from Iceland,

Lúdvík S. Georgsson, director
United Nations University
Geothermal Training Programme

## ACKNOWLEDGEMENTS

I wish to sincerely thank the United Nations University Geothermal Training Programme (UNU-GTP) for awarding the scholarship for this study; My employer Geothermal Development Company Ltd (GDC), for the study leave, allowing use of the data and continued support; the University of Iceland and ÍSOR – Iceland GeoSurvey for providing access to facilities and training required for successful completion of this study.

I wish to express my gratitude to my advisors Knútur Árnason and Páll Einarsson for the constructive feedback, knowledge, guidance and support. I salute them for their effort and collaboration towards the successful completion of this degree. I also wish to sincerely thank Andemariam Teklesenbet for his guidance and assistance with the data modelling and for being there whenever I needed his help. I thank the entire UNU-GTP staff; Special thanks to Dr. Ingvar Fridleifsson, director UNU-GTP (now retired), Mr. Lúdvík Georgsson, Málfríður, Þórhildur, Ingimar, and Markús for personal and technical support throughout my studies.

I am grateful to my colleagues at the Geophysics office for their effort during data collection and all the support they have given me all along. You will forever remain in my heart. I extend my gratitude to all the resource persons both in Kenya and Iceland, who aided me in one way or the other throughout this course.

To my beloved wife Joyce, sons Arnold, Emmanuel, Trevis and my daughter Precious, I have no words to express my sincere and heartfelt gratitude for your sacrifice, understanding and endurance throughout my long absence. May God bless you.

I wish most importantly to sincerely thank the Almighty God for the experience and for keeping me in good health during my entire stay in Iceland.

## DEDICATION

*I would like to dedicate this work to my beloved father Johana M'Lichoro who passed away during the course of my studies, for his encouragement to be the best I could in life and impressing on me on the importance of education at a very tender age.*

# ABSTRACT

With development of MT interpretation codes and advancement in computer hardware, 3-D electromagnetic data interpretation has become attainable. This study therefore seeks to compare results of Electromagnetic data using different interpretational techniques in order to provide reliable information about the presence, location, and size of geothermal systems in Silali field. Resistivity study of the Silali area in Kenya was carried out by the combined use of TEM and MT soundings. Joint inversion of the EM data was used to correct for static shifts in the MT data, which can be severe due to large near-surface resistivity contrasts. Joint 1-D inversion of 102 TEM/MT sounding pairs and a 3-D inversion of a 97 sounding subset of the MT data were performed. Additionally 2-D inversion of the same data set was done and results are compared with those of 1-D and 3-D inversion models. The robustness of the final 3-D inversion models was tested by using three different initial models, which gave similar results with RMS of between 1.5 and 1.7 for all three models. Similarly 2-D inversion modelling was done using two different inversion codes, REBOCC and WinGlink and their results compare fairly well.

The resistivity models resulting from the inversion were elevation corrected and smoothed and are presented as planar maps and cross sections. The inverted model of electrical resistivity reveals the presence of highly resistive near surface layer, identified as unaltered formations, which covers a low resistivity cap corresponding to the smectite-zeolite zone. Beneath this cap a more resistive zone is identified as the epidote-chlorite zone (the resistive core) and interpreted as the host of geothermal reservoir. Further at depth of about 6 km an electrically conductive feature has been imaged, and has been tentatively interpreted as a heat source for geothermal system in this field.

The aim of modelling EM data using all the three interpretational techniques is to compare results and establish which resistivity anomalies stand out irrespective of the dimensional inversion used. In this study results from 1-D, 2-D and 3-D models, recover near surface resistivity structure fairly well but differ somewhat at depth. The 3-D inversion however reveals much more consistent details than the 1-D and 2-D inversion confirming that the resistivity structures in the area is highly three dimensional. At depth below 6 km the three approaches give different results implying that the models do not resolve deeper structures. This has been attributed to noise in the data at long periods.

## TABLE OF CONTENTS

Page

## LIST OF FIGURES

Page

## LIST OF ACRONYMS

| | |
|---|---|
| MT | Magnetotelluric |
| TEM | Transient electromagnetic |
| EM | Electromagnetic |
| TE | Transverse electric |
| TM | Transverse magnetic |
| EDI | Electrical data interchange files |
| RRI | Rapid relaxation inversion |
| NLCG | Nonlinear conjugate gradients |
| REBOCC | Reduced basic OCCAM inversion |
| WSINV3DMT | 3-D inversion program |
| WinGlink | 2-D inversion program |
| m a.s.l. | Metres above sea level |
| m b.s.l. | Metres below sea level |
| TemxZ | Program for processing Zonge TEM data |
| TemxV | Program for processing V8 TEM data |
| TEMTD | Joint MT/TEM program |
| V8 | Phoenix TEM equipment |
| EAR | East African rift |
| ÍSOR | Iceland GeoSurvey |
| GDC | Geothermal Development Company |
| 1-D | One dimensional |
| 2-D | Two dimensional |
| 3-D | Three dimensional |

## MEANING OF SYMBOLS

| | |
|---|---|
| $\boldsymbol{E}$ (V m$^{-1}$) | Electric field intensity |
| $\boldsymbol{B}$ (T) | Magnetic induction |
| $\boldsymbol{H}$ (A m$^{-1}$) | Magnetic field intensity |
| $\boldsymbol{D}$ (C m$^{-2}$) | Electric displacement |
| $\eta$ (Cm$^{-3}$) | Electric charge density of free charges |
| $\boldsymbol{J}$ (Am$^{-2}$) | Electric current density |
| $\sigma$ (Sm$^{-1}$) | Electric conductivity |
| $\mu$ (H/m) | Magnetic permeability |
| $\varepsilon$ (F/m) | Electric permittivity |
| $\delta$ $(m)$ | Electromagnetic skin depth |
| T (s) | Period |
| f (Hz) | Frequency |
| t (s) | Time |
| $\omega$ (rad/s) | Angular frequency |
| $\rho$ ($\Omega$m) | Resistivity (specific resistance) |
| $\hat{Z}$($\Omega$) | Impedance tensor (2x2 matrices) |
| $\rho_a$ ($\Omega$m) | Apparent resistivity |
| $\phi$ (°) | Impedance phase |
| $i=\sqrt{-1}$ | Imaginary number |
| $k$ (m$^{-1}$) | Propagation constant (wave number) |
| x, y and $x'$, $y'$ | Reference frame and reference frame rotated through an angle $\alpha$ |
| $\mathcal{T}$ | Tipper |
| $\mathfrak{R}$ | Real part of the tipper |
| $\mathfrak{I}$ | Imaginary part of the tipper |
| $M_r$ | Length of the real part of the induction arrow |
| $M_q$ | Length of the imaginary part of the induction arrow |

# 1. INTRODUCTION

Kenya has high geothermal energy potential which is appropriate for power generation. However, most of these resources have not been explored and evaluated in detail. This huge un-tapped geothermal potential and high dependency on hydro power and fossil-fuelled energy sources are stimulating geothermal energy exploration and development projects in Kenya. The Geothermal Development Company (GDC) has explored for geothermal resource and is in the process of initiating development. Most of the geothermal fields in Kenya are found within the East African rift valley. In particular the presence of volcanic centres within the rift has motivated this study to image the shallow and deep resistivity structure of the crust in the region using Electromagnetic (EM) methods. This study is aimed at delineating the shallow as well as deeper resistivity structure of Silali geothermal field in order to determine the presence, location and geometry of geothermal systems in this field.

The Electromagnetic methods that include magnetotelluric (MT) and transient electromagnetic (TEM) are techniques of choice when it comes to geothermal exploration. This is because they give indirect information about the sub-surface, in terms of the resistivity structure of geothermal systems that may be connected to temperature and other components that are of interest. A total of 102 MT soundings and an equal number of TEM soundings are used in the interpretation. This report describes a multi-dimensional inversion of static shift corrected MT data set from Silali area.

The MT method suffers from the static shift problem. This is an inherent uncertainty in the MT data, caused mainly by local near-surface resistivity inhomogeneities close to the sounding site (Sternberg et al., 1988; Árnason, 2008). This phenomenon cannot be resolved using MT data alone. The static shift is expressed by scaling of the apparent resistivity by an unknown factor (shifted on log scale), so that apparent resistivity curves plot parallel to their true level. This may lead to very wrong and misleading interpretation of MT data if the static shift is not corrected. The TEM method does not suffer this problem, therefore joint inversion of TEM and MT soundings at the same location has been used to determine and correct for the static shift in the MT data.

Joint 1-D inversion of MT and TEM recovers resistivity variation only with depth, from which models have been stitched together to produce spatial resistivity variation and cross-sections in the area of interest. 2-D inversion models presents resistivity cross-sections where resistivity is assumed to vary with depth and in one horizontal direction, but being constant in the other orthogonal horizontal direction. Data has been interpreted by use of TE, TM and combined TE+TM modes with the aim of evaluating which of the modes recovers the resistivity structure more accurately. Recent developments of inversion codes and computer hardware (computer clusters) have made 3-D inversion of MT data practical. In this regard the 3-D MT inversion of the off-diagonal impedance tensor has been performed resulting in much more reliable and detailed results than previously attained. In order to study the robustness of the results, the 3-D inversion was done using three different initial models and the results are compared with the results of the joint 1-D inversion of the TEM and MT data and those of the 2-D inversion models.

The main objectives of this study is to use TEM and MT algorithms to fulfil the following:

1. Compare different approaches of interpreting Electromagnetic data (1-D, 2-D and 3-D) and testing the robustness of the models to recover resistivity structure
2. Study the resistivity structure of Silali in order to infer geothermal systems therein.

The MT theory is discussed in Chapter 2, with an introduction to basic Maxwell's equations and the concept of EM induction in the conductive earth. Additionally, descriptions of magnetotelluric transfer functions, impedance tensors as well as dimensionality and strike analysis are presented here and finally a brief description of TEM theory. Chapter 3 covers distortions in the earth and highlights the causes of these distortions with regard to the static shift problems and how they can be corrected. Emphasis is laid on the use of TEM soundings to resolve the static shift problem.

Chapter 4 discusses the application of resistivity methods in geothermal exploration, with an overview of resistivity of rocks and resistivity of high temperature geothermal systems. Silali geothermal area is highlighted in Chapter 5, in light of the kinematics that govern the East African rift structure, specifically the geology of Silali volcano and the formation of the caldera at Silali and briefly the previous work in the area is discussed. Chapter 6 presents the Electromagnetic methods used in the study area, field setups, instrumentation used and data processing procedures employed.

In Chapter 7 different inversion codes used in this thesis are discussed focussing on the algorithms used in 1-D, 2-D and 3-D inversions. Chapter 8 discusses the joint inversion of MT and TEM soundings with static shift correction upon which results from the 1-D joint inversion of TEM and MT data are presented. Geo-electric strike analysis of MT data is also discussed to aid in determination of polarization directions to be used in 2-D inversion and finally 2-D results are presented. Further this section presents 3-D inversion where results from different initial models are compared to estimate the robustness of the results. The 3-D inversion models are compared with results gotten from the earlier 1-D and 2-D inversion and finally concludes with the discussion on the geothermal interpretation of the results. An attempt has been made to interpret the deeper resistivity structure in terms of the tectonics around the Silali volcano.

## 2. THE MAGNETOTELLURIC (MT) METHOD

### 2.1 MT Theory

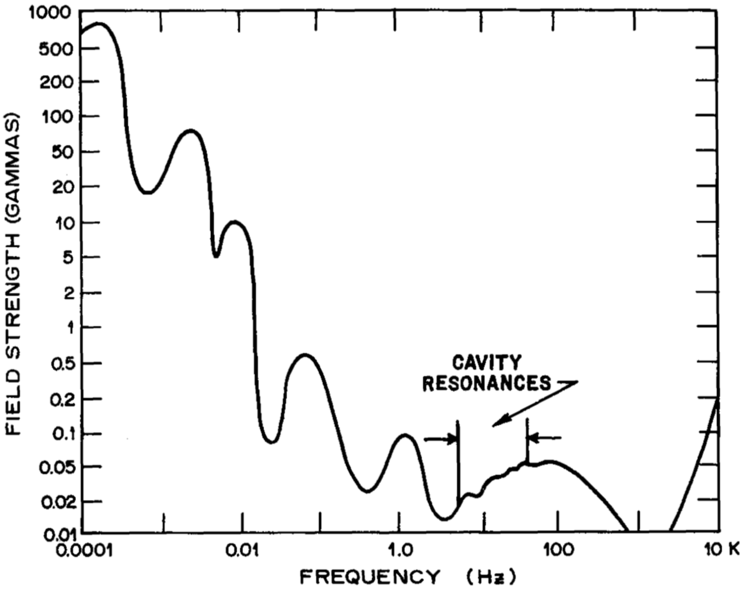

FIGURE 1: Earth's magnetic field spectrum (gamma = $10^{-9}$ T)

The magnetotelluric method utilizes natural variations in the Earth's magnetic and electrical field as a source for exploring subsurface resistivity structure (Vozoff, 1986). The Earth's electromagnetic field contains a wide frequency spectrum as seen in Figure 1. MT method is a passive electromagnetic technique for which the electric and magnetic fields are measured in orthogonal directions on the Earth's surface. Magnetotelluric fields are generated by two sources one below 1 Hz and the other above 1 Hz. The source field above 1 Hz emanates from the thunderstorm activity concentrated in the tropics. The EM signal produced propagates around the world, trapped in a wave-guide formed between the ionosphere and the earth's surface with the energy reflected back and forth between the lowermost layer of the ionosphere and the ground surface. The source field below 1 Hz originates from solar wind (plasma) interaction with the Earth's magnetic field. These geomagnetic variations induce eddy currents and secondary magnetic fields in the earth due to their transient behaviour. The geomagnetic fluctuations range between frequencies of $10^3$ to $10^{-4}$ Hz depending on their origin (Vozoff, 1991).

Data is acquired in a passive mode using a combination of electric sensors and induction coil magnetometers that can detect changes in resistivity to great depths. The electric sensors are used to determine the electric field which is derived from measurements of the voltage difference between electrode pairs $E_x$ and $E_y$. Induction coils are used to measure the magnetic fields $H_x$, $H_y$ and $H_z$ in 3 orthogonal directions. The measured variations in magnetic and electric fields [$(E_x/H_y\ (\omega))$] in the earth gives information about the subsurface resistivity structure. The EM waves are assumed to be planar and to propagate vertically into the Earth, which means that the source field has only horizontal components (the MT approximation, Vozoff, 1991). It follows that at a given period, only two horizontal electric components are necessary to describe any EM field component measured anywhere at the surface. The high frequency gives information about the shallow subsurface with the low frequency providing information about the deeper earth. The MT method can probe down to hundreds of kilometres, making it the EM method with the most exploration depth of all the EM methods. The depth of penetration of electromagnetic fields within the earth depends on the period and the earth's conductivity structure.

### 2.2 The Maxwell's equations in homogeneous conductive media

The theory of the magnetotelluric method used in resistivity studies is based on Maxwell's equations which relate electric and magnetic fields. The following sets of Maxwell's equations are used to describe the EM field in a conducting medium.

$$\nabla \times \mathrm{E} = -\mu \frac{\partial H}{\partial t} \tag{2.1}$$

$$\nabla \times \mathrm{H} = \sigma E + \varepsilon \frac{\partial E}{\partial t} \tag{2.2}$$

$$\nabla \cdot \mathrm{B} = 0 \tag{2.3}$$

$$\nabla \cdot \mathrm{E} = \frac{1}{\varepsilon}\eta \tag{2.4}$$

where, B = μH; μ = $\mu_0\mu_r$ $\varepsilon = \varepsilon_0\varepsilon_r$ D = $\varepsilon$E
$\mu_0 = 4\pi \cdot 10^{-7}$ Henry s/m; $\varepsilon_o = 8.85 \cdot 10^{-12}$Farad/m;

According to Faraday's Law the time variations in the magnetic field induce corresponding fluctuations in the electric field flowing in a closed loop with its axis oriented in the direction of the inducing field. This electric field then induces a secondary, internal magnetic field proportional to the total current flow in accordance with Ampere's Law. Ampere's law equation represents two kinds of current flow, one (J) in which charge carriers flow through a medium without hindrance which is usually called ohmic, and another, $\partial \mathrm{D}/\partial t,$ in which charge separation, and hence an opposing electric field, arises also known as displacement current.

Variations in $\mu_r$ and $\varepsilon_r$ are assumed negligible compared to variations in bulk conductivity, σ of rocks, and we assume:-

$$\mu_r \approx 1 \qquad \text{and} \qquad \varepsilon_r \approx 1$$

In a conducting media outside discontinuities, there is no charge density, η therefore equation (2.4) reduces to $\nabla \cdot \mathrm{E} = 0$.

By taking the time derivative of Equation 2.2 and multiplying by μ and using Equation 2.1, we get:

$$-\nabla \times (\nabla \times \mathrm{E}) = \mu\sigma\frac{\partial}{\partial t}\mathrm{E} + \mu\varepsilon\frac{\partial^2}{\partial t^2}\mathrm{E} \tag{2.5}$$

Using the vector identity:

$$\nabla \times (\nabla \times A) = -\nabla^2 A + \nabla(\nabla \cdot A) \tag{2.6}$$

And considering that $\nabla. \mathrm{E} = 0$, we get

$$\nabla^2\mathrm{E} - \mu\sigma\frac{\partial}{\partial t}\mathrm{E} - \mu\varepsilon\frac{\partial^2}{\partial t^2}\mathrm{E} = 0 \tag{2.7}$$

Similarly by performing the same procedure on Equation 2.1 and 2.2, we get:

$$\nabla^2\mathrm{H} - \mu\sigma\frac{\partial}{\partial t}\mathrm{H} - \mu\varepsilon\frac{\partial^2}{\partial t^2}\mathrm{H} = 0 \tag{2.8}$$

In insulators where σ = 0, Equations 2.7 and 2.8 reduces to the following wave equations;

$$\nabla^2\mathrm{E} - \mu\varepsilon\frac{\partial^2}{\partial t^2}\mathrm{E} = 0 \tag{2.9}$$

$$\nabla^2\mathrm{H} - \mu\varepsilon\frac{\partial^2}{\partial t^2}\mathrm{H} = 0 \tag{2.10}$$

The above equations describe the nature of electromagnetic wave propagation in a non-conductive medium with velocity $v = \frac{1}{\sqrt{\varepsilon\mu}}$. For highly conductive media the equations describe wave diffusion equations.

Assuming the fields vary harmonically with time, i.e. $e^{i\omega t}$ Equations 2.7 and 2.8 become:

$$\nabla^2\mathrm{E} - i\omega\mu\sigma\mathrm{E} + \omega^2\mu\varepsilon\mathrm{E} = 0 \tag{2.11}$$

$$\nabla^2\mathrm{H} - i\omega\mu\sigma\mathrm{H} + \omega^2\mu\varepsilon\mathrm{H} = 0 \tag{2.12}$$

For a homogeneous earth, with conductivity σ and a normally incident plane wave, the E and H fields are constant in direction and magnitude over planes perpendicular to the vertical (+z), direction of propagation.

The Equations 2.11 and 2.12 are in the form of the vector Helmholtz differential equations describing quasi-stationary electromagnetic field behaviour.

$$\nabla^2 \mathrm{E} + k^2 \mathrm{E} = 0; \qquad \nabla^2 \mathrm{H} + k^2 \mathrm{H} = 0 \tag{2.13}$$

where,
$$k^2 = \omega^2 \mu \varepsilon - i\omega\mu\sigma \tag{2.14}$$

Equations 2.13 have wave solutions which give;

$$\mathrm{E}(\mathrm{x}, t) = \mathrm{E}^+ e^{-i(\mathrm{k}\cdot\mathrm{x} - \omega t)} + \mathrm{E}^- e^{i(\mathrm{k}\cdot\mathrm{x} + \omega t)} \tag{2.15}$$

$$\mathrm{H}(\mathrm{x}, t) = \mathrm{H}^+ e^{-i(\mathrm{k}\cdot\mathrm{x} - \omega t)} + \mathrm{H}^- e^{i(\mathrm{k}\cdot\mathrm{x} + \omega t)} \tag{2.16}$$

where, $\mathrm{E}^+$, $\mathrm{E}^-$, $\mathrm{H}^+$ and $\mathrm{H}^-$are arbitrary constant vectors, which are in general complex, and usually determined by examining the exponential terms $e^{i\mathrm{k}\cdot\mathrm{x}}$ and $e^{-i\mathrm{k}\cdot\mathrm{x}}$. $\mathrm{k} = k\mathrm{u}$ is the propagation vector and u is normal to the planes of constant phase. The first terms in Equations 2.15 and 2.16 correspond to a wave propagating in the direction of u but the second terms represent a wave propagating in the opposite direction.

The wave number, $k$ is a complex number which is a square root of Equation 2.14:

$$k = \alpha - i\beta \tag{2.17}$$

where,
$$\alpha = \sqrt{\varepsilon\mu}\omega \sqrt{\left(\frac{1}{2}\sqrt{1 + \left(\frac{\sigma}{\varepsilon\omega}\right)^2} + 1\right)} \tag{2.18}$$

$$\beta = \sqrt{\varepsilon\mu}\omega \sqrt{\left(\frac{1}{2}\sqrt{1 + \left(\frac{\sigma}{\varepsilon\omega}\right)^2} - 1\right)} \tag{2.19}$$

For the electric field of wave propagating in the direction of u we have;

$$\mathrm{E}(\mathrm{x}, t) = \mathrm{E}^+ e^{-\beta\mathrm{u}\cdot\mathrm{x}} e^{-i(\alpha\mathrm{u}\cdot\mathrm{x} - \omega t)} \tag{2.20}$$

which is a wave propagating with velocity
$$v = \frac{\omega}{\alpha} \tag{2.21}$$

and exponentially decreasing in amplitude; For $\sigma = 0$, from Equations (2.18) and (2.19), $\beta = 0$ and hence there is no decrease in amplitude and $\alpha = \sqrt{\varepsilon\mu}\omega$ so that:

$$v_0 = \frac{1}{\sqrt{\varepsilon\mu}} \tag{2.22}$$

The resistivity of the rocks is in the range of 1 - $10^4$ Ohm-m so that σ is in the range of 1 - $10^{-4}$ S/m. The frequencies used in MT are lower than $10^3$ Hz and since $\varepsilon_r \approx 10$ for wet rocks.

Then,
$$\frac{\sigma}{\varepsilon\omega} \geq \frac{10^{-4}}{10 \cdot 8.85 \cdot 10^{-12} \cdot 2\pi \cdot 10^3} = 1.7 \cdot 10^2 \gg 1 \tag{2.23}$$

It can therefore be seen that,
$$\alpha \approx \beta \approx \sqrt{\frac{\mu\omega\sigma}{2}} = \frac{1}{\delta} \tag{2.24}$$

This is the quasi stationary approximation, and δ is called the skin depth. Equation 2.20 shows that the amplitude of the wave along the z-axis decreases as:

$$E(z) \propto e^{-z/\delta} \tag{2.25}$$

It follows that the amplitude decreases faster for higher conductivities and frequencies. From Equations 2.21 and 2.24 it can be seen that the velocity is given as;

$$v = \sqrt{\frac{2\omega}{\mu\sigma}} \tag{2.26}$$

and decreases with increasing conductivity.

For a wave propagating in the direction of u with the wave vector k = *k*u, we have from Equations 2.15 and 2.16:

$$\mathrm{E}(\mathrm{x}, t) = \mathrm{E}_0 e^{-i(\mathrm{k}\cdot\mathrm{x} - \omega t)}; \qquad \mathrm{H}(\mathrm{x}, t) = \mathrm{H}_0 e^{-i(\mathrm{k}\cdot\mathrm{x} - \omega t)}; \tag{2.27}$$

The positive exponential terms in both Equations 2.15 and 2.16 are dropped since they imply that the wave propagation is in the exponentially increasing direction which is un-physical, hence they are assumed to be zero.

From Maxwell's Equations 2.3 and 2.4:

$$\nabla \cdot \mathrm{B} = \mu \nabla \cdot \mathrm{H} = 0 \qquad \text{and} \qquad \nabla \cdot \mathrm{E} = \frac{1}{\varepsilon}\eta = 0$$

so that,

$$\mathrm{k} \cdot \mathrm{E} = ku \cdot \mathrm{E} = 0; \qquad \mathrm{k} \cdot \mathrm{H} = k\mathrm{u} \cdot \mathrm{H} = 0$$

Such that both E and H are perpendicular to the wave vector k.

From Maxwell's Equations 2.2

$$\nabla \times \mathrm{H} = \sigma \mathrm{E} + \varepsilon \frac{\partial}{\partial t} \mathrm{E} \tag{2.28}$$

It follows that;

$$-i\mathrm{k} \times \mathrm{H} = (\sigma + i\varepsilon\omega)\mathrm{E} = \frac{ik^2}{\mu\omega}\mathrm{E} \tag{2.29}$$

or

$$\mathrm{E} = -\frac{\mu\omega}{k} \mathrm{u} \times \mathrm{H}$$

If u is along the z-axis i.e. a vertically incident wave then,

$$\mathrm{u} = (0,0,1); \qquad \mathrm{u} \times \mathrm{H} = (-H_y, H_x, 0) \tag{2.30}$$

and we have

$$E_x = \frac{\mu\omega}{k} H_y; \qquad E_y = -\frac{\mu\omega}{k} H_x \tag{2.31}$$

which can be written as:

$$\begin{pmatrix} E_x \\ E_y \end{pmatrix} = \begin{pmatrix} 0 & Z_{xy} \\ Z_{yx} & 0 \end{pmatrix} \begin{pmatrix} H_x \\ H_y \end{pmatrix} \tag{2.32}$$

Where,

$$Z_{xy} = -Z_{yx} = \frac{\mu\omega}{k} \tag{2.33}$$

In the quasi stationary approximation $k = \sqrt{\mu\omega\sigma}\,\frac{1}{\sqrt{2}}\,(1 - i)$ and we have

$$Z = \sqrt{\frac{\mu\omega}{\sigma}}\,\frac{\sqrt{2}}{1-i} = \sqrt{\frac{\mu\omega}{\sigma}}\,\frac{1+i}{\sqrt{2}} = \sqrt{\frac{\mu\omega}{\sigma}}\,e^{i\pi/4} \tag{2.34}$$

From this we can solve for $\rho$:

$$\rho = \frac{1}{\sigma} = \frac{1}{\mu\omega}\left|\frac{E_x}{H_y}\right|^2 = \frac{1}{\mu\omega}\left|\frac{E_y}{H_x}\right|^2 \tag{2.35}$$

### 2.3 Non-vertical incidence on conductive half-space

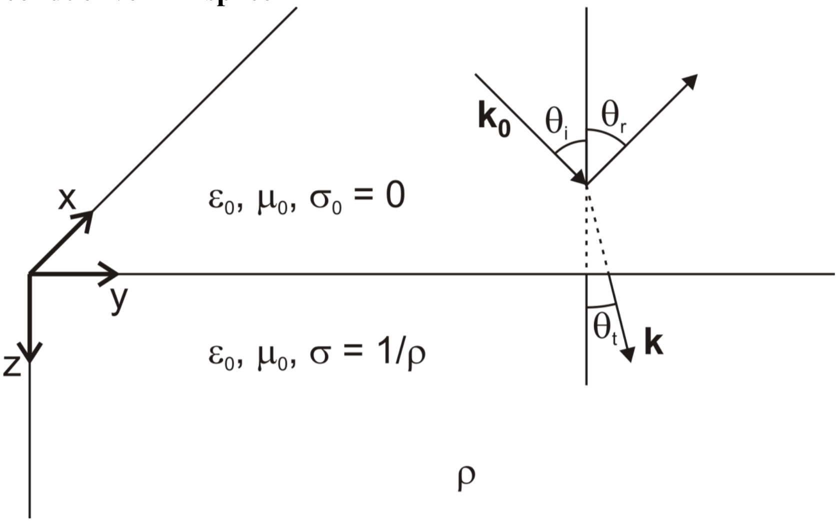

FIGURE 2: Reflected and refracted waves

Let us consider a plane electromagnetic wave of angular frequency $\omega$ and wave vector $k_0$ incident at the surface of a homogeneous earth with resistivity $\rho = 1/\sigma$. The wave vector $k_0$ makes an angle $\theta_i$ (angle of incidence) with the z-axis. In a downward-travelling plane elecromagnetic wave, the magnetic and electric vectors lie in horizontal planes.

A refracted wave propagates into the half-space with wave vector k making the angle $\theta_t$ with the z-axis (Figure 2).

Using Snell's law we have:

$$\frac{1}{v_0} sin\theta_i = \frac{1}{v} sin\theta_t \tag{2.36}$$

Where $v_0$ and $v$ are the velocities in the air and in the half-space respectively. From Equations 2.25 and 2.26 we have

$$v_0 = \frac{1}{\sqrt{\varepsilon_0 \mu_0}}; \qquad v = \sqrt{\frac{2\omega}{\mu_0 \sigma}} \tag{2.37}$$

which leads to;

$$\sin\theta_t = \sin\theta_i \sqrt{\frac{2\varepsilon_0 \omega}{\sigma}} \tag{2.38}$$

Assuming that the resistivity of subsurface rocks is $\rho = {}^{1}\!/_{\sigma} < 10^4 \Omega m$ and $\omega < 10^4$ Hz for MT measurements the;

$$\frac{2\varepsilon_0 \omega}{\sigma} < 10^{-3}$$

Therefore $\theta_t$ is practically zero and the refracted wave travels vertically downwards into the Earth for all angles of incidence $\theta_i$.

### 2.4 Penetration depth

In a uniform medium, a measure of inductive scale length is given by the skin depth $\delta$, which is the distance by which the exponentially decaying amplitude becomes $1/e$'th (37%) of its value at the surface. From Equation 2.24 skin depth is given by:

$$\delta(\omega) = \sqrt{\frac{2}{\omega\mu\sigma}} \tag{2.39a}$$

The above expression shows that the amplitude decreases faster with depth for higher conductivities and frequencies. Using that $\mu = \mu_0 = 4\pi . 10^{-7}$ V s/Am (assuming $\mu_r = 1$, in the earth) and $\omega = 2\pi/T$, where $T$ is the period of the field, we have:

$$\delta(\omega) \approx 0.5\sqrt{\rho T} \text{ [km]} \tag{2.39b}$$

For a given resistivity distribution of the subsurface, the depth of penetration increases according to the square root of the product of medium's resistivity and period. In order to realize deeper penetration, data needs to be acquired at sufficiently long periods. The skin depth explains the limitations of the EM technique, particularly the decreasing resolution with increasing depth of penetration.

## 2.5 Horizontally layered Earth

Consider a plane electromagnetic wave travelling into a flat earth consisting of a set of N horizontal layers, each with a uniform conductivity, $\sigma_i$ and of a thickness, $d_i$. The electromagnetic field is excited in the earth by a downward-travelling plane electromagnetic wave (Figure 3).

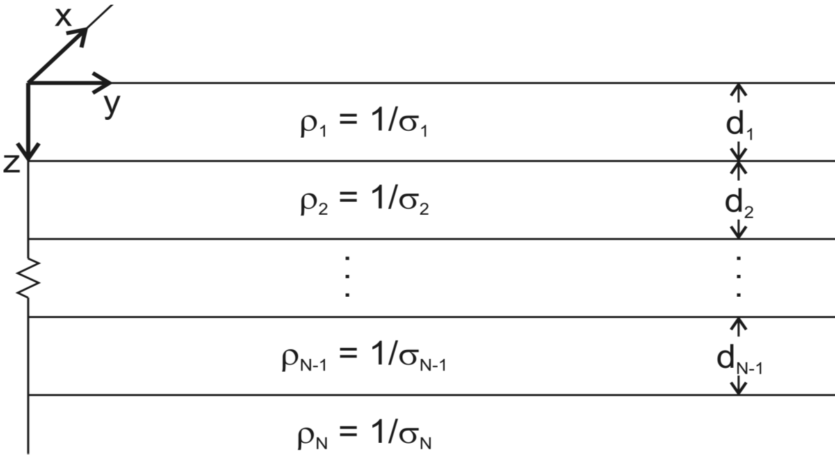

FIGURE 3: Layered earth representation

At the boundary between the atmosphere and the solid earth ($z$=0), we have:

$$\begin{pmatrix} E_x(\omega) \\ H_y(\omega) \end{pmatrix} = \begin{pmatrix} 0 & Z_{xy}(\omega) \\ Z_{yx}(\omega) & 0 \end{pmatrix} \begin{pmatrix} H_x(\omega) \\ H_y(\omega) \end{pmatrix} \tag{2.40}$$

Where the impedance tensor elements are;

$$Z_{xy}(\omega) = -Z_{yx}(\omega) = \hat{Z}_1 \tag{2.41}$$

The parameter $\hat{Z}_1$ is determined by a recursive relationship assuming the wave impedance is continuous across the surfaces between layers as follows:

$$\hat{Z}_i = Z_i \frac{\hat{Z}_{i+1} + Z_i \tanh(ik_i d_i)}{Z_i + \hat{Z}_{i+1} \tanh(ik_i d_i)} \tag{2.42}$$

This recursive procedure can be used to expand the expression for wave impedance at the earth's surface (where we can measure it physically) through any number of layers, removing the arbitrary constants, one by one:

For $i$ = N-1, ......, 1 and $\hat{Z}_N = Z_N$

$$Z_i = \frac{\mu_0 \omega}{k_i}; \qquad k_i = \sqrt{\mu_0 \varepsilon_0 \omega^2 - i\mu_0 \sigma_i \omega} \tag{2.43}$$

Therefore the tensor element can be written as

$$Z_i(\omega) = |\hat{Z}_i(\omega)| e^{i\phi(\omega)} \tag{2.44}$$

Where $\hat{Z}_i$ and $\phi$ are dependent on the resistivity of the i'th layer and angular frequency.

Similarly, with homogeneous half-space, apparent resistivity and phase which are functions of $\omega$ can be defined as:

$$\rho_a(\omega) = \frac{1}{\mu_0 \omega} |\hat{Z}_1|^2 = \frac{1}{\mu_0 \omega} \left|\frac{E_x}{H_y}\right|^2 = \frac{1}{\mu_0 \omega} \left|\frac{E_y}{H_x}\right|^2 \qquad \text{Phase, } \phi = tan^{-1}\left(\frac{Im\,\hat{Z}_1}{Re\,\hat{Z}_1}\right) \tag{2.45}$$

### 2.6 Magnetotelluric transfer functions

MT transfer functions contain information about the electrical conductivity in a hemisphere, with the magnetotelluric site located at the centre of the bounding horizon. MT transfer functions are responses that relate measured electromagnetic field components at a given frequencies. They depend on the electrical properties of the materials. Hence, they characterise the conductivity distribution of the underlying materials according to the measured frequency. The magnetotelluric transfer functions consist of the Impedance tensors and Geomagnetic transfer functions.

#### 2.6.1 Impedance tensor transfer functions

For real data the impedance tensor can be described by the relationship between electric and magnetic fields at each frequency. In matrix form this can be written as:

$$\begin{pmatrix} E_x \\ E_y \end{pmatrix} = \begin{pmatrix} Z_{xx} & Z_{xy} \\ Z_{yx} & Z_{yy} \end{pmatrix} \begin{pmatrix} H_x \\ H_y \end{pmatrix}$$

The linear relations of the fields can be written as:

$$E_x(\omega) = Z_{xx}(\omega)H_x(\omega) + Z_{xy}(\omega)H_y(\omega) \tag{2.46}$$

$$E_y(\omega) = Z_{yx}(\omega)H_x(\omega) + Z_{yy}(\omega)H_y(\omega) \tag{2.47}$$

where the on-diagonal elements relate fields measured in the same direction whereas the off-diagonal elements relate the orthogonally measured fields.

#### 2.6.2 Geomagnetic transfer functions

The geomagnetic transfer function is a complex vector giving the relationship between the horizontal and the vertical components of the magnetic field. The vertical component is generated by lateral conductivity gradients in the earth. This relationship is described by the tipper ($\mathcal{T}$).

$$\mathrm{H_z}(\omega) = \mathcal{T}_{zx}H_x(\omega) + \mathcal{T}_{zy}H_y(\omega) \tag{2.48}$$

For a 1-D Earth, there is no induced vertical magnetic field $H_z$, and hence $\mathcal{T}_{\mathrm{zx}} = \mathcal{T}_{\mathrm{zy}} = 0$. By contrast, close to a vertical boundary between low and high conductivity structures (for example, at the boundary between ocean and land), there is an induced vertical magnetic ($H_z$) field. For a 2-D earth, the coordinate system can be rotated so that the x-axis is in the strike direction, the so-called Tstrike, i.e. $\mathcal{T}_{\mathrm{zx}} = 0$, but $\mathcal{T}_{\mathrm{zy}} \neq 0$. This is done by minimizing $|\mathcal{T}_{\mathrm{zx}}|$. The tipper vector, normally called inductions arrows, can be decomposed into two real vectors in the horizontal xy plane. There exist two conventions of the real induction arrows called reversed (Parkinson convention, Parkinson, 1959) or non-reversed (Wiese convention). In the Wiese convention, the vectors point away from lateral increase in electrical conductivity (Wiese, 1962). The arrows have a real (in-phase) and imaginary (out-of-phase) part. The magnitude of induction arrows depends on both the proximity to the conductor and the conductivity contrast. The bigger the contrast the longer the arrows and the closer the conductor the longer is the arrow.

Length of the real ($M_r$) and imaginary ($M_q$) arrows are given by:

$$M_r = \left(\Re\mathcal{T}_{zx}{}^2 + \Re\mathcal{T}_{zy}{}^2\right)^{1/2} \tag{2.49}$$

$$M_q = (\Im\mathcal{T}_{zx}{}^2 + \Im\mathcal{T}_{zy}{}^2)^{1/2} \tag{2.50}$$

Where $\Re$ and $\Im$ are the real and imaginary parts of tipper, respectively. The directions of the arrows are similarly determined by:

$$\theta_r = \tan^{-1}\left(\frac{\Re\mathcal{T}_{zy}}{\Re\mathcal{T}_{zx}}\right) \tag{2.51}$$

$$\theta_q = \tan^{-1}\left(\frac{\Im T_{zy}}{\Im T_{zx}}\right) \tag{2.52}$$

$\theta_r$ and $\theta_q$ are clockwise positive from x-axis (usually geomagnetic north) along which the coherency between vertical and the horizontal magnetic field is at its maximum. In the 2-D case, the direction of the induction arrow is perpendicular to the true orientation of the regional strike. However, for the 3-D case, the direction varies and always points away from the conductive structure.

### 2.6.3 1-D impedance tensor

For a 1-D layered earth, the conductivity $\sigma$ varies only with depth and the MT transfer functions are independent of the orientation of the measured axes and are functions only of the frequency. In this case, the impedance tensor may be written as:

$$Z_{1D} = \begin{pmatrix} 0 & Z_{xy} \\ -Z_{yx} & 0 \end{pmatrix} \tag{2.53}$$

The diagonal elements of the impedance tensor, $Z_{xx}$ and $Z_{yy}$ are zero, whereas the off-diagonal components, which couple orthogonal electric and magnetic field components are equal in magnitude, but have opposite signs.

The apparent resistivity for the 1-D earth can be defined as:

$$\rho_a = \frac{1}{\mu_0\omega}|Z|^2 \tag{2.54}$$

and the phase of the complex impedance tensor is defined by:

$$\phi_a = tan^{-1}\left(\frac{Im\,Z}{Re\,Z}\right) \tag{2.55}$$

### 2.6.4 2-D impedance tensor

For a 2-D earth the conductivity varies with depth and one horizontal direction while remaining constant in the other horizontal direction. The direction along which the conductivity is constant is called the geo-electric strike.

Ordinarily the MT field layout is rarely in the strike direction, so that in order to perform 2-D analysis the data has to be rotated to the respective polarization direction (see section 2.7). The impedance tensor in 2-D case is therefore decoupled into two independent modes by rotating to a coordinate system where either x or y is parallel to strike and y or x perpendicular to strike. The mode with electric field parallel to strike is called Transverse electric (TE) mode or E-polarization and magnetic field parallel to strike is called Transverse magnetic (TM) mode or B-polarization. For a perfectly 2-D earth the diagonal elements of the impedance tensor are zero. However this condition is rarely satisfied with measured data due to distortion or 3-D induction.

$$Z_{2D} = \begin{bmatrix} 0 & Z_{xy} \\ Z_{yx} & 0 \end{bmatrix} \tag{2.56a}$$

where:

$$Z_{xy}(\omega) = Z_{TE} = \frac{E_x(\omega)}{H_y(\omega)} \tag{2.56b}$$

$$Z_{yx}(\omega) = Z_{TM} = \frac{E_y(\omega)}{H_x(\omega)} \tag{2.56c}$$

The above yields the following two sets of apparent resistivities and impedance phases;

TE-mode: $\rho_{xy} = \frac{1}{\mu_0\omega}\left|Z_{xy}\right|^2$; $\phi_{xy}$ and TM-mode: $\rho_{yx} = \frac{1}{\mu_0\omega}\left|Z_{yx}\right|^2$; $\phi_{yx}$ (2.57)

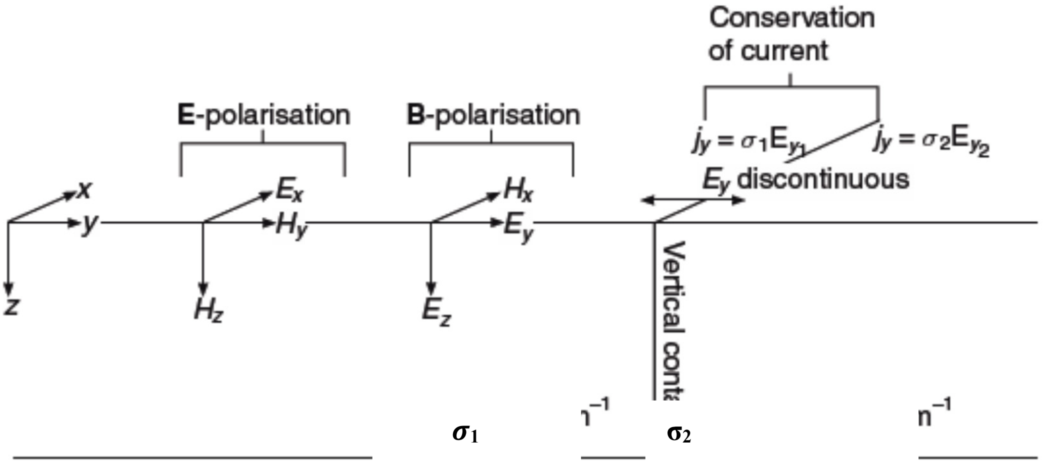

FIGURE 4: Simple 2-D model illustrating polarizations and vertical contact between two zones of different conductivity (adopted from Simpson and Bahr, 2005)

As shown in Figure 4 above, the TE-mode describes currents flowing parallel to strike which induces magnetic fields perpendicular to it, and can be described in terms of electromagnetic field components $E_x$, $H_y$, and $H_z$. Similarly, the TM-mode describes currents flowing perpendicular to strike which induces magnetic fields parallel to it, and can be described in terms of the electromagnetic field $H_x$, $E_y$ and $E_z$.

The electric field $E_y$ in the TM-mode is discontinuous across a vertical contact, therefore $Z_{yx}$ is also discontinuous. This means that $\rho_{TM}$ will also be discontinuous. As a result of the discontinuous behaviour revealed by $\rho_{TM}$, B-polarisation tends to resolve lateral conductivity variations better than E-polarisation. The E-polarisation apparent resistivities vary smoothly across vertical contacts and usually has an associated vertical magnetic field because its associated magnetic field component is perpendicular to strike.

### 2.6.5 3-D impedance tensor

The real Earth is 3-dimensional where conductivity varies in all directions, σ(x, y, z). The impedance tensor takes the general form:

$$Z_{3D} = \begin{pmatrix} Z_{xx} & Z_{xy} \\ Z_{yx} & Z_{yy} \end{pmatrix} \tag{2.59}$$

All the components of the impedance tensor are non-zero and the diagonal elements of the impedance tensor do not vanish in any coordinate system, therefore all the tensor elements are considered in the interpretation. Different forms of apparent resistivity can be derived from the full impedance tensor. The most common of these are:

The rotational dependent apparent resistivities ($Z_{xy}$ and $Z_{yx}$ ), given as

$$\rho_{xy} = \frac{1}{\omega\mu_0}\left|Z_{xy}\right|^2 \quad \text{and} \quad \rho_{yx} = \frac{1}{\omega\mu_0}\left|Z_{yx}\right|^2 \quad \text{Phase, } \phi = tan^{-1}\left(\frac{Im\,Z}{Re\,Z}\right) \tag{2.60}$$

and rotationally independent determinant, $Z_{det} = \sqrt{Z_{xx}Z_{yy} - Z_{xy}Z_{yx}}$. given as:

$$\rho_{det} = \frac{1}{\omega\mu_0}|Z_{det}|^2; \; \phi_{det} = \arg(Z_{det}) \tag{2.61}$$

Arithmetic mean, $Z_{ave} = \frac{Z_{xy} - Z_{yx}}{2}$ given as:

$$\rho_{ave} = \frac{1}{\omega\mu_0}|Z_{ave}|^2, \qquad \phi_{ave} = \arg(Z_{ave}) \tag{2.62}$$

## 2.7 Rotation of the impedance tensor

MT data can be collected within any arbitrary coordinate system. In data analysis we look for directional information in the data, in differently oriented coordinate systems. The matrix form of the full impedance tensor is;

$$\begin{pmatrix} E_x \\ E_y \end{pmatrix} = \begin{pmatrix} Z_{xx} & Z_{xy} \\ Z_{yx} & Z_{yy} \end{pmatrix} \begin{pmatrix} H_x \\ H_y \end{pmatrix}$$

If the coordinate system is rotated through an angle $\theta$, such that the co-ordinates change from x, y to x', y' as shown in Figure 5 to give;

The fields transform like $$\vec{\mathrm{E}}' = \overline{\overline{\mathrm{R}}} \cdot \vec{\mathrm{E}}; \qquad \vec{\mathrm{H}}' = \overline{\overline{\mathrm{R}}} \cdot \vec{\mathrm{H}} \tag{2.63}$$

and the tensor transforms: $$\mathrm{E}' = \mathrm{Z}' \cdot \mathrm{H}' = \mathrm{RZR^T H}' \tag{2.64a}$$

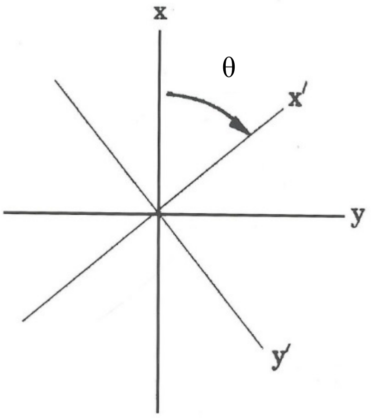

FIGURE 5: Rotation of reference frame

Therefore, $$\mathrm{Z}' = \mathrm{R}(\theta)\mathrm{Z} \cdot \mathrm{R}(\theta)^{\mathrm{T}} = \mathrm{RZR^T} \tag{2.64b}$$

where, $R(\theta) = \begin{bmatrix} \cos\theta & \sin\theta \\ -\sin\theta & \cos\theta \end{bmatrix}$; is the rotation operator and $\mathrm{R^T}$ is the transpose of R.

In full form this becomes,

$$Z'_{xx} = Z_{xx}cos^2\theta + \left(Z_{xy} + Z_{yx}\right) sin\,\theta\, cos\,\theta + Z_{yy}sin^2\,\theta \tag{2.65a}$$

$$Z'_{xy} = Z_{xy}cos^2\theta + \left(Z_{yy} - Z_{xx}\right) sin\,\theta\, cos\,\theta - Z_{yx}sin^2\theta \tag{2.65b}$$

$$Z'_{yx} = Z_{yx}cos^2\theta + \left(Z_{yy} - Z_{xx}\right) sin\,\theta\, cos\,\theta - Z_{xy}sin^2\theta \tag{2.65c}$$

$$Z'_{yy} = Z_{yy}cos^2\theta - \left(Z_{xy} + Z_{yx}\right) sin\,\theta\, cos\,\theta + Z_{xx}sin^2\theta \tag{2.65d}$$

To obtain the principal directions of the structure if the earth is two-dimensional involves minimizing $\left(|Z'_{xx}|^2 + |Z'_{yy}|^2\right)$ or maximizing $\left(|Z'_{xy}|^2 + |Z'_{yx}|^2\right)$, both of which give the same principal direction.

## 2.8 MT strike analysis

MT impedance tensor, Z contains information about dimensionality and directions. Strike analysis attempts to recover the directionality from the MT data such as determination of strike of dominant 2-D geoelectrical structure. This can be difficult in the presence of both noise and local distortion. Often the strike angle is the least-stable parameter that can be resolved from the MT data themselves (Jones and Groom, 1993). The choice of the interpretation coordinate frame, for the appropriate strike angle, is of critical importance in MT studies especially in 2-D interpretation. Although information from other sources, such as geological strike can be used, it should be demonstrated that the coordinate frame chosen is supported by the Zstrike of the MT data. Induction vectors are used as a measure to define regional geoelectric strike. The direction of the real component of the induction vector will be orthogonal to the local geoelectric strike and will point away from the more conductive regions (Wiese convention).

For 2-D structure the impedance tensor is given by:

$$Z_{2D} = \begin{pmatrix} 0 & Z_{TE} \\ Z_{TM} & 0 \end{pmatrix} \tag{2.66}$$

The impedances $Z_{TE}$ and $Z_{TM}$ relate fields parallel and perpendicular to the geoelectrical strike respectively, as discussed in section 2.6.4. The angle of strike $\theta_0$ is obtained from the measured impedances by maximizing suitable functions of off-diagonal impedance, $Z_{xy}$ and $Z_{yx}$ under rotation of the axis.

$$\theta_0 = 1/4\, tan^{-1} \frac{(Z_{xx}-Z_{yy})(Z_{xy}+Z_{yx})^{*}+(Z_{xx}-Z_{yy})^{*}(Z_{xy}+Z_{yx})}{|Z_{xx}-Z_{yy}|^{2}-|Z_{xy}-Z_{yx}|^{2}} \tag{2.67}$$

where * denotes the complex conjugate.

Equation 2.67 gives four angles which maximize the off-diagonal components to form two principal directions perpendicular to each other.

The computed strike direction contains a 90° ambiguity, since rotation by 90° only switches the location of the two principal impedance tensor elements within the tensor. This inherent ±90° ambiguity can be resolved by use of tipper strike, which uniquely defines the regional strike under the assumption of a 2-D regional structure (Zhang et al, 1987). Often the local strikes determined from MT data can deviate considerably from the geological strikes.

## 2.9 Dimensionality analysis

The dimensionality of the Earth structure can be investigated from MT data with an aid of some important parameters namely skew, ellipticity, tipper and by use of polar diagrams. These techniques are simple and they provide useful information before undertaking more detailed analysis on the data such as the 2-D or 3-D inversion.

### 2.9.1 Impedance polar diagrams

A polar diagram is the trace of the tip of a vector as the direction of that vector moves through 360°. In polar diagrams, the vectors have amplitude with length equal to the field amplitude of the tensor element and an angle equal to the rotation angle. Polarization diagrams can be used to make judgments about the geometry of an inhomogeneity and also provide information about the MT data dimensionality. For instance in a 1-D resistivity structure, the off-diagonal impedance polar diagrams are circular, while the polar diagrams for the diagonal impedances reduce to a point. For 2-D or 3-D resistivity structures, the principal impedances elongate in a direction either parallel or perpendicular to the strike (Reddy et al., 1977). The 2-D polar diagrams for $Z'_{xy}$ are oval, and elongate along the symmetry lines whereas the $Z'_{xx}$ polar diagrams attain the shape of a clover leaf. Away from the symmetry lines, polar diagrams start to distort and their magnitudes become greater, particularly at the lower frequency indicating 3-dimensionality. Examples of impedance polar diagrams for 1-D, 2-D and 3-D models are shown in Figure 6.

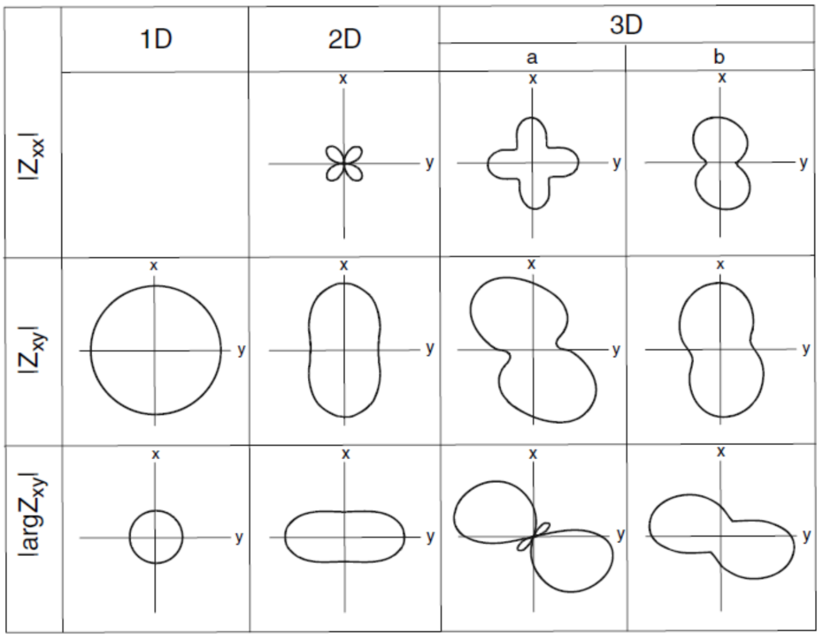

FIGURE 6: Polar diagrams of the impedance tensor (Adopted from Berdichevsky, M. N., and V. I. Dmitriev, 2002)

### 2.9.2 Skew

Skew is the measure of the EM coupling between the measured electric and magnetic field variations in the same direction, defined as ratio of the diagonal and off-diagonal impedance elements ( Swift, 1967).

$$S = \frac{|Z_{xx}+Z_{yy}|}{|Z_{xy}-Z_{yx}|} \tag{2.68}$$

Skew is invariant with the rotation angle. For both 1-D and 2-D structure, skew should be zero but this is rarely the case in practice due to noise in the data. However for 3-D structure there is always a higher value of skew, usually above 0.2 except at a point of radial symmetry, hence skew is regarded as a measure of 3-dimensionality of conductivity structure near the site.

## 2.10 The Transient Electromagnetic (TEM) Method

### 2.10.1 TEM Theory

In the central loop TEM method, a time varying magnetic field is generated by a controlled artificial source. In this method, a loop of wire is placed on the ground and a constant current is built up in it. The current is turned on and off at predetermined times. When the current is turned off, it causes sudden change in magnetic field which further causes current to flow in the earth. This current creates an image of the loops for a short time. Since there is no source to support the induced current it dies out generating a new secondary magnetic field that varies with time and which consequently induces a new current in the ground. This current density migrates downwards and outwards into the earth. The rate of magnetic field decay is measured at the centre of the loop by a receiver coil. The current distribution and the decay rate of the secondary magnetic field depend on the resistivity structure of the earth with the decay being more gradual over a more conductive earth (Árnason, 1989). The TEM configuration and the transient responses can be seen in Figures 7 and 8, respectively.

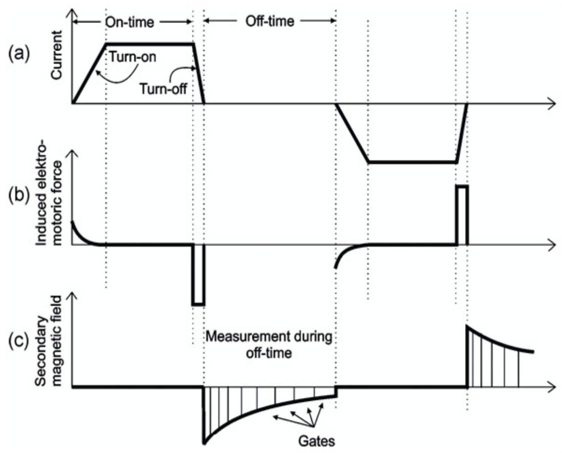

FIGURE 7: Basic principles of the TEM method (a) Shows the current in the transmitter loop. (b) Is the induced electromotive force in the ground, and (c) is the secondary magnetic field measured in the receiver coil (from Christensen et. al, 2006)

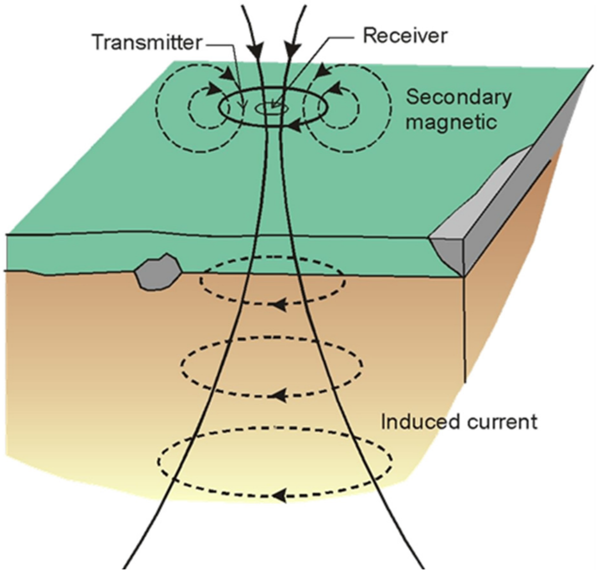

FIGURE 8: The central loop TEM configuration (from Hersir and Björnsson, 1991)

At the so called late times, the induced voltage in the receiving coil on a homogeneous half-space of conductivity, σ is (Árnason, 1989):

$$V(t, r) \approx I_0 \frac{C(\mu_0 \sigma r^2)^{3/2}}{10\pi^{1/2}\, t^{5/2}} \tag{2.69}$$

where, $C = A_r n_r A_s n_s \frac{\mu_0}{2\pi r^3}$

and, $n_r$ = Number of turns on the receiver coil;

$A_r$ = Area of the receiver coil [m$^2$];

$A_s$ = Area of the transmitting loop [m$^2$];

$n_s$ = Number of turns in transmitter loop;

t = Time elapsed after the current in the transmitter is turned off [s];

$\mu_0$ = Magnetic permeability [Henry/m];

$V(t,r)$ = Transient voltage [V];

$r$ = Radius of the transmitter loop [m];

$I_0$ = Current in the transmitting loop [A].

The transient voltage for late times after current in the transmitter is abruptly turned off, is proportional to $\sigma^{3/2}$ and falls off with time as $t^{-5/2}$. This leads to the definition of the late time apparent resistivity by solving for the resistivity in Equation 2.69 leading to Equation 2.70.

$$\rho_a = \frac{\mu_0}{4\pi}\left[\frac{2I_0\mu_0 A_r n_r A_s n_s}{5t^{5/2} V(t,r)}\right]^{2/3} \tag{2.70}$$

## 3. ANOMALOUS DISTORTIONS IN THE EARTH

Electromagnetic distortions are of two types; the galvanic part generated by the excess charges and the induction part which reflects the inductive interaction between the excess currents. Galvanic effects occur when the currents causing a distortion flow across boundaries in electrical conductivity. Induction effects occur when the currents causing a distortion flow entirely within a bounded region (eddy currents). The main difference is that the galvanic distortions occur due to secondary electric field arising from electric charge build-up on boundaries of different conductivities and they persist over the whole frequency range and do not vanish with lowering frequency, while the induction distortions result from induced currents within anomalous conductivity bodies which appear at high frequencies and vanish at low frequencies. A weakness in the MT sounding is that inhomogeneities in the uppermost layers may severely distort the electric field and consequently the impedance tensor along with the apparent resistivities. The dominant distortions are of galvanic nature and they extend over the whole range of frequencies, causing static shifts of the apparent resistivity curves. The near-surface inhomogeneities affect the apparent resistivities, no matter how low the frequency is. The galvanic distortions are very serious because they persist at low frequencies when the penetration depth of the normal field far exceeds the depth and dimensions of the inhomogeneities. Near surface distortions also result from the effects caused by variations in conductance of sediments underlain with resistive basements or by structures in the basement topography. A number of techniques for correcting these distortions have been proposed (Bahr, 1988; Jones, 1988; Groom and Bailey, 1989; Vozoff, 1991; Berdichevsky et al., 1998). But all these techniques are subject to certain approximations that can result in misleading results (false structures).

### 3.1 The MT static shift problem

Static shift in MT is a phenomenon that arises due to local surface or near-surface conductivity contrasts which change the electric field in direction and magnitude. Static shifts occur when the dimensions of anomalous body are much less than the skin depth. All resistivity methods that measure electric field at the ground surface, suffer from the static shift problem. This is occasioned by the accumulation of charges at resistivity boundaries causing the electrical field to be discontinuous close to this boundary. There are mainly two phenomenon that produce static shifts, i.e. voltage distortion and current distortion (current channelling), (Árnason, 2010). The static shift is expressed by scaling of the apparent resistivity by an unknown factor (shifted on log scale), so that apparent resistivity curves plot parallel to their true level. This shift is independent of frequency (Jones, 1988) and does not affect the phase curve.

The static shift factor S, cannot be determined directly from MT data recorded at a single site. A parallel shift between two polarisations of the apparent resistivity curves is a clear indicator that static shift is present in the data. The correct level of the apparent resistivity curves may lie above, below or between the measured responses. These parallel shifts in apparent resistivity curve can lead to large errors in inverted data. For instance a shift down by $S = 0.1$ will in interpretation, result in ten times too low resistivity values and about three times too small depths to resistivity boundaries (Árnason, 2008). In volcanic environments where near surface resistivity variations are often extreme, 2-D and 3-D models may contain extraneous structure if static shifts are not corrected. A static shift multiplier below 1 results in lower resistivities and decreased depth to boundaries whereas a multiplier above 1 results in higher resistivities and increased depth to boundaries. Therefore MT curves are shifted upwards when measuring directly over surficial resistive bodies and shifted downwards when measuring over conductive bodies. Several methods have been advanced as possible solutions for the static shift problem in MT. It has been claimed that the static shift problem can be dealt with by resolving the shallow resistivity structure around the dipole by measuring at high enough frequencies. This would be true if the earth was a pure Ohmic conductor, but in reality both capacitive and inductive effects are at play. DeGroot-Hedlin (1991) and Ogawa and Ushida (1996) have proposed use of an inversion algorithm on MT data themselves to correct for static shift, this assumes that the shift multipliers are random and that the product of the shift multipliers is close to one for many soundings. This may not be necessarily correct as will be seen later in the analysis of shift parameters in the Silali field. Another way and the one that has been used in this report is the use of Central loop-induction TEM sounding to correct for static shift in MT data by jointly inverting both MT and TEM data (Pellerin and Hohmann, 1990). This is based on the fact that, for TEM measurements at late time there are no distortions due to near surface inhomogeneities since TEM does not measure electrical field. This has been tested by model calculations (e.g. Sternberg et al., 1988, Árnason, 2008) and shown to be a useful method to correct for static shifts in MT soundings. It must therefore be born in mind that the success of MT interpretation depends greatly on reliability of the static shift correction.

The processes that cause static shift in MT measurements as proposed by Jiracek (1990), are described below.

### 3.1.1 Current distortion

Current flowing in the earth encounters a conductivity anomalies which affect its flow path. The type of anomalous conductivity determines how the current is altered. Currents are channelled into a higher conductivity anomaly but are deflected from a lower conductivity anomaly. Due to the primary electric field, charges build up on the boundaries of conductivity anomalies depending on the conductivity of the anomalous region compared to its surroundings. In a resistive region, the positive charges accumulate on the side facing the primary electric field, inducing a secondary electric field in and around the conductivity anomaly leading to lateral flow-around effect. Within the resistive body, the secondary field is in the direction of the primary field (Figure 9a). In a conductive anomaly, a negative charge build-up occurs on the side facing the primary electric field, inducing a secondary electric field that opposes the primary field due to lateral current gathering effect (Figure 9b). The distribution of secondary fields outside the anomalous body depends on the geometry of the primary fields.

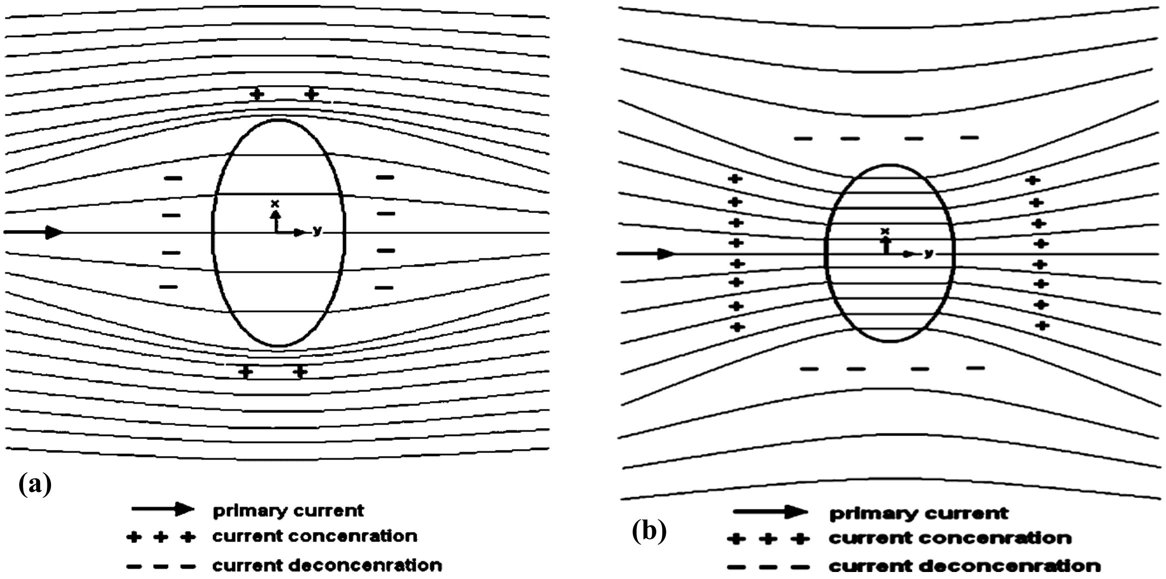

FIGURE 9: Current channelling due to an inhomogeneous conductivity showing; a) Flow-around effect in the vicinity of a resistive and b) Current-gathering effect in a conductive inclusion

Galvanic distortion is caused by charge distributions accumulated on the surface of shallow bodies, which produce anomalous electromagnetic field. This anomalous magnetic field is small, whereas the anomalous electric field is of the same order of magnitude as its regional counterpart and is frequency independent (Bahr, 1988; Jiracek,1990). Hence the galvanic distortion is treated as the existence of an anomalous electric field, $E_a$ (Zhang et al., 1987; Bahr, 1988; Groom and Bailey, 1989; Smith, 1995).

### 3.1.2 Topographic effects

Rough topography can produce static distortion where currents concentrate beneath depressions and disperse under peaks. This leads to electric field increase in valleys and reduction on hills due to galvanic effects. Therefore the current density and the associated MT field is higher in a valley and lower on a hill. This presents as an apparent shift of a resistivity curve shift up or down which can be treated as static shift. Shift correction by TEM can considerably account for the topographical effects (Figure 10).

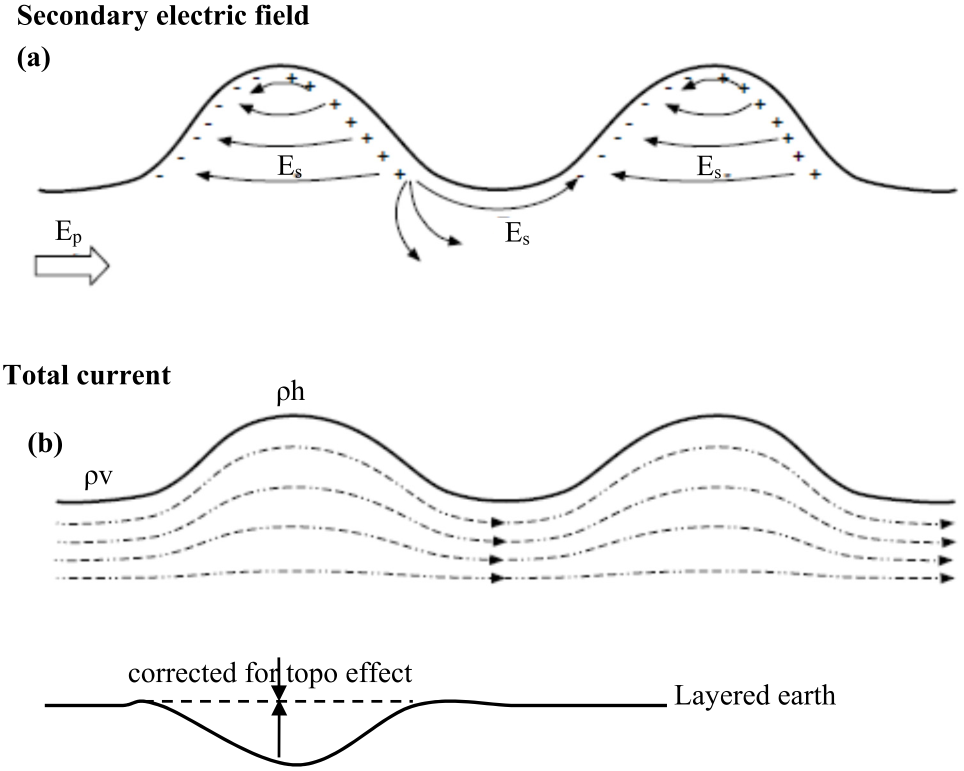

FIGURE 10: Total current distribution and secondary electric field due to topography and correction for the topographical effect

Resistivity at the valley, $\rho_v$ is greater than resistivity at the top of the hill $\rho_{h}$, (i.e. $\rho_v > \rho_h$). In the central-loop TEM method, the measured signal is the decay rate of the magnetic field from the current distribution induced by the current turn-off in the source loop. As these currents diffuse downwards in the earth with time, they are only dependent on the near-surface resistivity structure at very early times. At late times the distortions due to near-surface inhomogeneity disappear, and apparent resistivity is only dependent on the conductivity structure at depth and has no influence from the shallow topographical effects. Therefore the current distortion at shallow depth due to topographic effects has vanishing influence on the TEM data at late times when the induced currents have diffused deep below the surface. Therefore, central loop TEM soundings can be used to correct for static shifts in MT soundings (Pellerin and Hohmann, 1990). Several studies exist on the effect of topography on MT measurements, most of which adopt a numerical modelling approach (Wannamaker et al., 1984; Jiracek et al., 1986). Any attempts to model topography and incorporate it in an inversion would be to introduce topography again after it has been eliminated by static shift correction. Topographic effects on MT responses in 3-D are more complicated than in 2-D because they produce both inductive and galvanic effects in any polarization (Nam et al. 2008), hence carrying out 3-D inversion might considerably reduce them.

## 4. APPLICATION OF RESISTIVITY METHODS IN GEOTHERMAL EXPLORATION

Electrical resistivity surveys have proven to be a method of choice in geothermal exploration for a long time now. This is because they relate directly to the properties that characterize geothermal systems such as permeability, porosity, salinity, temperature and degree of hydrothermal alteration of the rocks (Hersir and Björnsson, 1991). Geoelectrical measurements provide information on the distribution of the subsurface electrical resistivity. High temperature geothermal systems have characteristic subsurface resistivity structure owing to hydrothermal alteration zones (Árnason et al., 2000). The hot fluids of a geothermal system lead to the formation of a sequence of hydrothermal alteration minerals depending on the temperature. Resistivity methods are used to determine variations in electrical conductivity of the sub-surface both laterally and with depth. Among the methods used are the natural-source methods (magnetotelluric) and controlled-source induction methods. EM methods are more sensitive to conductive (low-resistivity) structures compared to direct current (DC) techniques. Several resistivity methods have been applied in geothermal resource assessment for several decades.

### 4.1 Resistivity of rocks

The capability of electromagnetic methods to define geologic structures depends on relations of electrical resistivity to the composition of rocks and geologic processes affecting rocks. Most rock-forming minerals are electrical insulators. Measured resistivities in the Earth materials are primarily controlled by the movement of charged ions in pore fluids or by conduction of secondary minerals. Although water itself is not a good conductor of electricity, ground water generally contains dissolved compounds that greatly enhance its ability to conduct electricity. Hence, connected porosity and fluid saturation tend to dominate electrical resistivity. In addition to pores, fractures within crystalline rock can lead to low resistivities if they are filled with fluids.

The resistivity of a material is defined as the resistance in ohms (Ω) between the opposite faces of a unit cube of the material (Kearey and Brooks, 1994). For a conducting cylinder of resistance (R), length (L) and cross-sectional area (A) the resistivity is given by:

$$\rho = \frac{RA}{L} \tag{4.1}$$

where, $\rho$ is the specific resistivity (Ωm), R is the resistance (Ω), A is area (m$^2$), and $L$ is length (m).

Electrical resistivity depends on degree of water/brine saturation, porosity and the electrical resistivity of the fluid filling the pore space (Palacky, 1987). In fractured media, porosity and permeability are dominated by that of the fractures. Porosity tends to decrease with depth and this reduces the effect of pore fluid conditions, thus reinforcing the resistivity increase, countering to some extent the effect of higher salinity that is commonly inferred to lie in deeper parts of most systems. The electrical resistivity of the pore water is controlled mainly by salinity and less so by temperature. The mineral composition of the rocks, particularly the amount and type of clays present, has the biggest contribution to the bulk electrical resistivity of the rock mass. The influence of pore water on the resistivity of a rock or sediment can be expressed by Archie's Law (1942).

$$\rho_0 = A\rho_f\varphi^{-m} \tag{4.2}$$

where $\rho_0$ is the bulk resistivity, $\rho_f$ is the resistivity of the pore fluid and $\varphi$ is the porosity. The term $m$ is the cementation factor which depends on the degree of interconnectivity of the pore fluids, its values lies between 1.5 and 2.0. Higher values of $m$ in Archie's law reflect less well-connected and low-permeability fluid distribution. The term $A$ depends on pore geometry.

Archie's Law implies that for a given pore fluid the lower the porosity the larger the bulk resistivity. This equation does not take into account conducting mineral grains such as clay. Such conducting grains, if they are electrically connected, will lower the bulk resistivity of a rock from that predicted by Archie's law. Indeed, in the case of clay, the bulk conductivity can come almost entirely from conducting clay minerals rather than pore water.

## 4.2 Resistivity structure of geothermal systems

Geothermal systems are found in zones in the sub-surface that contain abundant heat and sufficient network of pores and fractures for fluids to flow in, such that heat may be transferred by convection to the near surface. Geothermal systems are frequently associated with major tectonic regimes, where heat originates from igneous or volcanic events and fracturing occurs due to crustal movement or above hotspots. If fluids are present within these fractured zone, a geothermal system is developed. The resistivity structure of high temperature geothermal systems has been studied (e.g. Árnason et al., 2000; Ussher et al., 2000), and shown to have typically, a low resistivity cap at the outer limits of the geothermal system with more resistive core towards the centre of the system. This character is found both in fresh water and saline geothermal systems but the overall resistivity is lower in saline systems.

A correlation between the resistivity structure and the hydrothermal alteration of rocks in geothermal systems is discussed in Árnason et al. (2000) and Flóvenz et al. (2005). The boundary between the low resistivity coat and the higher resistivity core has been found to correlate with the change from smectite to chlorite dominated alterations. This alteration change is known to occur at a temperature of approximately 230°C. The low resistivity is dominated by conductive minerals in the smectite-zeolite zone at temperatures of 100-220°C. In the temperature range of 230-240°C zeolite disappear and smectite is gradually replaced by resistive chlorite. At temperatures exceeding 250°C chlorite and epidote are the dominant minerals and the resistivity is probably dominated by the pore fluid conduction in the high-resistivity core. Normally, resistivity decreases with increasing temperature but in high temperature volcanic areas the situation is the reverse particularly in the chlorite and chlorite-epidote alteration zone; where resistivity increases with increasing temperature. This high resistivity exhibited by chlorite and epidote is due to a low concentration of mobile cations.

Care must be exercised when interpreting resistivity due to hydrothermal alteration since alteration might be fossil. This is because if the geothermal system has cooled down then alteration remains and the resistivity structure can be misleading since it reflects the alteration that was formed in the past.

## 5. SILALI GEOTHERMAL AREA

### 5.1 Introduction

The Silali volcanic system is located within the East African rift system (EARS) consisting of a central volcano with a caldera aligned in NW-SE direction and fissures and faults trending in NNE-SSW. This area has experienced immense volcanism and faulting which has motivated investigation of its geothermal potential. Kenya's Geothermal Development Company (GDC) has explored for geothermal resource in this prospect and is in the process of initiating development soon. Extensive geophysical surveys including resistivity (TEM and MT) have been done to delineate the geothermal anomaly. This study seeks to examine the resistivity distribution within the Silali volcanic region in order to define the magmatic, geothermal, and structural features of this active volcano. Recent fissure eruptions occurred about 200-300 years ago in the eastern sector of the Silali volcano. At volcanoes where there has been recent eruption activity, like Silali caldera, magma remnants at depth can be imaged using resistivity investigation.

### 5.2 Kinematics of the East African Rift

Here, reviews for kinematics within this sector of the Rift valley where Silali volcano lies will be presented to highlight the evolution of the Rift and processes therein. The EARS presents a classic example of continental rifting where the African plate is being torn apart by extensional forces. EARS consists of two branches, the western and eastern branches of the rift (Figure 11). The eastern branch of the EARS where the area of study is located extends over 2000 km from the Red Sea in the north to Mozambique in the south, traversing two regions of topographic uplift, the Ethiopia and Kenya domes which are regarded as the surface manifestation of mantle plumes (Nyblade et al., 2000).

This extensional deformation occurs because of an underlying mantle plume (Zeyen et al, 1997) rising from below and stretching the overlying continental crust. Upwelling mantle may melt to produce magmas, which then rise to the surface, often along volcanic fissures produced by the extensional deformation. Basaltic and rhyolitic volcanism is common in these volcanic regimes.

The East African Rift is a fault-bounded depression roughly oriented in the NS direction and marks the divergent boundary between two major tectonic plates, Somalia and Nubia. The Nubia-Somalia Euler pole is located at 54.8°S; 37.0°E with magnitude of 0.069°/Ma (Fernandes, et al., 2004*),* implying distinct opening in the Ethiopian Rift of magnitude about 7 mm/year and azimuth N94°E, whereas in South-most sector of the rift this value is reduced to 2 mm/year in almost the same direction. This decrease in extension is consistent with decrease in seismicity and with progressive disappearance of prominent active faults southwards along the eastern branch as it propagates into colder Tanzania craton. In addition to far-field plate motions, the kinematics of the EAR itself remains an open question. Some authors have proposed that the EAR consists of a mosaic of rigid lithospheric blocks bounded by localized deformation within narrow seismically and volcanically active Rift valleys (e.g., Hartnady, 2006). Recent studies using both INSAR, GPS and earthquake slip vectors (Baer et al., 2008 and Ebinger et al., 2009) within the EAR show evidence of crustal deformation in some sectors of the Rift with eruptions occurring in Afar, Ethiopia in the North and Oldoinyo Lengai, Tanzania in the south. Similar deformations could be occurring in the other sectors within the East Africa Rift system.

### 5.3 Location and geology of Silali area

The Silali volcano (Figures 11 and 12) is the largest of the Quaternary shield volcanoes, in the northern sector of the Kenya Rift, measuring 30 km by 25 km (Dunkley et al., 1993; Smith et al.,1995). Activity commenced at 400-220 ka with the construction of a low relief lava shield whose summit area was subsequently modified by faulting and subsidence. The caldera formed at about 63 ka with the youngest eruption about 200-300 years ago (Dunkley et al., 1993). This volcano stands 800 m above the Rift floor and was formed by alternating episodes of faulting, subsidence and infilling associated with pyroclastic deposition and basaltic volcanism that created a 7.5 km by 5 km caldera with 300 metres near vertical walls at its summit. These processes were accompanied by fracturing and decompression of a magma chamber, regional extension and injection of dykes beneath the volcano (Smith et al., 1995; Williams et al., 1984). The caldera elongation in NW-SE has been interpreted as a reflection of an elliptical shape in the underlying magma chamber (Bosworth et.al, 2000).

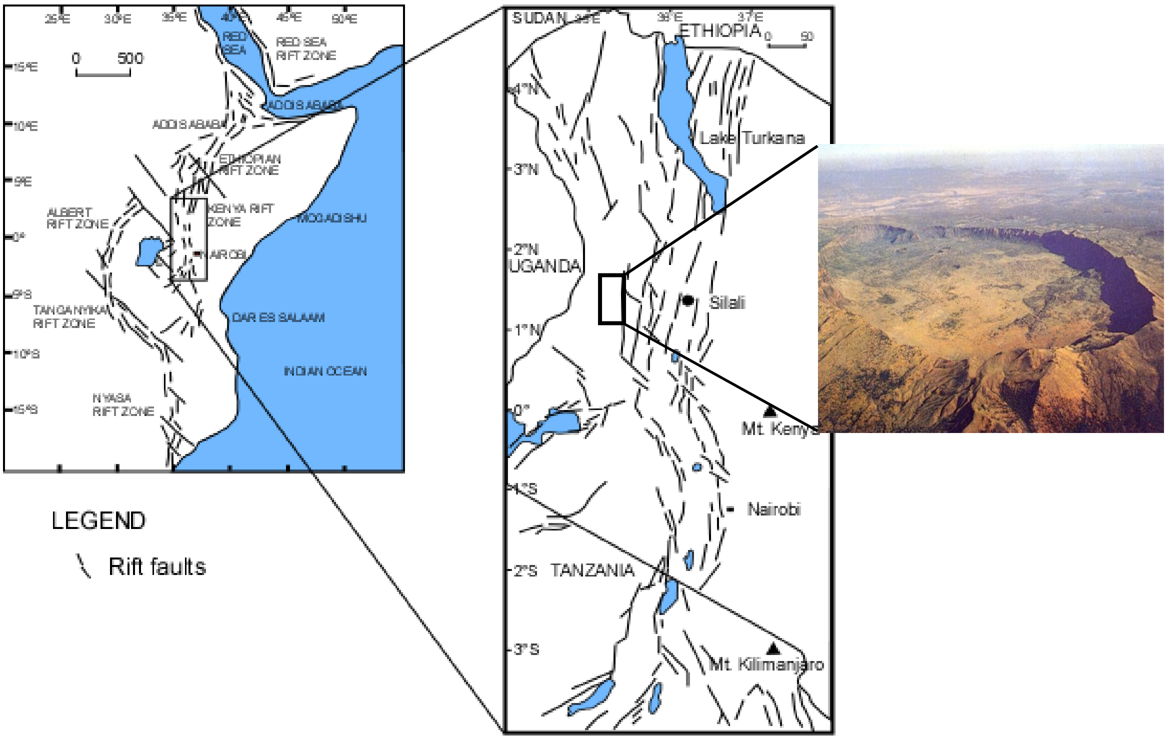

FIGURE 11: Map showing the Kenya Rift and the volcanic centers and lakes.
Silali (rectangular box) is the volcanic centre of focus for this study

The geology of the Silali region can be divided into groups based on the times of emplacement as: The post caldera group, the pre-caldera group, the western flank group, and the caldera wall group. The post caldera group consists of the intra-caldera and extra-caldera sub-groups that are mainly basalts and trachytes. The Katenmening lava and the Kapedo tuffs are distinctive markers for the pre-caldera group and the caldera wall group, respectively (Smith et al., 1995;Williams et al., 1984).

The western flank of the caldera is covered by the Arzett tuff and the Summit and Discoid trachytes (Macdonald et al., 1995). Fault surfaces have exposed the different sequences. For example, east of the volcano, basalts overlie or are faulted against west dipping Miocene trachytes and basalts, while on the west, basalts are exposed near Kapedo and overlie trachytes and pyroclastic deposits (Smith et al., 1995). The numerous faults around the Silali volcano have a generalized north to northeast trend, with a zone of intense faulting, approximately 10 km wide, which defines a series of en echelon grabens (Figures 12 and 14). The eastern part of the caldera is more fractured than the western part, and fissures within the intensely faulted region may have favoured the flow of material, like lava, to the surface (Smith et al., 1995). The recent eruption occurred in the Black Hills where lava erupted mainly from the vents to the east of the caldera. These lavas may have been derived from a separate reservoir via a dyke system (Smith et al., 1995). All Silali basalts are relatively evolved; primitive basalts were probably held close to the Moho, where they evolved by gabbro fractionation to produce basalts with less than 8% MgO (Smith et al., 1995). These magmas were subsequently held at several levels in the crust, including the Rift-axial lava-sediment sequence. Magma mixing between basalt and trachyte has been common at Silali, implying complexity of the plumbing system. Evolution of the trachytes was by fractional crystallization combined with assimilation of crust during or after fractionation. The basalts and inferred trachytic derivatives were derived from at least two mantle sources that are distinct in both isotopic and trace element characteristics. Geological evidence suggest lateral movement of magma along a dyke swarm cutting through the volcanic system (Smith et al., 1995), implying that these mantle sources may not lie directly beneath Silali.

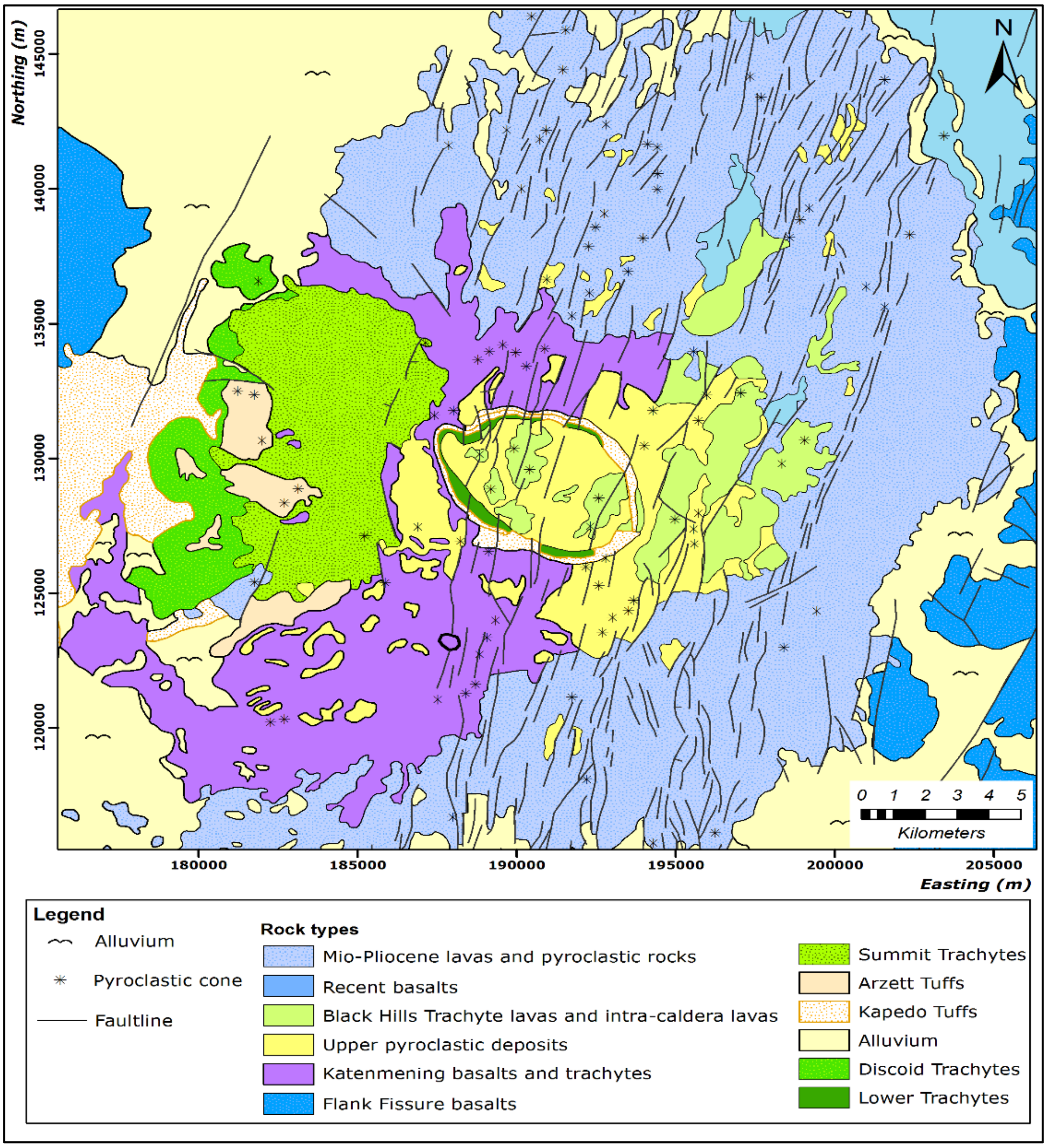

FIGURE 12: A simplified geological map of the Silali area modified from Dunkley et al. (1993). The Silali caldera is defined by the shield trachyte.

### 5.4 Formation of Silali caldera

Kenya rift valley developed in response to E-W tensional stresses during late Neogene. Similarly axial volcanoes align parallel to the rift with the vents and features in the vicinity also aligning in similar direction, which is in agreement with minimum horizontal stress direction ($SH_{min}$) of approximately E-W (Figure 13a). In the region of Silali a large number of pyroclastic and lava cone orient in N10°E direction. This implies that older surface vents are generally aligned parallel to the local maximum horizontal stress direction ($SH_{max}$).

Generally rows of small vents, cones, domes and collapse pits are common in volcanic terrains. These features are thought to form above feeder dikes. Although dike orientation can be influenced by the orientation of pre-existing faults and other structures, in general the strongest control on dike orientation is the country rock stress field, with intrusion perpendicular to the least principal stress (Delaney et al., 1986). For Silali caldera to have formed, a huge magma must have been withdrawn from below the volcano and erupted on the surface but this evidence seems to be lacking around Silali. It is postulated that magma could have been injected into the more dominant N-S oriented structures to accommodate the collapse.

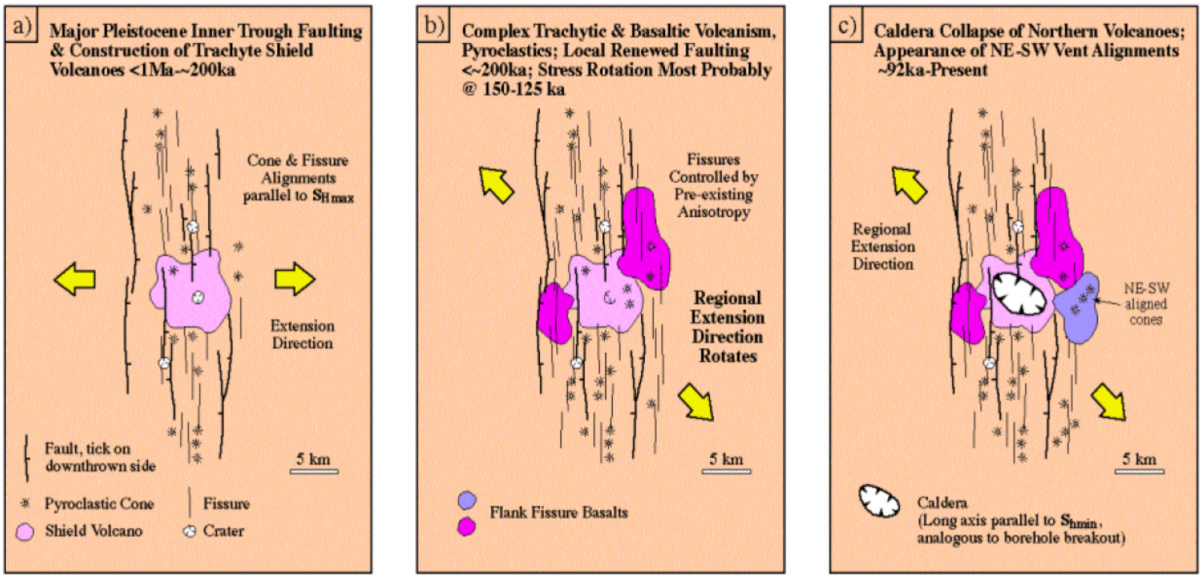

FIGURE 13: Evolution of inner rift and Silali caldera orientation as result of minimum horizontal stress direction (Adopted from Bosworth et.al, 2000)

In the area around Silali volcano young vents (Figure 13b) are predominantly aligned NE-SW, also indicating NW-SE $SH_{min}$, this means that this NW-SE $SH_{min}$ is a very young stress field orientation (Bosworth et al., 2000). To the East of Silali caldera, in the Black Hills, very young trachyte lavas display two fissure and cone alignment trends, one older N-S and the other N50°E (Figure 5.3c). The presence of N50°E volcanic alignments in the youngest units of the rift axial volcanoes supports the interpretation that a new stress field is evident within the rift valley axis. This places the NW-SE trending long axes of the Silali caldera sub parallel to $SH_{min}$ of this new stress field. This demonstrates that despite the very strong N-S structural and volcanic fabric of the inner rift, feeder dikes have been forced to change to the new, mechanically most efficient orientation. This elongation is most likely related to the stress state in this sector of the rift, and not to pre-existing fractures (Bosworth et al., 2000). The Silali caldera collapse was probably a result of rapid withdrawal of magma from beneath the active volcano, and the violent eruption of these magma from volcanic flanks was probably due to rotation of the regional Shmin direction, and possibly changes in its magnitude. The caldera elongation reflects a similar shape in the underlying magma chamber, which in turn represents a mechanical response to the presence of non-hydrostatic stresses in the adjacent country rock.

### 5.5 Structures controlling geothermal system in Silali area

The main faults and fracture form a prominent NNE-SSW trending volcanic rift zone, 10 km wide and up to 30 km long that probably represents important conduits for circulation of thermal waters. Generally N-S trending fault structures, the main rift faults and the fractured Plio-Pleistocene lavas within the rift floor influences the geothermal system of the Silali volcano by acting as conduits for recharging the system. Additionally the Silali caldera structure presents a unique feature which is a result of collapse into the top of a magma chamber after eruptive activities. The caldera elongation in NW-SE reflects a similar shape in the underlying magma chamber. A lineament structure trends in NW-SE direction (Figure 14) cutting Silali caldera walls in the South-Eastern and the North-Western flanks. Where the structure intersects the caldera walls, a lot of geothermal manifestations occur in the form of fumaroles and altered grounds.

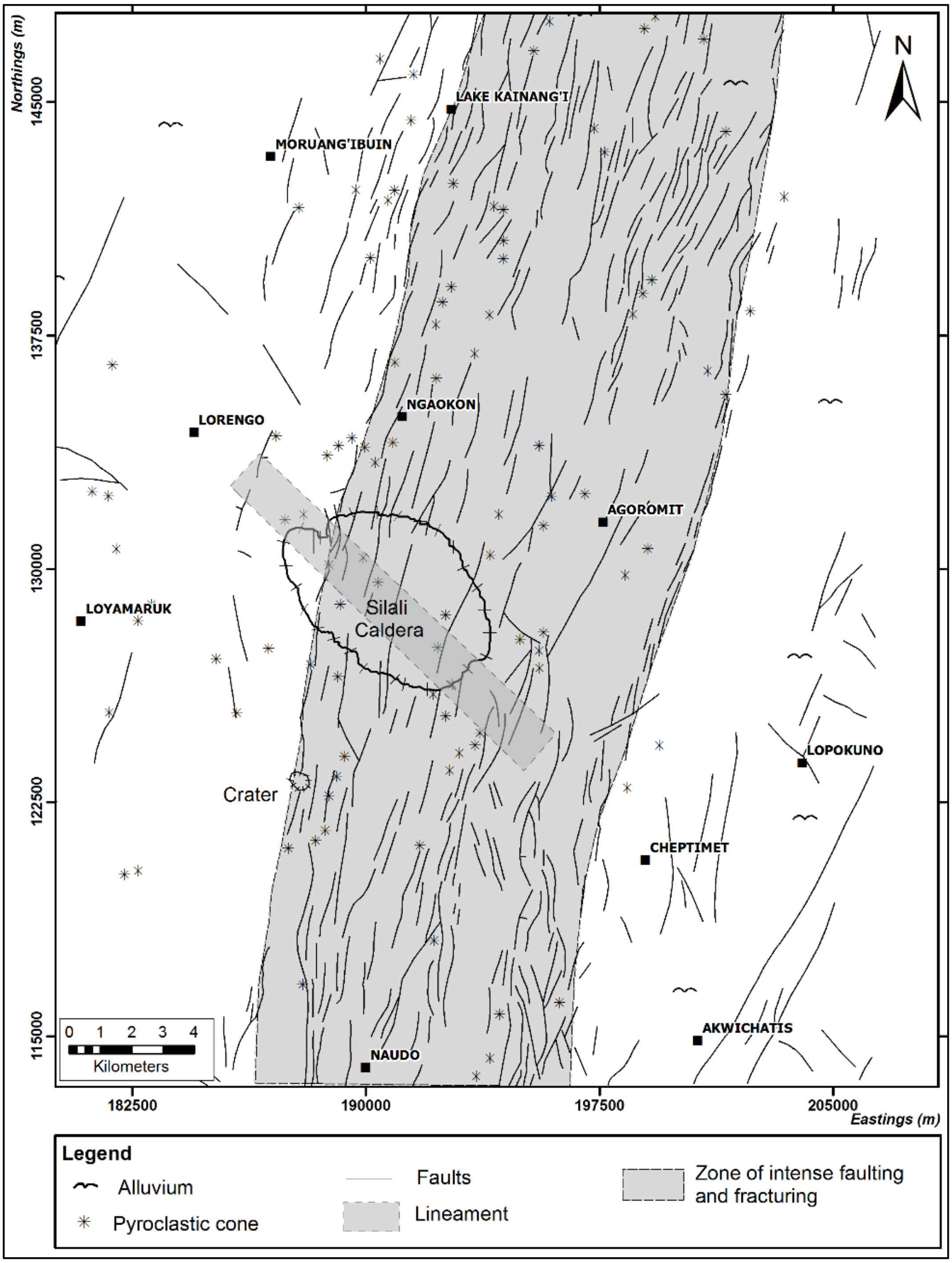

FIGURE 14: Structural map of Silali prospect showing zones of intensive faulting and the lineament

### 5.6 Geothermal manifestations

The major geothermal manifestations occur within the caldera floor and on the eastern highly faulted slopes of the volcano and cover an area of about 20 km$^2$ (Figure 15). Some manifestations also occur along river Suguta in the west and along fractures in the far north of the volcano. Manifestations mainly occur in form of altered grounds, steaming grounds, hot springs, and fumaroles. The hottest and most extensive activities occur in the eastern half of the caldera floor, where most hot altered ground are aligned to the N-S fissure zone. At the foot of the South Eastern walls, highly altered grounds and fumaroles were mapped. Fumaroles and hot grounds occur mainly within the fissures trending N-S on the Eastern flanks of the caldera. These fumaroles are active and temperatures above 80°C have been recorded. At Kapedo, fault zones directly below the discoid trachyte result in a series of hot springs at the riverbed. These hot springs at the base of the western slopes of the Silali volcano are the source of River Suguta and they discharge at temperatures of 55ºC with a combined estimated flow rate of about 1,000 l/s. Further northwest at Lorusio main manifestations include hot springs with measured temperatures between 65-81.7°C occurring on a lowland. The hot springs flow eastwards away from ranges of hills hosting dyke swarms and volcanic cones.

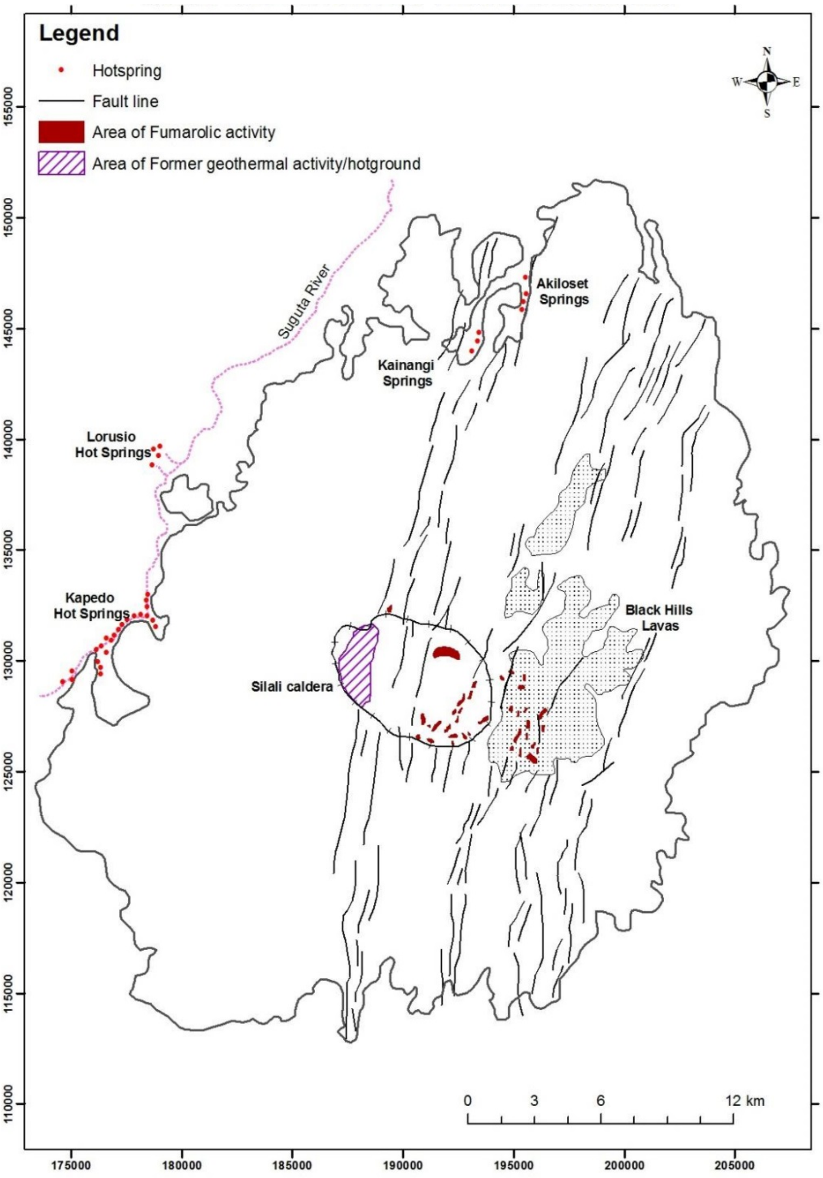

FIGURE 15: Tectonics of the Silali region showing numerous faults and fissures. Modified from Smith et al., (1995)

There are a series of springs occurring within a discharge area of about 2 km$^2$, the largest spring has an estimated flow rate of 15 l/s (Dunkley et al, 1993). The warm springs of Akiloset and Kalnangi are located around the periphery of the northern flanks of Silali and drain northwards and detour westwards to join Suguta river. These warm springs discharge at a temperatures of 38ºC with low individual flow rates.

## 5.7 Previous studies

The Kenya Rift has been extensively studied as the basis for understanding the processes of continental plate breakup (e.g. Keller et al., 1994; Simiyu and Keller, 1997 and 2001; Mariita and Keller, 2007). However, detailed studies that focus on the various volcanic centres along the Rift are limited. Due to the rugged terrain that limits accessibility, the Silali volcano had not been studied in much detail. However, the growing need for geothermal energy development in Kenya has given incentive to the first detailed geophysical data collection around the caldera region which will be the focus of this study.

### 5.7.1 Gravity

Previous studies (Fairhead, 1976; Simiyu and Keller, 1997; Mariita and Keller, 2007) have indicated that the location of the volcanic centres along the Rift, including the Silali volcano, coincides with a 50 km wide gravity maximum with an amplitude of about 20 mGals which has been used to infer an uplift of an asthenospheric body. This amplitude is typical for most geothermal fields around the world (Monastero et al., 2005). This high gravity anomaly was interpreted as the result of a shallow magma chamber and dykes along the Rift axis. The gravity data distribution however is sparse (about 5 km spacing) and hence could not adequately image detailed structures around the volcano.

### 5.7.2 Aero-Magnetics

Regional aero-magnetics survey was carried out along the Rift Valley (NOCK, 1987) at a terrain clearance of 2996 masl. The results show areas marked by a series of high amplitude magnetic anomalies with amplitudes reaching several hundred gammas and shapes that are either isometric or oval. The positive anomalies coincide closely with known Quaternary volcanoes showing magnetic field typical of what is observed over basaltic volcanics. These high magnetic makers would suggest massive basalts in the subsurface (if not exposed), whereas the overlying terrain would have negligible susceptibility compared to that of basalt.

### 5.7.3 Seismic studies

Past studies have shown that the Eastern rift which has eruptive centres along its length also has moderate seismic activity, except near its southern termination at the edge of the Tanzania craton (e.g., Nyblade & Langston 1995). A regional seismic refraction study was carried out on a traverse covering 750 km along the Rift as seen in the section below (Figure 16). It indicates that a thinner crust of about 20 km exist below the Northern Kenya Rift increasing Southwards reaching 35 km below the Kenya dome. Thus, it can be concluded that the presence of a heat anomaly for the past 20 Ma in the southern part of the Kenya dome, in the southern part of the Rift is compatible with the present-day observations of a steep-sided region of anomalously low P-wave velocities (Simiyu and Keller, 1997). Below the surface expression of the Rift a sharp transition to mantle material with normal P-wave velocities down to 100-150 km depth is evident. Further work by Keller et al. (1994) have described a sharply defined lithospheric thinning, with low upper mantle velocities down to depths of over 150 km. A distinct relative positive residual anomaly in the middle of the graben is due to dyke injection, related to reservoirs of magma.

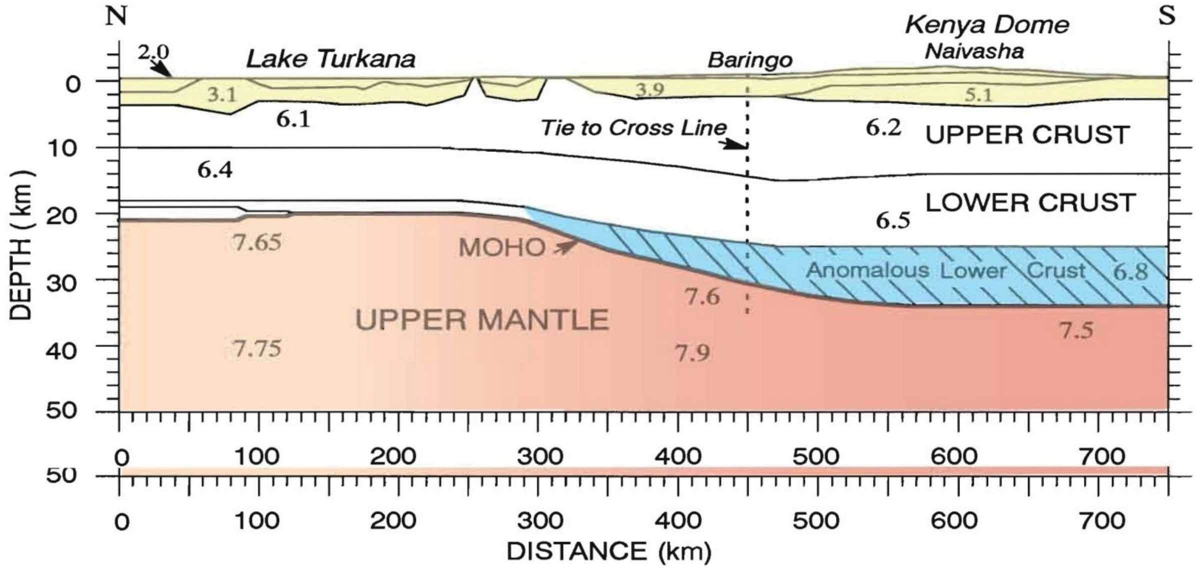

FIGURE 16: Axial crustal model (Modified from Simiyu and Keller, 1997).
P-wave velocities in km/s are shown.

# 6. MT AND TEM FIELD SETUP AND DATA PROCESSING IN SILALI FIELD

## 6.1 TEM survey and instrumentation

The TEM data in Silali prospect has been collected since the year 2010. A total of 154 TEM soundings have been done in the area, but only 102 soundings which are in close proximity of the MT soundings are used in this study (Figure 17). Two different TEM systems have been used in these surveys namely Zonge and V8-Phoenix TEM equipment, respectively. Usually, the data was collected for two different frequencies of the current signal, 16 Hz and 4 Hz for Zonge TEM and 25 and 5 Hz for V8 TEM. Both equipment comprise of a current transmitter, a data logger, a receiver coil with effective area of 10000 m$^2$, a power source and a transmitter loop.

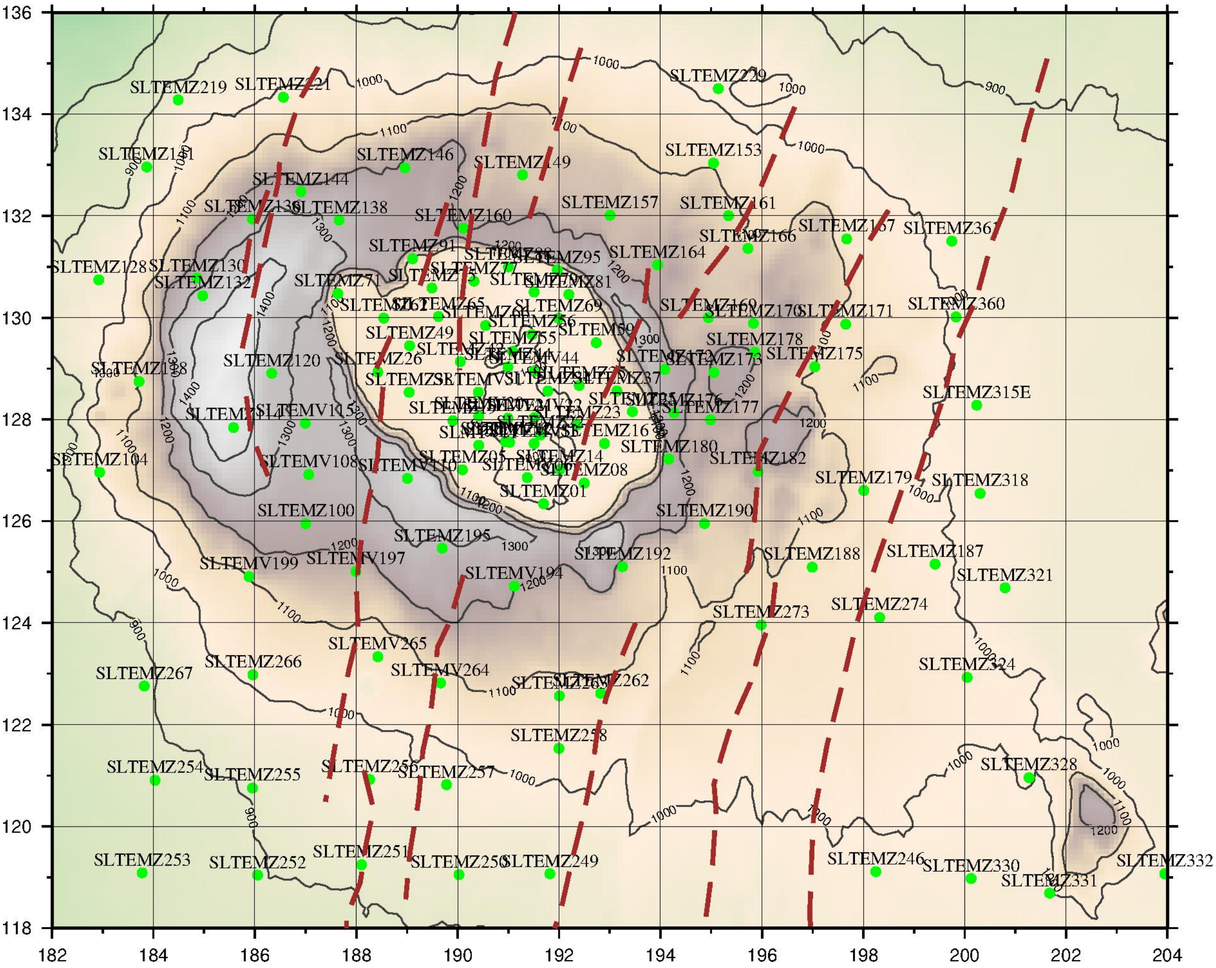

FIGURE 17: TEM sounding locations; the topography data on the basemap was downloaded from the internet. Shown on the map is the Silali caldera and the brown broken lines represent faults. The green dots represent TEM soundings.

For the Zonge TEM the transmitter controller high-precision crystals are warmed up for a period of about an hour and then synchronized to ensure that induced voltage is measured by the receiver at the correct time after the current turn-off. Whereas for the V8 TEM the synchronization is achieved by a radio link between the transmitter and the V8 receiver. In the field setup depending on the available space either a 300m x 300m or 200m x 200m transmitter wire loop was used and a half-duty square wave current transmitted at frequencies stated above. In both cases the transient signal was recorded at the centre of the loop at time intervals logarithmically-spaced sampling gates after the current turn-off.

## 6.2 TEM data processing and 1-D interpretation

The raw TEM data was processed by the program TemxZ for Zonge data and TemxV for V8 data, a modified version of Temx to handle Zonge and V8 data (Árnason, 2006). This program averages data acquired at same frequency and calculates late time apparent resistivity as a function of time after turn-off. It also enables visual editing of raw data to remove outliers and unreliable data points before the data can be used for interpretation. 1-D inversion of TEM is achieved by software called TEMTD a UNIX program (developed at Icelandic Geosurvey by Knutur Árnason). The forward algorithm calculates the induced transient voltage in the receiver as the sum of the responses from successive current turn-on and turn-off times. The transient response is calculated both as induced voltage and late time apparent resistivity as a function of time.

The inversion algorithm used in this program is a nonlinear least-squares inversion of the Levenberg-Marquardt type as described by (Árnason, 1989). The misfit function is the mean-square difference between measured and calculated values (chi$^2$), weighted by the standard deviation of the measured values. In this study the measured voltages were chosen for inversion. The damping is achieved by utilizing both first derivatives and second derivatives, to obtain smooth models. The actual function that is minimized is the potential ($\varsigma$) instead of the weighted mean-square misfit ($chi^2$).

$$\varsigma = chi^2 + \alpha D_{S1} + \beta D_{S2} + \gamma D_{D1} + \delta D_{D2} \tag{6.1}$$

where $D_{S1}$ and $D_{S2}$ are the first and second order derivatives of log-conductivities in the layered model, and $D_{D1}$ and $D_{D2}$ are the first and second order derivatives of the logarithms of the ratios of layer depths. The coefficients, α, β, γ and δ are the relative contributions of the different damping terms. The half-space or basement depth was set at 1500 m while the number of layers for the initial model depended on the data, but in most cases it was fixed at 5. The inversion searches for conductivities of the layers as well as finding the optimal thickness of each layer.

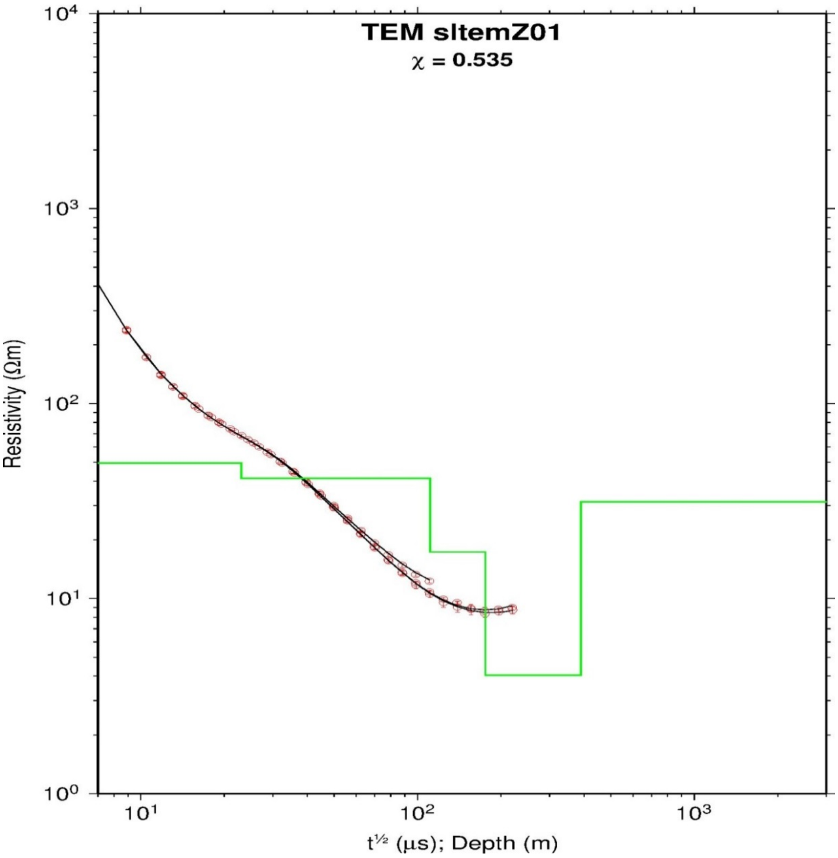

FIGURE 18: TEM sounding from Silali area and its 1-D inversion. It illustrates the TEM apparent resistivity curve and its interpretation, the red dots are measured late-time apparent resistivities and the black solid line is the apparent resistivity calculated from the model shown in green

All the TEM soundings in Silali area have been interpreted by 1-D (layered earth) inversion (Appendix I) as shown in (Figure 18), with as smooth models as possible. In 1-D inversion it is assumed that the earth consists of horizontal layers with different resistivity and thickness. The 1-D interpretation seeks to determine the layered model whose response best fits the measured responses. When interpreting TEM resistivity it must be born in mind that the depth of investigation of the TEM soundings is much greater in resistive earth than in conductive environments.

## 6.3 MT field survey and instrumentation

A total of 102 MT soundings are considered for interpretation in the Silali prospect as seen in (Figure 19). The data was acquired using 5-channel MT data acquisition system (MTU-5A) from Phoenix Geophysics. Instruments used for MT survey include a data logger (MTU), 2 pairs of electric dipoles for sensing the electric potentials and 3 magnetic sensors for sensing the magnetic induction. The data logger controls the acquisition process, amplifies and filters the data and converts to digital format for storage into a flash memory. Usually the data logger has 5 channels, 2 for the orthogonal horizontal electrical fields ($E_x$, $E_y$) and 3 for the orthogonal horizontal and vertical magnetic fields $H_x$, $H_y$, and $H_z$ (Figure 20). The electric field components ($E_x$ and $E_y$) are realized by measuring the potential difference, $\Delta V$, between pairs of electrodes, which are connected via a shielded cable to form a dipole and buried in the ground at known distance, d, which gives electric field, $E = \Delta V/d$. In the field setup, one electric dipole is oriented in the magnetic N-S direction, and the other in the magnetic E-W direction. Contact resistance and noise is reduced by installing electrodes in wet pits moments before they are used to allow the electrochemical environment to stabilize.

The use of non-polarisable electrodes is preferred. These consist of a plastic pot with a porous bottom filled with a metal in contact with a solution of a salt of the same metal. A common combination is to use lead (Pb) and a solution of lead-chloride ($PbCl_2$) in the electrodes. The magnetic fields are measured with magnetic field coils oriented in the x, y, z directions. When setting up an MT sounding in the field, a spirit level and a compass are used to align all the measurement axes such that the x, y directions are horizontal and orthogonal to each other and the z is vertical. Conventional alignment requires that x is positive to magnetic North, y positive to the magnetic East and z positive vertical down.

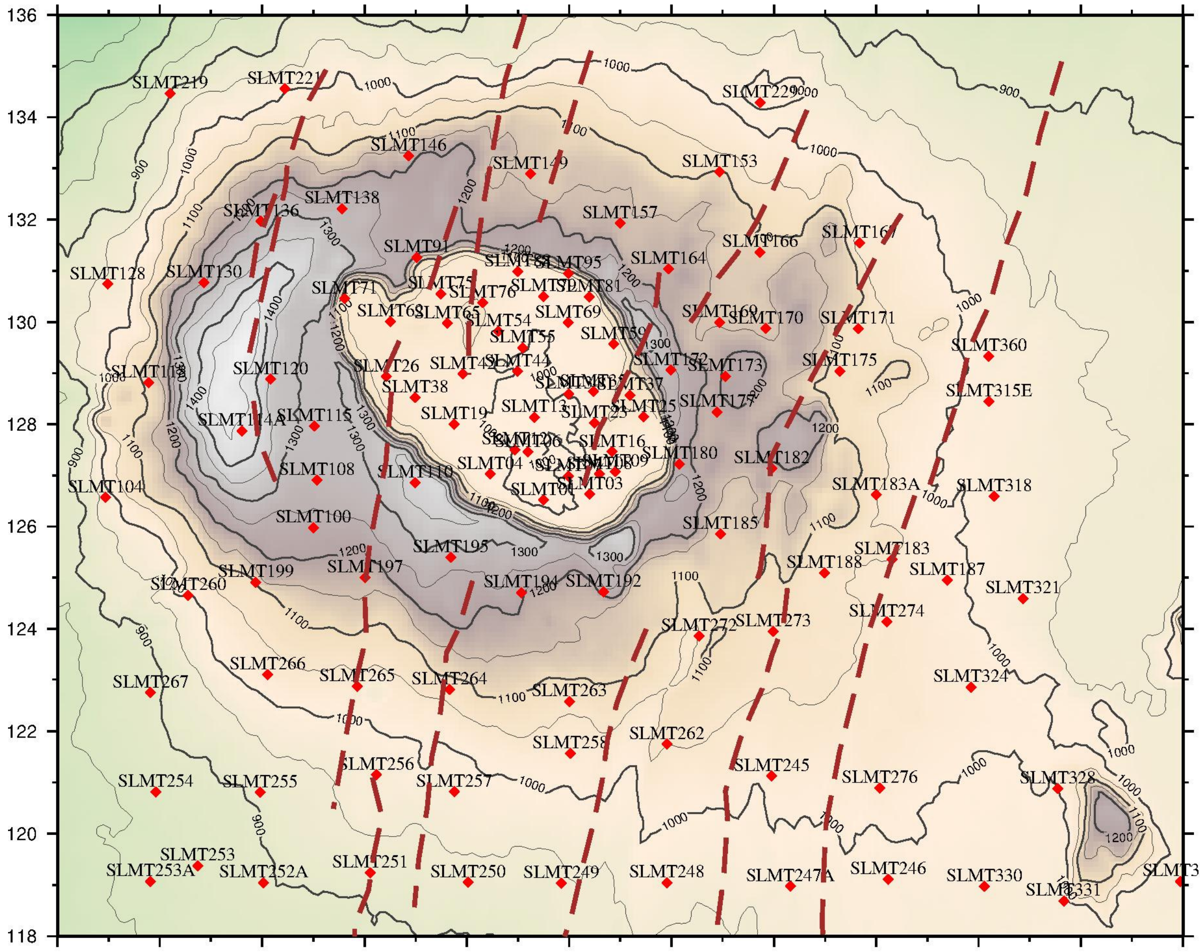

FIGURE 19: The sounding distribution over the prospect area, Datum used is Arc 1960. Shown on the map is the Silali caldera and the brown broken lines represent faults. The red dots represent MT soundings

During data acquisition one 5-component MT station was installed away from the field of focus and maintained as a remote reference station which was later used during data processing to reduce effect of local cultural noise. This is based on the fact that magnetic signal tends to be the same over large area and that local disturbances at the local station may not necessarily be recorded at the remote site (Gamble et al., 1979). During Robust processing, estimates of magnetotelluric and geomagnetic response functions are determined using the coherency and expected uniformity of the magnetic source field as quality criteria. In some extreme cases, where noise was either negligible or far greater than signal, the remote reference approach was unable to improve results, and data had to be processed using single site robust processing (Smirnov, 2003). All the stations were time synchronized via signals from Global Positioning System (GPS) satellites so that time-series data from the remote reference station was processed in combination with data acquired at same time from the other stations to reduce the effects of local noise and improve the quality of the survey results.

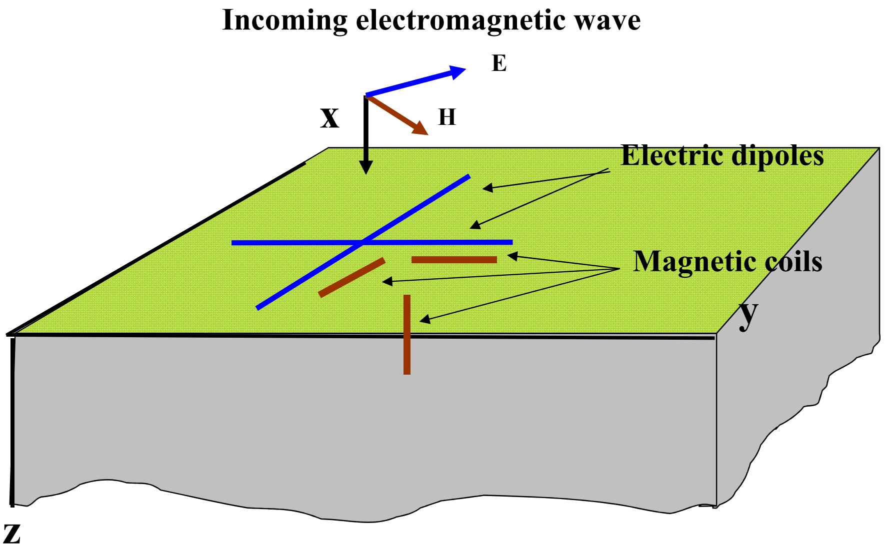

FIGURE 20: Field MT layout

### 6.4 MT data processing

As a first step after downloading time-series data from the MT equipment the data is inspected using the Synchro-Time Series Viewer program provided by the manufacturer, Phoenix Geophysics of Canada (Phoenix Geophysics, 2005). This program allows viewing and printing of graphical representations of the raw time-series data, power spectra derived from the time-series data and coherence between pairs of orthogonal electric and magnetic components. Time series processing is achieved by the SSMT2000 program, provided by the equipment manufacturer, (Phoenix Geophysics, 2005). Prior knowledge of the magnetic declination is needed to be provided into the start-up file so that the program rotates the impedance tensor elements to the geographic north-south direction. In the study area magnetic declination was zero and therefore rotation was not necessary. First a parameter file was edited to reflect the data acquisition setup and the resulting time-series data were Fourier transformed to the frequency domain.

### 6.4.1 Time series to frequency domain conversion

Fast Fourier Transforms (FFT) are commonly used to transform the measured time series to the frequency domain (Vozoff, 1991). Usually a raw spectrum with a number of data points divided into 2 frequencies is obtained. These frequencies are equally distributed on a log scale, optimally 6-10 period per decade. The final spectra are smoothed by averaging over neighbouring frequencies using a window function. The auto and cross spectra segments which are products of the field components and their complex conjugates, are calculated from segments of the original time series for each frequency. To determine the tensor elements time series are Fourier transformed by:

$$H_x(t) \rightarrow H_x(\omega); \qquad H_y(t) \rightarrow H_y(\omega)$$

$$E_x(t) \rightarrow E_x(\omega); \qquad E_y(t) \rightarrow E_y(\omega) \tag{6.2}$$

### 6.4.2 MT transfer function estimation

The evaluation of MT transfer functions need averaging of spectra over a number of closely spaced frequencies of the corresponding field components in the frequency domain, which can be obtained from the electric and magnetic field spectra segments as:

$$E_x(\omega) = Z_{xx}H_x(\omega) + Z_{xy}H_y(\omega) \tag{6.3a}$$

$$E_y(\omega) = Z_{yx}H_x(\omega) + Z_{yy}H_y(\omega) \tag{6.3b}$$

The impedance equations are solved assuming $Z_{ij}$ to be constant over an averaging band (window), which is physically reasonable if the bands are narrow enough. In each band, each equation has cross-power taken with $H_x$ and $H_y$ in turn, giving equations:

$$\langle E_x H_x^* \rangle = Z_{xx}\langle H_x H_x^* \rangle + Z_{xy}\langle H_y H_x^* \rangle \tag{6.4a}$$

$$\langle E_y H_x^* \rangle = Z_{yx}\langle H_x H_x^* \rangle + Z_{yy}\langle H_y H_x^* \rangle \tag{6.4b}$$

$$\langle E_x H_y^* \rangle = Z_{xx}\langle H_x H_y^* \rangle + Z_{xy}\langle H_y H_y^* \rangle \tag{6.4c}$$

$$\langle E_y H_y^* \rangle = Z_{yx}\langle H_x H_y^* \rangle + Z_{yy}\langle H_y H_y^* \rangle \tag{6.4d}$$

where $H_x^*(\omega)$ and $H_y^*(\omega)$ are conjugates of the horizontal magnetic field components.

Equations 6.4a-d can be solved for $Z_{ij}$ as follows:

$$Z_{xx} = \frac{\langle E_x {H_x}^* \rangle\langle H_y {H_y}^* \rangle - \langle E_x {H_y}^* \rangle\langle H_y {H_x}^* \rangle}{\langle H_x {H_x}^* \rangle\langle H_y {H_y}^* \rangle - \langle H_x {H_y}^* \rangle\langle H_y {H_x}^* \rangle} \tag{6.5a}$$

$$Z_{xy} = \frac{\langle E_x {H_x}^* \rangle\langle H_x {H_y}^* \rangle - \langle E_x {H_y}^* \rangle\langle H_x {H_x}^* \rangle}{\langle H_y {H_x}^* \rangle\langle H_x {H_y}^* \rangle - \langle H_y {H_y}^* \rangle\langle H_x {H_x}^* \rangle} \tag{6.5b}$$

$$Z_{yx} = \frac{\langle E_y {H_x}^* \rangle\langle H_y {H_y}^* \rangle - \langle E_y {H_y}^* \rangle\langle H_y {H_x}^* \rangle}{\langle H_x {H_x}^* \rangle\langle H_y {H_y}^* \rangle - \langle H_x {H_y}^* \rangle\langle H_y {H_x}^* \rangle} \tag{6.5c}$$

$$Z_{yy} = \frac{\langle E_y {H_x}^* \rangle\langle H_x {H_y}^* \rangle - \langle E_y {H_y}^* \rangle\langle H_x {H_x}^* \rangle}{\langle H_y {H_x}^* \rangle\langle H_x {H_y}^* \rangle - \langle H_y {H_y}^* \rangle\langle H_x {H_x}^* \rangle} \tag{6.5d}$$

### 6.4.3 Remote-reference estimates

In remote referencing method (Gamble et al., 1979; Clarke et al., 1983) sensors are deployed at a site remote from the local measurement site. The natural part of the induced EM field can be coherent over several kilometres, noise is generally random and incoherent at two locations far away from each other (10-100 km). Therefore, by measuring selected electromagnetic components at both local and remote sites, bias effects arising from the presence of noise that is uncorrelated between sites can be removed. On the other hand correlated noise that is present in both local and remote sites cannot be removed by this method. To achieve uncorrelated noise the distance between local and remote sites is dictated by the anticipated noise source, intended frequency range of measurement and general conductivity of the sounding locations. The noise can be wind-induced noise, for which the remote needs to be some hundreds of metres away, to cultural disturbances, for which in extreme cases the remote has to be many tens to hundreds of kilometres away.

Both at the local and remote site, the electric and magnetic field spectrum are linearly related. Multiplying these equations by the spectra ${R^*}_x(\omega)$ and ${R^*}_y(\omega)$ and averaging over frequency intervals, we get:

$$\langle E_x {R_x}^* \rangle = Z_{xx}\langle H_x {R_x}^* \rangle + Z_{xy}\langle H_y {R_x}^* \rangle \tag{6.6a}$$

$$\langle E_y {R_y}^* \rangle = Z_{yx}\langle H_x {R_y}^* \rangle + Z_{yy}\langle H_y {R_y}^* \rangle \tag{6.6b}$$

$$\langle E_x {R_y}^* \rangle = Z_{xx}\langle H_x {R_y}^* \rangle + Z_{xy}\langle H_y {R_y}^* \rangle \tag{6.6c}$$

$$\langle E_y R_x^{*}\rangle = Z_{yx}\langle H_x R_x^{*}\rangle + Z_{yy}\langle H_y R_x^{*}\rangle \qquad (6.6d)$$

These four equations can be solved for the four desired remote reference estimates of the impedance tensor elements $Z_{ij}$ as given below:

$$Z_{xx} = \frac{\langle E_x R_x^{*}\rangle\langle H_y R_y^{*}\rangle - \langle E_x R_y^{*}\rangle\langle H_y R_x^{*}\rangle}{\langle H_x R_x^{*}\rangle\langle H_y R_y^{*}\rangle - \langle H_x R_y^{*}\rangle\langle H_y R_x^{*}\rangle} \qquad (6.7a)$$

$$Z_{xy} = \frac{\langle E_x R_x^{*}\rangle\langle H_x R_y^{*}\rangle - \langle E_x R_y^{*}\rangle\langle H_x R_x^{*}\rangle}{\langle H_y R_x^{*}\rangle\langle H_x R_y^{*}\rangle - \langle H_y R_y^{*}\rangle\langle H_x R_x^{*}\rangle} \qquad (6.7b)$$

$$Z_{yx} = \frac{\langle E_y R_x^{*}\rangle\langle H_y R_y^{*}\rangle - \langle E_y R_y^{*}\rangle\langle H_y R_x^{*}\rangle}{\langle H_x R_x^{*}\rangle\langle H_y R_y^{*}\rangle - \langle H_x R_y^{*}\rangle\langle H_y R_x^{*}\rangle} \qquad (6.7c)$$

$$Z_{yy} = \frac{\langle E_y R_x^{*}\rangle\langle H_x R_y^{*}\rangle - \langle E_y R_y^{*}\rangle\langle H_x R_x^{*}\rangle}{\langle H_y R_x^{*}\rangle\langle H_x R_y^{*}\rangle - \langle H_y R_y^{*}\rangle\langle H_x R_x^{*}\rangle} \qquad (6.7d)$$

where the remote fields are denoted by $R_x$ and $R_y$.

As with single-station estimation, typically the magnetic field contains less noise than the electric fields, and thus the remote fields $R_x$ and $R_y$ used for the above equations are the remote magnetic fields.

In Silali data set the Fourier transform band averaged cross- and auto- powers were calculated using robust processing method. The cross-powers were then graphically edited using the MTeditor program by masking the noisy data points in order to evaluate coherences for both phase and apparent resistivity (Figure 21). The final cross- and auto powers, as well as all relevant MT parameters calculated from them (impedances, apparent resistivity, phase coherences, strike directions etc) are stored in Electrical Data Interchange format (EDI). This file is ready for plotting and export to interpretation software for eventual 1-D, 2-D and 3-D inversion (Figure 21).

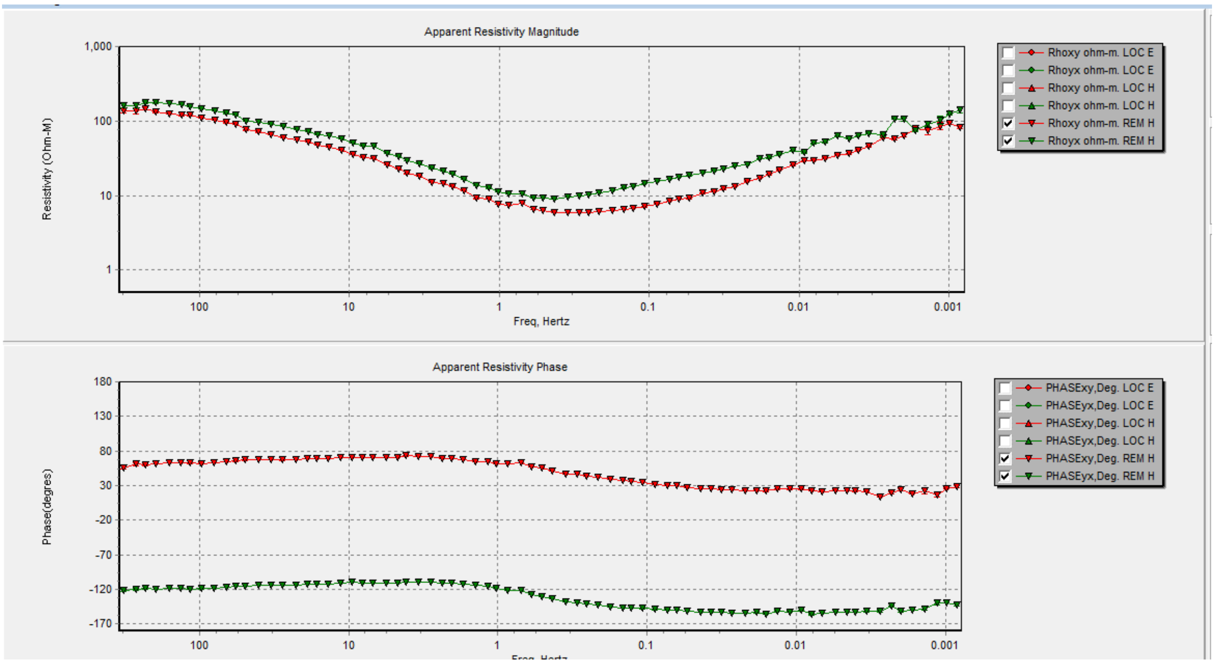

FIGURE 21: MTeditor output showing apparent resistivity and phase curves (using Remote H as reference for processing in the program SSMT2000)

The EDI file from MTeditor was then run through a Linux programme called spect2edi developed at ÍSOR which calculates several MT parameters some of which are not implemented in MTeditor and produces the result in the standard EDI format which is ready for interpretation. Figure 22 illustrates typical examples of processed MT apparent resistivity and phase curves from Silali area. Generally at periods below 1 second they exhibit 1-D response with decreasing apparent resistivity values and decreasing phase with increasing period. For periods above 10 seconds all curves split apart implying non one-dimensionality with one apparent resistivity increasing as the other decreases. High phase values (> 45°) at short periods indicate a conductor at shallow depth.

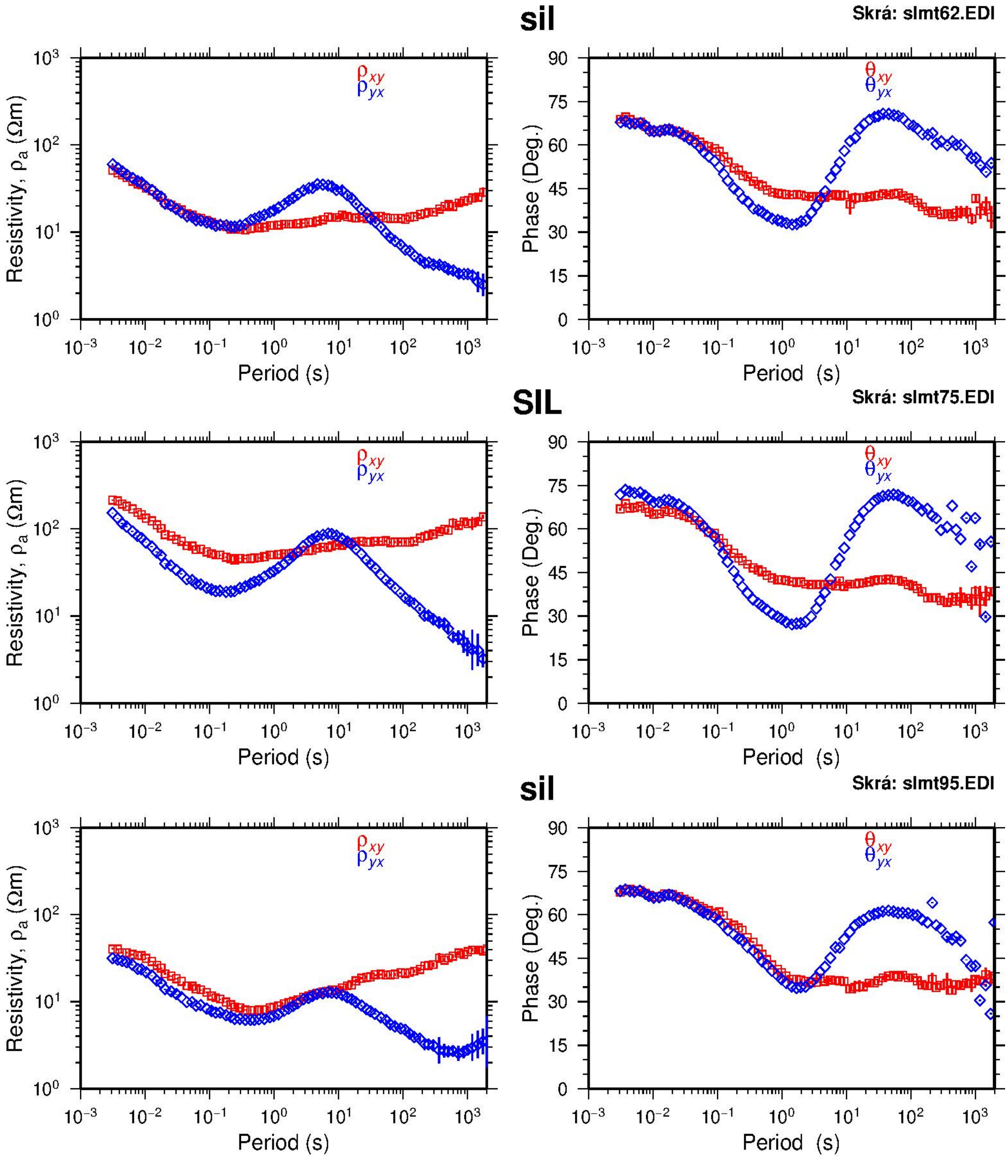

FIGURE 22: Typical examples of apparent resistivity and phase curves of MT soundings in the Silali area (red and blue symbols are xy and yx data respectively). A non 1-D resistivity pattern is indicated by the non-parallel divergence of the red and blue apparent resistivity curves for periods longer than 1 s for sites 62 and 75 and above 10 s for site 95

# 7. 1-D, 2-D AND 3-D MT INVERSION CODES USED

This section describes codes used in the three types of inversions that have been applied to the data from Silali. The programs used in the inversions are TEMTD (Árnason, 2006), REduced Basis OCCam (REBOCC) (Siripunvaraporn and Egbert, 2000), and WSINV3DMT (Siripunvaraporn et al., 2005) for 1-D inversion, 2-D inversion and 3-D inversion of MT data respectively. As a comparison for 2-D results WinGlink software has been used in order to compare with the results gotten from REBOCC.

## 7.1 1-D inversion program

The TEMTD program is used to perform 1-D joint inversion of EM data. The program was developed by Knútur Árnason at ÍSOR (Árnason, 2006). The TEMTD program does 1-D inversion of TEM and MT data separately or jointly. In this study the software was used to invert MT apparent resistivity and phase derived from the rotationally invariant determinant of the MT tensor elements. In the joint inversion, one additional parameter was also inverted for, namely a static shift multiplier needed to fit both the TEM and MT data with the response of the same model. The programme can do both standard layered inversion (inverting resistivity values and layer thicknesses) and Occam's (minimum structure) inversion with exponentially increasing fixed layer thicknesses with depth. It offers a user specified damping of first (sharp steps) and second order derivatives (oscillations) of model parameters (logarithm of resistivity and layer thicknesses), (Árnason, 2006). Occam's inversion seeks the "smoothest", or minimum norm, model subject to an appropriate fit to the data (Constable et al., 1987).

The TEMTD program solves forward and inverse problems. The inversion problem is to determine those model parameters which give the model response close to the measured response. The forward problem calculates the response from a given model. The model response depends non-linearly on the model parameters; the inversion algorithm used in the programme is the non-linear least-square inversion of the Levenberg-Marquardt type (Levenberg, 1944; Marquardt, 1963). The misfit function is the mean-square difference between measured and calculated values chi$^2$ ($\chi^2$), weighted by the standard deviation of the measured values. Chi$^2$ is regarded as the measure of misfit between the measured and calculated data.

Is it desirable to have a small $\chi^2$, indicating that the model resolves data. Fitting electromagnetic data closely may result in rough model, and it is generally desirable to sacrifice fit to a dataset in favour of smooth resistivity variation (Constable et al., 1987). Under-parameterisation of the inverse problem tends to suppress structure that could be significant, whilst over-parameterisation introduces structure that is redundant, and not truly resolvable by the available data (Constable et al., 1987).

## 7.2 2-D inversion program

### 7.2.1 REBOCC code

2-dimensional interpretation was done by the REBOCC (REduced Basis OCCam**)** code. Inversion was done for TE and TM apparent resistivity and phase separately or simultaneously. REBOCC is based on the OCCAM algorithm of deGroot-Heldin and Constable (1990), Siripunvaraporn and Egbert (2000). The code can invert for apparent resistivity ($\rho_a$) and phase ($\phi$) of TM and TE-modes as well as real and imaginary parts of the vertical magnetic transfer function (tipper). The 2-D inversion method is based on an iterative technique that minimizes a misfit function between the data and the 2-D model calculation in both TE and TM-modes. REBOCC is stable in terms of convergence and requires moderate memory to run as a result of the transformation from model-space to data-space. It is also freely available for academic use and easy to use. REBOCC code utilizes redundancy of the electromagnetic data and interpolates response functions and their derivatives in the frequency-space domain.

### 7.2.2 Overview of REBOCC inversion

The inverse models are discretized into M constant resistivity blocks, m = [$m_1$, $m_2$. . ., $m_M$] and N observed data, d =[ $d_1$,$d_2$, ..., $d_N$] with uncertainties e =[$e_1$, $e_2$,...,$e_n$]. The data misfit functional $X_d{}^2$ can be expressed as:

$$X_d{}^2 = (d - F[m])^T C_d{}^{-1}(d - F[m]) \tag{7.1}$$

Where $F[m]$ denotes the model response, the superscript T represents matrix transpose and $C_d$ is the diagonal data covariance matrix, which contains the data uncertainties. The normalized mean square (RMS) misfit of the data is defined as $1/_N\, X_d{}^2$. Due to the non-uniqueness of the inverse problem, an infinite number of models can produce the same misfit in Equation 7.1. Most modern MT inversion schemes resolve non-uniqueness by seeking models that have minimum possible structure for a given level of misfit (Parker, 1994), which leads to the introduction of a model structure functional $X_m{}^2$.

$$X_m{}^2 = (m - m_0)^T C_m{}^{-1}(m - m_0) \tag{7.2}$$

Where $m_0$ is the prior model, and $C_m$ is a model covariance matrix, which characterizes the magnitude and smoothness of the resistivity variation with respect to the prior model $m_0$. The minimum structure inverse problem is to minimize $X_m{}^2$ subject to $X_d{}^2 = X_*{}^2$, where $X_*{}^2$ is the desired level of misfit. The two functional together with the desired level of misfit are combined to yield the unconstrained functional U(m,λ) as:

$$U(m, \lambda) \; = X_m{}^2 + \lambda^{-1}\big( X_d{}^2 - X_*{}^2\big) \rightarrow minimum \tag{7.3}$$

In Equation 7.3 the Lagrange multiplier λ acts as a “trade off” between minimizing the norm of data misfit and the norm of the model (Tikhonov and Arsenin, 1977; and Parker, 1994). When λ is large, the data misfit becomes less important and more weight is given toward producing a smoother model. In contrast, as λ goes to zero, the inverse problem becomes closer to the ill-conditioned least square problem, resulting in a rough model (Parker, 1980). In order to minimize Equation 7.3, the stationary points have to be found with respect to m and λ.

Instead of solving the minimization problem in the model-space, REBOCC code transforms the problem into the data-space, by expressing the solution as a linear combination of “representers” (i.e. rows of the sensitivity matrix smoothed by the model covariance). This transformation reduces the size of the system of equations to be solved from M x M to N x N (where M is the number of model parameters and N is number of data parameters). Since the number of model parameters M is often much larger than the number of data parameters N, this approach reduces the CPU time and memory requirement significantly. Therefore, in the data-space approach, there is no need to use all representers. A subset of this basis function (of dimension L) is sufficient to construct the model without significantly loss of detail. Hence, the size of the system of equations to be solved further reduces to L x L (where L << N and M). Even though the construction of the solution is made from the subset of the smoothed sensitivities, the goal of the inversion remains to find the norm minimization model subject to fitting all of the data well enough. Since the aim is to search for the minimum norm model, the REBOCC inversion can be divided into two stages: Phase I for bringing down the misfit to the desired level $X_*{}^2$, and Phase II for searching for the model with minimum norm while keeping the misfit at the desired level (or smoothing process). Phase II is necessary in order to wipe out the spurious features occurring while the program tries to reduce the misfit. Since the MT inverse problem is non-linear, the desired misfit may never be reached and phase II will never be executed. It is better to restart the inversion process with a higher desired misfit, and a model from the previous run as a starting model.

### 7.2.3 WinGlink Program

Another program, WinGlink (Geosystem user guide, 2011) was also used in the interpretation of 2-D MT data. It is based on nonlinear conjugate gradient (NLCG) inversion code which is a forward and inverse modelling algorithm developed by Rodi and Mackie (2001). Recalling that in the 2-D case Maxwell’s equations can be formulated in terms of the decoupled TE and TM polarizations for currents flowing parallel and perpendicular to strike, complex apparent resistivities for the TE and TM mode are expressed as:

$$\rho_{TE} = \frac{1}{\omega\mu}\left|\frac{E_x}{H_y}\right|^2 \qquad \text{and} \qquad H_y = \frac{1}{i\omega\mu}\frac{\partial E_x}{\partial z} \tag{7.4}$$

$$\rho_{TM} = \frac{1}{\omega\mu}\left|\frac{E_y}{H_x}\right|^2 \qquad \text{and} \qquad E_y = \rho\frac{\partial H_x}{\partial z} \tag{7.5}$$

The algorithms used by Rodi and Mackie (2001), solve Equations 7.4 to 7.5 by segmenting the half space into rectangular blocks of different dimensions, each assigned a constant resistivity. The forward model is computed using finite difference equations. The 2-D mesh is user defined and it incorporates topography with the forward response saved as station data.

The inversion routine finds regularized (smooth) solutions assuming a 2-D resistivity distribution using the NLCG method to match the MT data. The NLCG method is used to minimize an objective function that is the summation of the normalized data misfits and the smoothness of the model. The trade-off between data misfits and model smoothness is controlled by a regularized user defined parameter, which penalizes data residuals and spatial second order resistivity (Rodi and Mackie, 2001).

The inverse problem relates the observed data vector $(d)$ to a forward function $(F)$ of the model vector $(m)$ and the error vector $(e)$ as shown below (Rodi and Mackie, 2001). The inverse problem is then formulated as shown below:

$$d = F(m) + e \tag{7.6}$$

For either TE or TM polarization, $d = [d^1 \; ..... \; d^N]$ or $d^i$ where $i = [1.....N]$, the number of log amplitude or phase apparent resistivity for any given frequency, $m = [m^1 \; .....m^M]$ is a vector of parameters which define the resistivity model. If $M$ is the number of model blocks such that $m^j$ is log of the apparent resistivity, the forward function $F$ is defined by using the Taylor series about a starting model $(m)$. Details of the inversion and minimization can be found in Rodi and Mackie (2001). The inverse problem is solved by taking a regularized solution to the model by minimizing an objective function, $\psi$, defined as:

$$\psi(m) = (d - F(m))^T V^{-1}(d - F(m)) + \lambda m^T L^T Lm \tag{7.7}$$

for given values of $\lambda$, $V$ and $L$ where $\lambda$ is a positive regularization parameter, $V$ is equivalent to the variance of the error vector $e$, and $L$ is the Laplacian of the apparent resistivity ($\log\rho$). The minimization of the objective function in Equation 7.7 is carried out through the NLCG in WinGlink. The inversion seeks to achieve the lowest RMS error and the smoothest model.

### 7.3 3-D inversion Program

The 3-D forward and inverse modelling was done by WSINV3DMT code (Siripunvaraporn et al., 2005) which implements Occam's inversion (Constable, 1987; deGroot-Hedlin and Constable, 1990). The WSINV3DMT code uses the data-space variant of the Occam inversion approach similar to REBOCC (Siripunvaraporn et al., 2005; Siripunvaraporn and Egbert ,2000), See discussion in (section 7.2.1) on REBOCC.

WSINV3DMT requires large memory to store the sensitivity matrix. The total size of the dataset is defined by the data parameter N described below:

$$N = N_p N_S N_r \tag{7.8}$$

where $N_p$, is the number of periods, $N_S$ is the number of stations and *N,* is the number of responses (a maximum of 8 for all impedances). The model parameter size $M$ is defined by the product of number of discretization blocks in the north-south direction ($M_x$), east-west direction ($M_y$), and the vertical direction ($M_z$);

$$M = M_x M_y M_z \tag{7.9}$$

Occam inversion on which this code is implemented is stable and converges to the desired misfit in relatively small number of iterations compared to most other methods which are based on the model space method. As discussed in Siripunvaraporn and Egbert (2000), the transformation of the inverse problem to the data space can significantly improve the computational efficiency for the 3-D MT problem. The 3-D forward modelling algorithm is based on a staggered grid finite difference solution of Maxwell's equations. This approach allows for complicated model structures (Siripunvaraporn et al., 2005).

WSINV3DMT program requires RAM storage memory at least $1.2 \times (8N^2 + 8NM)$ to store the N × N representer matrix and N × M sensitivity matrix. The program requires extra memory for other computations. The factor 1.2 which accounts for this is not exact, but is generally an average approximation.

## 8. MULTI-DIMENSIONAL INTERPRETATION OF EM DATA

### 8.1 Joint 1-D inversion of TEM and MT soundings

The one-dimensional joint inversion is performed simultaneously for both TEM and MT data by fitting both data sets to obtain one model. This is achieved by use of an algorithm which determines the appropriate shift factor to be used to constrain the MT data to fit the TEM response. Both the MT and TEM data collected on approximately the same location are brought together in a joint inversion which also determines a static shift multiplier to correct for static shift that is inherent in MT data.

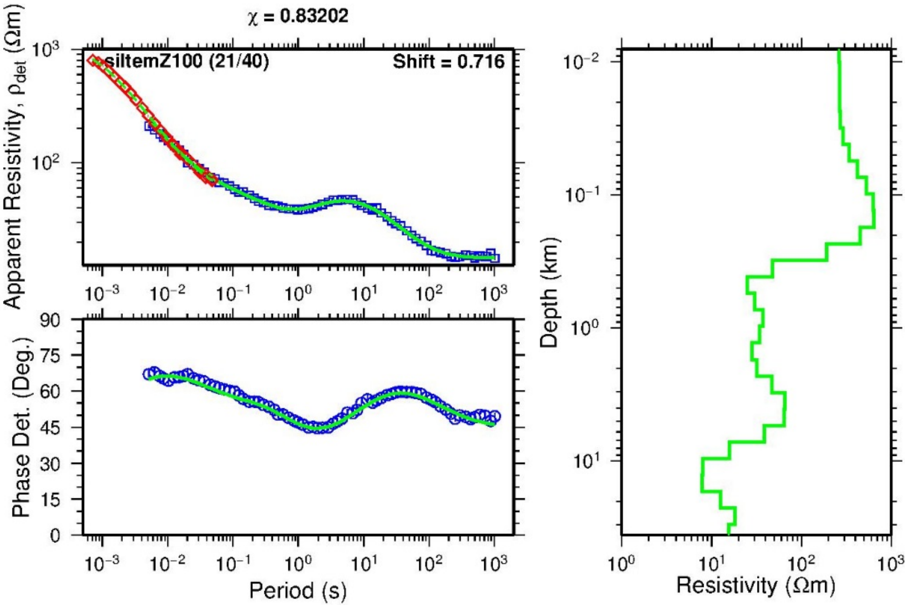

FIGURE 23: Typical result of a joint 1-D inversion of TEM and MT soundings; where the red diamonds are measured TEM apparent resistivities and blue squares are the MT apparent resistivities and phase. Solid lines show the response of the resistivity model to the right. The shift multiplier is shown in the upper right hand corner of the apparent resistivity panel

Joint 1-D Occam inversion has been done for the rotationally invariant determinant apparent resistivity and phase of all the MT soundings and their nearest TEM soundings in the Silali field (Appendix II). Determinant data is preferred because it is rotationally invariant and averages out all "dimensionality" of data. It is unique and independent of the strike direction. An example of a 1-D joint inversion of MT and TEM data is shown on Figure 23. The shift multiplier is shown in the upper right hand corner of the apparent resistivity panel. The best fit for this pair was achieved with a shift parameter of S = 0.716. This means that the MT apparent resistivity has to be divided by this value to be consistent with the associated TEM sounding.

### 8.2 The MT static shifts correction in Silali

Static shift analysis of the 102 MT sounding was done in the Silali area where shift factors in the range of 0.1 to 1.9 have been observed as seen in Figure 24(a). The histogram also shows that the majority of the soundings were shifted down (shift < 1) and only a few shifted upwards (shift > 1). Out of a total of 102 soundings only 9 sites were not shifted and the mean shift for all the soundings being 0.654. Therefore if interpretation was to be done without the static shift correction then we would have serious error in resolving the resistivity structure and depths for this field (Lichoro, 2009). Figure 24(b) shows the spatial distribution of the shift multipliers in the Silali area, indicating that there are larger areas where the MT apparent resistivity is consistently shifted downwards and other smaller zones where it is shifted upwards, with only small portions which have not been affected by static shift. In conclusion it has been found out that correction for static shift by use of a TEM sounding in a joint inversion with MT data can be very effective in providing a more accurate picture of the resistivity structure of the earth.

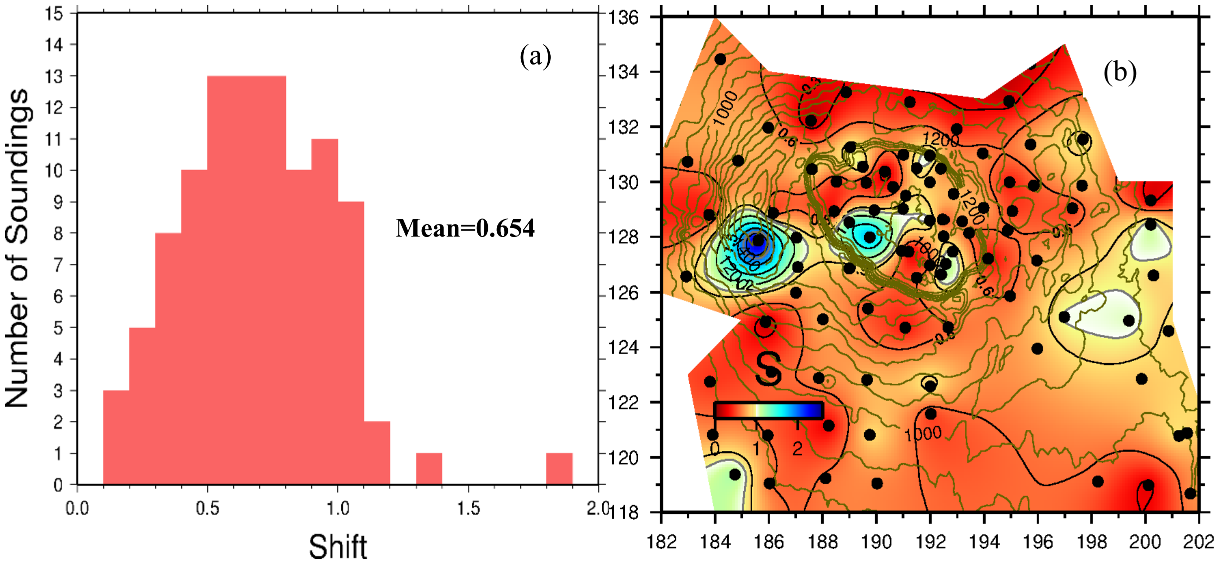

FIGURE 24: Histogram (a) and Spatial distribution (b) of static shift parameters for determinant apparent resistivity in the Silali area. The black dots are location of MT stations; topographic contour lines are in m a.s.l; Distances are given in km

## 8.3 Joint inversion 1-D Results

### 8.3.1 1-D Cross-sections

Resistivity cross-sections are plotted for results obtained from 1-D inversion by a program called TEMCROSS (Eysteinsson, 1998), developed at Iceland GeoSurvey. The program calculates the best line between selected soundings on a profile, and plots resistivity isolines based on the 1-D model for each sounding. It is actually the logarithm of the resistivity that is contoured so the colour scale is exponential but numbers at contour lines are actual resistivity values. Several cross-sections were made through the survey area and profiles were positioned perpendicular to the inferred geoelectrical strike direction (N10°E) as discussed in Section 8.4.

**Cross-section EW10_4,** shown in Figure 25 cuts through the northern sector of the caldera. The figure shows two plots, the upper panel representing shallow resistivity and the lower one representing the deeper structures. The top layer of about 300 m exhibits a high resistivity across the entire profile reflecting un-altered rock formation. Underlying the high resistivity is a low resistivity layer, of less than 10 Ωm from below the caldera and spreading to the east. This low resistivity could be reflecting the low temperature alteration minerals like smectite-zeolite. Below the alteration layer two fairly higher resistivity zones of > 50 Ωm appear, one below the caldera and the other more to the east. These could be probable high temperature reservoirs for this geothermal field. At depth of 5-6 km below sea level a low resistivity dominates rising to shallow depths at two portions of the profile, one at the eastern edge of the caldera and the other to the western edge of the profile. The eastern conductive column could be attributed to an up-flow zone or probably due to large fractures with fluids present in the vicinity, as can be manifested by the altered grounds and fumaroles on the surface directly above it, which could be as a result of deep circulation of the geothermal fluids enhancing water-rock interaction. The western lowest resistivity is not well understood but could possibly be a result of conductive sediments. In absence of other geophysical information like density it might not be possible to attribute the low resistivity to a geothermal reservoir.

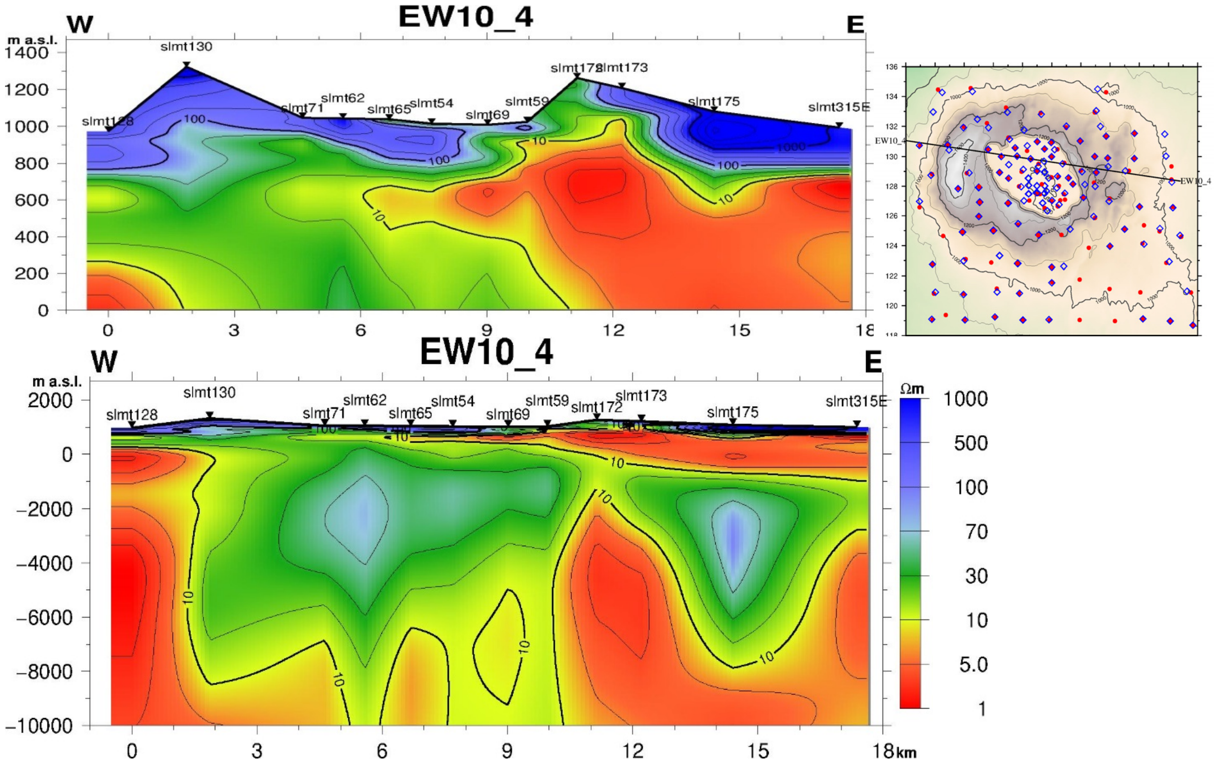

FIGURE 25: Resistivity cross-section for two different depth ranges obtained from the joint 1-D inversion of TEM and determinant MT data for profile EW10_4. Inverted triangles: MT stations; Section location is shown as black line in the map to the right. Red and blue points in the map are MT and TEM stations respectively

**Cross-section EW10_3,** on Figure 26 cuts through the southern portion of the caldera. The top most portion of the section shows a high resistivity for almost entire length apart from a small discontinuity

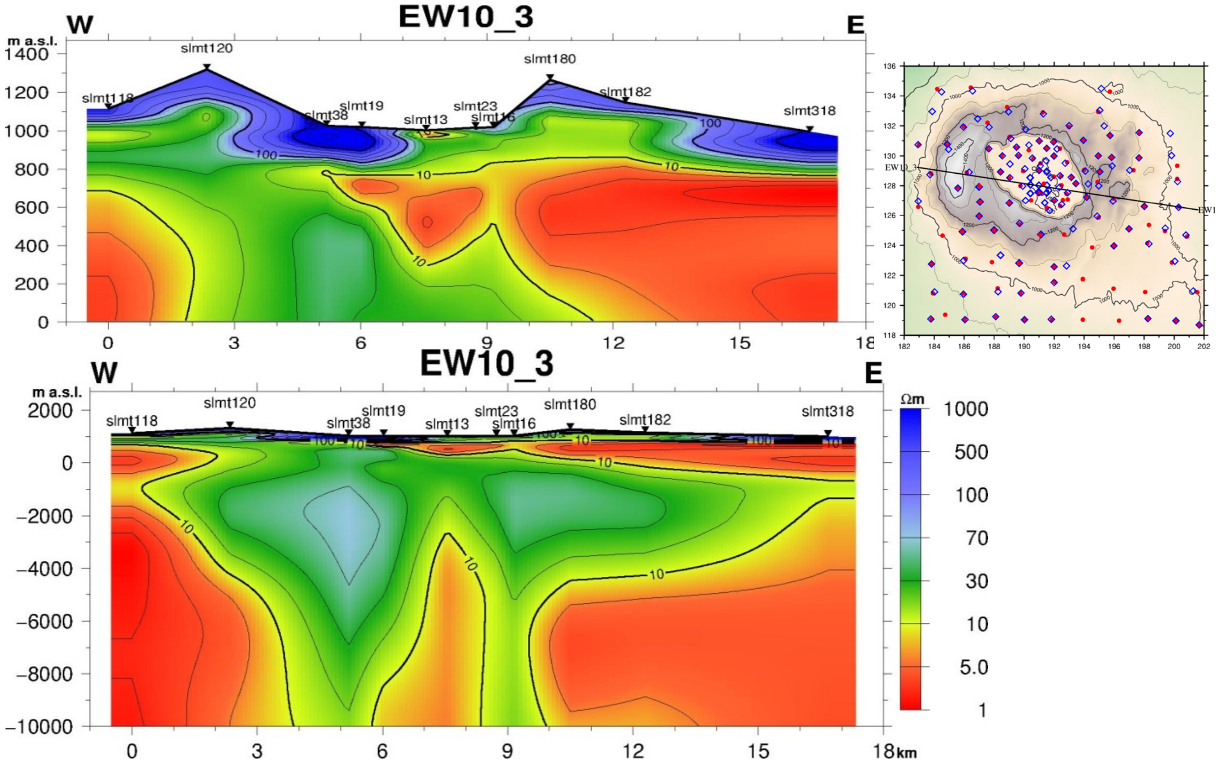

FIGURE 26: Resistivity cross-section for two different depth ranges obtained from the joint 1-D inversion of TEM and determinant MT data for profile EW10_3. Inverted triangles: MT stations; Section location is shown as black line in the map to the right. Red and blue points in the map are MT and TEM stations respectively

below sounding slmt13 where lower resistivity persists all the way to the surface, this is an area marked by surface manifestations. Below the surface layer a low resistivity covers the entire caldera and spreads to the east of the caldera. Again this very conductive layer is probably the zeolite zonation of the volcanic rocks. Similarly a low resistivity protrudes to the western most edge of the profile below site slmt118. Underlying the alteration layer are two distinct higher resistivity zones, one below the caldera and the other to the east of the caldera separated by a low resistivity discontinuity which rises from depth to 3km below sea level. These high resistivity structure could be reflecting high temperature alteration and a probable geothermal reservoir for this field. At the base of the profile a conductive body dominates rising to shallow depths below the caldera and to the west of the caldera.

**Cross-section EW10_1**, on Figure 27 cuts through the prospect area to the southern-most sector. The top most portion shows generally a high resistivity for the entire length along the cross-section. Below the surface layer a low resistivity covers the eastern zone of the profile which again represents the alteration layer despite there being no obvious surface manifestations around this area. This suggests that a hydrothermal fluid circulation exists at depth. A third layer shows two distinct high resistivity zones one on the east part of the profile and the other to the west rising from depth all the way to the near-surface. The eastern high resistivity anomaly could be as result of high temperature alteration and a probable geothermal reservoir for this sector, the cause of the vertically elongated high resistivity to the west is not well understood but it's unlikely to be a geothermal reservoir since it lacks the signatures that define a high temperature. At greater depth below the eastern high resistivity lies a deeper conductor.

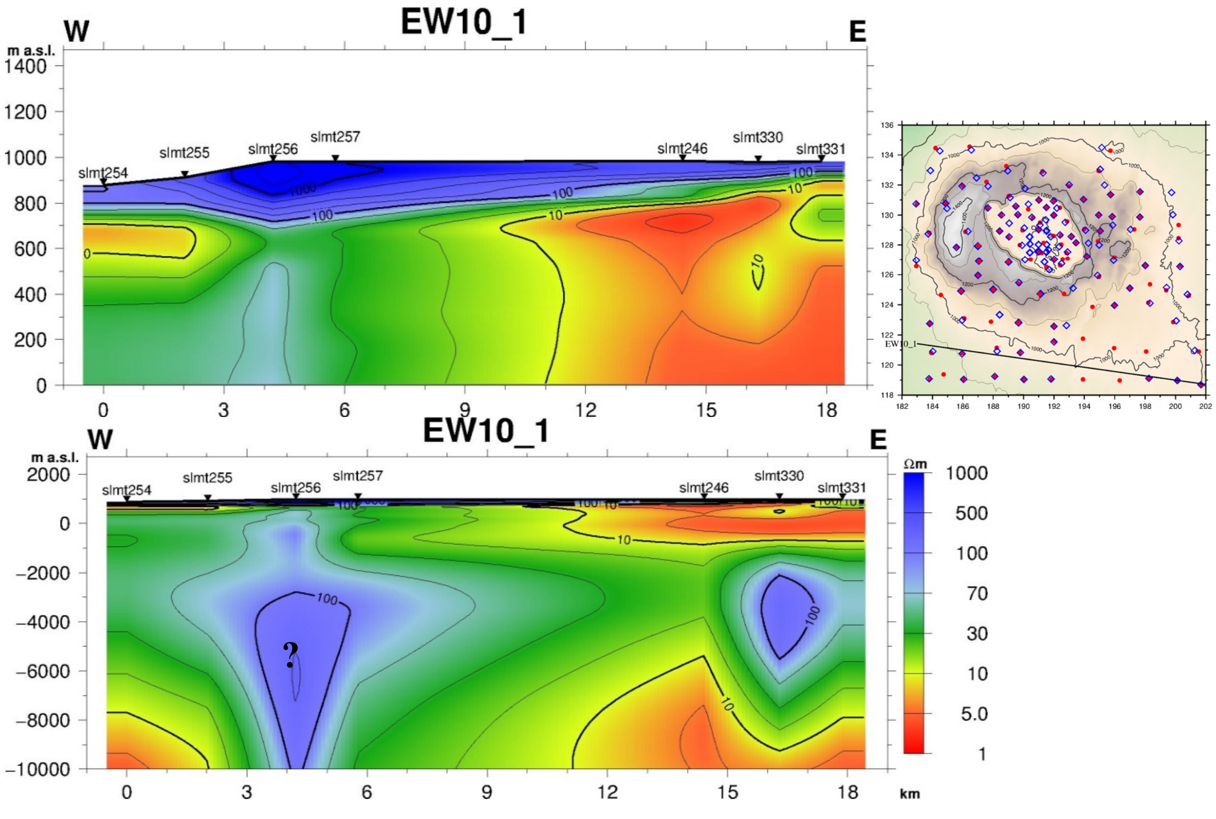

FIGURE 27: Resistivity cross-section for two different depth ranges obtained from the joint 1-D inversion of TEM and determinant MT data for profile EW10_1. Inverted triangles: MT stations; Section location is shown as black line in the map to the right. Red and blue points in the map are MT and TEM stations respectively

**Cross-section NW-SE,** on Figure 28 cuts through the caldera in the NW-SE direction**.** The top most resistivity layer shows generally a high resistivity for the entire cross-section. Underlying the surface layer is a low resistivity layer which smears almost the entire profile. This layer is attributed to low temperature alteration. A third layer appears dominantly at the centre of the profile which act as the core of the geothermal system in this field. At about 5km depth below sea level a deeper conductor is evident almost the entire length along the profile which probably could be related to the heat sources for this part of the field. The deeper low resistivity seems to elongate in the north-western sector of the profile approaching near surface. All the cross-sections show evidence of a discrete low resistivity layer deep below Silali caldera and to the east of the caldera which is in line with the interpretation of a possible magmatic heat source.

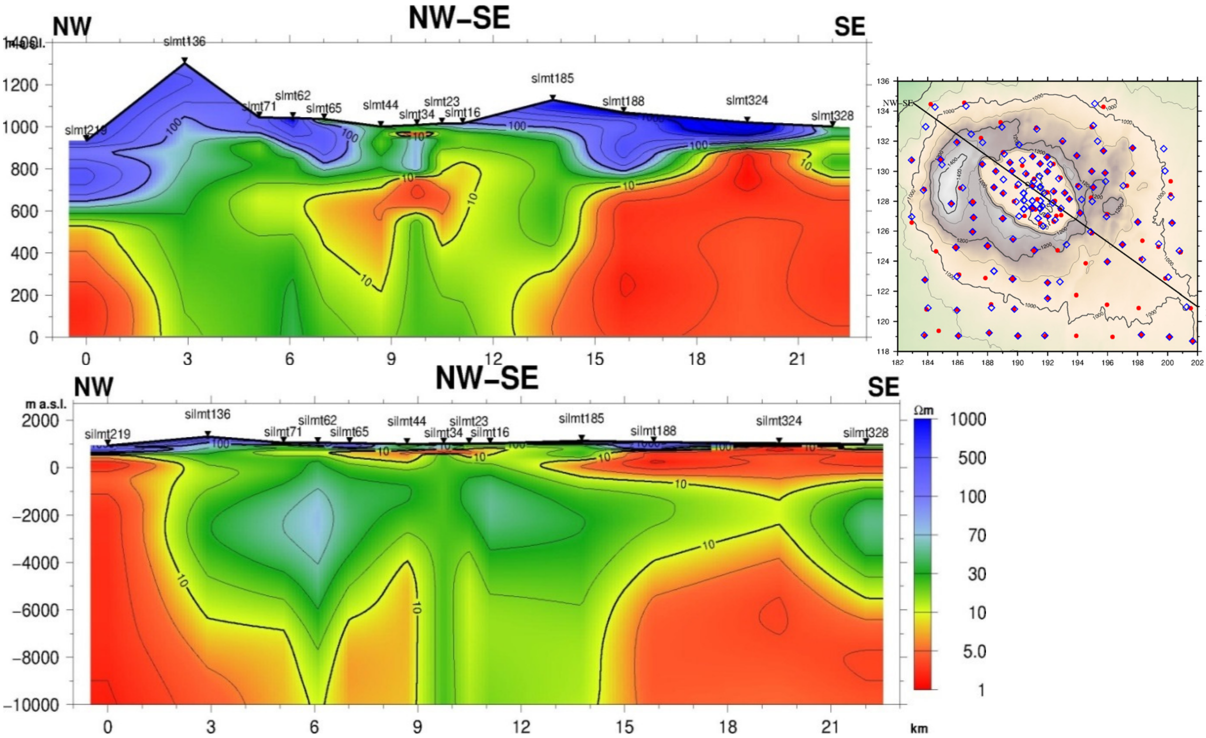

FIGURE 28: Resistivity cross-section for two different depth ranges obtained from the joint 1-D inversion of TEM and determinant MT data for profile SW-NE4. Inverted triangles: MT stations; Section location is shown as black line in the map to the right. Red and blue points in the map are MT and TEM stations respectively

### 8.3.2 1-D iso-resistivity maps

Iso-resistivity maps are made by a program known as TEMRESD which generates iso-resistivity maps at fixed elevations derived from the 1-D Occam models (Eysteinsson, 1998). The resistivity is contoured and coloured in a logarithmic scale. The general elevation of the Silali volcano is about 1000 - 1200 m a.s.l. In the following section Iso-resistivity maps are presented from 700 m a.s.l. down to 4000 m b.s.l. The maps show that resistivity varies considerably both laterally and with depth.

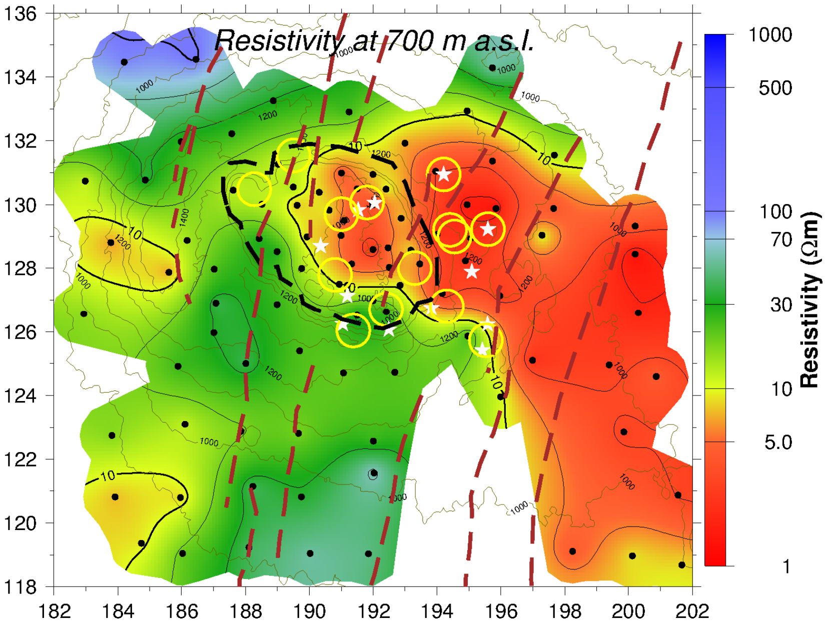

FIGURE 29: Resistivity in the Silali area at 700 m a.s.l. from joint 1-D inversion of TEM and MT data. The brown broken lines are faults mapped on the surface, the stars are fumaroles and the circles represent the altered grounds

Resistivity map at **700 m a.s.l.**, is shown on Figure 29. The low resistivity predominantly covers almost the entire caldera and spreads to the east and further to the south east of the study area. Two more patches of lower resistivity are visible to the west of the caldera and south west respectively. The low resistivity structure is associated with the alteration cap immediately on top of the high resistivity core and probably reflects a zone where hydrothermal alteration products such as smectite and zeolite are abundant. High resistivity anomalies are also seen to the south of the caldera. This high resistivities probably reflects the un-altered volcanics covered by the pyroclastic material.

Resistivity map at **200 m b.s.l.,** is shown on Figure 30. At this elevation high-temperature alteration (resistive core) is visible from the caldera and spreading mainly to the east and southwest of the caldera marked by resistivity > 10 ohm-m. This high resistivity core could be probably as a result of high temperature minerals like epidote and chlorite. Despite the presence of fractures which could be thought as possible conduits for reservoir fluids, resistive alteration clays seems to influence much more the resistivity structure than the fluid-filled fractures. To the south east and southern sector of the area low resistivity is still prevalent possible due to alteration to low temperature minerals.

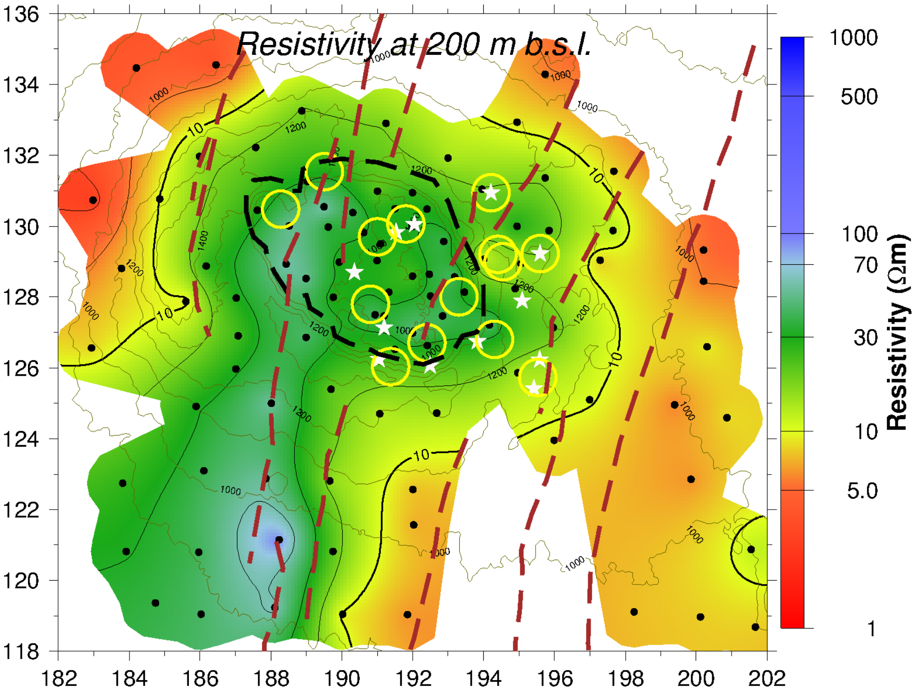

FIGURE 30: Resistivity in the Silali area at 200 m b.s.l. from joint 1-D inversion of TEM and MT data.

Resistivity map at **4000 m b.s.l.,** is shown on Figure 31. This elevation is about 5 km below the surface. It shows mainly deeper conductors one beneath the caldera and spreading to the east which seems to connect with another one to the south east. This deeper conductors may be related to the heat source for this field. To the western sector of the area a fairly high resistivity structure is evident aligning in the north-south direction, this structure persist for several kilometres

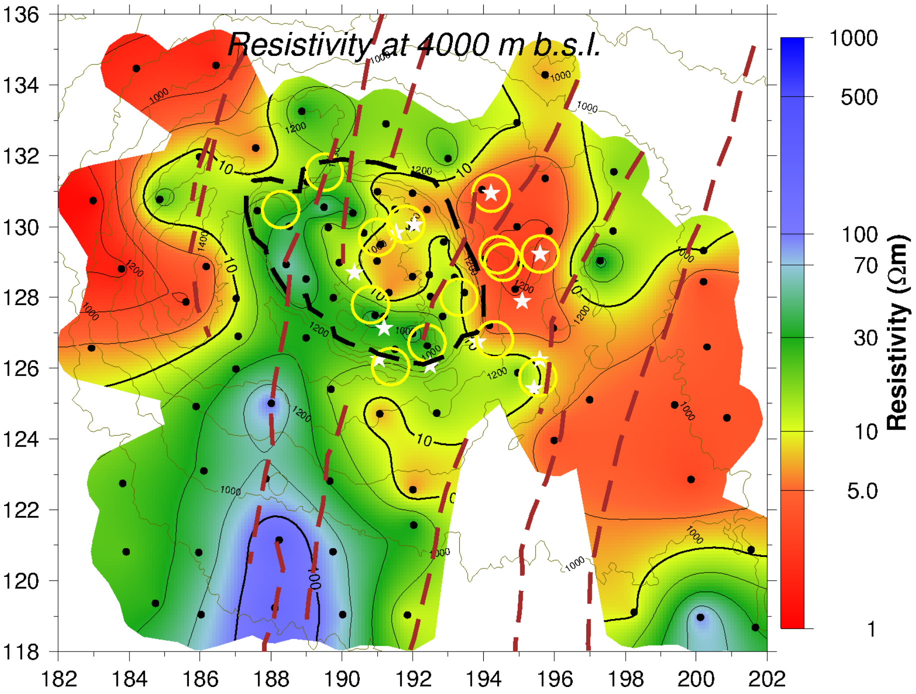

FIGURE 31: Resistivity in the Silali area at 4000 m b.s.l. from joint 1-D inversion of TEM and MT data.

depth as seen in the cross-sections. It seems to divide the western conductive sector from the eastern one. The cause of this high resistivity anomaly is not clear yet.

### 8.3.3 Discussion of 1-D inversion results

Joint inversion of TEM and rotationally invariant determinant MT data reveals a resistivity structure consisting generally of a shallow low-resistivity layer particularly around the caldera, in the uppermost 1 km, underlain by high resistivity. At greater depth, a second conductive layer is observed in the northeast, southeast and in the west of the caldera. The upper low-resistivity layer presumably reflects conductive hydrothermal alteration minerals formed at temperatures between 100 and 240 ◦C. The resistive core reflects the change in alteration to resistive high temperature minerals which could be hosting the geothermal system in Silali field. The nature of the deep conductive layer is not as clear in absence of other geophysical data, but could be attributed to magmatic heat sources.

## 8.4 Geo-electric strike analysis of MT data

MT field measurements are rarely done in the geo-electric strike direction. Normally the elements of the MT impedance tensor are dependent on the orientation of the x and y-directions of the field layout. For a homogeneous and 1-D earth, the impedances $Z_{xy} = -Z_{yx}$ and $Z_{xx} = Z_{yy} = 0$. For a 2-D earth, the resistivity varies with depth and in one horizontal direction. The horizontal direction perpendicular to that direction is called the geoelectrical strike and the angle it makes with geographical north is the Zstrike. Before modelling the resistivity structures, impedance tensors are studied for dimensionality and strike direction of the geoelectrical structure. Therefore to undertake 2-D inversion the impedance tensor has to be rotated so that the fields align parallel and perpendicular to strike respectively. This is achieved by carrying out strike analysis where the off-diagonal elements of the MT tensor are maximized: $|Z_{xy}|^2 + |Z_{yx}|^2$ or the diagonal ones minimized by $|Z_{xx}|^2 + |Z_{yy}|^2$ with respect to the rotation of the coordinate system. The resulting strike angle is called Zstrike (principal angle). Geo-electrical strike analysis can indicate the directions of resistivity contrasts which could be used to infer geological features, not necessarily seen on the surface. If the earth is 2-D and the coordinate system has one axis parallel to the geoelectrical strike direction, $Z_{xx} = Z_{yy} = 0$ and $Z_{xy} \neq Z_{yx}$. There is however, a 90° ambiguity in the Zstrike determination where the diagonal elements of the tensor are minimised as if either the x- or y-axis is along the geo-electrical strike. The direction it points corresponds to either a minimum or a maximum of $Z_{xy}$ and therefore there is no way of distinguishing between $\theta$ and $\theta+90°$, from the tensor alone. At short periods (< 1 s), the strike estimates of the Silali data scatter, reflecting shallow local structure whereas at longer periods, there is a consistent strike direction for the dataset except in areas with strong structural influence like within and around the caldera.

The rose diagrams on Figure 32 above shows Zstrike for the periods between 10 to 100 seconds for all the MT soundings in the Silali field. It indicates that the Zstrike angle varies from site to site. The Zstrike on most of the rose diagram are trending generally in a Northerly direction about N10°E direction except for soundings around the caldera which seems to be influenced by its morphology. The failure by all Zstrikes to align in same direction imply that the structure is 3-dimensional. The inferred main geo-electric strike direction (N10°E) is also in fair agreement with the geological strike as seen from the faults mapped on the surface. Since the geo-electrical strike is generally in N10°E direction, the impedance tensor elements were rotated to make the x-axis align to this direction for all MT sites with xy as TE-mode and yx as TM-mode.

### 8.4.1 Tipper strike

As mentioned above the impedance strike suffers from the 90° ambiguity and the strike direction can't be determined using MT impedance strike data alone. This ambiguity can be resolved by the information from tipper vector if vertical magnetic field ($H_z$) is available. As discussed previously tipper, $\mathcal{T}$ is a parameter that relates the vertical component of the magnetic field to its horizontal components (Equation 2.48). Rose diagram of the Tipper strike is shown for period intervals 0.1–1 seconds in Figure 33. Similar to the Zstrike, Tstrike is roughly aligned along the dominant geological strike, except around and within the caldera where Tstrike seems to align with the orientation of the caldera structure.

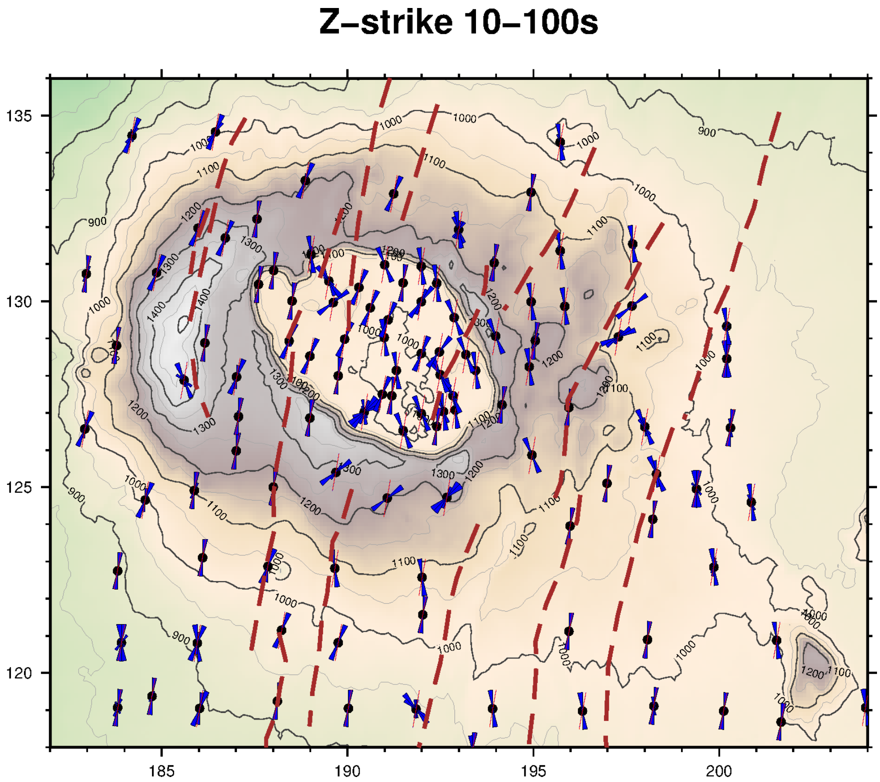

FIGURE 32: Rose diagrams showing Zstrike for MT data in the Silali field. The red line show the inferred geo-electric strike direction and the broken lines are faults as mapped on the surface

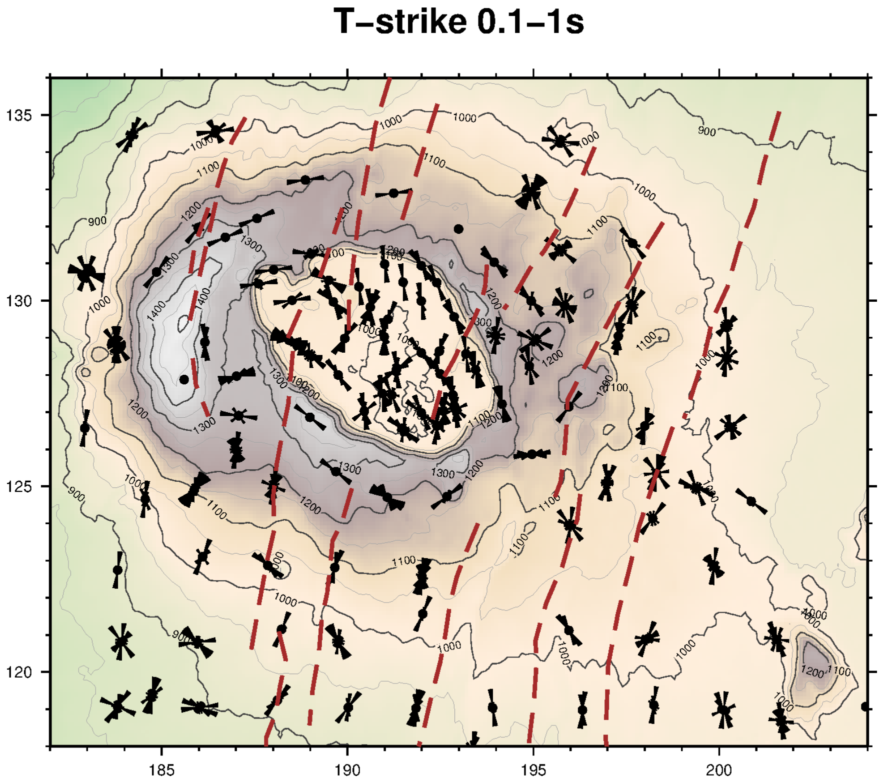

FIGURE 33: Rose diagram of the Tipper strike for the period, 0.1–1 s. The broken lines are faults as mapped on the surface

Strike usually vary with frequency and may not orient in the direction of known geological strike. If a stable strike does not exist, it will be impossible to define a single coordinate system in which the entire period range of the data can be satisfactorily decoupled into TE- and TM-modes. If the data are rotated to an average strike and modelled two-dimensionally then the resulting 2-D model may contain artefacts at depth that arise from structure that is laterally displaced from the profile.

Strike variation with frequency in the Silali field may be attributed to dynamic processes that have continually modified the Earth's structure culminating to the formation of the caldera. As a consequence of these processes, remnants of past tectonic events are often preserved, giving rise to tectonic environments in which structural lineaments trend in more than one direction. One such environment exists in this sector of the rift where a major generally N–S strike trending is prominent but on approaching the caldera the direction changes to NW-SE within and around the caldera. The electromagnetic strike was found to be both period- and site-dependent. This behaviour could be as a result of three-dimensionality influence on the data.

The Tipper, $\mathcal{T}$ is a complex vector represented as induction arrows, the real part and the imaginary part. Generally the imaginary part is more sensitive to resistivity close to the measurement site and the real part to broader resistivity contrasts. As seen from Figure 34 the real induction arrows point away from a zone of high conductivity and towards a zone of lower conductivity in line with Wiese convention (Wiese 1962, Berdichevsky and Dmitriev, 2002). These induction arrows are influenced by different conductivity gradients and only indicate the approximate location of the main conductor. In this case the size of the induction arrow is dependent on the magnitude of the vertical magnetic field, such that if vertical magnetic field is small then the induction arrow is also small and vice versa.

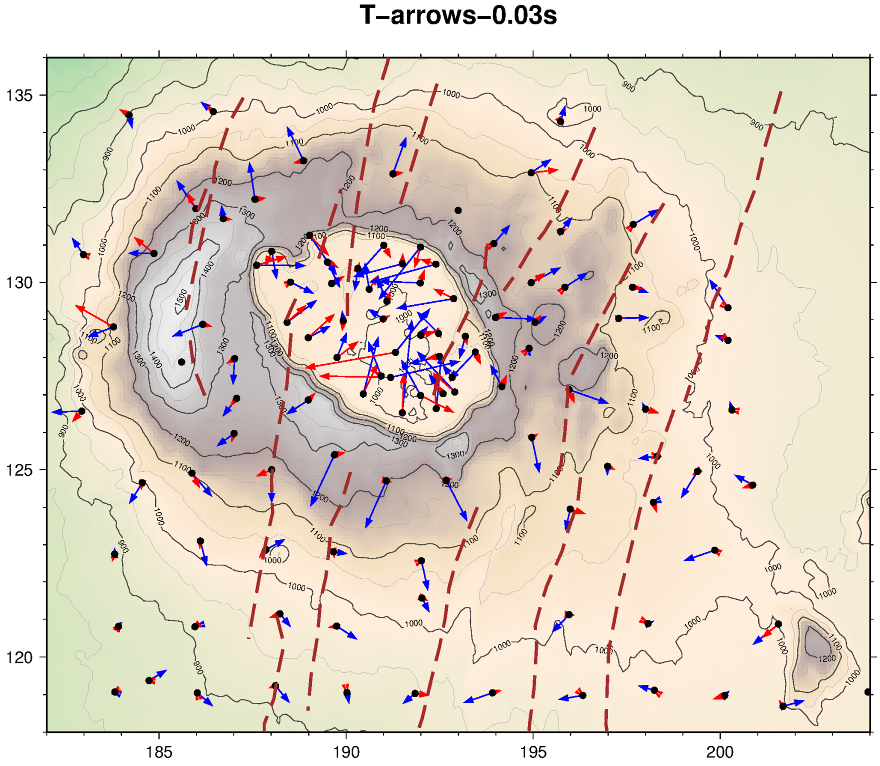

FIGURE 34: Induction arrows for the period 0.03 s from Silali field. Blue arrows denote the real part and red arrows the imaginary part. Thick broken lines are faults as mapped on the surface

## 8.5 2-D interpretation of EM data

### 8.5.1 Data preparation for 2-D inversion

Before embarking on 2-D inversions certain things needs to be set up. Firstly the geo-electric strike analysis is done to aid in determination of TE and TM-modes to be used in inversions. In the Silali prospect the strike direction was taken as N10°E which was supported both by the Zstrike of the impedance data and the geological structural orientation, and all data points were mathematically rotated to this direction. The rotated impedance tensors are separated into individual polarizations of $Z_{xy}$ and $Z_{yx}$ and then jointly inverted with a nearby TEM sounding to correct for static shift. The 2-D inversion was carried out, with xy data assigned to the TE-mode (current flowing parallel to strike) and yx data to the TM-mode (current crossing the structure). 2-D resistivity profiles were set perpendicular to the strike and cross-sections for TE-mode, TM-mode and joint TE+TM-modes were plotted. Any single mode may not be sufficient to explain all the resistivity structures at all depths, for example it has been established that TE-mode is more robust to near surface whereas TM-mode is more sensitive to the deeper structures (Berdichevsky et. al, 1998). This way both TE and TM-modes complement each other, however in presence of 3-D structures spurious features can be introduced into the 2-D resistivity structure.

## 8.6 Static shift correction for 2-D and 3-D inversions

After rotating all the MT soundings to the geo-electric strike directions, the MT data need to be static shift corrected. It is assumed that the shift is mainly due to distortion of the electric field and joint 1-D inversion between each of the polarizations and the TEM sounding nearby is performed to determine the shift in the MT data. If $S_{xy}$ and $S_{yx}$ are the shift multipliers for the xy and yx polarization of apparent resistivities respectively, then the shift corrected tensor $Z^c$ is given by the following formula (Árnason et al., 2010):

$$\begin{bmatrix} Z_{xx}^c & Z_{xy}^c \\ Z_{yx}^c & Z_{yy}^c \end{bmatrix} = \begin{bmatrix} C_x & 0 \\ 0 & C_y \end{bmatrix} \begin{bmatrix} Z_{xx} & Z_{xy} \\ Z_{yx} & Z_{yy} \end{bmatrix}; \qquad 7.1$$

Where, $$C_x = \sqrt{1/S_{xy}} \; ; \; C_y = \sqrt{1/S_{yx}} \qquad 7.2$$

Figures 35 and 36 shows histograms and spatial distribution maps of the static shift multipliers respectively for xy and yx polarizations of all the 97 MT soundings. The shift multipliers $S_{xy}$ are in the range from 0.1 – 2.6 whereas those for $S_{yx}$ are in the range of 0.1 – 2.7 with $Z_{yx}$ having more shifts above 1. It is evident that most soundings in this area have shifted down and that the shift down or shift up is localized in particular areas and it's not random. An example of 1-D joint inversion of TEM and both $Z_{xy}$ and $Z_{yx}$ of MT data is shown in (Figure 37).

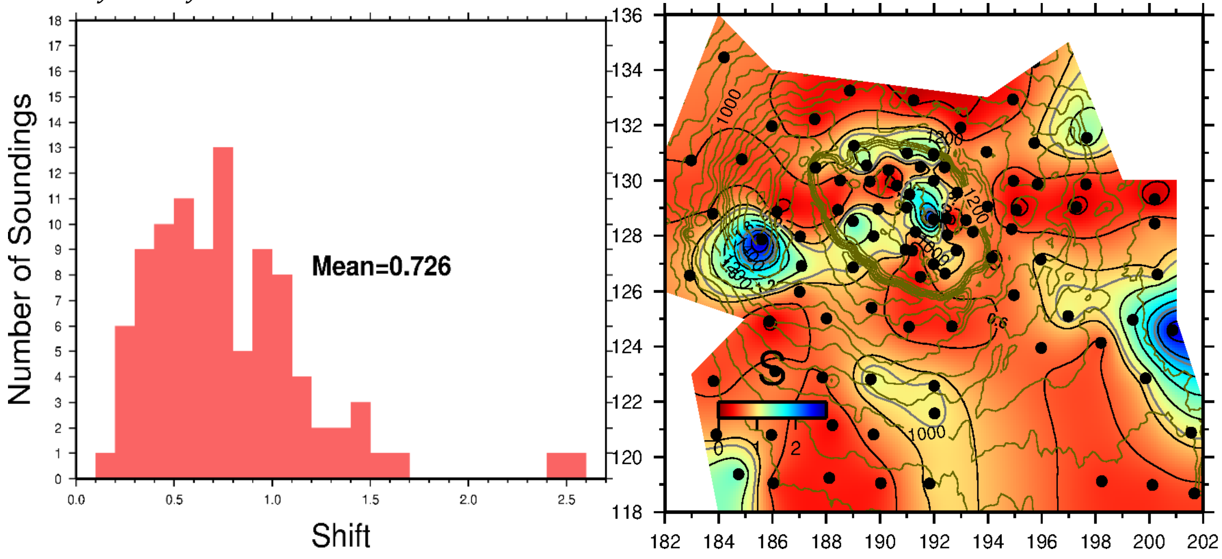

FIGURE 35: Histogram and spatial distribution map of static shift multipliers for determinant apparent resistivity for $Z_{xy}$ in the Silali area

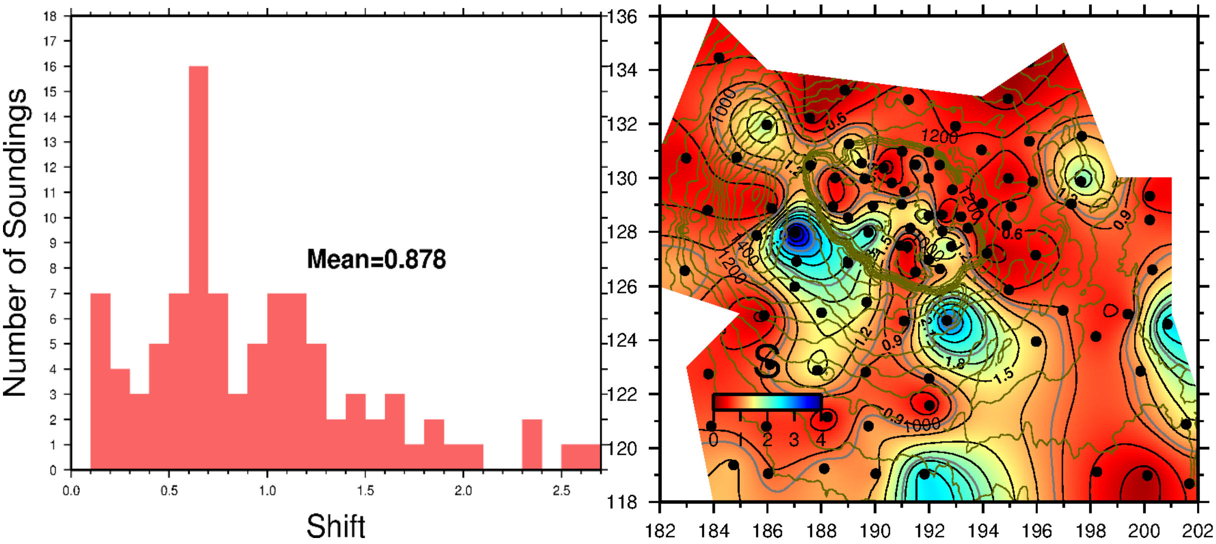

FIGURE 36: Histogram and spatial distribution map of static shift parameters for determinant apparent resistivity for $Z_{yx}$ in the Silali area

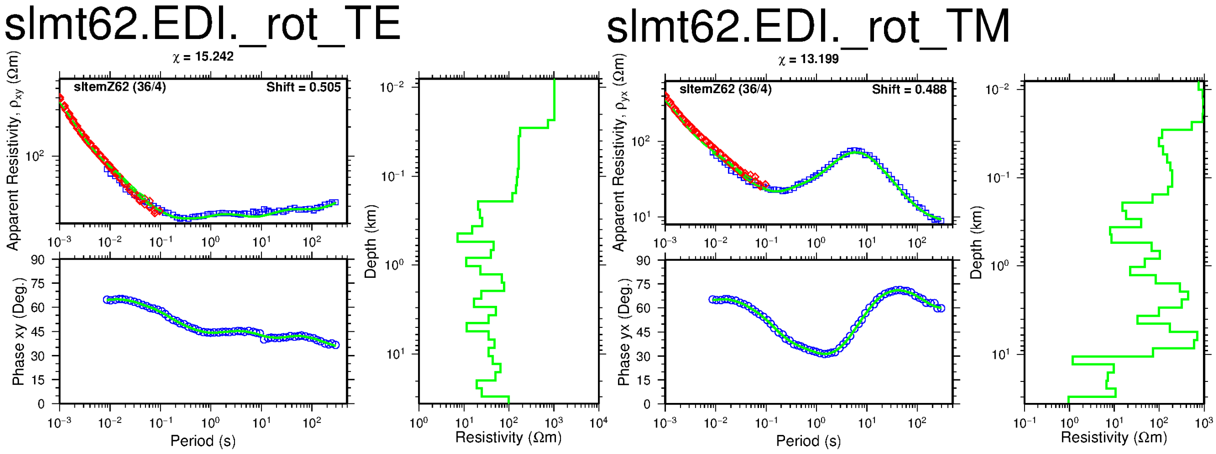

FIGURE 37: Joint inversion of (a) TEM and $Z_{xy}$ and (b) TEM and $Z_{yx}$ of MT data. Red diamonds are the measured TEM apparent resistivity. Blue squares and circles are the apparent resistivity and phase from the $Z_{xy}$ and $Z_{yx}$. The solid curves in the left panels are calculated responses from Occam inversion. On the right top corner of the resistivity panel are the shift multiplier, 0.505 for $Z_{xy}$ and 0.488 for $Z_{yx}$. This implies that the MT apparent resistivity has to be divided by 0.505 for $Z_{xy}$ and 0.488 for $Z_{yx}$ to tie in with the TEM response

### 8.7 2-D model mesh grid design

Prior to running 2-D inversions an appropriate model grid for the resistivities and frequencies to be used is setup. In this case a 2-D mesh grid was designed based on basic rules described in Simpson and Bahr (2005). The model mesh used for the inversion comprised of 120 horizontal and 39 vertical grid planes with a total of 4680 cells of varying sizes (Figure 38). In the middle of the mesh where soundings are located, the distance between grid planes is kept as dense as possible (in this case 200 m spacing) and incremented on each side logarithmically according to Simpson and Bahr (2005). The block thickness in the z-direction increases gradually from 10 m on the surface to 9000 m at depth of 43 km to correspond with loss of resolution with depth. The initial model also includes an additional 10 air layers which are required by REBOCC during inversion.

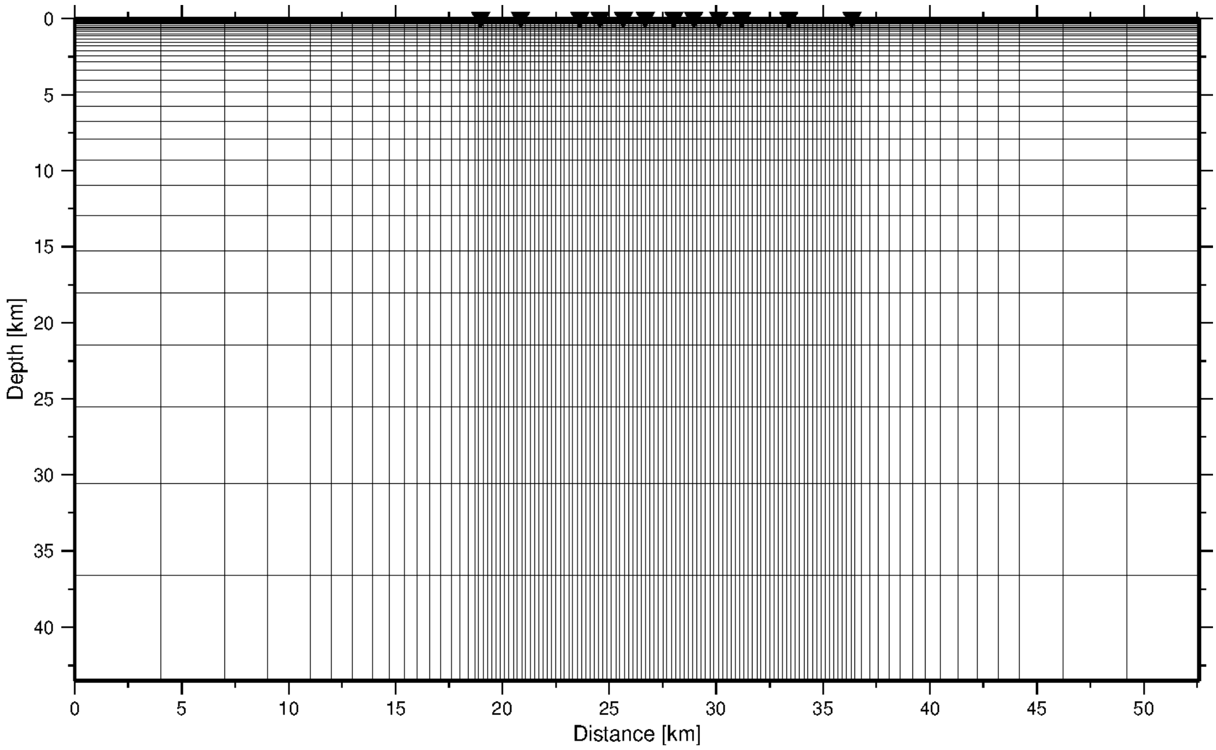

FIGURE 38: A mesh grid design for 2-D inversion using REBOCC. Black inverted triangles located at the top of the dense portion of the mesh are MT stations projected onto the profile

### 8.7.1 2-D inversion of MT data

The inversions of MT data was performed by use of REBOCC program along the four profiles running perpendicular to the regional strike. The program aims at finding a minimum structure model subject to a desired misfit level. The starting model used in the 2-D inversion was a 10 ohm-m homogeneous half-space, and the iterations were set to 10 with RMS misfit of 1. It should be noted that the desired RMS achieved in all profiles was in the range between 5 and 11, this was as a result of the model responses not fitting well to the data which imply that the data was not fully 2-dimensional. Location of the profiles is as shown below. For each profile two data responses and their corresponding error responses for both apparent resistivity and phase were generated each for TE and TM-mode and used as input to REBOCC. A total of 73 periods ranging from 0.0031 to 877 seconds were included in the data file for each profile. Several half-space initial models were used to check model convergence and fitting to the data and 10 ohm-m homogeneous half-space was found to be the best. REBOCC is very fast and converges to more reliable inversion with minimal memory usage.

### 8.7.2 2-D inversion results

This section shows results from three profiles running perpendicular to the strike direction. Each of the profiles present three cross-sections for TE-mode, TM-mode and a combined TE+TM-mode. Two-dimensional models usually have anisotropic responses. For instance by inverting each mode separately, yields two different resistivity structures. This difference in modes is due to different sensitivity to complex structures and does not always imply anisotropy. Appendix III shows plots of the model-fit to the field data for the apparent resistivity and impedance phase.

**Profile EW10_4:** Cuts through the northern part of the caldera. The TE-mode, TM-mode and combined TE+TM-modes resistivity structure (Figures 39, 40 and 41) show a resistive ( $\geq 100\ \Omega$m) surface layer, underlain by low-resistivity layer of about 10 Ωm across the entire length of the profile. Below the conductive layer, higher resistivity is observed in all the 2-D modes but its more pronounced in TE-mode and extends to the base of the profile. At depths greater than 5 km for TM-mode (Figure 40) low resistivity dominates, this resistivity structure closely resembles that of 1-D inversion (Figure 25). The TE+TM-mode resistivity cross-section presents a low-resistivity vertical structure at a depth below 6 km in the central part beneath MT sites 54 and 69 which is bounded on both sides by high resistivity. The reason as to why the three modes produce different results might indicate the non 2-D resistivity structure at depth.

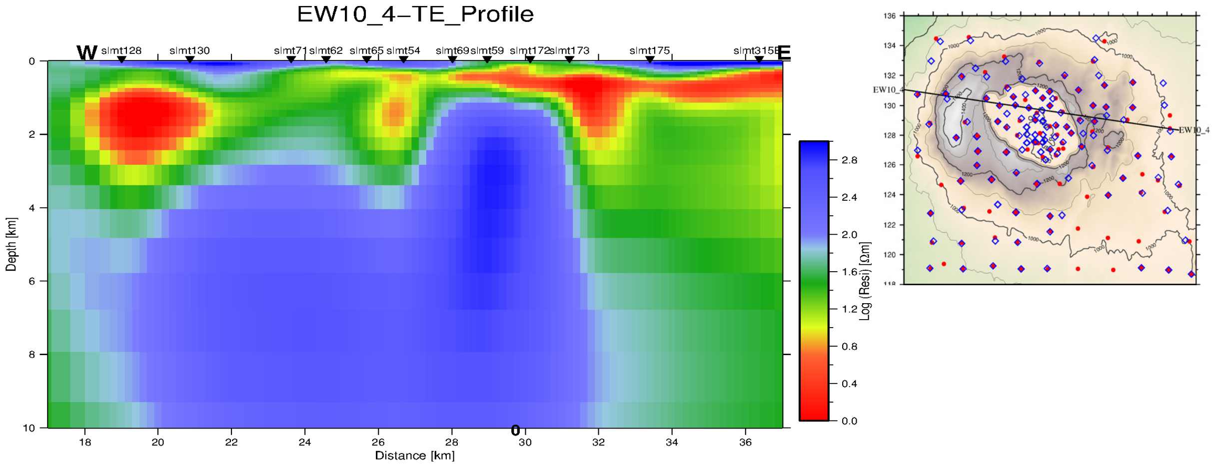

FIGURE 39: 2-D model obtained by inverting the TE data for Profile EW10_4. This resistivity model was obtained after 7 iterations and RMS of 8. Location map is shown to the right of the map

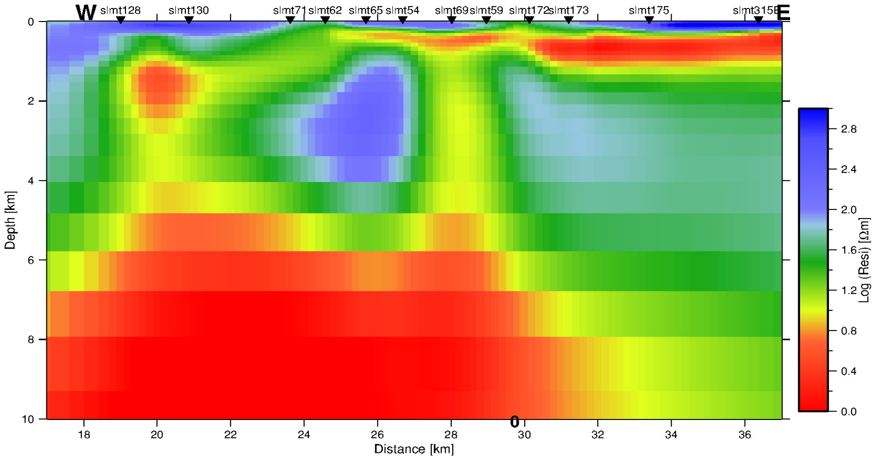

FIGURE 40: 2-D model obtained by inverting the TM data for Profile EW10_4. This resistivity model was obtained after 7 iterations and RMS of 6.2

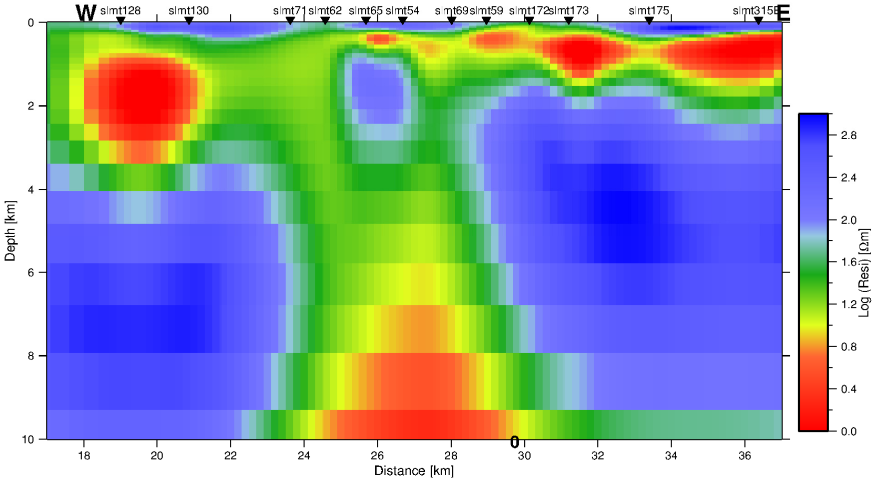

FIGURE 41: 2-D model obtained by jointly inverting TE and TM-mode data for ProfileEW10_4. This resistivity model was obtained after 8 iterations and RMS of 11.5

**Profile EW10_3:** Cuts through the centre of the caldera. The TE-mode, TM-mode and joint inversion of TE+TM-mode models are shown in Figures 42, 43 and 44, respectively. The resistivity structure show a resistive (≥ 100 Ωm) surface layer, underlain by low-resistivity layer of about 10 Ωm almost the entire length of the profile. This low resistivity could be attributed to the alteration minerals which further overlays a high resistivity zone of about 100 Ωm in the middle of the profile. This high resistivity structure could be as a result of high temperature alteration mineralogy and a probable geothermal reservoir for this field. At depth TE-mode presents high resistivity structure which is different from the TM and TE+TM-modes. Both TM and TE+TM shows low resistivity at depth with TM-mode smearing the entire section with low resistivity. This could partly be as a result of modelling artefact caused by deeper conductors which are not sufficiently resolvable by TM-mode.

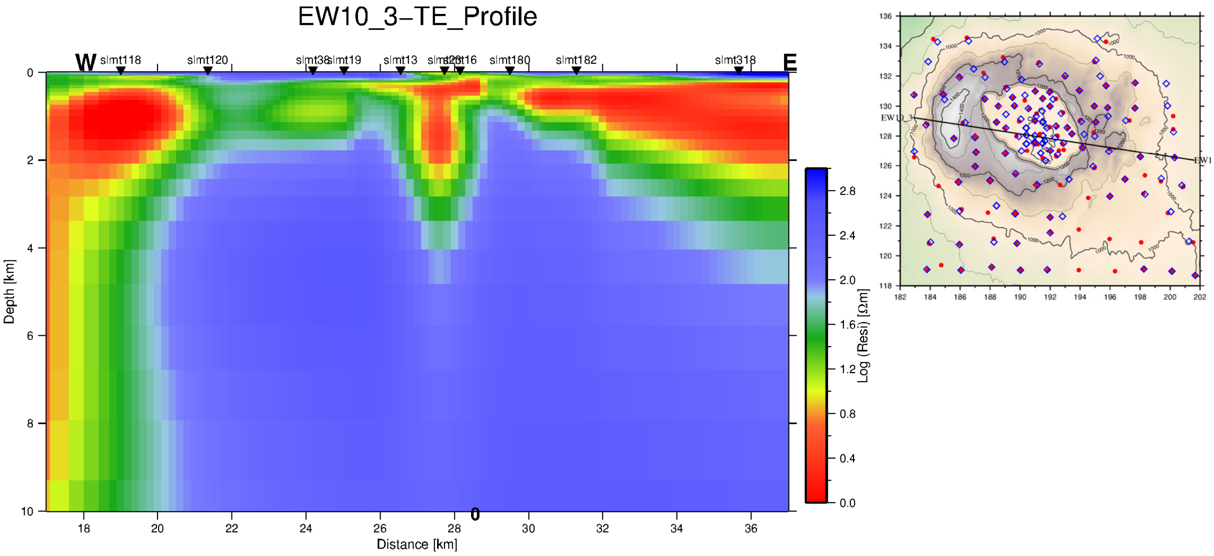

FIGURE 42: 2-D model obtained by jointly inverting TE-mode data for Profile EW10_3. This resistivity model was obtained after 6 iterations and RMS of 6. Location map is shown to the right of the map

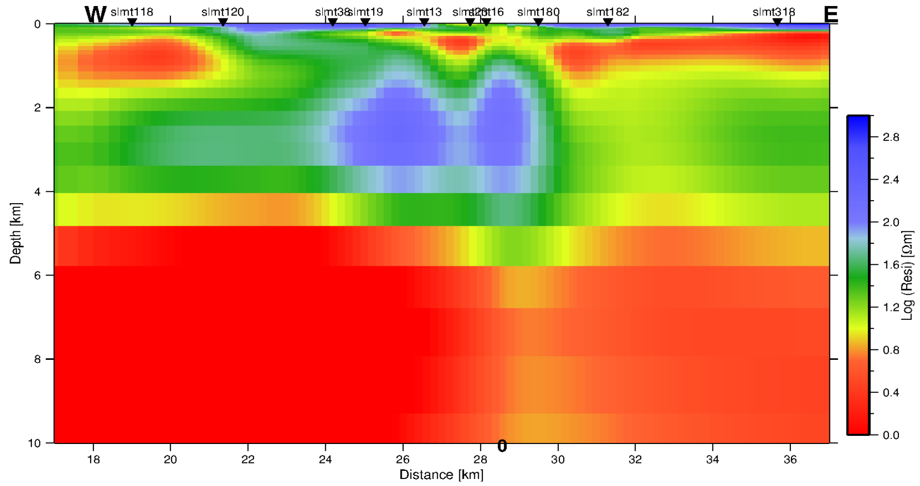

FIGURE 43: 2-D model obtained by jointly inverting TM-mode data for Profile EW10_3. This resistivity model was obtained after 4 iterations and RMS of 6.5

**Profile EW10_2:** This is a profile passing through the south of the caldera. The TE-mode, TM-mode and joint inversion of TE+TM-mode models are shown in Figures 45, 46 and 47, respectively. The resistivity structure show a resistive (≥ 100 Ωm) surface layer probably as a result of unaltered formations in the near sub-surface, underlain by low-resistivity layer of about 10 Ωm on the eastern half of the cross-section. This low resistivity cap is correlated to that seen in 1-D interpretation linked to the alteration clay minerals. Below the low resistivity cap all modes seems to differ somewhat with TM-mode and joint TE+TM-modes showing some high resistivity at similar depths in the middle of the profile. Similarly all modes of MT impedance seems to present a deeper conductor with TM and TE+TM-modes roughly in agreement on the location but TE-mode is offset to the east.

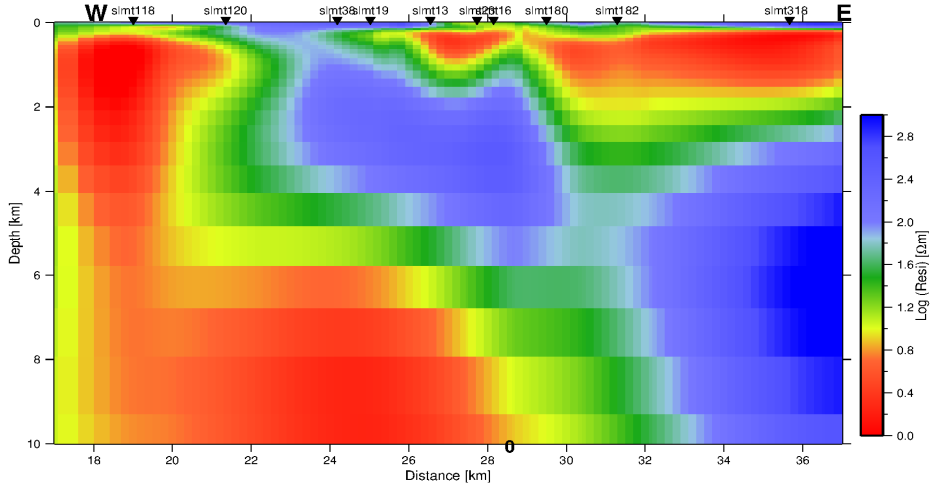

FIGURE 44: 2-D model obtained by jointly inverting TE and TM-mode data for Profile EW10_3. The model was obtained after 9 iterations and RMS of 8.3

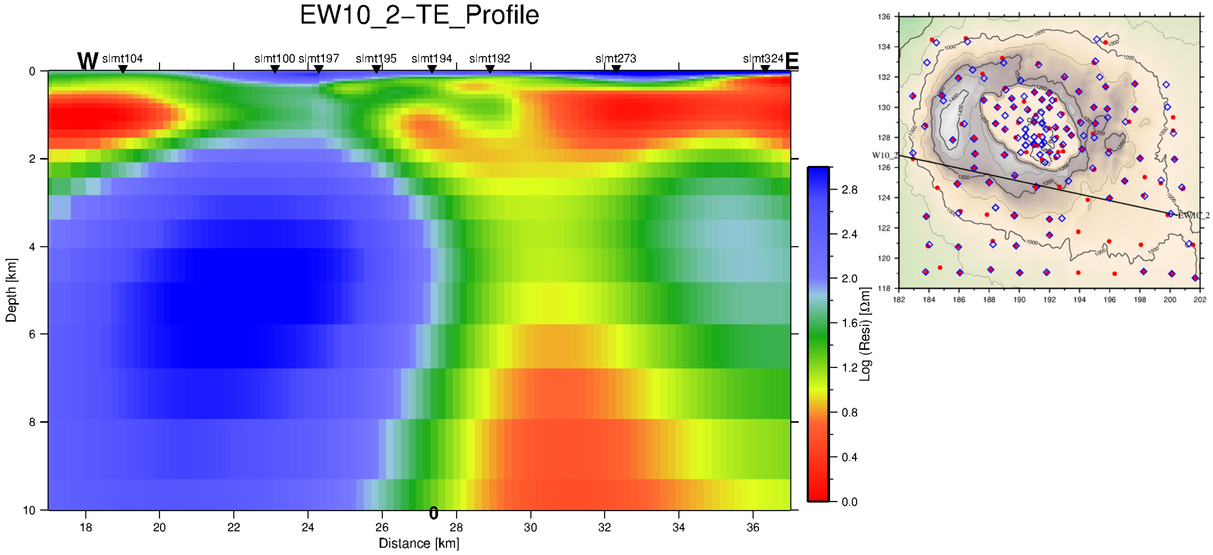

FIGURE 45: 2-D model obtained by jointly inverting TE-mode data for Profile EW10_3. This resistivity model was obtained after 6 iterations and RMS of 6. Location map is shown to the right of the map

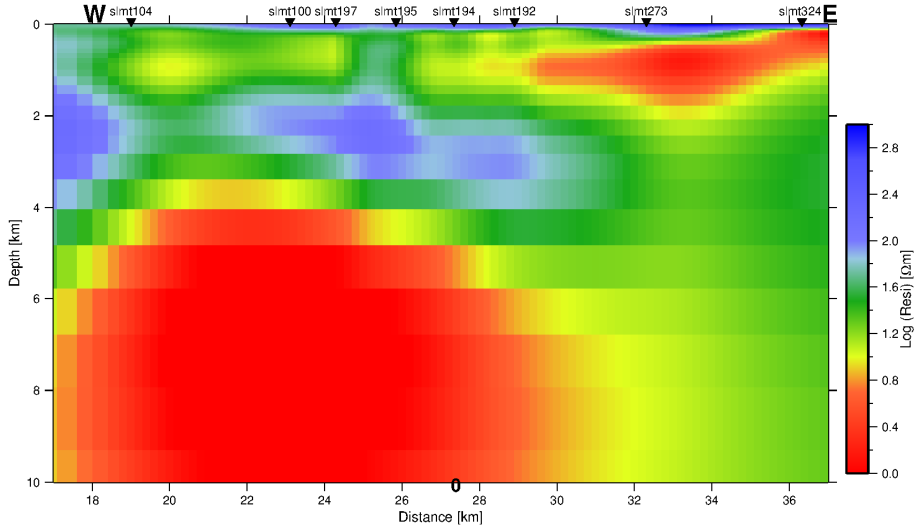

FIGURE 46: 2-D model obtained by jointly inverting TM-mode data for Profile EW10_2. This resistivity model was obtained after 8 iterations and RMS of 6.1

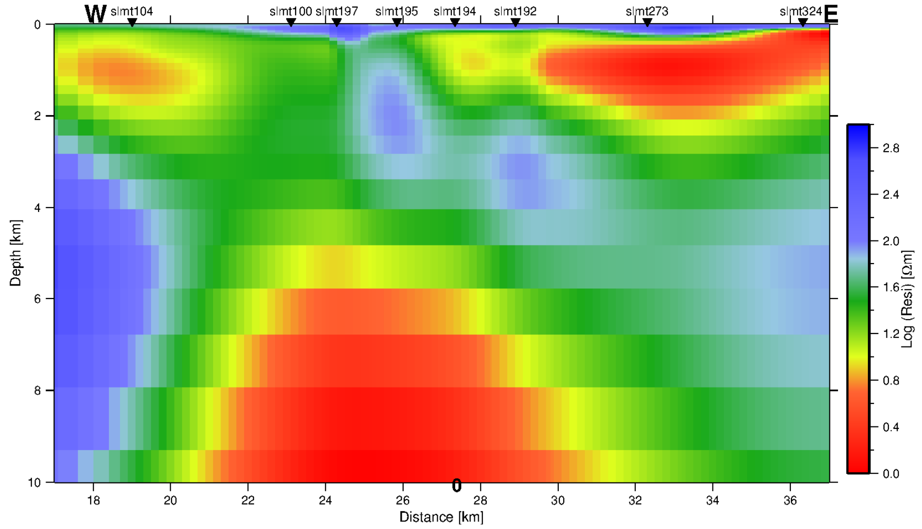

FIGURE 47: 2-D model obtained by jointly inverting TE and TM-mode data for Profile EW10_2. This resistivity model was obtained after 9 iterations and RMS of 11.1

### 8.7.3 Discussion of 2-D inversion results

2-D inversions were carried out to define subsurface conductive structures but a single model that explains both TE and TM models may not exist. The TM-model provides better resolution of higher resistive blocks, which can be explained in terms of boundary conditions. The electric field in the TM-mode is perpendicular to strike and thus, discontinuous across lateral changes in resistivities. In this case the TM-mode is more robust to the presence of 3-D structures (Wannamaker et al., 1991).

The main result from inversion of profiles presented above can be summarized as follows: Four main resistivity layers are revealed from the 2-D inversion. These are a thin surface layer of high resistivity (≥ 100 Ωm) followed by conductive layer of about 10 Ωm, underlain by a high resistivity core of about 100 Ωm and a deep low resistivity of (≤ 10 Ωm). The surface high-resistivity layer can be correlated to unaltered basaltic lava flows and other eruptive materials. The second layer is very conductive and can be associated with altered formations and clays (smectite-zeolite or mixed layer clay alteration zone). The high resistivity core below the conductive layer can be correlated to chlorite-epidote alteration zone down to a depth of about 3 km. This high-resistivity zone below the conductive layer could be related to the reservoir of the geothermal system. At depth of 5-6 km a deeper conductor appears on mainly the TM and TE+TM-mode cross-sections. This deeper conductive structure, if real, could be the heat source of the geothermal system. Although the results of the inversion model seems to reproduce main structures, the poor fit of the model responses to the some data would not guarantee enough confidence in the inversion model obtained. 2-D inversions are known to introduce spurious features in the interpretation when they cannot resolve the features due to off-profile 3-D structures (Siripunvaraporn et al., 2005). Moreover, the resistivity distribution of real geological structures is often very complex and does not satisfy the 2-D assumption. Therefore to solve this problem, 3-D MT inversion of the MT data is essential.

## 8.8 3-D inversion of MT data

With the development of MT interpretation codes and advances in computer hardware 3-D electromagnetic data interpretation has become attainable. Dimensionality analysis of the MT data from Silali field show non one-dimensional resistivity structure mainly at long periods. It is therefore necessary to carry out 3-D inversion to determine the correct resistivity structure. This is achieved by use of a 3-D inversion program, WSINV3-DMT version 1.1.0 (Siripunvaraporn et al., 2005) which seeks to find a model with a response that fits the data. This inversion code uses finite difference forward algorithm and formulates the inversion problem in data-space rather than the more computationally demanding model-space approach. Therefore this scheme significantly reduces the computational time and memory required for the inversion making the 3-D inversion of MT data possible.

### 8.8.1 Data preparation

The modelling data used for the 3-D inversion are; 97 MT soundings, 30 periods and 4 impedance tensor elements (real and imaginary part of the two off-diagonal elements). The MT soundings chosen were those that were less noisy and with long period data points and evenly distributed over the entire area. All the MT impedances were rotated to N10°E which is the strike direction. After rotating the data, joint inversion for each polarisation was performed to determine the shift multipliers as discussed in section 8.6. In order to minimize the computational time and memory the impedance data was sampled at 30 periods equally spaced on a log scale, ranging from 0.0031 to 700 seconds. The 30 periods which were sampled for were; 0.0031, 0.0047, 0.0073, 0.0111, 0.0170, 0.0260, 0.0397, 0.0608, 0.0930, 0.1422, 0.2175, 0.3327, 0.5090, 0.7786, 1.1910, 1.8219, 2.7871, 4.2634, 6.5218, 9.9766, 15.2614, 23.3456, 35.7122, 54.6297, 83.5680, 127.8356, 195.5524, 299.1402, 457.6004 and 700. This not only reduces the data size but also makes the data to be smoother. If there are any noisy data points in the resampled data set a skipfile is prepared to be used during inversion to skip those noisy data points so that they are not included in the inversion.

### 8.8.2 3-D Model mesh grid design

When setting up a 3-D model grid, it must be ensured that it is accurate for the resistivities and frequencies to be used. In designing the mesh a trade-off is sought between the size of the grid and the computational time it would require to obtain reasonable solutions to the models. This is because the finer the grid the larger the time and memory resource required. Forward modelling solutions depend significantly on the mesh grid discretization used. The finite difference code for the forward problem requires a cubic grid, in this case a grid of 73 x 86 x 28 in x, y, and z directions was used. This gave a total model size M to be equal to $73 \times 86 \times 28 = 175{,}784$. At the centre of the grid a uniform model discretization with a cell width of 350 m for 49 x 62 grid squares in x and y directions was used within the area containing MT stations. This grid increases exponentially in size to 139.4 km and 141.8 km in the x and y directions respectively. In the z direction the grid planes are dense at shallow depth with the first layer set at 16 m and then increased progressively by 1.4 times of the overlying block to depths of 160.8 km. The grid was oriented with the x-axis in the strike direction (N10°E), x positive to N with an internal coordinate system of model centred at UTM coordinate 193000, 126000 marked with a star in Figure 48.

### 8.8.3 3-D modelling parameters and initial models

The model grid size used in the 3-D inversion was $M = 73 \times 86 \times 28 = 175{,}784$ for x, y and z respectively. This represents the number of unknowns in the forward modelling problem. If the inverse problem was to be solved in the model-space this would present a huge computational problem. In the given data set comprising of 97 stations at 30 periods and 4 impedance responses, reduces the problem in data-space to N=97 x 30 x 4 equal to 11,640 which can be solved with achievable computational cost and memory done by data-space 3-D inversion. The inversion program was run using a parallel processing version of the WSINV3DMT code using the Message Passing Interface (MPI) parallel computing environment. This was setup on a special machine cluster at ÍSOR running on 32 cores and 132 GB of memory to be able to deal with a big data set like this one. The inversions were done with three different initial models being used as the base models for the 3-D inversions. The first initial model was derived from the 1-D layered models interpolated from joint 1-D TEM and MT inversions. The initial RMS for this starting model is about 13.6 reducing to 1.6 after 15 iterations. The second initial model was 100 ohm-m homogeneous half-space with initial RMS of 41.5 reducing to 1.7 after 15 iterations. The final initial model was based on 10 ohm-m homogeneous half-space with initial RMS of 11.5 reducing to 1.5 after 15 iterations. The 10 ohm-m homogeneous half-space initial model was repeated with adjusted smoothing criteria (i.e. parameters set at 0.25 instead of the default of 0.1 used in the prior model) to try to recover the smoothed resistivity structure of the models, attaining RMS of 1.7 after 15 iterations. The RMS defines the data misfit between the measured and calculated values of the off diagonal tensor elements (real and imaginary parts), weighted by the variance of the measured values.

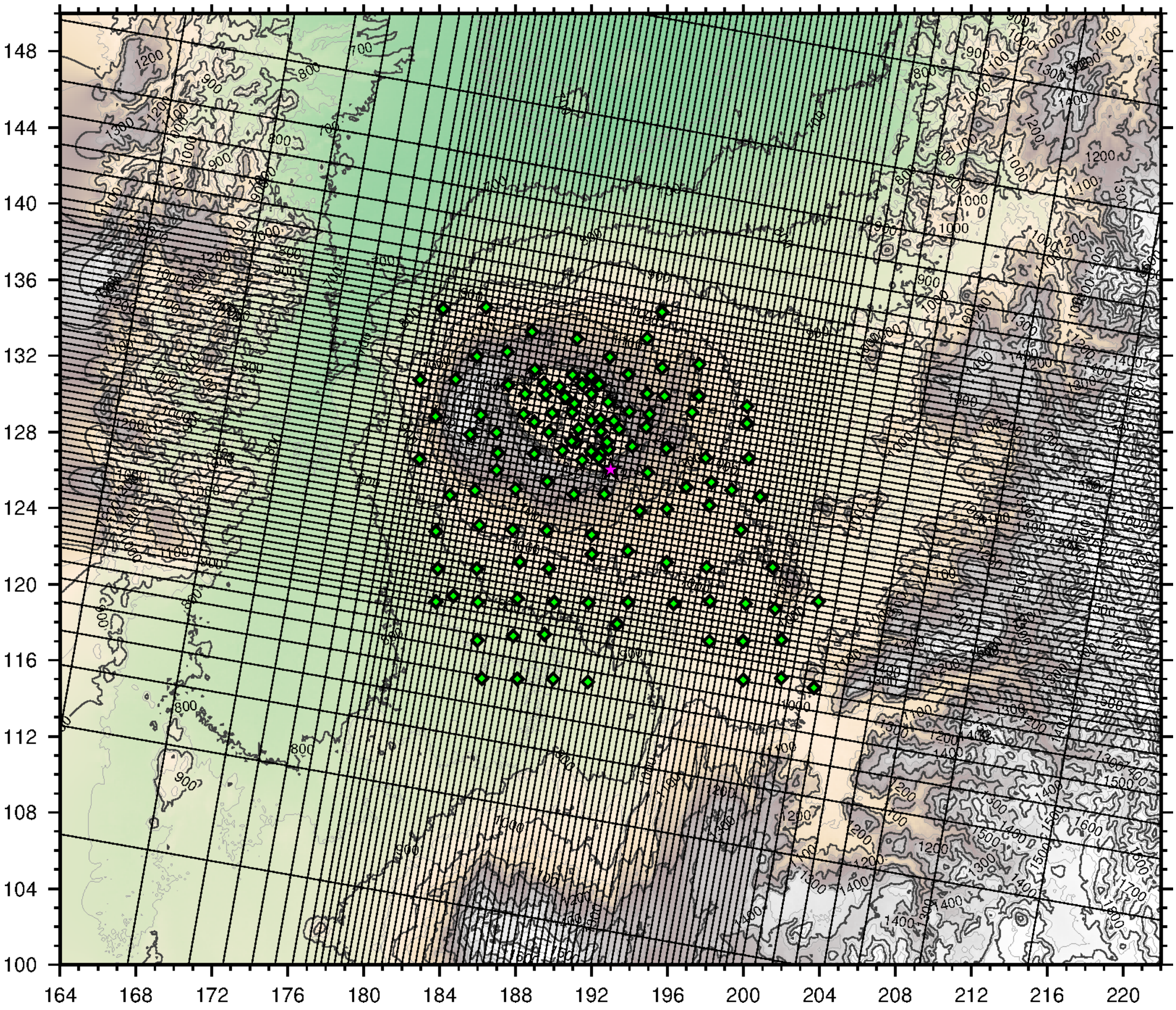

FIGURE 48: 3-D model grid showing location of MT soundings in the central part of mesh surface (x-y direction). The fine grid squares are 350 m x 350 m in dimension. The MT and TEM sites are shown as green/black symbol

Figure 49 shows results from model response fitting to the data. In most cases the measured data were fitted quite well. For each initial model three runs were performed and 5 iterations were allowed for each run. After every run the inversion was restarted with the model that gave the best fit as the initial model for the successive runs. Through these step-runs the inversion gradually relaxes the limitation of the prior model, until the data fit can no longer be improved. This is achieved by regularization where a reference (prior) model is used to constrain the inversion model not to deviate too much from the prior model. Each iteration took 27 hours, yielding a total computing time of 1620 hours (about 68 days) for the 60 iterations. Most of the CPU time is spent in constructing the sensitivity matrix for solving inverse problems.

### 8.8.4 3-D inversion results based on different initial models

This section aims at drawing comparison in 3-D resistivity structure using different initial models to emphasize some of the correlation patterns (and lack thereof) discussed later. In order to investigate to what extent a certain feature is required by the data we undertook inversion using different initial models. Three initial models are considered to test the robustness of the final inversion model, one based on the one-dimensional layered model, another based on 100 ohm-m homogeneous half-space a third one based on 10 ohm-m homogeneous half-space and finally a more smoothed prior model with 10 ohm-m homogeneous half-space. This comparison aims at identifying resistivity structure that is robust enough irrespective of whichever initial model is used in the inversion. From the results of the 1-D inversion, a reasonable starting model can be constructed for three-dimensional (3-D) inversion.

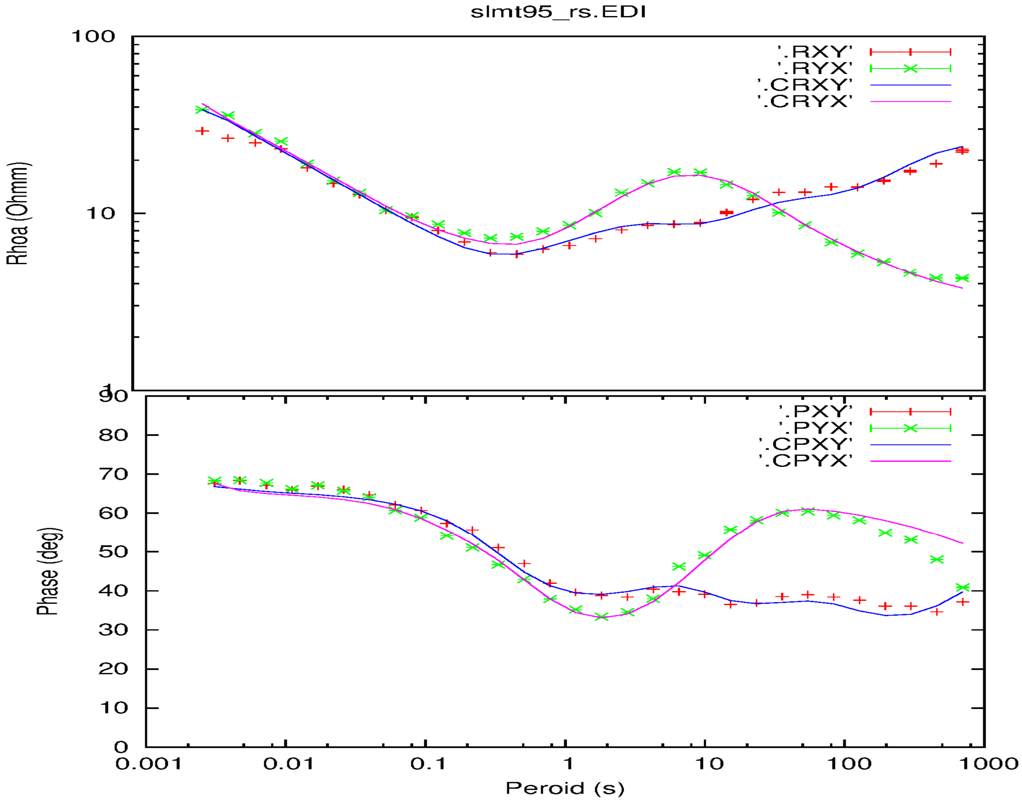

FIGURE 49: An example of data fit between the measured data (calculated from static shift corrected impedance) and model response. The red and green symbols are data points whereas the pink and blue lines are model responses. A full set of all the calculated responses of the final model from the initial models is shown in Appendix IV.

The 100 ohm-m homogeneous half-space initial model is intended to reproduce the high resistivity structure and let the inversion introduce lower resistivity structures where needed. The 10 ohm-m homogeneous half-space initial model is intended to reproduce the low resistivity structure and try to recover higher resistivity structure by inserting high resistivity where required. In this regard confidence is placed on low resistivity structure recovered by the high resistivity initial model and on the other hand a high resistivity structure recovered by the low resistivity initial model. The parts of the final models, from different initial models that agree are considered reliable.

As mentioned previously, the 3-D program assumes flat surface. The MT data were static shift corrected prior to the inversion and this correction removes topographic effects in the data to a large extent. At the end, the resistivity models resulting from the inversion were elevation corrected, i.e. the depths below each model cell were converted to meters above or below sea level and are presented as smoothed resistivity maps at different elevations and as resistivity cross sections.

The results obtained from 3-D inversion based on the four runs are presented as resistivity maps at same elevations (Appendix V) and cross-sections (Appendix VI) for comparison. It is critical to inspect anomalies that are similar in all the models to test the robustness of the resistivity models. Figure 50 compares resistivity structure at 1000 m a.s.l., Figure 51 at sea level and Figure 52 a cross-section through the caldera to see whether the four initial models are consistent at every level. As seen in the figures it is evident that results from all the four initial models agree quite well at 1000 m a.s.l where the low resistivity structure is prominently around the caldera. At depths of sea level there is a striking correlation of the high resistivity anomalies within the caldera separated by a lower resistivity linear structure, similarly the increasing resistivity seems to be oriented towards the south-west of the study area.

Comparison of the cross-sections show fair agreement in the resistivity structure at both the shallow zones and intermediate depths up to about 5000 m b.s.l. At greater depths all inversion results demand

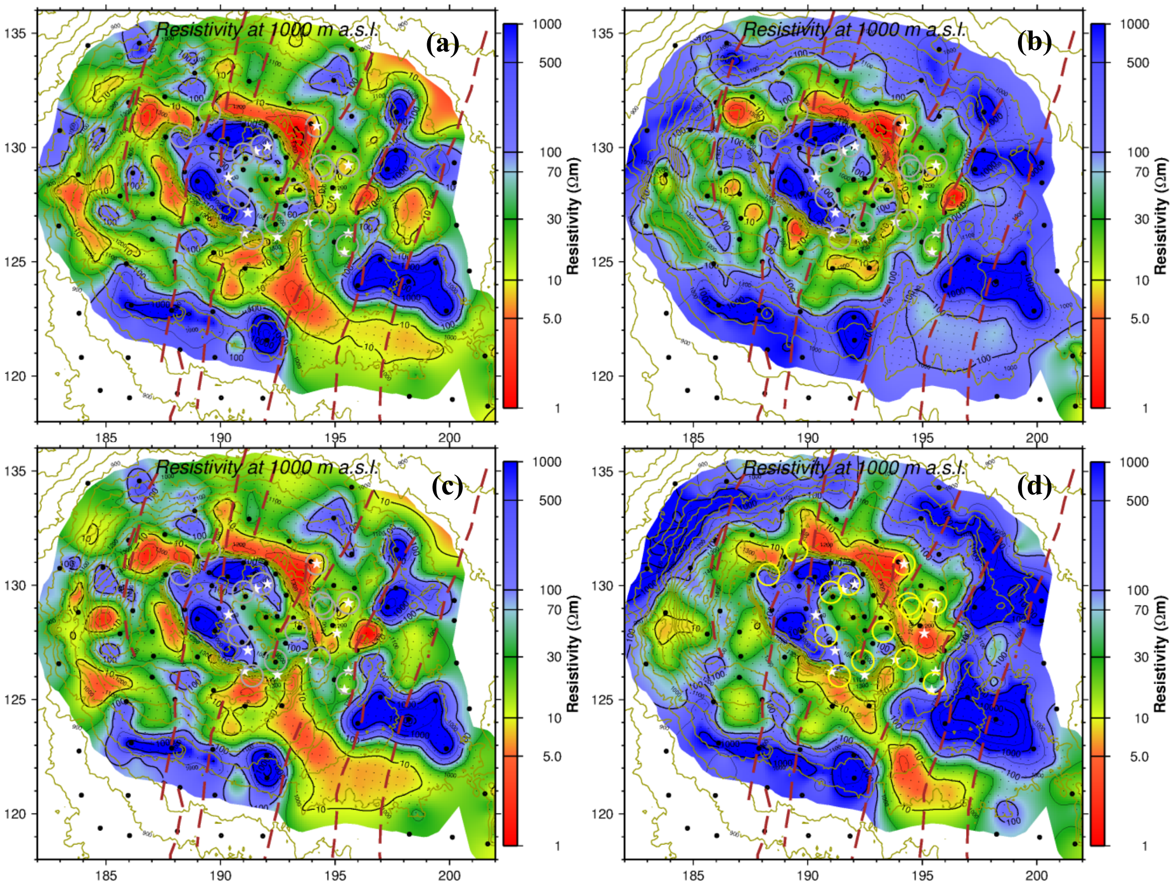

FIGURE 50: Resistivity at 1000 m a.s.l showing comparison of results from initial models a) 1-D layered model, b) 100 ohm-m homogeneous half-space, c) 10 ohm-m homogeneous half-space and d) smoothed 10 ohm-m homogeneous half-space

a deeper conductor but its exact shape and location differs somewhat depending on which initial model is used, this could be attributed to the noisy data sets at long periods hence limited depth of exploration. This is because the noisy portion of the data can be fitted by different models. Therefore the depth of resolution is limited to 6 km.

The above results indicate that the major features of the resistivity structure in the upper 6km depth are reproduced for both cases, but there are minor differences at depth. Four distinct electrical units can be identified from the 3-D inversion results from the initial models considered. A relatively thin resistive surface layer, a conductive unit at a depth less than a kilometre, distinct zones of resistive material separated by a conductive zone below the caldera, and a deep (> 6km) conductive basal zone. Based on the comparison it is concluded that the results obtained from smoothed 10 ohm-m homogeneous half-space initial model inversion recovers the resistivity structure well and is therefore considered for interpreting the results.

### 8.9 3-D inversion results

This section presents 3-D inversion results derived using the smoothed 10 ohm-m homogeneous half-space initial model. Ordinarily the 3-D program assumes flat surface, but as mentioned earlier the MT data were static shift corrected prior to the inversion and this correction considerably removes topographic effects in the data. The resistivity models resulting from the inversion were elevation corrected, and results are presented as smoothed iso-resistivity maps and cross-sections.

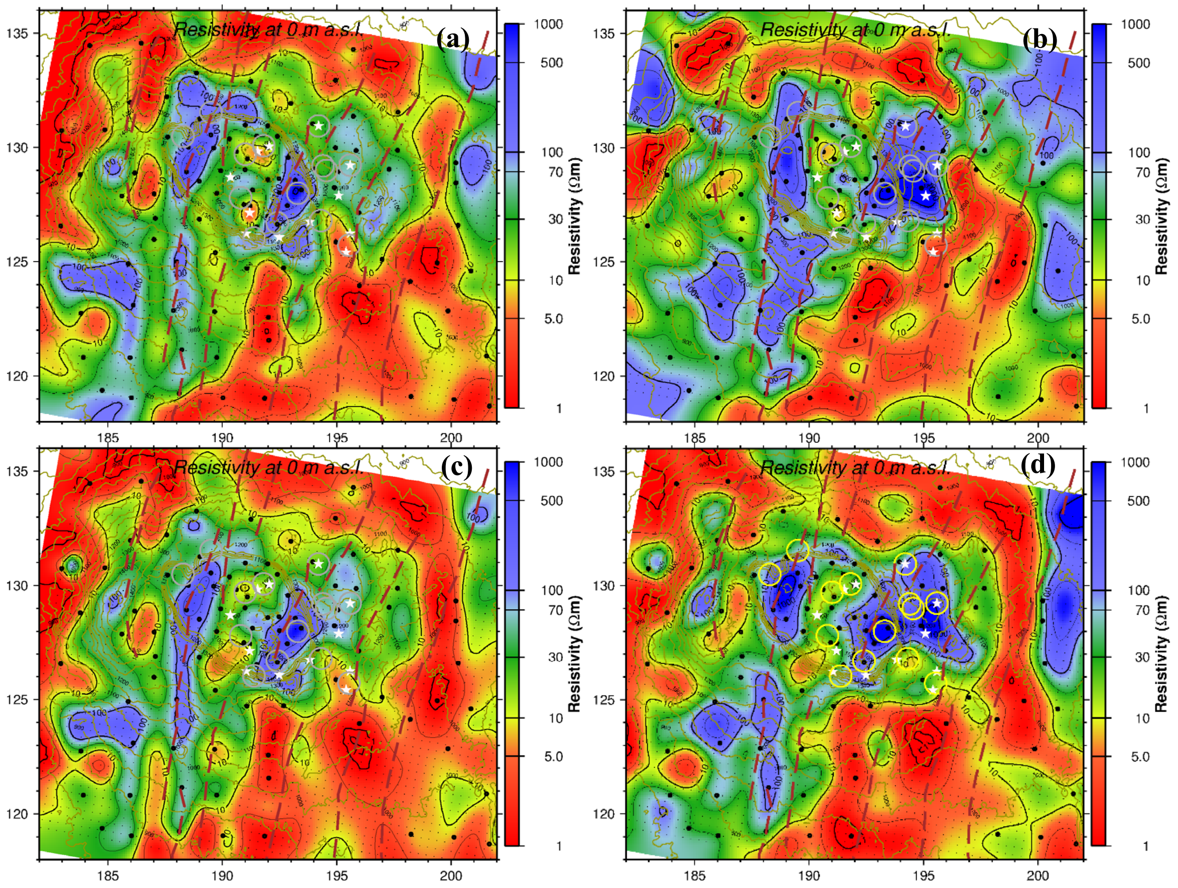

FIGURE 51: Resistivity at sea level showing comparison of results from initial models a) 1-D layered model, b) 100 ohm-m homogeneous half-space, c) 10 ohm-m homogeneous half-space and d) smoothed 10 ohm-m homogeneous half-space

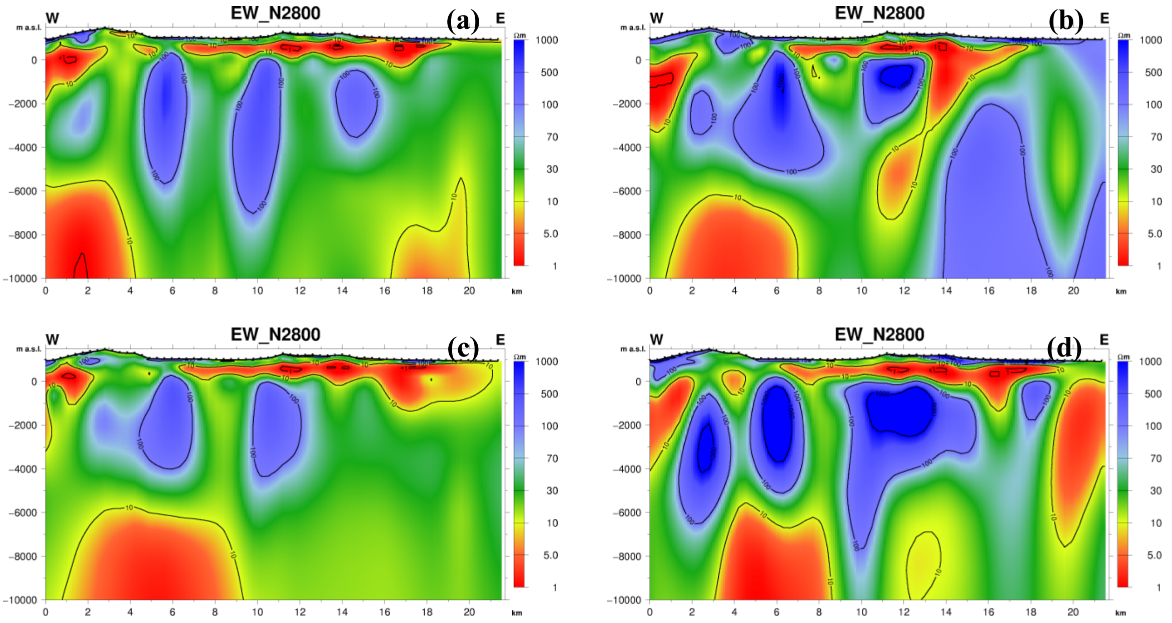

FIGURE 52: Resistivity cross-sections in EW direction through the caldera showing comparison of results from initial models a) 1-D layered model, b) 100 ohm-m homogeneous half-space, c) 10 ohm-m homogeneous half-space and d) smoothed 10 ohm-m homogeneous half-space

### 8.9.1 3-D Resistivity maps

Elevation corrected iso-resistivity maps are presented from the near-surface shallow maps to the deeper elevations. Figure 53 shows resistivity at 1000 m a.s.l., a circular shaped shallow conductive cap is seen, presumably reflecting the smectite and zeolite alteration zone. This is also an area where most of the fumaroles and altered grounds are located mainly within and around the caldera. Elsewhere there is a higher resistivity zone which could be un-altered formations in the shallow sub-surface.

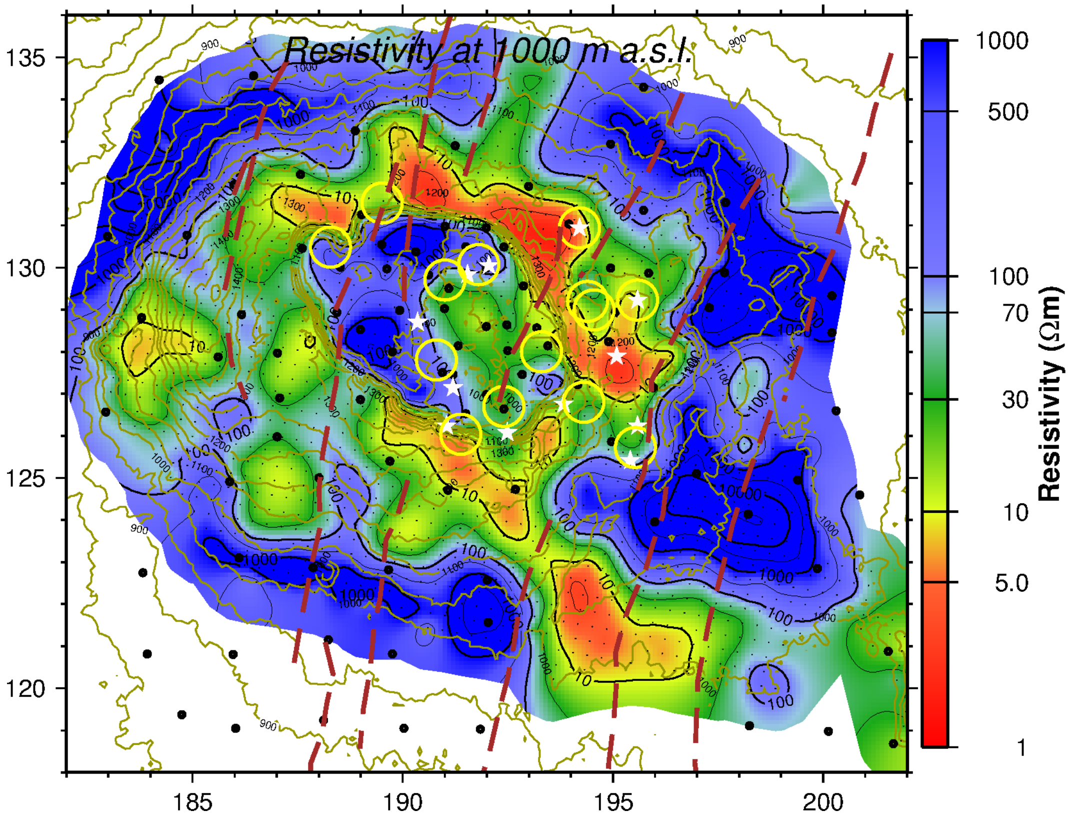

FIGURE 53: Resistivity at 1000 m a.s.l. Fumaroles are denoted by white stars, altered grounds by yellow circles and broken brown lines show faults as mapped on the surface

At 800 m a.s.l. (Figure 54) the conductive cap spreads further to the southwest and southeast and becomes dominant inside the caldera. Portions of resistive zones are still evident both in the south and northwest of the caldera.

At sea level (Figure 55), two resistive cores show up inside the caldera spreading eastwards and southwards out of the caldera. These zones could most likely be reflecting the chlorite and epidote alteration zone and hence a high temperature geothermal reservoir. A relatively lower resistivity linear structure cuts through the centre of the caldera separating the two high resistivity anomalies. On the outer margins of the restive core conductive zones dominate becoming more extensive in the south of the caldera.

At 1600 m b.s.l. (Figure 56) the resistive core has increased considerably in areal extent within the caldera spreading more to the east and south of the caldera. This could be mapping the extent of the high temperature geothermal resource area. The low resistivity structure inside the caldera is more pronounced and elongates on both sides outside the caldera. This conductive linear anomaly occurs beneath the row of volcanic cones in that sector of the Silali volcano. On the outer margins of the resistive core are conductive zones running parallel on both eastern and western sectors of the map.

At 5000 m b.s.l. and 8000 m b.s.l. (Figures 57 and 58) respectively shows the deeper resistivity structure in the prospect area with deeper conductors showing up to the north and southwest of the caldera. At 8000 m b.s.l. the low resistivity seems to align in N-S direction through the western sector of the caldera.

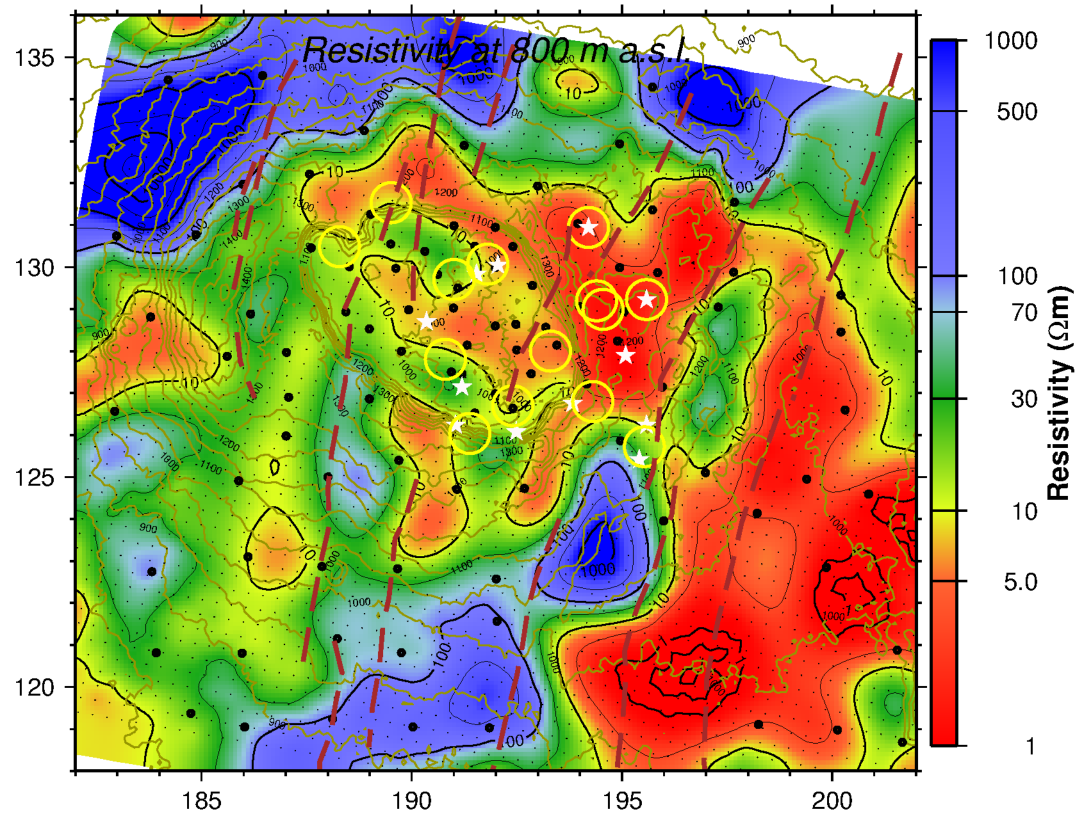

FIGURE 54: Resistivity at 800 m a.s.l. Fumaroles are denoted by white stars, altered grounds by yellow circles and broken brown lines show faults as mapped on the surface

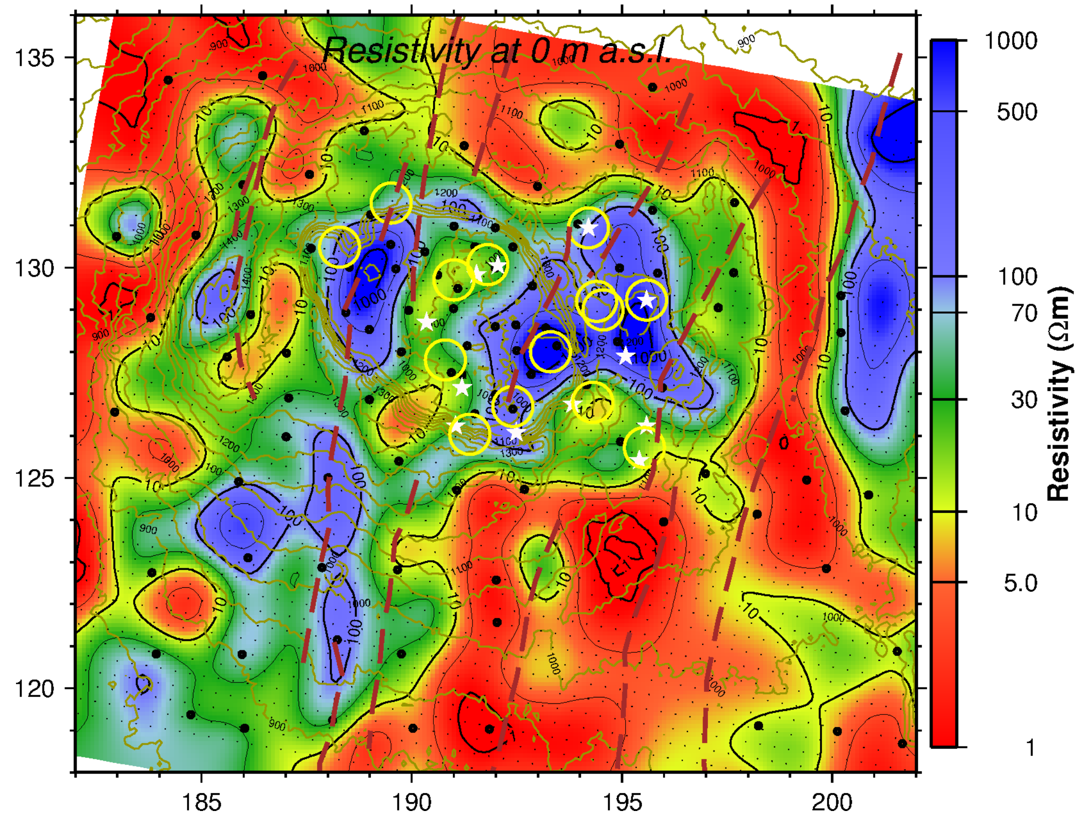

FIGURE 55: Resistivity at sea level. Fumaroles are denoted by white stars, altered grounds by yellow circles and broken brown lines show faults as mapped on the surface

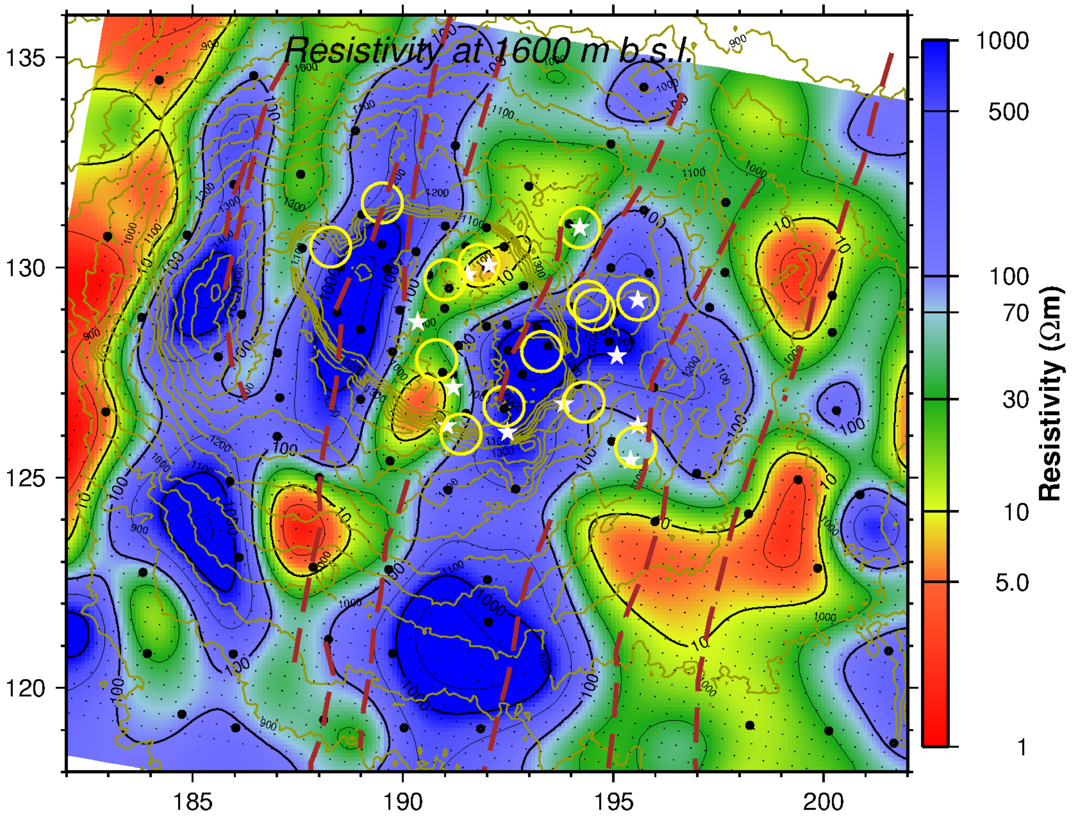

FIGURE 56: Resistivity at 1600 m b.s.l. Fumaroles are denoted by white stars, altered grounds by yellow circles and broken brown lines show faults as mapped on the surface

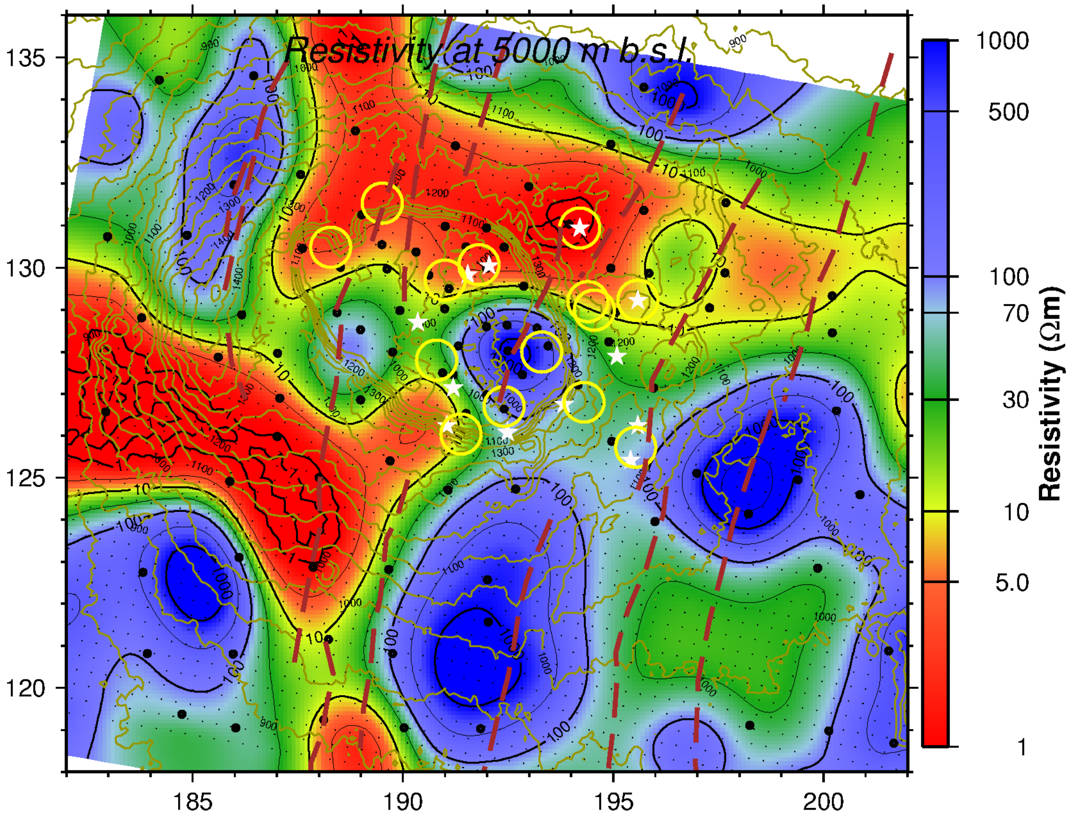

FIGURE 57: Resistivity at 5000 m b.s.l. Fumaroles are denoted by white stars, altered grounds by yellow circles and broken brown lines show faults as mapped on the surface

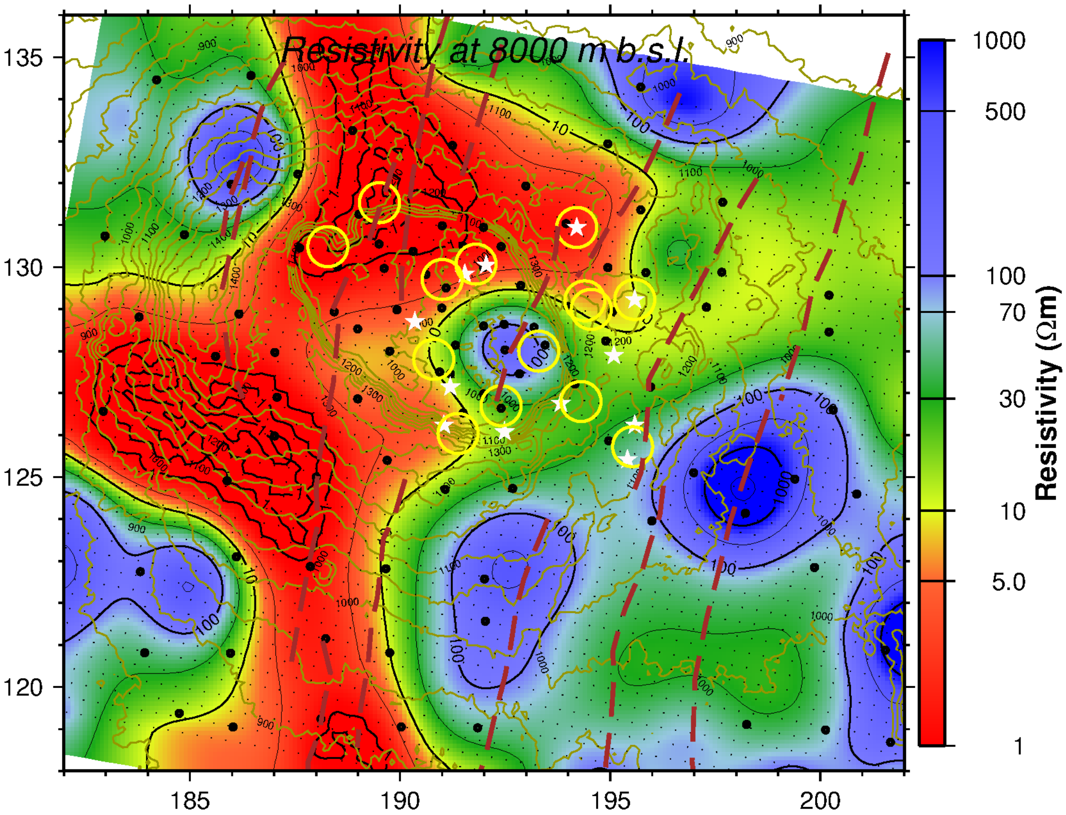

FIGURE 58: Resistivity at 8000 m b.s.l. Fumaroles are denoted by white stars, altered grounds by yellow circles and broken brown lines show faults as mapped on the surface

At 5000 m b.s.l. a resistive zone appears between the two conductive segments aligning in NW-SE direction which coincides approximately with the lineament that is thought to cut the caldera in the same direction. Elsewhere higher resistivity zones are present bordering the deeper conductor from all directions as seen in Figure 58.

### 8.9.2 3-D cross-section maps

This section presents five resistivity cross-sections for profiles in East-West (Figure 59) and North-South (Figure 60) directions. All the cross-sections show main features, similar to those that have been reported elsewhere in high temperature areas. Generally the resistivity structure reveals a resistive top layer probably reflecting unaltered rocks, underlain by a shallow conductive cap presumably caused by smectite-zeolite hydrothermal mineral alteration. Underlain, is a resistive core which reflects chlorite-epidote alteration and a zone presumed to host the geothermal reservoir. Still at the base of the resistive core a deeper conductor is evident at different locations along the cross-sections.

### 8.9.3 Discussion of 3-D inversion results

The 3-D MT inversion of the off-diagonal impedance tensor for the 97 MT sites and 30 periods revealed the main parts of the subsurface resistivity structures at the Silali geothermal field. The resistivity models revealed a typical resistivity structure for a high-temperature geothermal field as found elsewhere, i.e. a low-resistivity cap underlain by a resistive core which presumably is related to the geothermal reservoir (Flóvenz et al., 1985; Eysteinsson et al., 1994; Árnason et al., 2000).

The low-resistivity anomaly observed at shallow depth particularly around the caldera and to the south of the caldera is attributed to low temperature alteration minerals. Underlain high resistivity is related to the change in alteration minerals to higher temperature mineralogy within the caldera spreading to south of the caldera. At depth of about 6 km a conductive segment dominates; this deep low-resistivity region could be associated with presence of partial melt which has been interpreted as the heat source for the geothermal system in this field. It should, however, be noted that the resolution of MT data at

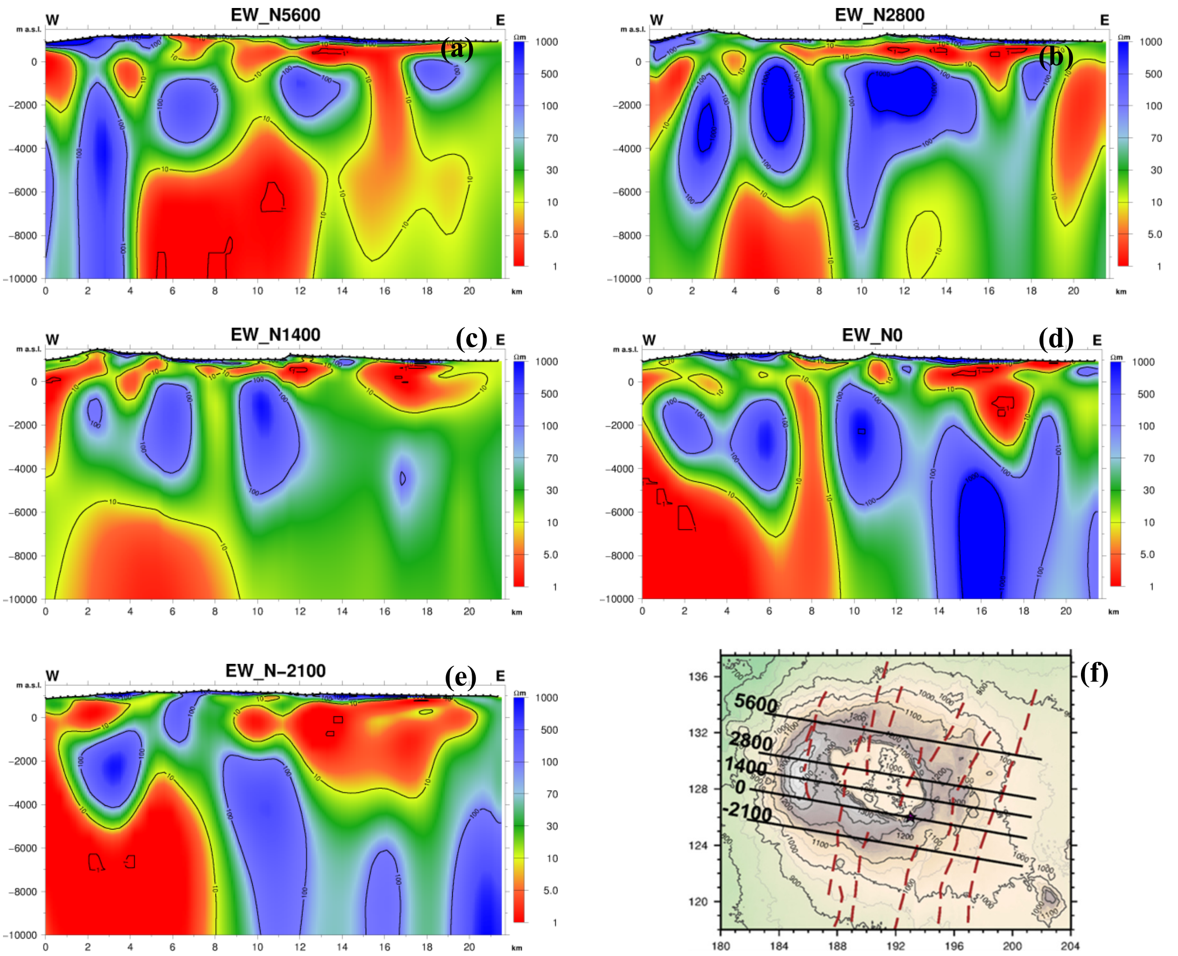

FIGURE 59: Topography corrected E-W cross-sections showing resistivity along the profiles as shown on location map Figure (f). The vertical sections across the model at (a) EW_N5600, (b) EW_N2800, (c) EW_N1400, (d) EW_N0, and (e) EW_N-2100 are oriented across the geological strike, Brown broken lines represent faults as mapped on the surface

long period may not be trusted due to noise, this therefore underscores the importance of collecting good data particularly at long periods. Results from the above models show that resistivity structure up to a depth of 6 km is stable but below that the models may not be entirely correct.

### 8.10 Comparison of 1-D, 2-D and 3-D results

Results for two profiles will be compared for the 1-D, 2-D and 3-D inversion of MT data. Both 1-D and 3-D are elevation-corrected but 2-D is not. From the evaluation of the 3-modes of 2-D inversion, TM-mode result are preferred to be compared with both 1-D and 3-D models.

The 1-D, 2-D and 3-D vertical resistivity cross-sections of Profile EW10_4 (for location see Figure 25) are shown in Figure 61. All the three resistivity cross-sections generally show a three layer resistivity structure down to depth of 6 km, with a high resistivity surface layer (> 100 Ωm) underlain by a low resistivity layer (< 10 Ωm) and a third high resistivity zone (> 70 Ωm). The deeper basal layer differs somewhat with 1-D model smearing low resistivity across the entire section rising to shallow depth at the western most end of the profile and at the eastern edge of the caldera below site slmt172. On the other hand the 2-D profile shows low resistivity on the western half of the profile rising to shallow depths on both sides of the caldera. The 3-D model shows low resistivity at depth of 6 km b.s.l. beneath the caldera with a fairly low resistivity elongation towards the surface. In all the models there is a low resistivity linear structure between the high-resistivity anomaly in the intermediate depths. It should be noted that the 3-D model reveals the resistivity structure reliably well particularly the high resistivity zone where the two anomalies are clearly resolved.

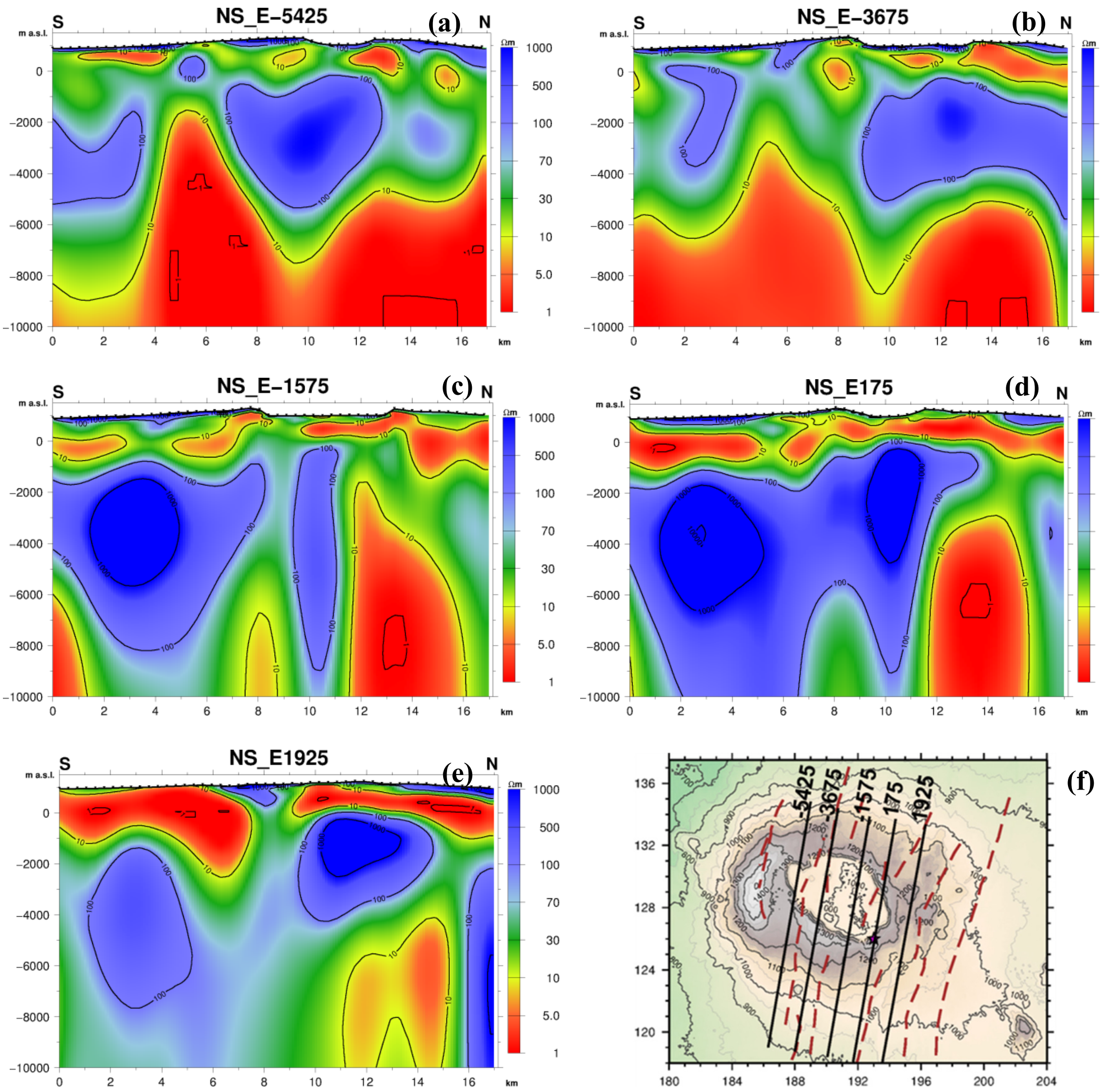

FIGURE 60: Topography corrected N-S cross-sections showing resistivity along the profiles as shown on location map Figure (f). The vertical sections across the model at (a) N-S_E-5425, (b) N-S_E-3675, (c) N-S_E-1575, (d) N-S_E175, and (e) N-S_E1925 are oriented along the geological strike, Brown broken lines represent faults as mapped on the surface

Similarly resistivity structure for profile EW10_3 (for location see Figure 28) is compared in Figure 62. Likewise this profile shows a resistivity structure with a top high resistivity underlain by a low resistivity second layer followed by a higher resistivity structure. However the 3-D model has better resolved resistivity geometries both at the shallow low resistivity and the underlying high resistivity core. Of special significance are the two high resistivity anomalies separated by a lower resistivity linear structure below the caldera. At depth of 5 km b.s.l. both 1-D and 2-D models present a deeper low resistivity smeared all across the entire profile. The 3-D model presents a localized deeper low resistivity beneath the caldera and extending to the west of the caldera. From this comparison it seems reasonable to conclude that the anomalies revealed are real.

The next section compares iso-resistivity maps of 1-D and 3-D developed using Linux program with 2-D maps from WinGlink program. 2-D cross-section shown above are made using REBOCC. It should be noted that colour scales for 2-D WinGlink maps differ from those of 1-D and 3-D model maps. On the WinGlink maps the caldera structure and the faults are marked by brown and black symbols respectively whereas on the other maps faults are marked by brown broken lines.

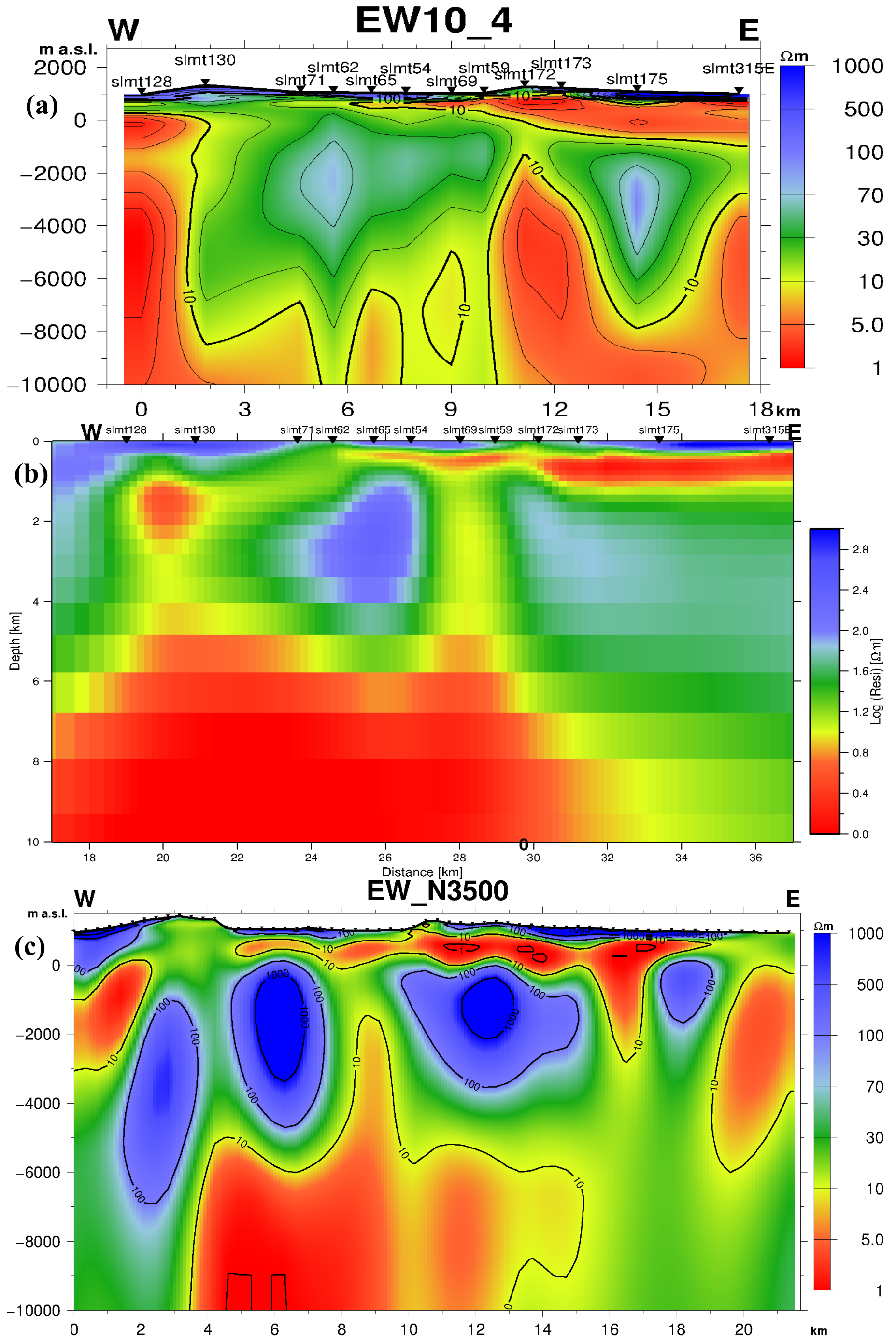

FIGURE 61: Comparison of 1-D, 2-D and 3-D vertical resistivity cross-sections for Profile EW10_4: (a) from joint 1-D inversion of TEM and determinant MT data. (b) 2-D inversion of TM mode MT data. (c) 3-D model at EW_N3500

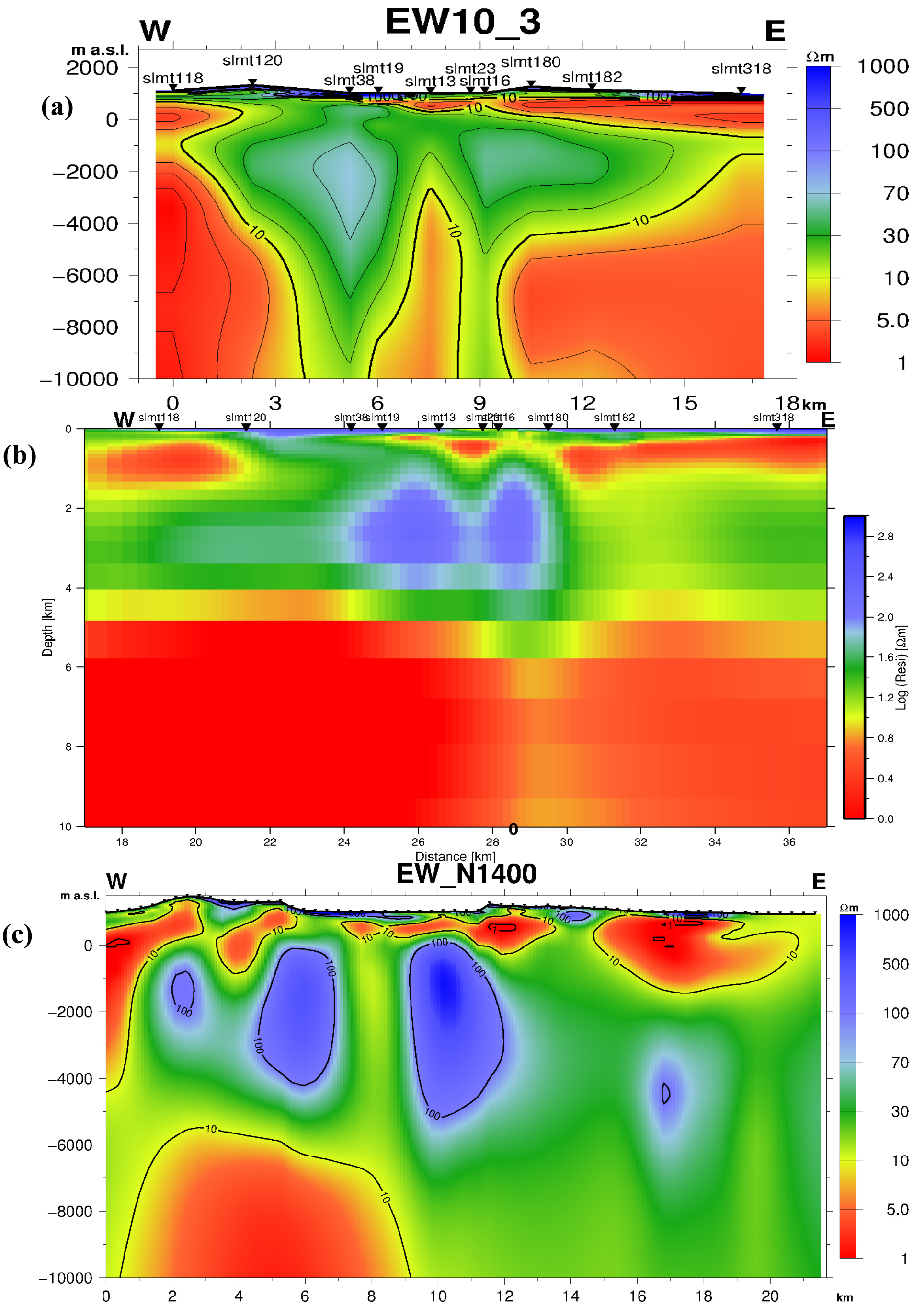

FIGURE 62: Comparison of 1-D, 2-D and 3-D vertical resistivity cross-sections for Profile EW10_3: (a) from joint 1-D inversion of TEM and determinant MT data. (b) 2-D inversion of TM mode MT data. (c) 3-D model at EW_N1400

Figure 63 shows resistivity at sea level with a generally high resistivity trending in a NE-SW direction from the caldera to the extreme SW end. This high resistivity zone, maps high resistivity core of the geothermal system in this field. 1-D and 2-D models smear the resistivity indiscriminately while 3-D models seems to sharpen the resistivity structure much better as seen in Figure 63(c) showing the two high resistivity anomalies inside the caldera. Similarly, Figure 64 shows resistivity at 1000 m a.s.l for 1-D, 2-D WinGlink and 3-D models respectively. For all the three models there is a striking correlation between the low resistivity which has been attributed to the low temperature mineral alteration and the surface manifestations at shallow depth encircling the caldera. Elsewhere a high resistivity is seen on the outer margins all around the low resistivity.

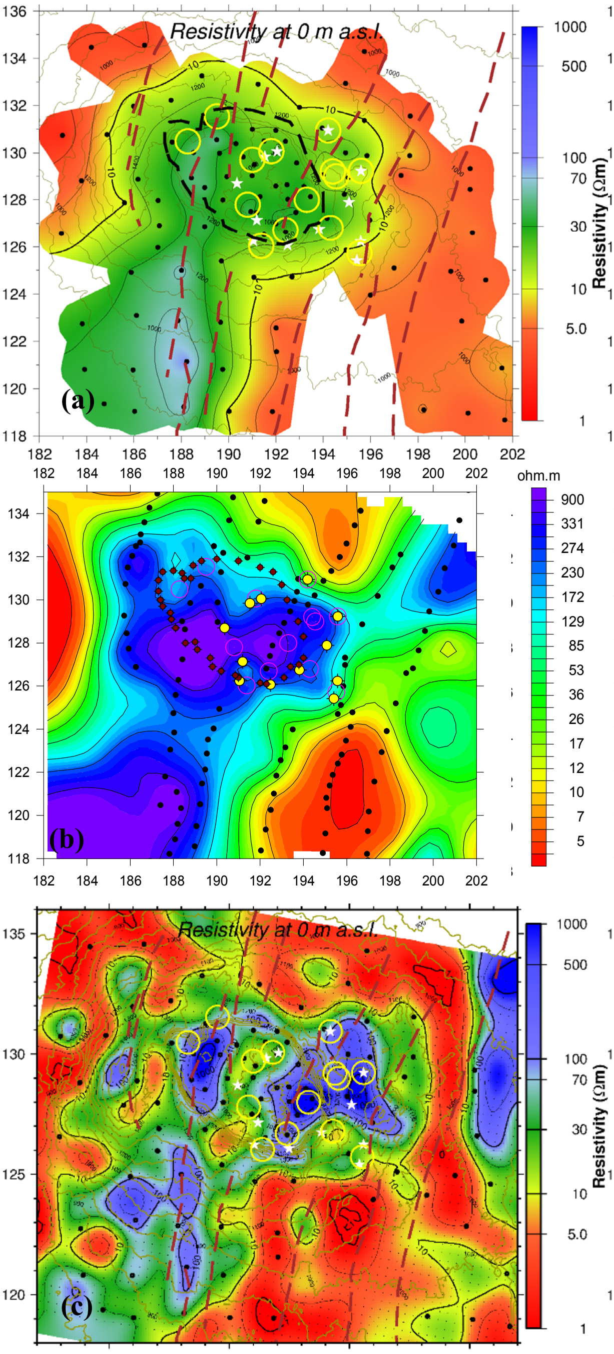

FIGURE 63: Comparison of 1-D, 2-D and 3-D horizontal resistivity map at sea level (a) joint 1-D inversion of TEM and determinant MT data. (b) 2-D resistivity map from WinGlink. (c) 3-D resistivity map from 10 ohm-m initial model

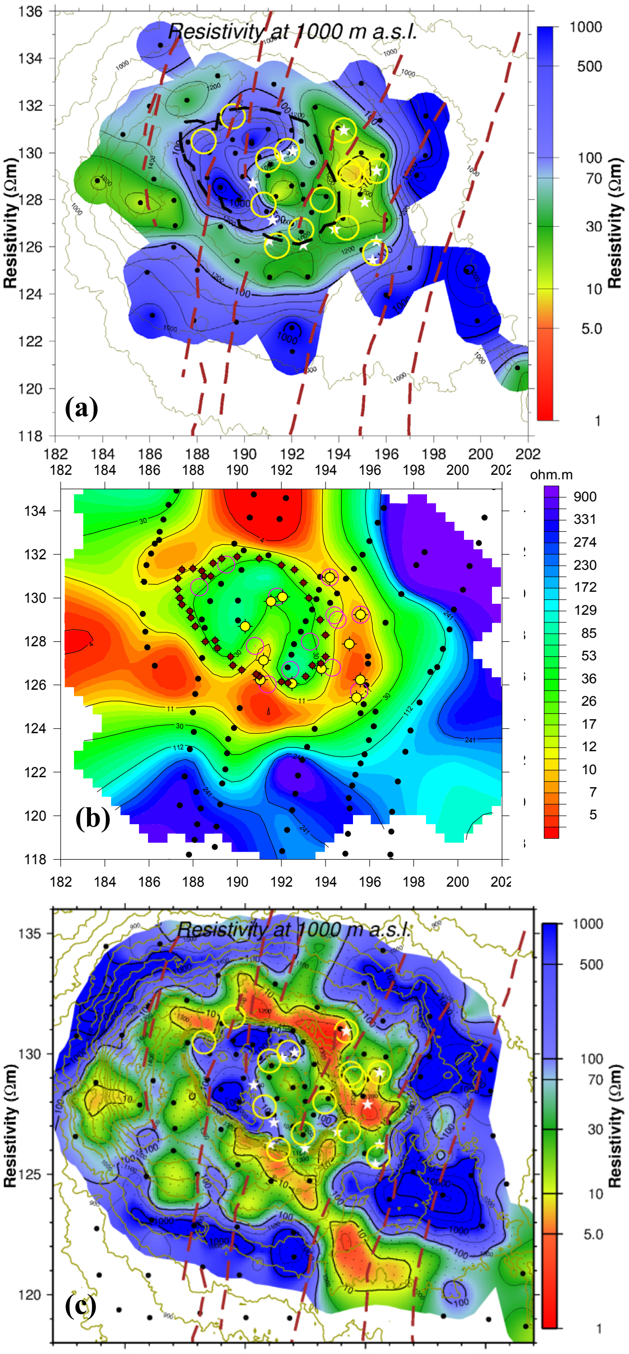

FIGURE 64: Comparison of 1-D, 2-D and 3-D horizontal resistivity map at 1000 m a.s.l (a) joint 1-D inversion of TEM and determinant MT data. (b) 2-D resistivity map from WinGlink. (c) 3-D resistivity map from 10 ohm-m initial model

### 8.10.1 Discussion of 1-D, 2-D and 3-D comparison

The 1-D and 2-D inversion of MT data on the two profiles (Figures 61 and 62) show three main resistivity structures down to a depth of 6 km. A high resistivity surface layer associated with fresh basaltic lava, a very low resistivity second layer (< 10 Ωm) of variable thickness was observed along the vertical cross-sections. The conductive layer is presumably associated with smectite and mixed layer clay alteration. A high resistivity (> 70 Ωm) is observed underlying the conductive layer along the cross-sections, more resolved in the 3-D model both for Figure 61(c) and 62(c). The high resistivity could be related to high-temperature alteration (chlorite-epidote alteration zone) down to a depth of about 4 km. The 3-D inversion revealed a more resolved deeper conductive structure than the 1-D and 2-D inversion models. The deep conductive body is presumably associated with the heat source of the geothermal system. Generally 1-D models give a rough picture, 2-D models can be difficult to resolve but 3-D resistivity models sharpen the resistivity structure.

It should however be noted that due to noise in the data at long period the results from 1-D, 2-D and 3-D differ widely and may not resolve the anomalies deeper than 6 km. This is because the noisy portion of the data can be fitted by different models. Therefore the depth of resolution is limited to 6 km.

In conclusion, it must always be borne in mind that in the real earth there are no such components as 2-D anomalies, all anomalies are 3-Dimensional. Again since two-dimensional (2-D) interpretations frequently cannot explain important features present in field data sets from geologically complex regions, then it is inevitable that 3-D inversion has to be carried out. Often a 2-D inversion is undertaken of data that exhibit weak 3-D effects because of the inadequacy of spatial coverage (only a single profile of data rather than a grid) or because of the complexity of 3-D modelling. 2-D techniques applied to 3-D data are merely indicative and can be misleading if interpreted without consideration.

## 8.11 Comparison of REBOCC and WinGlink models

Figure 65 shows comparisons of results from REBOCC and WinGlink softwares respectively. This is a profile cutting through the southern sector of the caldera (see Figure 29). REBOCC model is not elevation corrected so resistivity will be referenced with depth but WinGlink model is elevation-corrected. Both models show a thin surface layer, underlain by a conductive second layer. The third layer differs somewhat, with the REBOCC model showing a high resistivity zone in the middle of the profile between soundings slmt38 and slmt180. On the other hand the WinGlink model reveals a high resistivity layer spread across the entire profile. Both models show a deeper low resistivity layer, at shallower depth of 3000 m b.s.l. for the WinGlink model and 5000 depth for the REBOCC model.

### 8.11.1 Discussion of WinGlink and REBOCC comparisons

Despite the fact that the two models are generated from different algorithms they seem to reproduce similar resistivity structure for the EM data particularly for the TM-mode. The shallow resistivity structure show fair resemblance at least in the upper 1 km depth. However the resolution of the models at depth differ and may not be reliable due to presence of noise at long period and/or the effects of 3-dimensionality in the data.

## 8.12 Tectonic and geothermal interpretation of results

Active hydrothermal systems are found in areas of fluid circulation, in tectonically and volcanically active areas. Heat sources for hydrothermal systems include magma chambers, young dikes, and general heat flow. Faulting zones buried below the surface control fluid circulation in hydrothermal system. They can be hard to delineate using surface geological mapping.

High temperature geothermal systems commonly found in basaltic rocks are characterised by a low resistivity cap (< 10 ohm-m) on the outer margins of a more resistive core deeper in the reservoir (Árnason et al., 2000). This high resistivity core has about an order of magnitude higher resistivity than the conductive cap (Eysteinsson et al., 1994; Árnason et al., 2000). This sequence of resistivity structure is evident from the results gotten so far from Silali geothermal field. Additionally a conductive zone has been interpreted beneath the resistive core which has been presumed as the heat source for the geothermal system in this field. A similar resistivity structure has been reported elsewhere in developed geothermal fields around the world, and has been correlated with both alteration mineralogy and reservoir temperature (Árnason et al., 2000; Ussher et al., 2000, Lichoro, 2009).

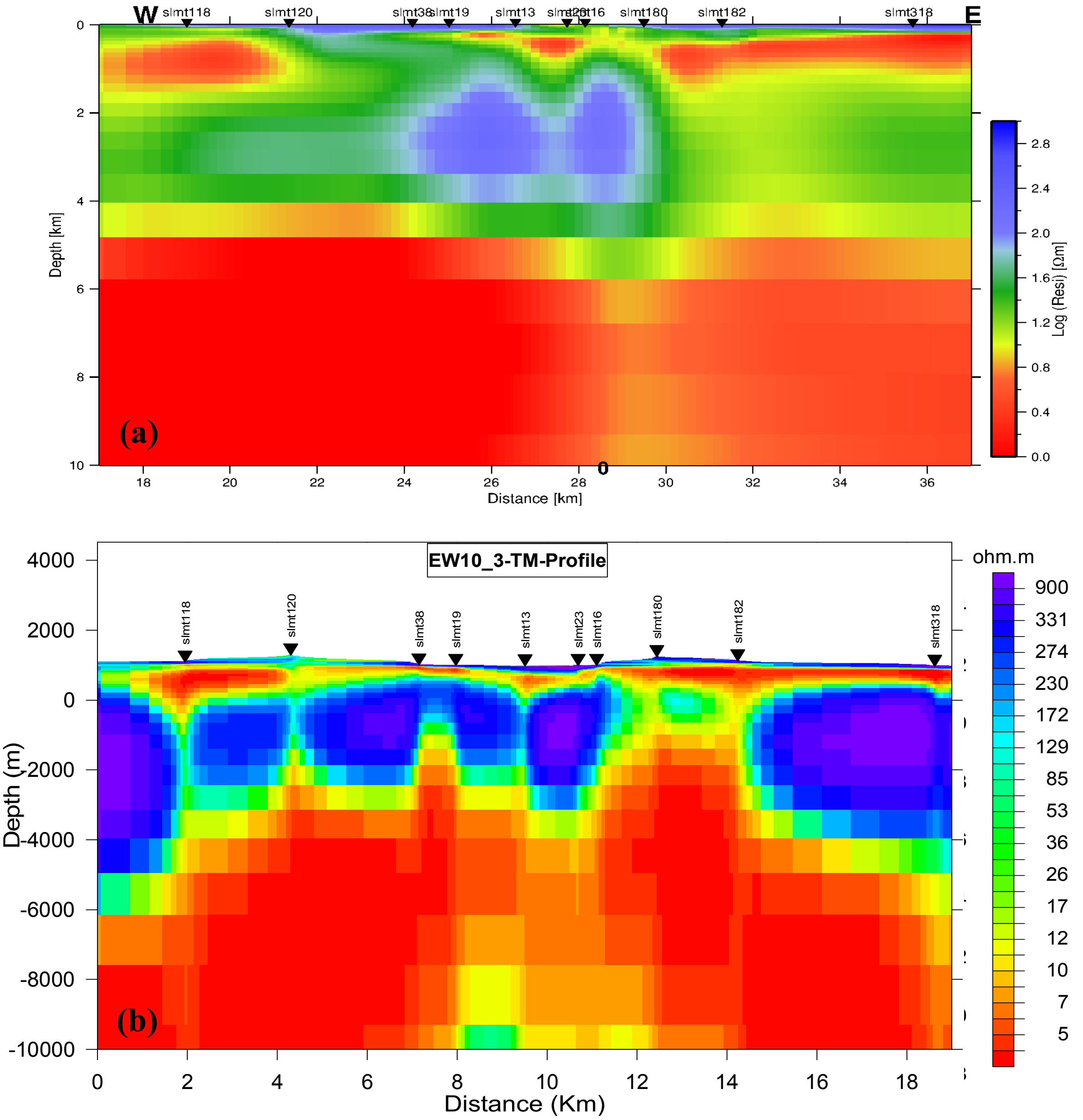

FIGURE 65: Comparison of 2-D vertical resistivity models based on
(a) REBOCC inversion results (b) WinGlink inversion

Generally like many other geothermal systems in the world, Silali geothermal system comprises a low-resistivity layer underlain by higher resistivity core. These structures are associated with alteration minerals having different electrical conductivity. In the low-resistivity cap, conductive alteration minerals in the smectite-zeolite zone dominate, with inferred temperature of 50-200°C. As temperature approach 240°C, mixed layer clays form and then chlorite dominate with increased resistivity (Haraldsdóttir et al., 2010).

In the formation of the Silali caldera, a huge magma must have been withdrawn from below the volcano but surface evidence of this material seems to be lacking around Silali. A possibility lies in using geophysical methods to look for probable solutions to this. From the resistivity results there seems to be a deeper conductor at a depth greater than 6 km below Silali volcano. The geometry of this anomaly seems to be aligned in N-S direction (Figure 8.36) more to the western sector of the volcano. This study therefore could suggest that the mass withdrawn from below the volcano must have been injected into the crust parallel to the rift axis in N-S direction which is in agreement with the inferred direction of the maximum horizontal stress field (Bosworth et al., 2000). Therefore this deeper conductive anomaly could be attributed to magma remnants/injected mass which might be the heat source for the geothermal system in Silali.

## 9. CONCLUSION AND RECOMMENDATION

A multi-dimensional interpretation of Electromagnetic data was performed for the Silali area, where 102 MT soundings have been inverted using the 1-D joint inversion of determinant MT and TEM and a 3-D inversion of the off-diagonal impedance tensor elements for 97 MT surroundings. In the 3-D inversion 30 periods were used logarithmically distributed from 0.0031 to 700 s. The robustness of the final inversion model was tested using three different initial models: A model compiled from the joint 1-D inversion of TEM and MT soundings, a homogeneous half-space model of 100 Ωm and a 10 Ωm homogeneous half-space model. The RMS was between 1.5-1.7 for all three models. The resulting models were elevation corrected and are presented as smoothed resistivity maps at different elevations and as resistivity cross sections. Similarly 2-D inversions have been done using two different algorithms (REBOCC and WinGlink) and their results are compared.

The objective of this study was two-fold: Firstly to compare different approaches of interpreting Electromagnetic data (1-D, 2-D and 3-D) and testing the robustness of the models to recover resistivity structure and, Secondly to study the resistivity structure of Silali in order to infer presence of geothermal systems.

Results from the three initial models of the 3-D inversion reproduced very similar features, especially in the upper 6 km depth. The 100 ohm-m homogeneous half-space initial model is intended to let the inversion introduce lower resistivity structures where needed. The 10 ohm-m homogeneous half-space initial model is intended to recover higher resistivity structure by inserting high resistivity where required. In this regard confidence is placed on low resistivity structure recovered by the high resistivity initial model and on the other hand a high resistivity structure recovered by the low resistivity initial model. The parts of the final models, from different initial models that agree are considered reliable.

At depth greater than 6 km the three initial models show different resistivity structure, this can be attributed to noise in the data at long period where the noisy portion of the data is fitted by different models. Therefore depth of resolution is limited to 6 km below which models differ somewhat. This shows the necessity of checking the robustness of the inversion to avoid misleading interpretation of results.

Comparison of different inversion approaches show that 1-D and 3-D inversion results are comparable, such that 1-D inversion reproduces the main resistivity structures but smears them out while the 3-D inversion sharpens the picture considerably. 2-D results are generally questionable since different modes from the same data reproduce different results.

Generally the resistivity structure of the Silali area present four resistivity segments: A surface high resistivity zone of unaltered formations, a second low-resistivity anomaly observed at shallow depth, particularly around the caldera and to the south of the caldera, is attributed to low temperature alteration minerals. Underlain high resistivity is related to the change in alteration minerals to higher temperature mineralogy within the caldera spreading to south of the caldera. At depth of about 6 km a conductive segment dominates; this deep low-resistivity region could be associated with presence of partial melt which has been interpreted as the heat source for the geothermal system in this field. It should however be noted that the resolution of MT data at long period may not be trusted due to noise, this therefore underscores the importance of collecting good data particularly at long periods in order to resolve deeper structure.

It is recommended that other geophysical methods like seismic refraction, magnetics and gravity be undertaken in the area so as to have a joint interpretation of all studies. This will aid in confirming the nature of the deeper low resistivity structure.

# REFERENCES

Árnason, K., 1989: Central-loop transient electromagnetic sounding over a horizontally layered earth. Orkustofnun, Reykjavík, report OS-89032/JHD-06, 129 pp.

Árnason, K., 2006. TEMTD, a programme for 1-D inversion of central-loop TEM and MT data. Short manual. Iceland GeoSurvey - ISOR, internal report, 17 pp.

Árnason, K., 2008: *The Magneto-telluric static shift problem*. Iceland GeoSurvey - ISOR, report, ISOR-08088, 17 pp.

Árnason K., Eysteinsson H., and Hersir G.P., 2010: Joint 1-D inversion of TEM and MT data and 3-D inversion of MT data in the Hengillarea, SW Iceland. *Geothermics 39, 13–34.*

Árnason, K., Karlsdóttir, R., Eysteinsson, H., Flóvenz, Ó.G., and Gudlaugsson, S.Th., 2000: The resistivity structure of high-temperature geothermal systems in Iceland. *Proceedings of the World Geothermal Congress 2000*, *Kyushu-Tohoku, Japan,* 923-928.

Archie, G.E., 1942: The electrical resistivity log as an aid in determining some reservoir characteristics. *Trans. AIME, 146,* 54-67.

Baer, G., Hamiel, Y., Shamir, G., and Nof, R., 2008. Evolution of a magma-driven earthquake swarm and triggering of the nearby Oldoinyo Lengai eruption, as resolved by InSAR, ground observations and elastic modelling, East African Rift, 2007. *Earth and Planetary Science Letters, 272*, 339–352.

Bahr, K., 1988: Interpretation of the magnetotelluric impedance tensor: regional induction and local telluric distortion, *J. Geophys*., *62*, 119-127.

Berdichevsky, M.N., Dmitriev, V.I. and Pozdnjakova, E.E.: 1998, On two-dimensional interpretation of magnetotelluric soundings, *Geophys. J. Int*., *133*, 585–606.

Berdichevsky, M.N., and Dmitriev, V.I., 2002: *Magnetotellurics in the context of the theory of ill-posed problems*. Society of Exploration Geophysicists, USA, 215 pp.

Bosworth, W., Burke, K. and Strecker, M. 2000. Magma chamber elongation as an indicator of intraplate stress field orientation: "borehole break-out mechanism" and examples from the Late Pleistocene to Recent Kenya Rift Valley. In: Jessell, M.W., and Urai, J.L. (eds.), *Journal of the Virtual Explorer, Vol. 2A, in honour of W.D. Means.*

Christensen, A., Auken, E., and Sørensen, K., 2006. The transient electromagnetic method. *Groundwater Geophysics, 71*, 179-225.

Clarke, J., Gamble, T.D., Goubau, W.M., Koch, R.H., Miracky, R.F., 1983: Remote reference magnetotellurics: Equipment and procedures. *Geophys. Prosp., 31*, 149-170.

Constable, S. C., Parker, R. L., and Constable, C. G., 1987. Occam's inversion: A practical algorithm for generating smooth models from electromagnetic sounding data: *Geophysics*, *52*, 289–300.

Delaney, P.T., Pollard, D.D., Ziony, J.I., and McKee, E.H., 1986, Field relations between dikes and joints; emplacement processes and paleostress analysis: JGR. *Journal of Geophysical Research, B, v. 91,* 4920-4938.

DeGroot-Hedlin, G., 1991. Removal of static shift in 2 dimensions by regularized inversion. *Geophysics, 56,* 2102-2106.

DeGroot-Hedlin, C., and Constable, S., 1990, Occam's inversion to generate smooth, two-dimensional models from magnetotelluric data. *Geophysics, 55*, 1613–1624.

Dunkley, P.N., Smith, M., Allen, D.J., and Darling, W.G., 1993. *The geothermal activity and geology of the northern sector of the Kenya Rift valley*. British Geological Survey Research, Report SC/93/1, 185 pp.

Ebinger, J.C., Ian, J. H., Atalay A., Laura, B., Eric, C., Derek, K., Elias, L., Tim, J.W., and Gezahegn, Y., 2009. Geodetic observations of the ongoing Dabbahu Rifting episode: New dyke intrusions in 2006 and 2007. *Geophys. J. Int.*, *178*, 989-1003.

Eysteinsson, H., 1998: *TEMMAP and TEMCROSS plotting programs*. Iceland GeoSurvey - ÍSOR, unpublished programs and manuals.

Eysteinsson, H., Árnason, K., and Flóvenz, Ó.G., 1994: Resistivity methods in geothermal prospecting in Iceland. *Surv. Geophy.*, *15*, 263–275.

Fairhead, J.D., 1976. The structure of the lithosphere beneath the Eastern Rift, East Africa, deduced from gravity studies. *Tectonophysics* 30, 269-298.

Fernandes, R.M.S., Ambrosius, B.A.C., Noomen, R., Bastos, L., Combrinck, L., Miranda, J.M ., and Spakman, W., 2004. Angular velocities of Nubia and Somalia from continuous GPS data: Implications on present-day relative kinematics. *Earth and Planetary Science Letters, 222-1,* 197-208.

Flóvenz, Ó.G., Georgsson, L.S., and Árnason, K., 1985: Resistivity structure of the upper crust in Iceland. *J. Geophys. Res.*, *90*, 10136–10150.

Flóvenz, O., Spangenberg, E., Kulenkampff, J., Árnason, K., Karlsdóttir, R., and Huenges, E., 2005. The role of electrical interface conduction in geothermal exploration. *Proceedings World Geothermal Congress* 2005 *Antalya, Turkey*, 24-29.

Gamble, T.D., Goubau, W.M., and Clarke, J. 1979: Magnetotelluric with a remote magnetic reference. *Geophysics,* 44, 53–68.

Geosystem User Guide, 2011: *WinGLink® user's guide, release 2.20.12.* Geosystem SRL; www.geosystem.net.

Hartnady C, Calais E, Ebinger C.J, and Nocquet J.M., 2006. Kinematics of the East African Rift from GPS and earthquake slip vector data. *Geological Society, London, Special Publication, 2006,* 259-922.

Hersir, G.P., and Björnsson, A., 1991: *Geophysical exploration for geothermal resources. Principles and applications.* UNU-GTP, Iceland, report 15, 94 pp.

Jiracek, G., 1990: Near-surface and topographic distortions in electromagnetic induction. *Surv. Geophys.*, *11*, 163-203.

Jiracek, G.R., Reddig, R.P., and Kojima, R.K., 1986, Application of the Rayleigh-FFT technique to magnetotelluric modelling and correction: *Presented at 8th Workshop on Electromagnetic Induction, Neuchatel, Switzerland.*

Jones, A.G., 1988: Static shift of magnetotelluric data and its removal in a sedimentary basin environment. *Geophysics, 53-7*, 967-978.

Jones, A.G., and Groom, R.W., 1993, Strike-angle determination from the magnetotelluric impedance tensor in the presence of noise and local distortion: rotate at your peril! *Geophys. J. Int., 113*, 524–534.

Kearey, P., and Brooks, M., 1994: *An introduction to geophysical exploration* (2nd edition). Blackwell Scientific Publ., London, 236 pp.

Keller, G.R., Mechie, J., Braile, L.W., Mooney, W.D and Prodehl, C., 1994. Seismic structure of the uppermost mantle beneath the Kenya Rift, in Crustal and upper Mantle structures of the Kenya Rift. *Tectonophysics, 236,* 201-210.

Levenberg, K., 1944: A method for the solution of certain problems in least squares. *Quart. Appl. Math., 2*, 164-168.

Lichoro, C.M., 2009: Joint 1-D inversion of TEM and MT data from Olkaria domes geothermal area, Kenya. Report 16 in: *Geothermal training in Iceland 2009.* UNU-GTP, Iceland, 289-318.

Macdonald, R., Davies, G.R., Upton, B.G.J., Dunkley, P.N., Smith, M. and Leat, P.T., 1995: Petrogenesis of Silali volcano, Gregory Rift, Kenya. *J. Geological Society, London , 152*, 703-720.

Mariita, N.O., and Keller, G.R., 2007. An integrated geophysical study of the northern Kenya Rift. *J. Afr. Earth Sc., 48,* 80-94.

Marquardt, D., 1963: An algorithm for least-squares estimation of nonlinear parameters. *SIAM J. Appl. Math., 11*, 431-441.

Monastero, F.C., Katzenstein, A.M., Miller, J.S., Unruh, J.R., Adams, M.C. and Richards-Dinder, K., 2005. The Coso geothermal field: A nascent metamorphic core complex., *Geol. Soc of America Bulletin, 117,* 1534-1553.

Nam, M.J., Kim, H.J., Song, Y., Lee, T.J., and Suh, J.H., 2008. Three-dimensional topographic and bathymetric effects on magnetotelluric responses in Jeju Island, Korea. *Geophys. J. Int., 176,* 457–466.

NOCK 1987. Aeromagnetic data interpretation of the Winam Gulf and the east African Rift areas in Kenya. *National Oil Corporation of Kenya, unpubl report no. 26/2 16D.*

Nyblade, A.A. et al., 2000. Seismic evidence for a deep upper mantle plume thermal anomaly beneath east Africa. *Geology,* 28, 599-602.

Nyblade, A.A., and Langston, C.A., 1995. East African earthquakes below 20 km depth and their implications for crustal structure. *Geophys. J. Int., 121,* 49-62.

Ogawa, Y and Ushida, T., 1996: A two-dimensional magnetotelluric inversion assuming Gaussian static shift. *Geophys. J. Int., 126*, 69-76.

Palacky, G.J., 1987: Resistivity characteristics of Geologic targets. In: *Electromagnetic methods in applied geophysics, 1. Theory.* Soc. Expl. Geophys., Tusla, OK, USA.

Parker, R.L., 1980: The inverse problem of electromagnetic induction: existence and construction of solutions based upon incomplete data. *J. Geophys. Res*., *85*, 4421-4425.

Parker, R.L., 1994: *Geophysical inverse theory.* Princeton University Press.

Parkinson, W., 1959: Directions of rapid geomagnetic variations. *Geophys. J.R. Astr. Soc., 2*, 1–14.

Pellerin, L. and Hohmann, G.W., 1990: Transient electromagnetic inversion – a remedy for magnetotelluric static shifts, *Geophysics,* 55, 1242–1250.

Phoenix Geophysics, 2005: *Data processing user guide.* Phoenix Geophysics Ltd., ON Canada.

Reddy, I.K., Rankin, D., and Phillips, R.J. 1977: Three-dimensional modelling in magnetotelluric and magnetic variational sounding. *Geophys. J. R. Astr. Soc.*, *51*, 313-325.

Rodi, W.L., Mackie, R.L., 2001: Nonlinear conjugate gradients algorithm for 2-D magnetotelluric inversion. *Geophysics, 66*, 174–187.

Simiyu, S.M., Keller, G.R., 1997: An integrated analysis of the lithospheric structure across the east African plateau based on gravity analysis and recent seismic studies. *Tectonophysics, 278*, 327-352.

Simiyu, S.M., Keller, G.R., 2001: An integrated geophysical analysis of the upper crust of the Southern Kenya rift. *Geophys. J. Int., 147,* 543-561.

Simpson, F., and Bahr, K., 2005: *Practical magnetotellurics*. Cambridge University Press, Cambridge, UK, 254 pp.

Siripunvaraporn, W., Egbert, G., 2000: An effcient data-subspace inversion method for 2D magnetotelluric data. *Geophysics, 65-3,* 791–803.

Siripunvaraporn, W., Egbert, G., Lenbury, Y., Uyeshima, M., 2005: Three-dimensional Magnetotelluric inversion: data-space method. *Phys Earth Plan Int. 150:3–14.*

Smirnov, M.Yu., 2003: Magnetotelluric data processing with a robust statistical procedure having a high breakdown point. *Geophys., J.. Int., 152*, 1–7.

Smith, M., Dunkley, P.N., Deino, A., Williams, L.A.J., and McCall, G.J.H., 1995: Geochronology, stratigraphy and structural evolution of Silali volcano, Gregory Rift, Kenya. *J. Geol. Soc. London, 152*, 297-310.

Smith, J.T., 1995: Understanding telluric distortion matrices. *Geophys. J. Int., 122*, 219-226.

Sternberg, B.K., Washburne, J.C., and Pellerin, L., 1988: Correction for the static shift in magnetotellurics using transient electromagnetic soundings. *Geophysics, 53*, 1459-1468.

Swift, C.M., 1967: *A magnetotelluric investigation of electrical conductivity anomaly in the southern United States.* Massachusetts Institute of Technology, PhD Thesis, Cambridge, MA.

Tikhonov, A.N., and Arsenin, V.Y., 1977: *Solution to ill- posed problems*. John Wiley, New York.

Ussher, G., Harvey, C., Johnstone, R., and Anderson, E., 2000: Understanding the resistivities observed in geothermal systems. *Proceedings of the World Geothermal Congress 2000, Kyushu–Tohoku, Japan,* 1915–1920.

Vozoff, K., and Juppe D.L.B., 1986. Two-dimensional magnetotelluric inversion. In: Vozoff, K. (ed.), *Magnetotelluric methods. Geophysics Reprint Series, 5*, *Soc. Expl. Geophys.*, 460-479.

Vozoff, K., 1991. *The magnetotelluric method.* In: Nabighian, M.N. (ed.), *Electromagnetic methods in applied geophysics, vol. 2B.* Tulsa, OK, USA, 641–711.

Wannamaker, P. E., 1991. Advances in three-dimensional magnetotelluric modelling using integral equations, *Geophysics*, 56, 1716–1728.

Wannamaker, P.E., Hohmann, G.W., and Ward, S.H., 1984: Magnetotelluric responses of three-dimensional bodies in layered earth. *Geophysics*, *49*, 1517–1533.

Wiese, H., 1962: Geomagnetische Tiefensondierung. Teil II: Die Streichrichtung der Untergrundstrukturen des elektrischen Widerstandes, erschlossen aus geomagnetischen Variationen. *Geofis. Pura et Appl., 52*, 83–103.

Williams, L.A.J., Macdonald, R., and Chapman, G.R. 1984: Late Quaternary caldera volcanoes of the Kenya Rift. *J. Geophysical Research, 89, B10*, 8553-8570.

Zeyen, H., Volker, F., Wehrle, V., Fuchs, K., Sonolev, S. V. and Altherr, R., 1997. Styles of continental Rifting: Crust-mantle detachment and plumes. *Tectonophysics, 278, 329-352*.

Zhang, P., Roberts, R.G. and Pedersen, L.B., 1987: Magnetotelluric strike rules, *Geophysics*, *52*, 267–278.

# APPENDIX I: 1-D inversion of TEM data

1-D inversion of the TEM data is shown for all the TEM soundings used in this report. Red circles: measured apparent resistivity as a function of √t , where t is the current turn-off time in µs. Black lines denote the synthetic TEM apparent resistivity – the response of the model shown as green lines. Number on the top of the figure: name of the TEM station; number below the TEM station: chi (χ) – a measure of the fit between the measured data and the model data. The resistivity model is plotted in a logarithmic scale (log10).

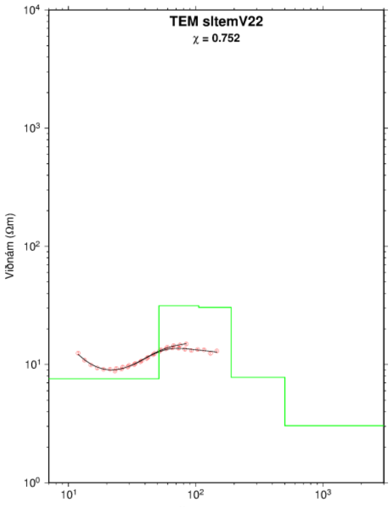

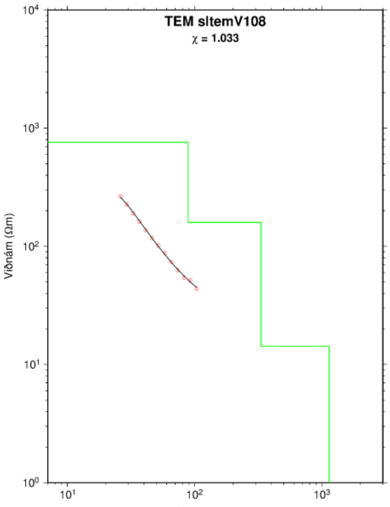

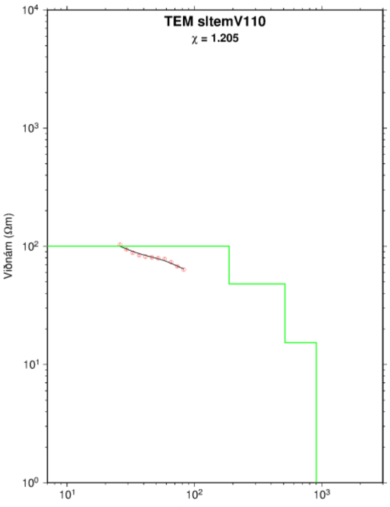

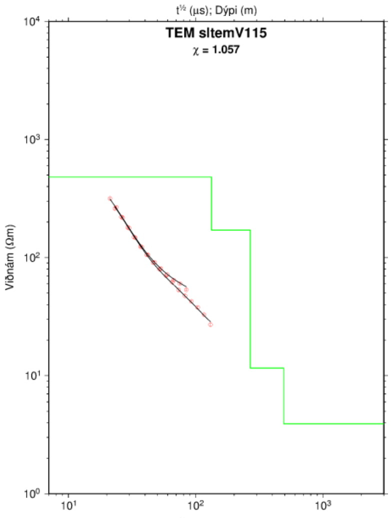

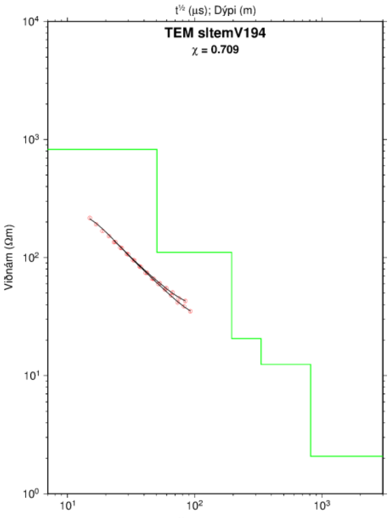

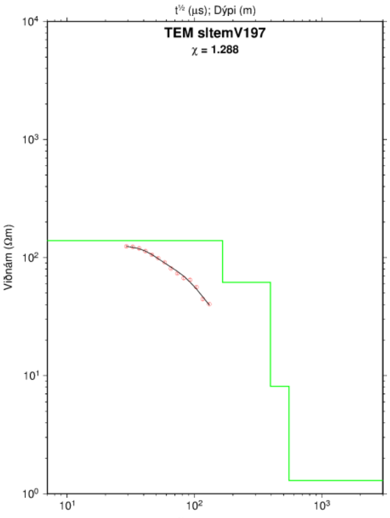

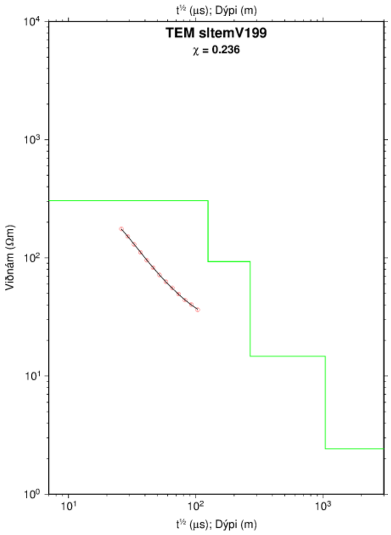

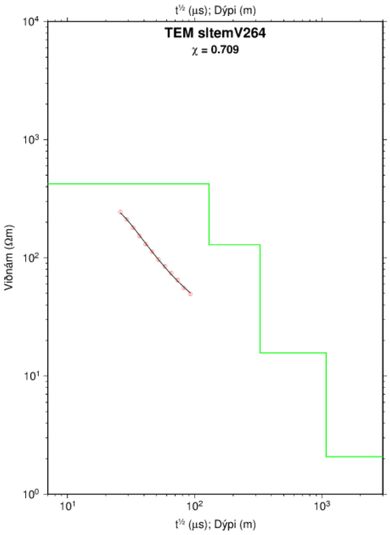

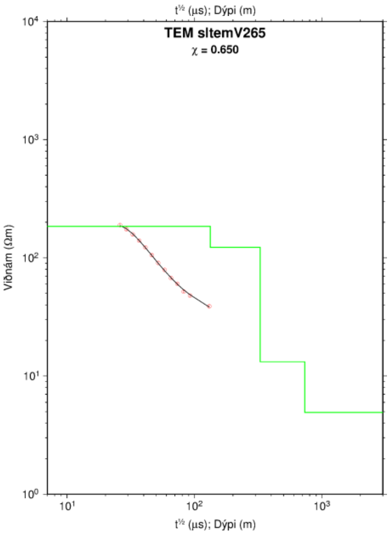

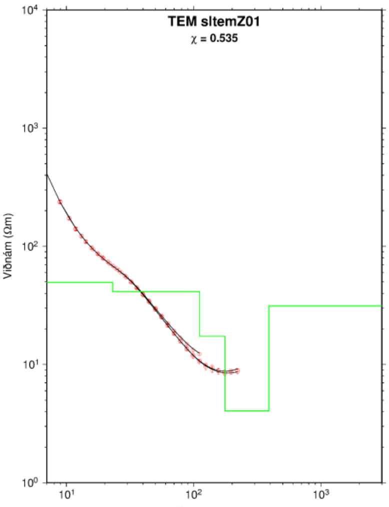
TEM sltemZ01
χ = 0.535
$10^4$
$10^3$
$10^2$
$10^1$
$10^0$
Viðnám (Ωm)
$10^1$
$10^2$
$10^3$
t½ (µs); Dýpi (m)

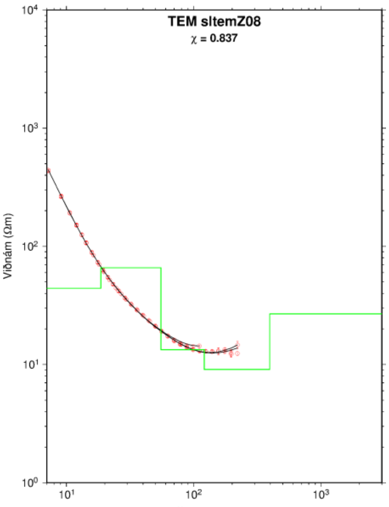
TEM sltemZ08
χ = 0.837
$10^4$
$10^3$
$10^2$
$10^1$
$10^0$
Viðnám (Ωm)
$10^1$
$10^2$
$10^3$
t½ (µs); Dýpi (m)

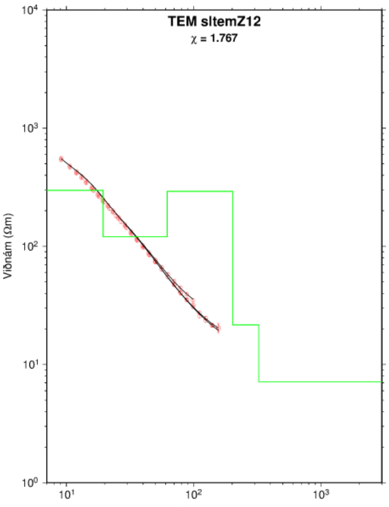
TEM sltemZ12
χ = 1.767
$10^4$
$10^3$
$10^2$
$10^1$
$10^0$
Viðnám (Ωm)
$10^1$
$10^2$
$10^3$
t½ (µs); Dýpi (m)

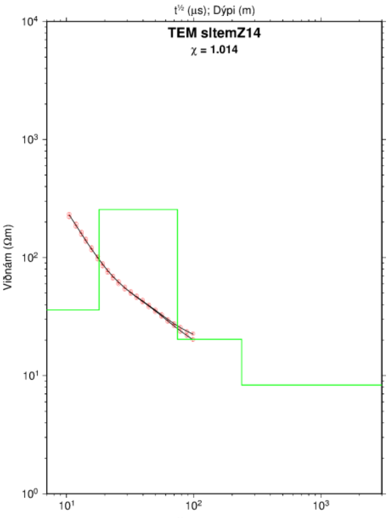
TEM sltemZ14
χ = 1.014
$10^4$
$10^3$
$10^2$
$10^1$
$10^0$
Viðnám (Ωm)
$10^1$
$10^2$
$10^3$
t½ (µs); Dýpi (m)

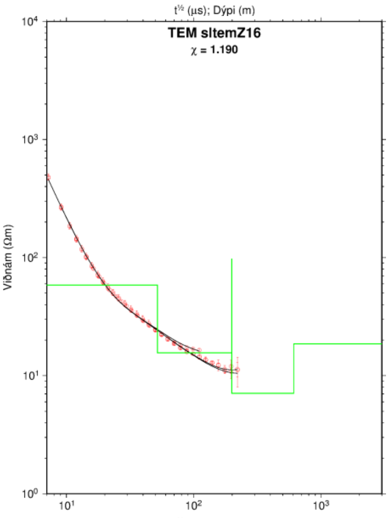
TEM sltemZ16
χ = 1.190
$10^4$
$10^3$
$10^2$
$10^1$
$10^0$
Viðnám (Ωm)
$10^1$
$10^2$
$10^3$
t½ (µs); Dýpi (m)

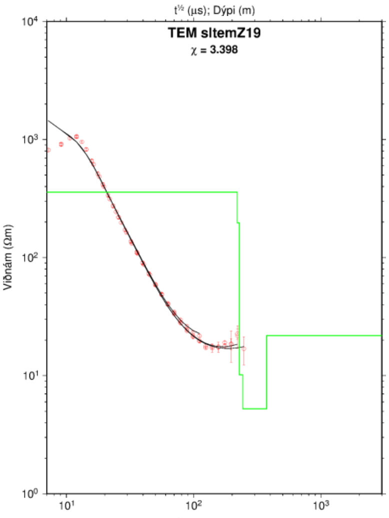
TEM sltemZ19
χ = 3.398
$10^4$
$10^3$
$10^2$
$10^1$
$10^0$
Viðnám (Ωm)
$10^1$
$10^2$
$10^3$
t½ (µs); Dýpi (m)

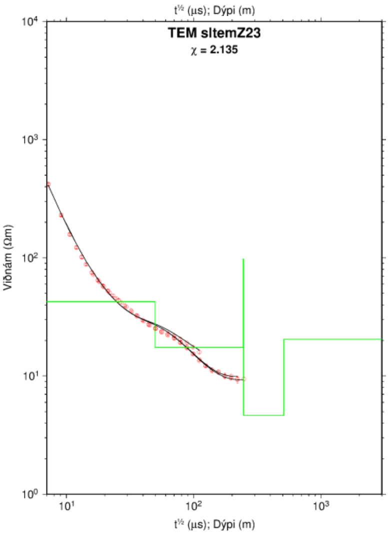
TEM sltemZ23
χ = 2.135
$10^4$
$10^3$
$10^2$
$10^1$
$10^0$
Viðnám (Ωm)
$10^1$
$10^2$
$10^3$
t½ (µs); Dýpi (m)

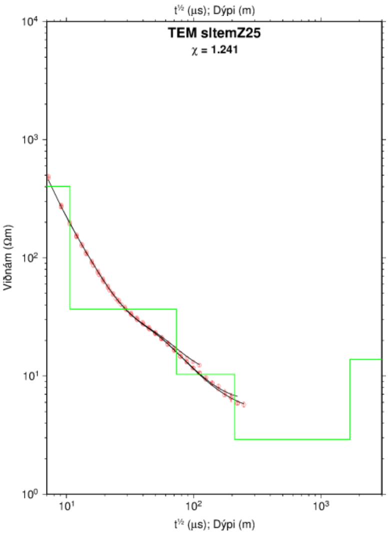
TEM sltemZ25
χ = 1.241
$10^4$
$10^3$
$10^2$
$10^1$
$10^0$
Viðnám (Ωm)
$10^1$
$10^2$
$10^3$
t½ (µs); Dýpi (m)

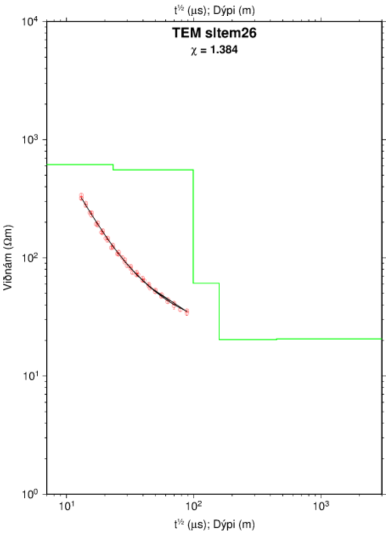
TEM sltem26
χ = 1.384
$10^4$
$10^3$
$10^2$
$10^1$
$10^0$
Viðnám (Ωm)
$10^1$
$10^2$
$10^3$
t½ (µs); Dýpi (m)

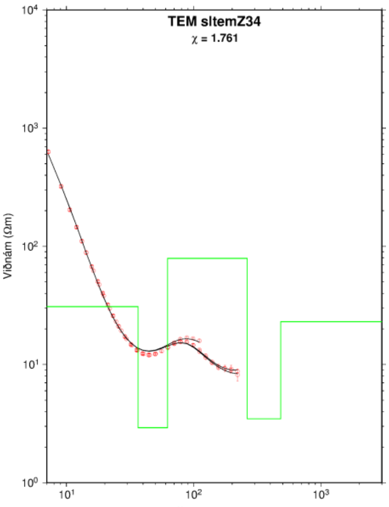
TEM sltemZ34
χ = 1.761
Viðnám (Ωm)
t½ (µs); Dýpi (m)
10⁰
10¹
10²
10³
10⁴
10¹
10²
10³

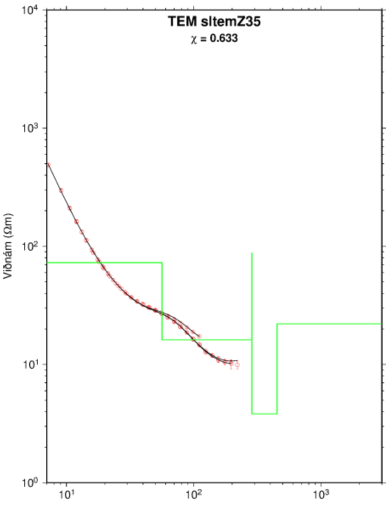
TEM sltemZ35
χ = 0.633
Viðnám (Ωm)
t½ (µs); Dýpi (m)
10⁰
10¹
10²
10³
10⁴
10¹
10²
10³

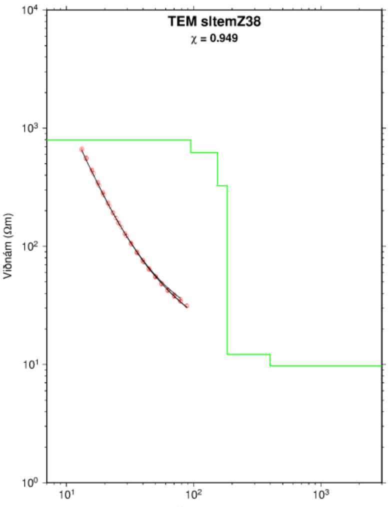
TEM sltemZ38
χ = 0.949
Viðnám (Ωm)
t½ (µs); Dýpi (m)
10⁰
10¹
10²
10³
10⁴
10¹
10²
10³

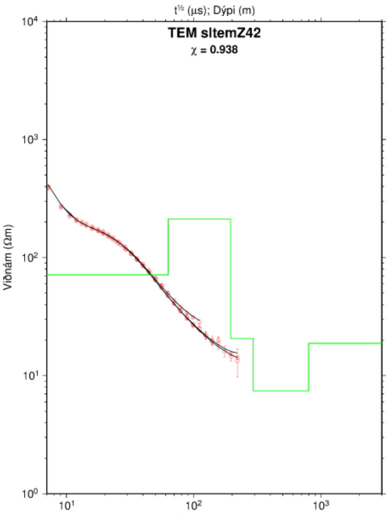
TEM sltemZ42
χ = 0.938
Viðnám (Ωm)
t½ (µs); Dýpi (m)
10⁰
10¹
10²
10³
10⁴
10¹
10²
10³

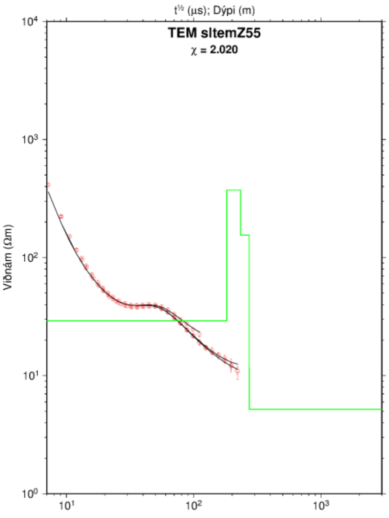
TEM sltemZ55
χ = 2.020
Viðnám (Ωm)
t½ (µs); Dýpi (m)
10⁰
10¹
10²
10³
10⁴
10¹
10²
10³

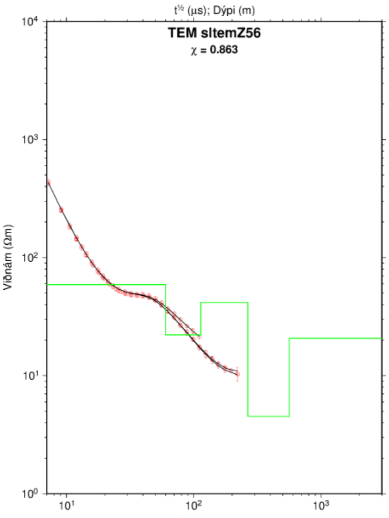
TEM sltemZ56
χ = 0.863
Viðnám (Ωm)
t½ (µs); Dýpi (m)
10⁰
10¹
10²
10³
10⁴
10¹
10²
10³

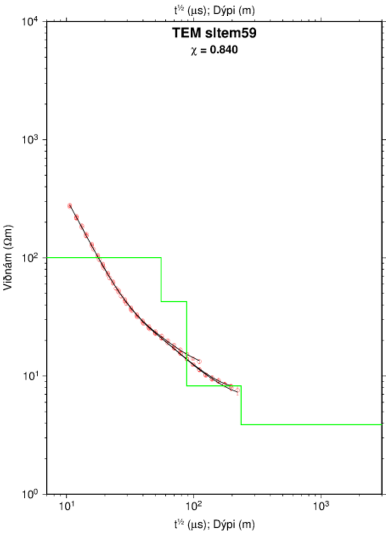
TEM sltem59
χ = 0.840
Viðnám (Ωm)
t½ (µs); Dýpi (m)
10⁰
10¹
10²
10³
10⁴
10¹
10²
10³

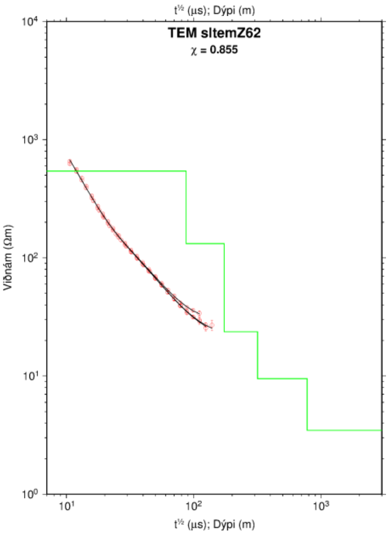
TEM sltemZ62
χ = 0.855
Viðnám (Ωm)
t½ (µs); Dýpi (m)
10⁰
10¹
10²
10³
10⁴
10¹
10²
10³

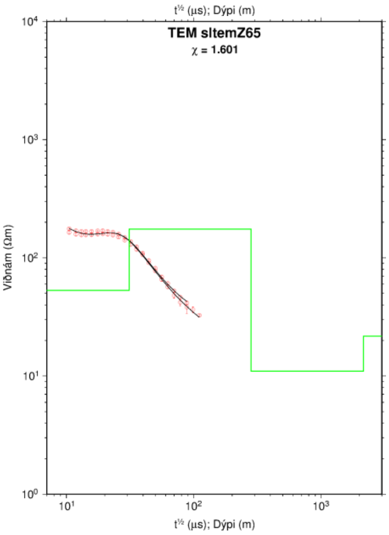
TEM sltemZ65
χ = 1.601
Viðnám (Ωm)
t½ (µs); Dýpi (m)
10⁰
10¹
10²
10³
10⁴
10¹
10²
10³

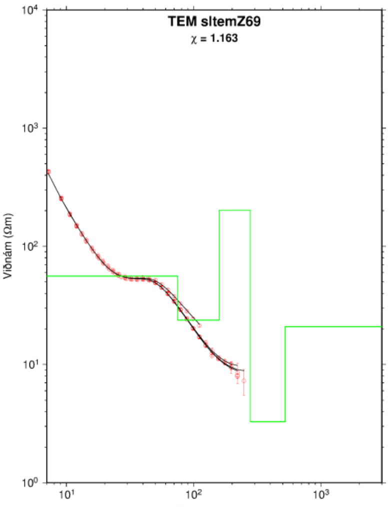
TEM sltemZ69
χ = 1.163
Viðnám (Ωm)
$10^0$
$10^1$
$10^2$
$10^3$
$10^4$
$10^1$
$10^2$
$10^3$
t½ (µs); Dýpi (m)

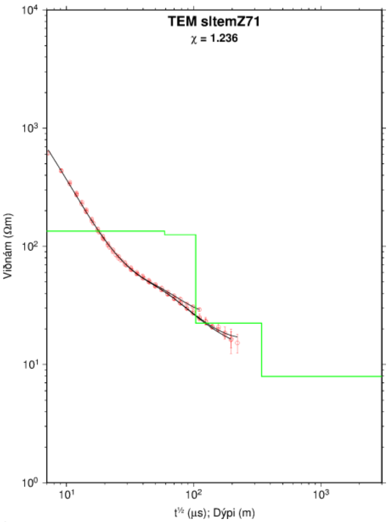
TEM sltemZ71
χ = 1.236
Viðnám (Ωm)
$10^0$
$10^1$
$10^2$
$10^3$
$10^4$
$10^1$
$10^2$
$10^3$
t½ (µs); Dýpi (m)

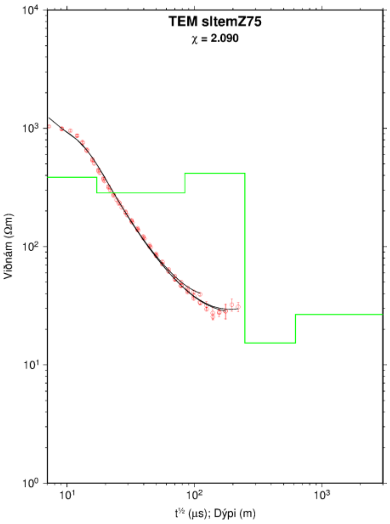
TEM sltemZ75
χ = 2.090
Viðnám (Ωm)
$10^0$
$10^1$
$10^2$
$10^3$
$10^4$
$10^1$
$10^2$
$10^3$
t½ (µs); Dýpi (m)

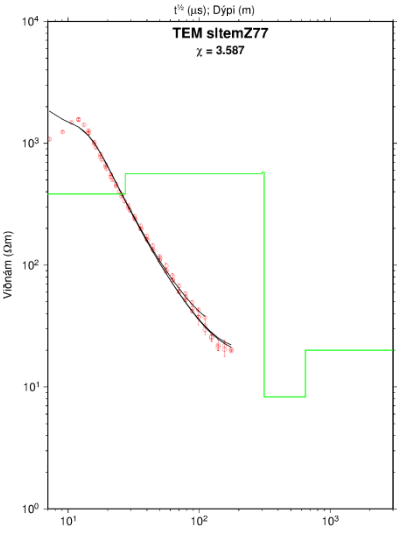
TEM sltemZ77
χ = 3.587
Viðnám (Ωm)
$10^0$
$10^1$
$10^2$
$10^3$
$10^4$
$10^1$
$10^2$
$10^3$
t½ (µs); Dýpi (m)

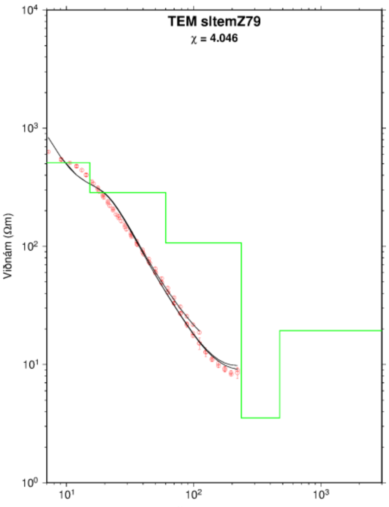
TEM sltemZ79
χ = 4.046
Viðnám (Ωm)
$10^0$
$10^1$
$10^2$
$10^3$
$10^4$
$10^1$
$10^2$
$10^3$
t½ (µs); Dýpi (m)

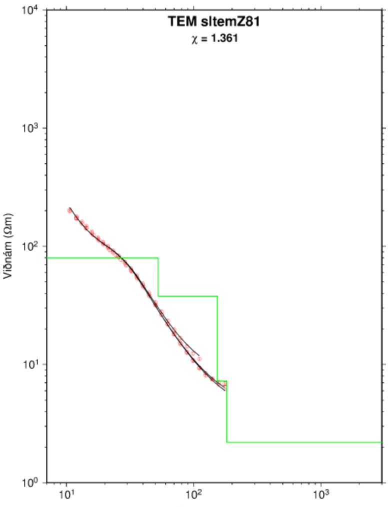
TEM sltemZ81
χ = 1.361
Viðnám (Ωm)
$10^0$
$10^1$
$10^2$
$10^3$
$10^4$
$10^1$
$10^2$
$10^3$
t½ (µs); Dýpi (m)

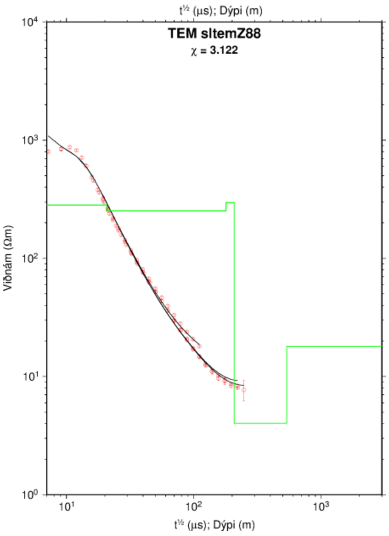
TEM sltemZ88
χ = 3.122
Viðnám (Ωm)
$10^0$
$10^1$
$10^2$
$10^3$
$10^4$
$10^1$
$10^2$
$10^3$
t½ (µs); Dýpi (m)

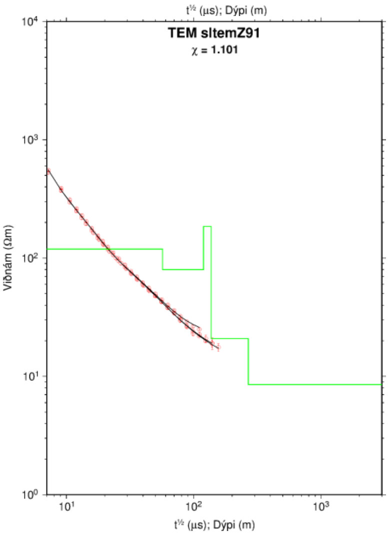
TEM sltemZ91
χ = 1.101
Viðnám (Ωm)
$10^0$
$10^1$
$10^2$
$10^3$
$10^4$
$10^1$
$10^2$
$10^3$
t½ (µs); Dýpi (m)

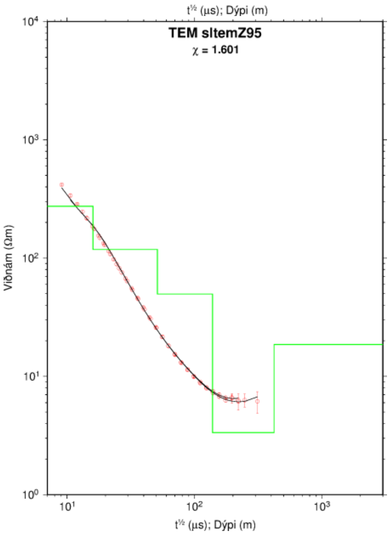
TEM sltemZ95
χ = 1.601
Viðnám (Ωm)
$10^0$
$10^1$
$10^2$
$10^3$
$10^4$
$10^1$
$10^2$
$10^3$
t½ (µs); Dýpi (m)

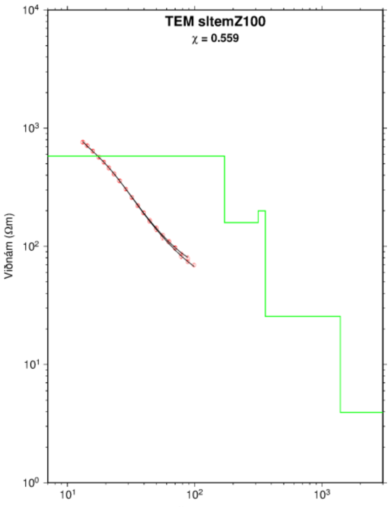
TEM sltemZ100
χ = 0.559
Viðnám (Ωm)
t½ (µs); Dýpi (m)
10^0
10^1
10^2
10^3
10^4

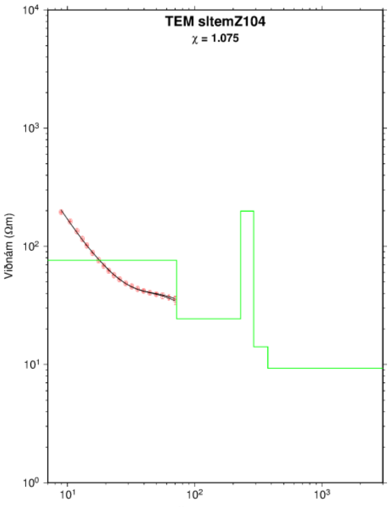
TEM sltemZ104
χ = 1.075
Viðnám (Ωm)
t½ (µs); Dýpi (m)
10^0
10^1
10^2
10^3
10^4

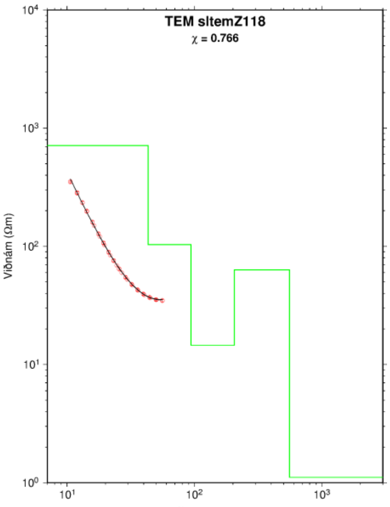
TEM sltemZ118
χ = 0.766
Viðnám (Ωm)
t½ (µs); Dýpi (m)
10^0
10^1
10^2
10^3
10^4

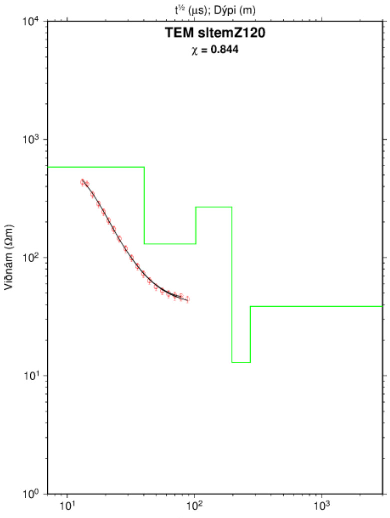
TEM sltemZ120
χ = 0.844
Viðnám (Ωm)
t½ (µs); Dýpi (m)
10^0
10^1
10^2
10^3
10^4

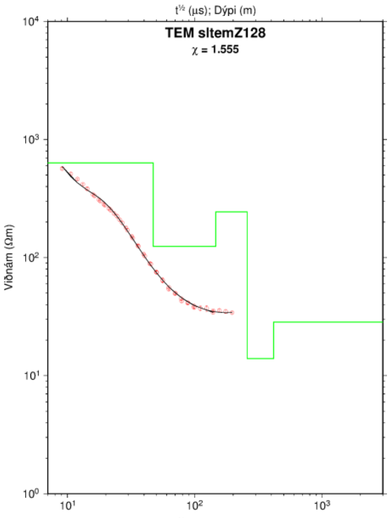
TEM sltemZ128
χ = 1.555
Viðnám (Ωm)
t½ (µs); Dýpi (m)
10^0
10^1
10^2
10^3
10^4

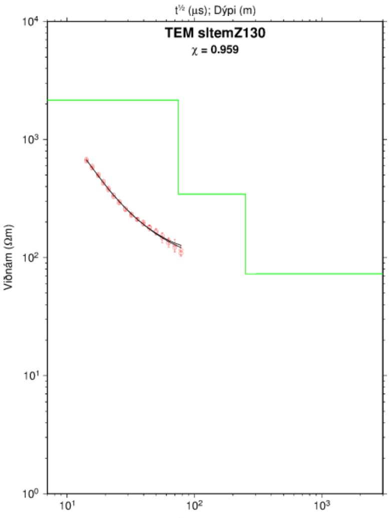
TEM sltemZ130
χ = 0.959
Viðnám (Ωm)
t½ (µs); Dýpi (m)
10^0
10^1
10^2
10^3
10^4

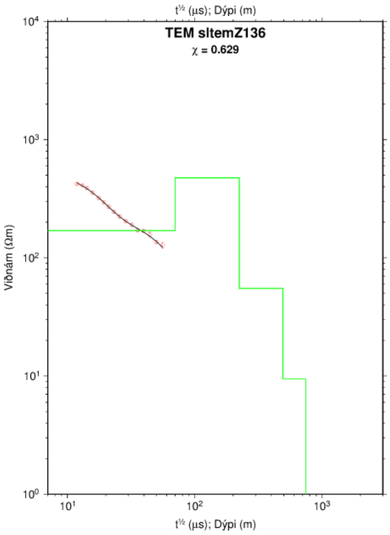
TEM sltemZ136
χ = 0.629
Viðnám (Ωm)
t½ (µs); Dýpi (m)
10^0
10^1
10^2
10^3
10^4

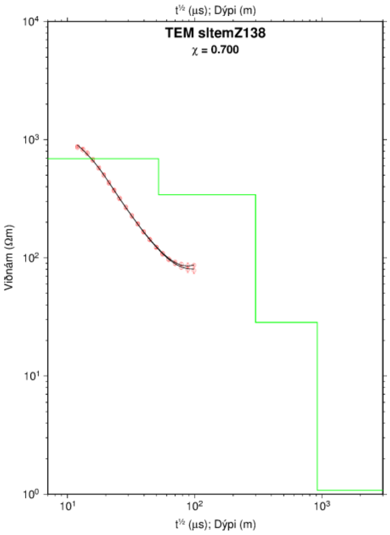
TEM sltemZ138
χ = 0.700
Viðnám (Ωm)
t½ (µs); Dýpi (m)
10^0
10^1
10^2
10^3
10^4

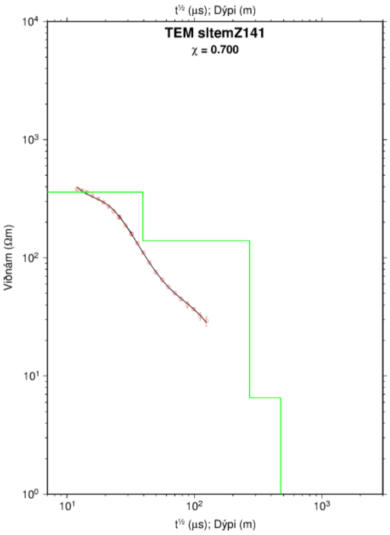
TEM sltemZ141
χ = 0.700
Viðnám (Ωm)
t½ (µs); Dýpi (m)
10^0
10^1
10^2
10^3
10^4

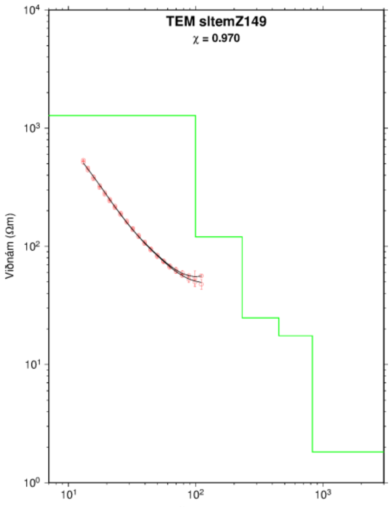
TEM sltemZ149
χ = 0.970
Viðnám (Ωm)
t½ (µs); Dýpi (m)
10⁴
10³
10²
10¹
10⁰
10¹
10²
10³

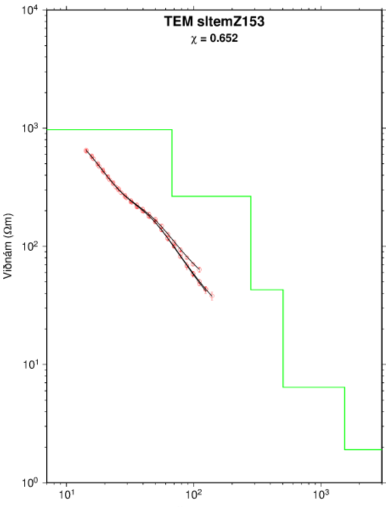
TEM sltemZ153
χ = 0.652
Viðnám (Ωm)
t½ (µs); Dýpi (m)
10⁴
10³
10²
10¹
10⁰
10¹
10²
10³

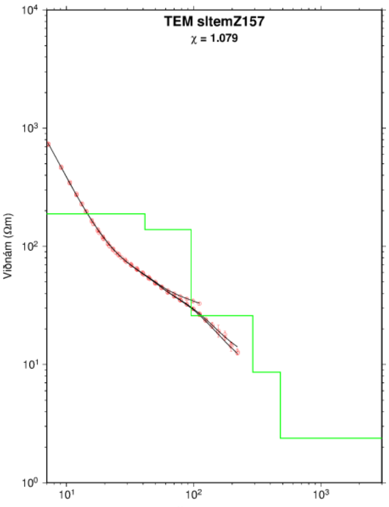
TEM sltemZ157
χ = 1.079
Viðnám (Ωm)
t½ (µs); Dýpi (m)
10⁴
10³
10²
10¹
10⁰
10¹
10²
10³

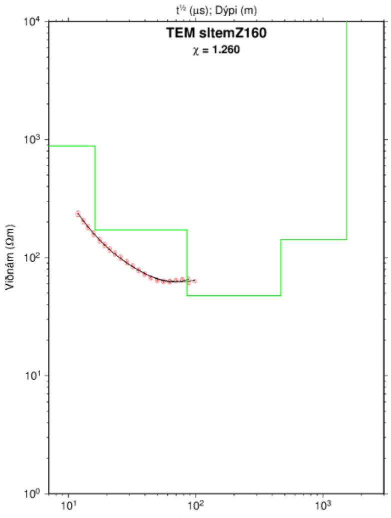
TEM sltemZ160
χ = 1.260
Viðnám (Ωm)
t½ (µs); Dýpi (m)
10⁴
10³
10²
10¹
10⁰
10¹
10²
10³

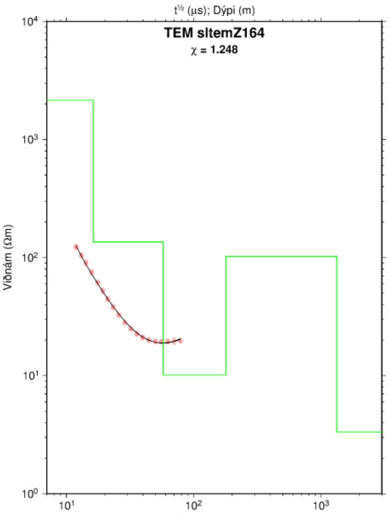
TEM sltemZ164
χ = 1.248
Viðnám (Ωm)
t½ (µs); Dýpi (m)
10⁴
10³
10²
10¹
10⁰
10¹
10²
10³

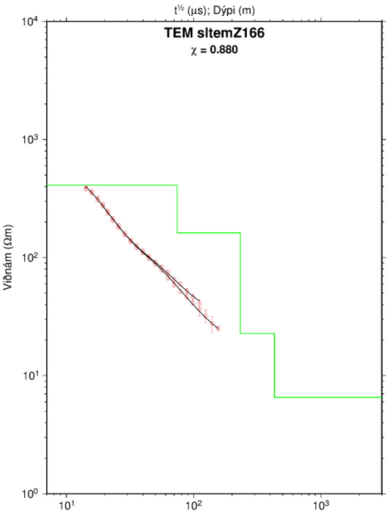
TEM sltemZ166
χ = 0.880
Viðnám (Ωm)
t½ (µs); Dýpi (m)
10⁴
10³
10²
10¹
10⁰
10¹
10²
10³

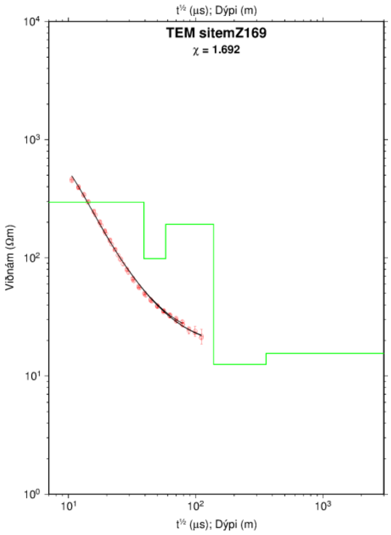
TEM sitemZ169
χ = 1.692
Viðnám (Ωm)
t½ (µs); Dýpi (m)
10⁴
10³
10²
10¹
10⁰
10¹
10²
10³

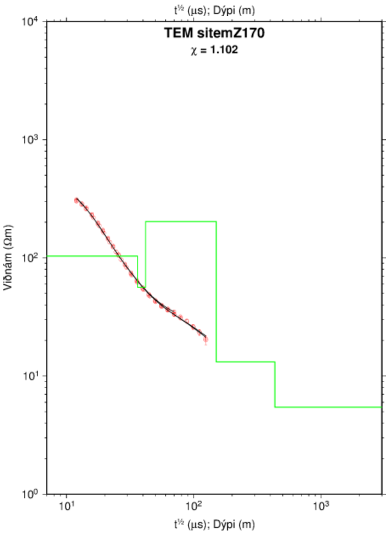
TEM sitemZ170
χ = 1.102
Viðnám (Ωm)
t½ (µs); Dýpi (m)
10⁴
10³
10²
10¹
10⁰
10¹
10²
10³

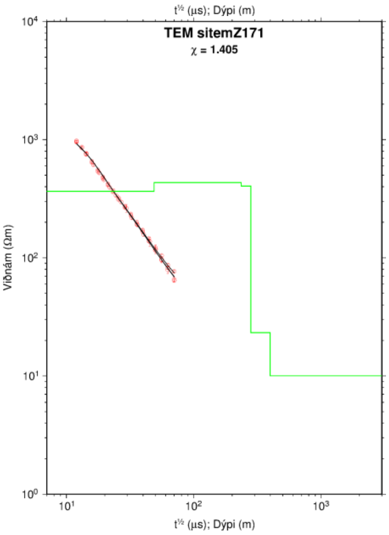
TEM sitemZ171
χ = 1.405
Viðnám (Ωm)
t½ (µs); Dýpi (m)
10⁴
10³
10²
10¹
10⁰
10¹
10²
10³

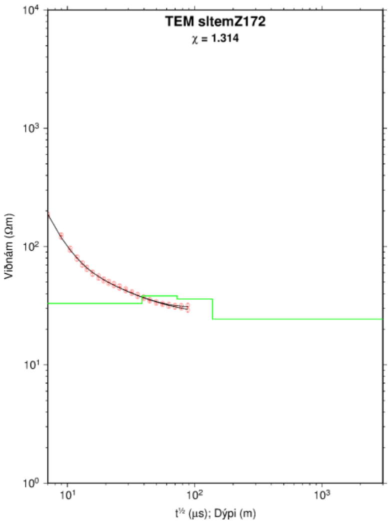
TEM sltemZ172
χ = 1.314
10⁴
10³
10²
10¹
10⁰
Viðnám (Ωm)
10¹
10²
10³
t½ (µs); Dýpi (m)

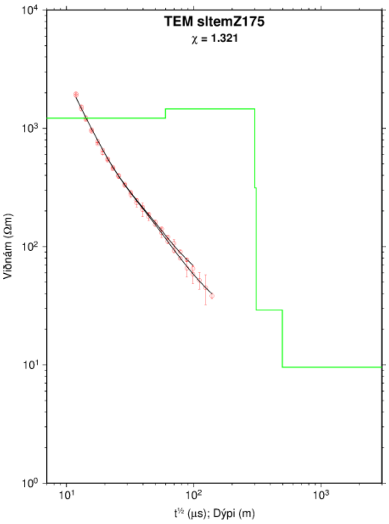
TEM sltemZ175
χ = 1.321
10⁴
10³
10²
10¹
10⁰
Viðnám (Ωm)
10¹
10²
10³
t½ (µs); Dýpi (m)

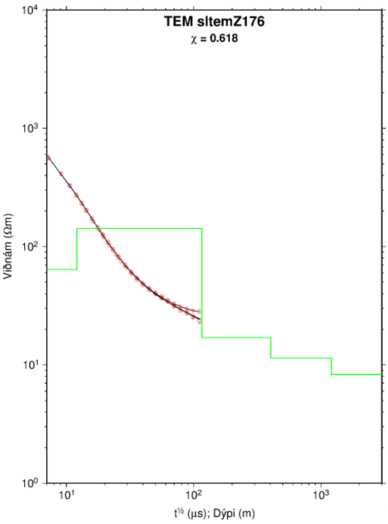
TEM sltemZ176
χ = 0.618
10⁴
10³
10²
10¹
10⁰
Viðnám (Ωm)
10¹
10²
10³
t½ (µs); Dýpi (m)

7

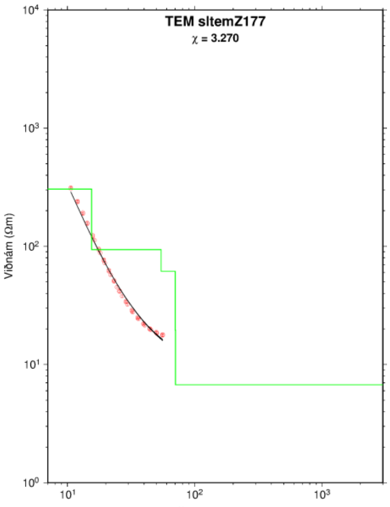
TEM sltemZ177
χ = 3.270
10⁴
10³
10²
10¹
10⁰
Viðnám (Ωm)
10¹
10²
10³
t½ (µs); Dýpi (m)

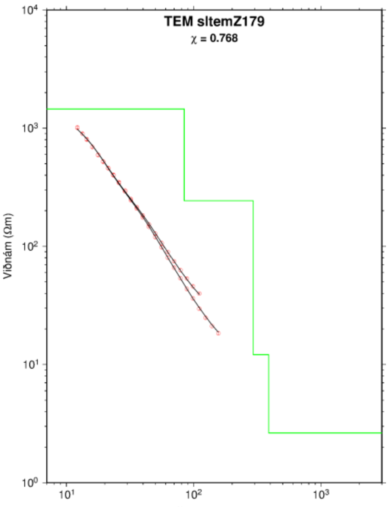
TEM sltemZ179
χ = 0.768
10⁴
10³
10²
10¹
10⁰
Viðnám (Ωm)
10¹
10²
10³
t½ (µs); Dýpi (m)

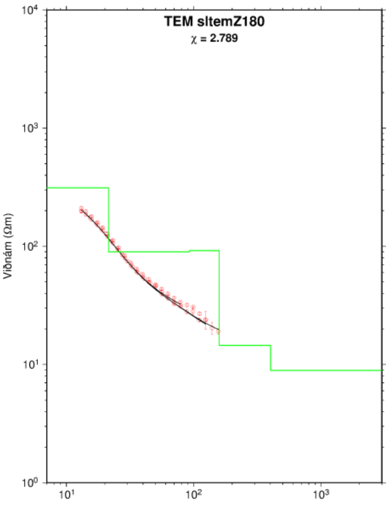
TEM sltemZ180
χ = 2.789
10⁴
10³
10²
10¹
10⁰
Viðnám (Ωm)
10¹
10²
10³
t½ (µs); Dýpi (m)

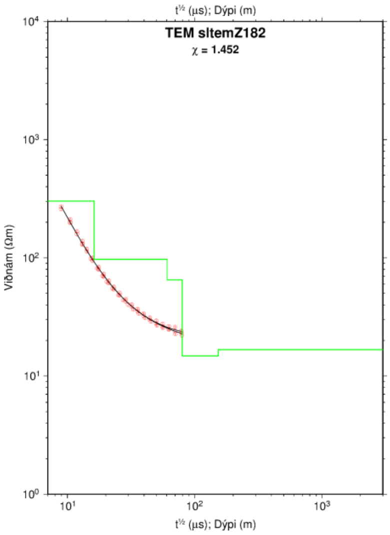
TEM sltemZ182
χ = 1.452
10⁴
10³
10²
10¹
10⁰
Viðnám (Ωm)
10¹
10²
10³
t½ (µs); Dýpi (m)

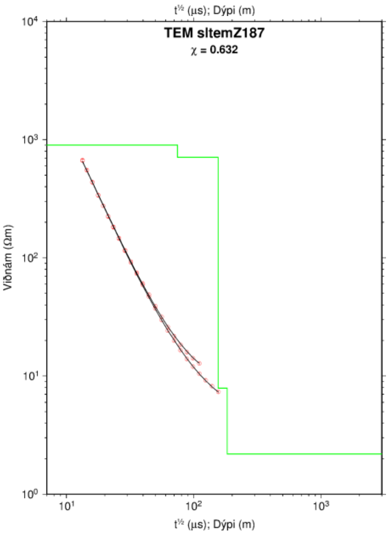
TEM sltemZ187
χ = 0.632
10⁴
10³
10²
10¹
10⁰
Viðnám (Ωm)
10¹
10²
10³
t½ (µs); Dýpi (m)

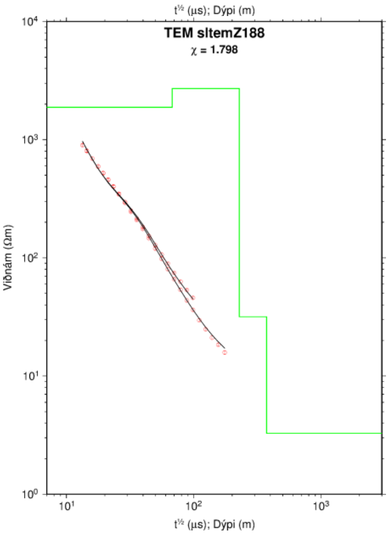
TEM sltemZ188
χ = 1.798
10⁴
10³
10²
10¹
10⁰
Viðnám (Ωm)
10¹
10²
10³
t½ (µs); Dýpi (m)

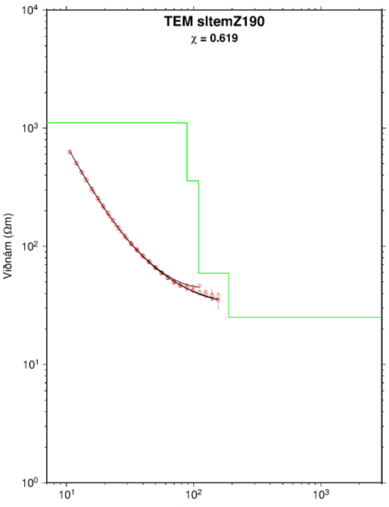
TEM sltemZ190
χ = 0.619
Viðnám (Ωm)
10⁴
10³
10²
10¹
10⁰
10¹
10²
10³
t½ (µs); Dýpi (m)

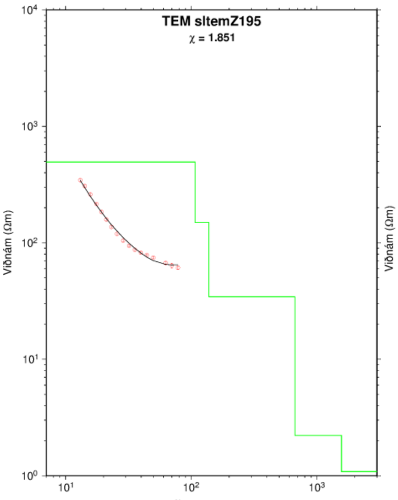
TEM sltemZ195
χ = 1.851
Viðnám (Ωm)
10⁴
10³
10²
10¹
10⁰
10¹
10²
10³
t½ (µs); Dýpi (m)

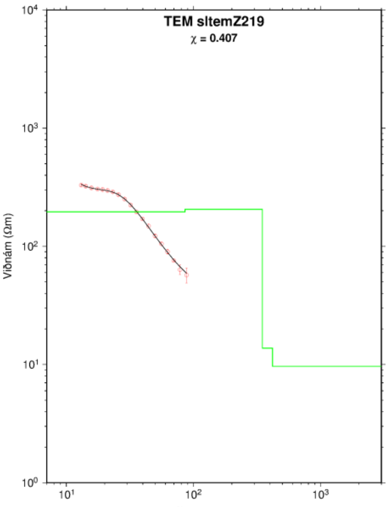
TEM sltemZ219
χ = 0.407
Viðnám (Ωm)
10⁴
10³
10²
10¹
10⁰
10¹
10²
10³
t½ (µs); Dýpi (m)

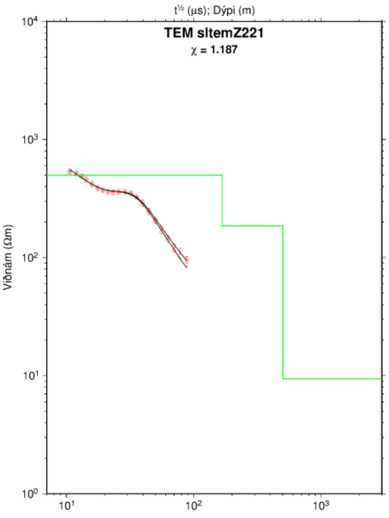
TEM sltemZ221
χ = 1.187
Viðnám (Ωm)
10⁴
10³
10²
10¹
10⁰
10¹
10²
10³
t½ (µs); Dýpi (m)

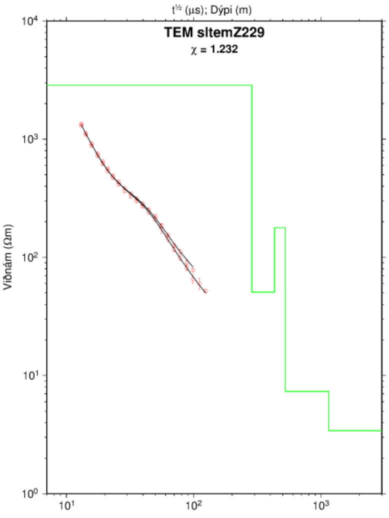
TEM sltemZ229
χ = 1.232
Viðnám (Ωm)
10⁴
10³
10²
10¹
10⁰
10¹
10²
10³
t½ (µs); Dýpi (m)

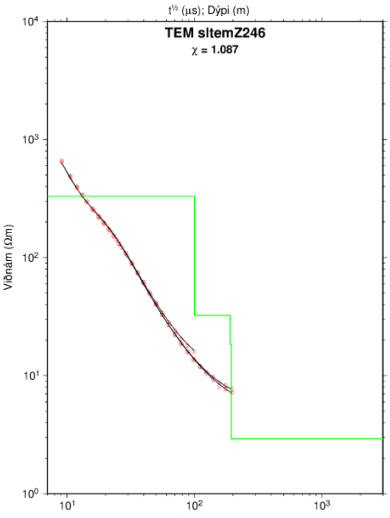
TEM sltemZ246
χ = 1.087
Viðnám (Ωm)
10⁴
10³
10²
10¹
10⁰
10¹
10²
10³
t½ (µs); Dýpi (m)

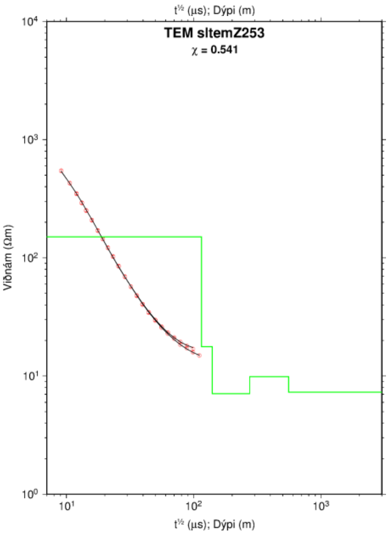
TEM sltemZ253
χ = 0.541
Viðnám (Ωm)
10⁴
10³
10²
10¹
10⁰
10¹
10²
10³
t½ (µs); Dýpi (m)

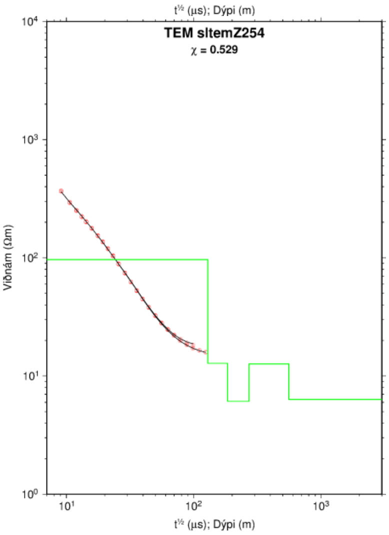
TEM sltemZ254
χ = 0.529
Viðnám (Ωm)
10⁴
10³
10²
10¹
10⁰
10¹
10²
10³
t½ (µs); Dýpi (m)

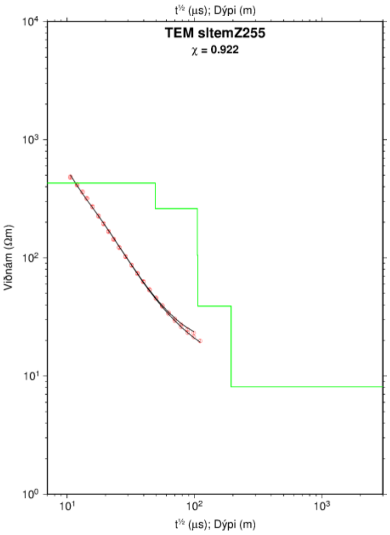
TEM sltemZ255
χ = 0.922
Viðnám (Ωm)
10⁴
10³
10²
10¹
10⁰
10¹
10²
10³
t½ (µs); Dýpi (m)

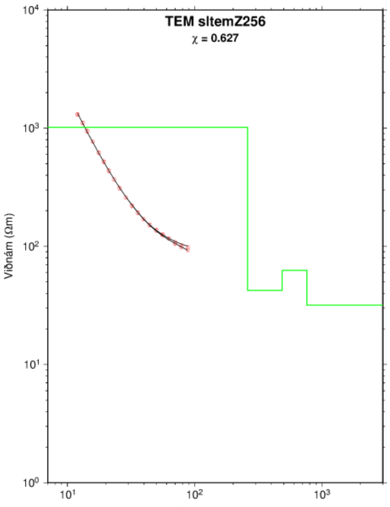
TEM sltemZ256
χ = 0.627
Viðnám (Ωm)
t½ (µs); Dýpi (m)
10⁰
10¹
10²
10³
10⁴

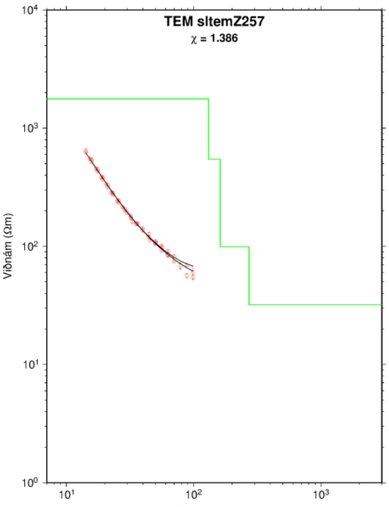
TEM sltemZ257
χ = 1.386
Viðnám (Ωm)
t½ (µs); Dýpi (m)
10⁰
10¹
10²
10³
10⁴

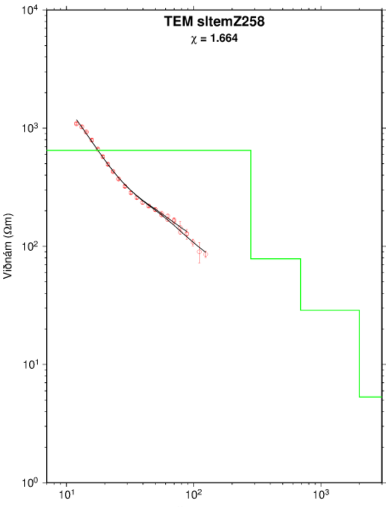
TEM sltemZ258
χ = 1.664
Viðnám (Ωm)
t½ (µs); Dýpi (m)
10⁰
10¹
10²
10³
10⁴

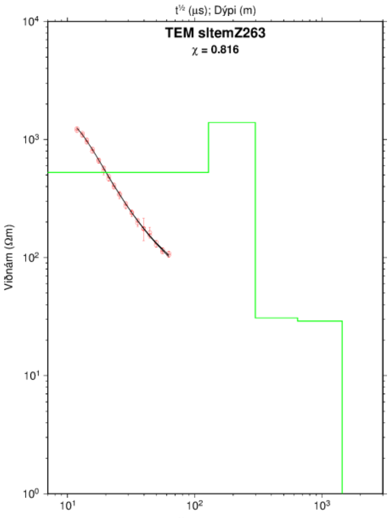
TEM sltemZ263
χ = 0.816
Viðnám (Ωm)
t½ (µs); Dýpi (m)
10⁰
10¹
10²
10³
10⁴

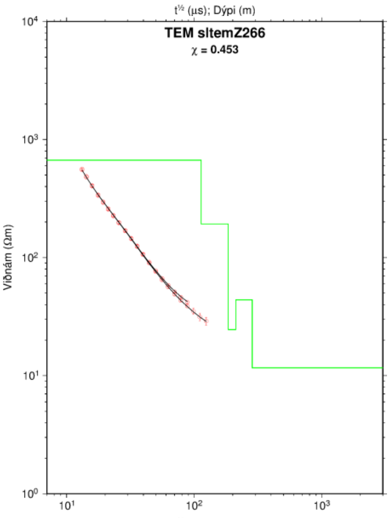
TEM sltemZ266
χ = 0.453
Viðnám (Ωm)
t½ (µs); Dýpi (m)
10⁰
10¹
10²
10³
10⁴

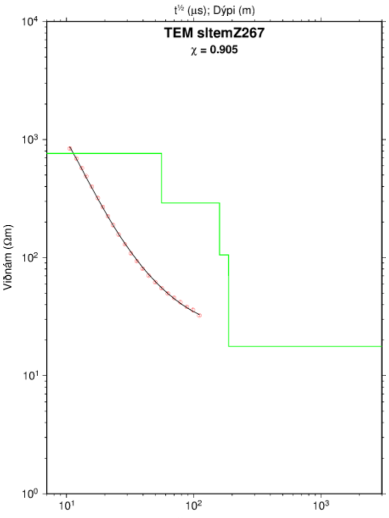
TEM sltemZ267
χ = 0.905
Viðnám (Ωm)
t½ (µs); Dýpi (m)
10⁰
10¹
10²
10³
10⁴

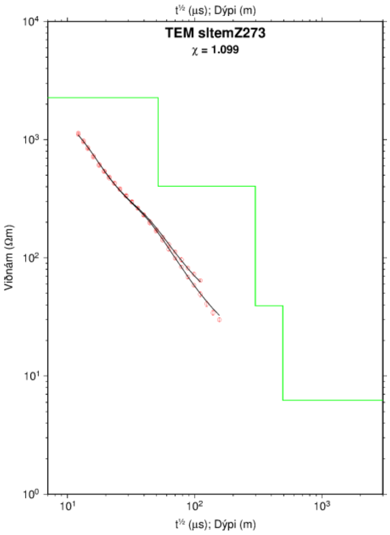
TEM sltemZ273
χ = 1.099
Viðnám (Ωm)
t½ (µs); Dýpi (m)
10⁰
10¹
10²
10³
10⁴

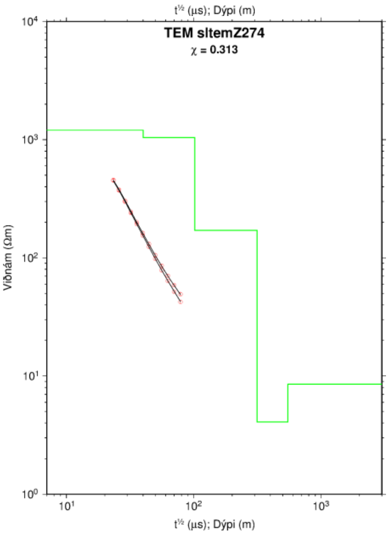
TEM sltemZ274
χ = 0.313
Viðnám (Ωm)
t½ (µs); Dýpi (m)
10⁰
10¹
10²
10³
10⁴

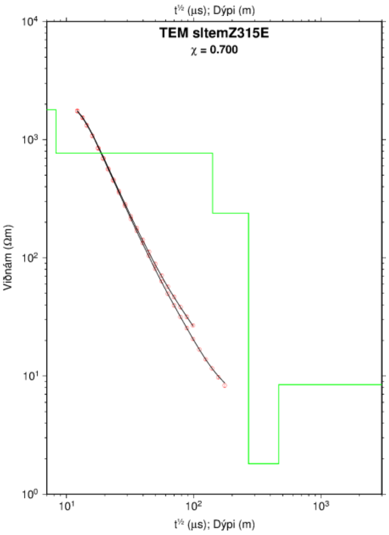
TEM sltemZ315E
χ = 0.700
Viðnám (Ωm)
t½ (µs); Dýpi (m)
10⁰
10¹
10²
10³
10⁴

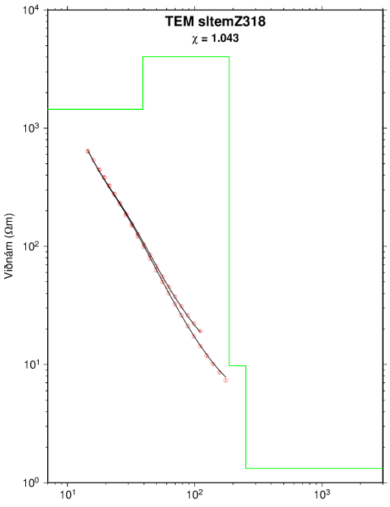
TEM sltemZ318
χ = 1.043
Viðnám (Ωm)
t½ (µs); Dýpi (m)
10⁰
10¹
10²
10³
10⁴
10¹
10²
10³

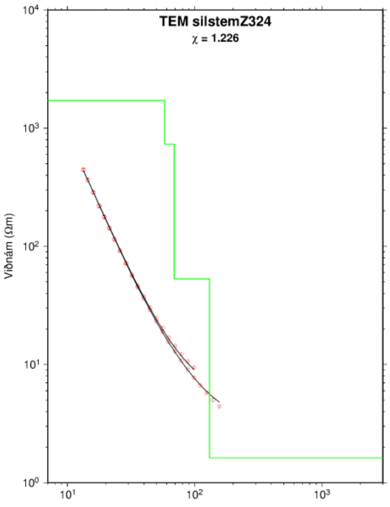
TEM silstemZ324
χ = 1.226
Viðnám (Ωm)
t½ (µs); Dýpi (m)
10⁰
10¹
10²
10³
10⁴
10¹
10²
10³

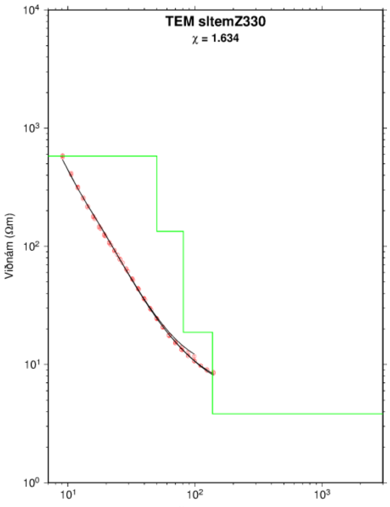
TEM sltemZ330
χ = 1.634
Viðnám (Ωm)
t½ (µs); Dýpi (m)
10⁰
10¹
10²
10³
10⁴
10¹
10²
10³

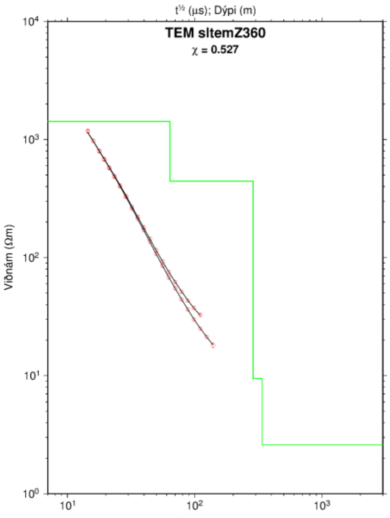
TEM sltemZ360
χ = 0.527
Viðnám (Ωm)
t½ (µs); Dýpi (m)
10⁰
10¹
10²
10³
10⁴
10¹
10²
10³

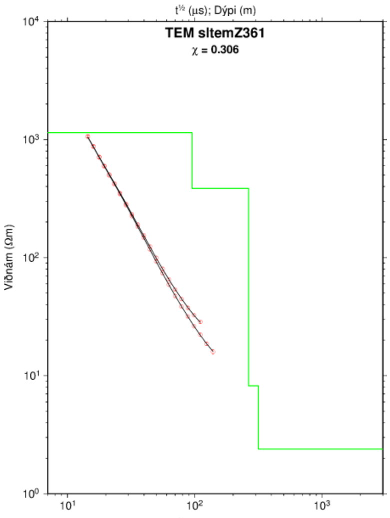
TEM sltemZ361
χ = 0.306
Viðnám (Ωm)
t½ (µs); Dýpi (m)
10⁰
10¹
10²
10³
10⁴
10¹
10²
10³

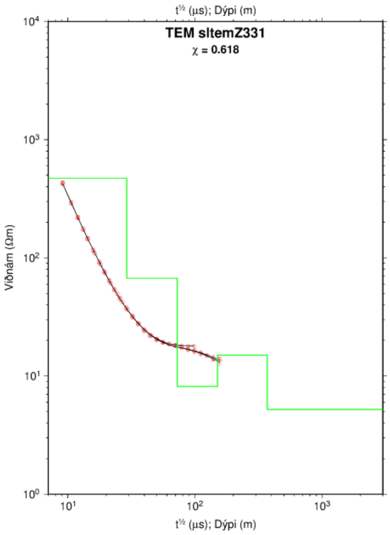
TEM sltemZ331
χ = 0.618
Viðnám (Ωm)
t½ (µs); Dýpi (m)
10⁰
10¹
10²
10³
10⁴
10¹
10²
10³

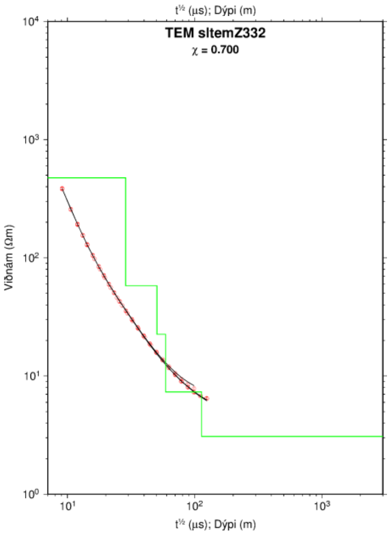
TEM sltemZ332
χ = 0.700
Viðnám (Ωm)
t½ (µs); Dýpi (m)
10⁰
10¹
10²
10³
10⁴
10¹
10²
10³

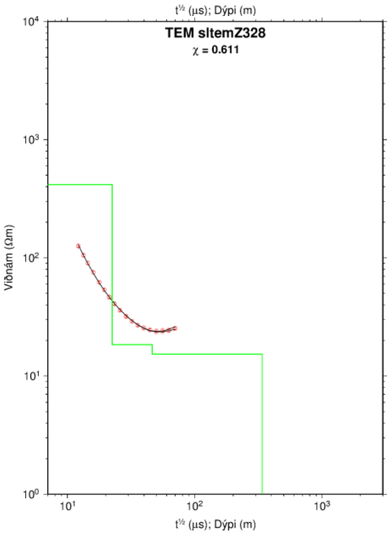
TEM sltemZ328
χ = 0.611
Viðnám (Ωm)
t½ (µs); Dýpi (m)
10⁰
10¹
10²
10³
10⁴
10¹
10²
10³

# APPENDIX II: 1-D joint inversion of TEM and MT data

This appendix shows results from all the joint 1-D inversion of TEM and MT. Red diamonds represent TEM apparent resistivity transformed to a pseudo-MT curve; blue squares are measured apparent resistivity; blue circles are apparent phase derived from the determinant of MT impedance tensor; green lines on the right represent results of the 1-D resistivity inversion model. The number above the left panel corresponds to the name of the MT station; number below the MT station: chi (χ) – a measure of the fit between the measured data and the model data. The number to the left in the left panel: the name of the TEM station. The number in the parentheses (x/z) represents the distance between the two stations and their elevations difference respectively. The resistivity model is plotted in a logarithmic scale (log10) both for the resistivity and the phase.

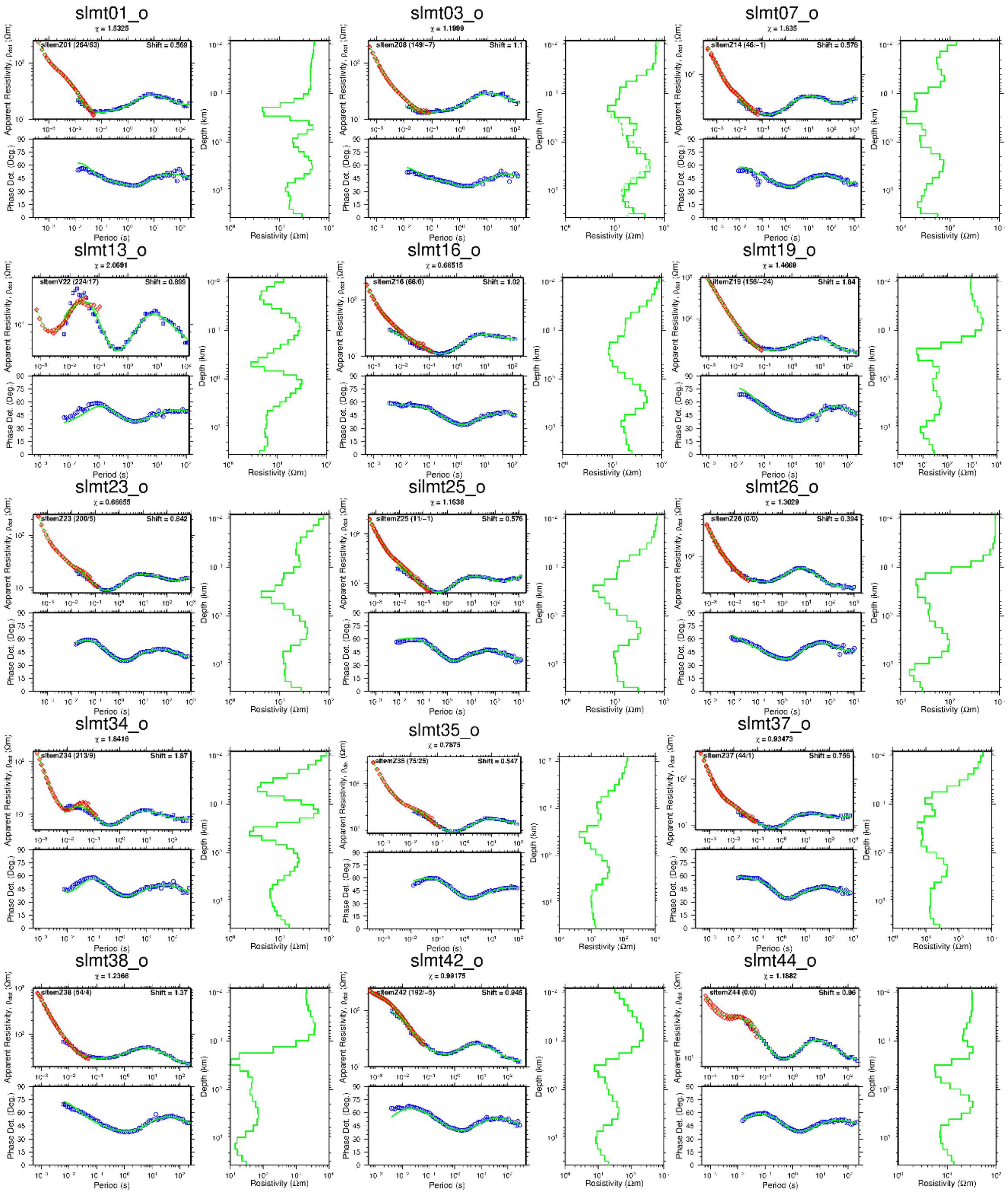

slmt54_o
χ = 0.9094

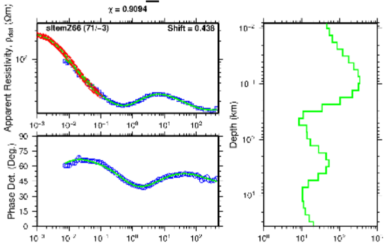

slmt55_o
χ = 0.96617

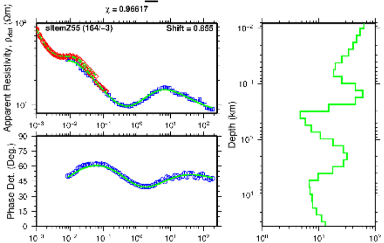

slmt59_o
χ = 1.2835

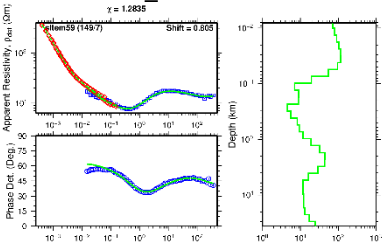

slmt62_o
χ = 0.90009

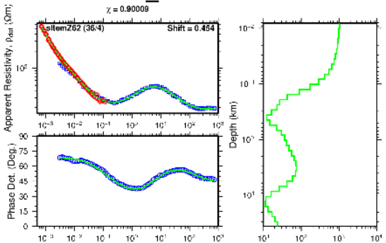

silmt65_o
χ = 1.806

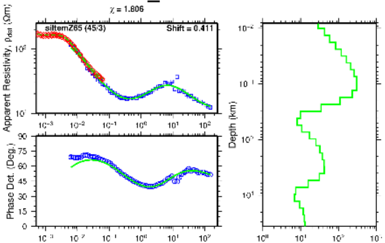

slmt69_o
χ = 1.3741

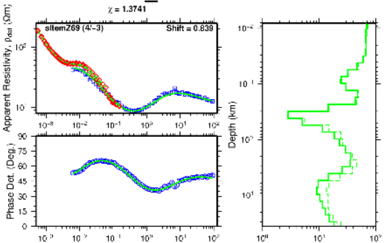

silmt71_o
χ = 1.2929

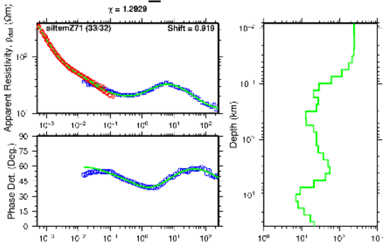

slmt75_o
χ = 1.1607

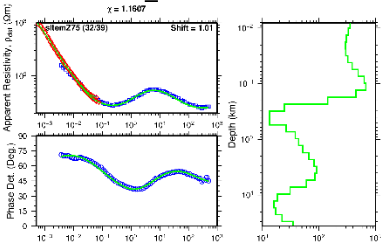

slmt76_o
χ = 1.6727

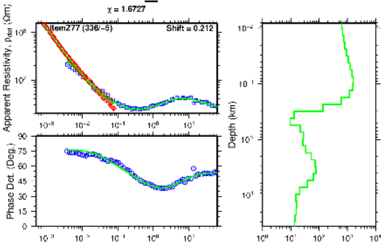

slmt79_o
χ = 1.5937

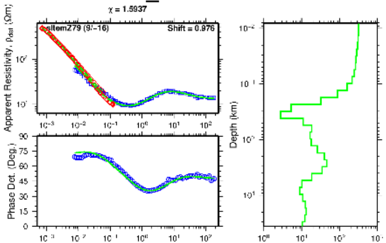

slmt81_o
χ = 1.3414

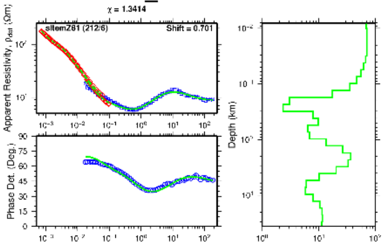

slmt88_o
χ = 2.4242

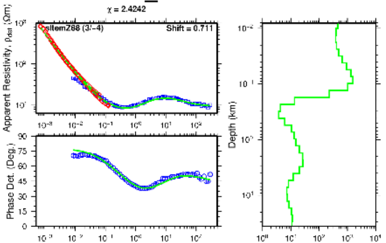

slmt91_o
χ = 1.0786

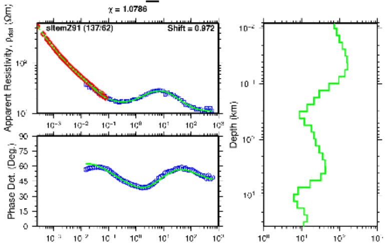

slmt95_o
χ = 1.8756

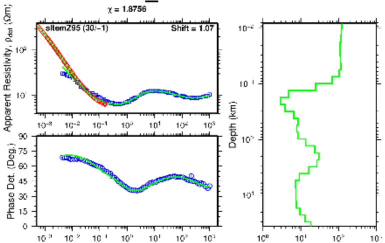

silmt100_o
χ = 0.83202

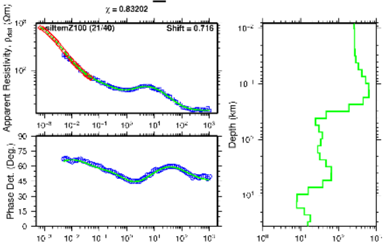

silmt104_o
χ = 3.5714

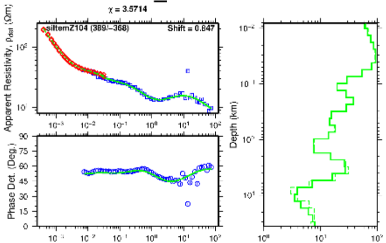

slmt108_o
χ = 1.9977

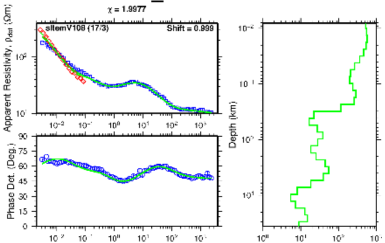

slmt110_o
χ = 1.1933

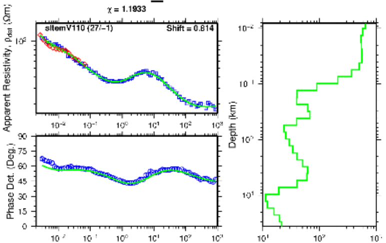

slmt114a_o
χ = 1.1186

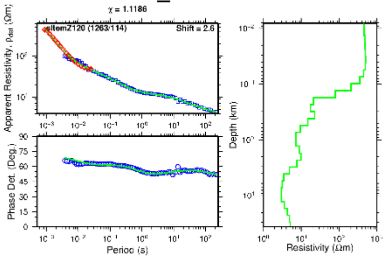

slmt115_o
χ = 1.0972

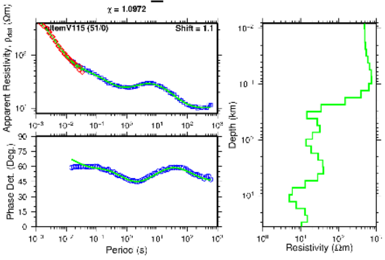

slmt118_o
χ = 1.1932

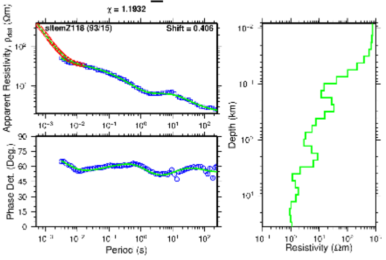

slmt120_o

χ = 1.1186

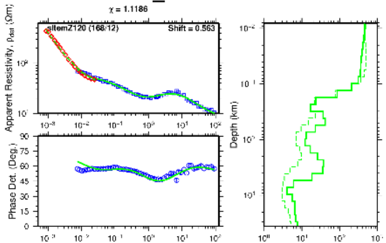

slmt128_o

χ = 1.2555

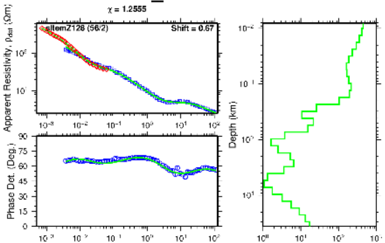

silmt130_o

χ = 1.8761

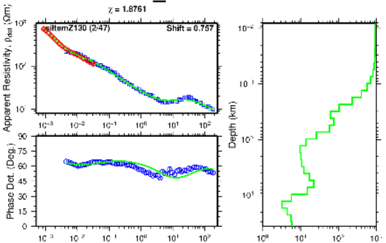

slmt136_o

χ = 1.6842

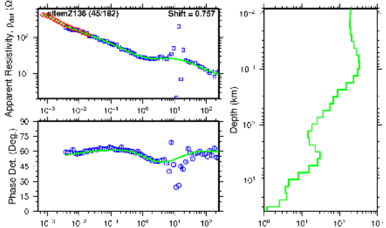

slmt138_o

χ = 0.89542

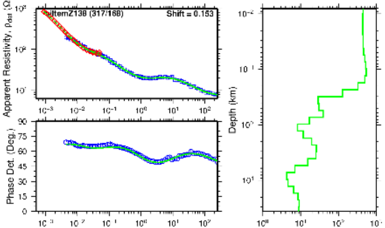

silmt146_o

χ = 1.4086

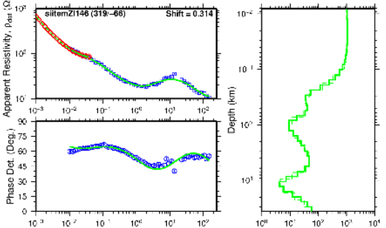

slmt149_o

χ = 1.0598

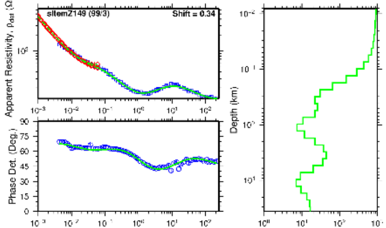

silmt153_o

χ = 4.4152

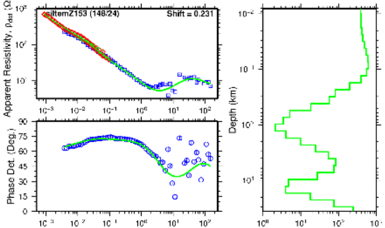

silmt157_o

χ = 2.3029

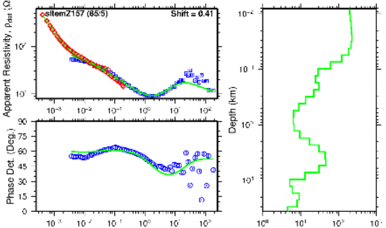

slmt164_o

χ = 2.0441

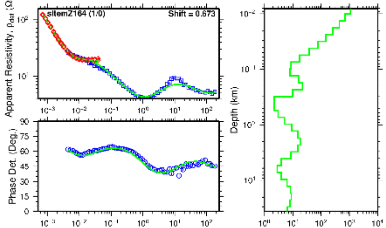

silmt166_o

χ = 1.4956

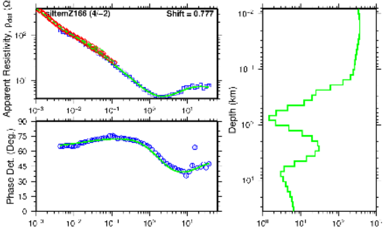

silmt167_o

χ = 2.1504

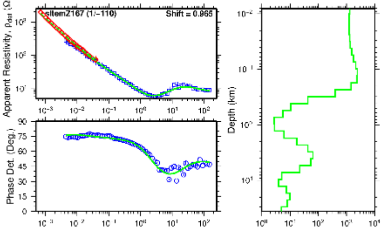

slmt169_o

χ = 1.3007

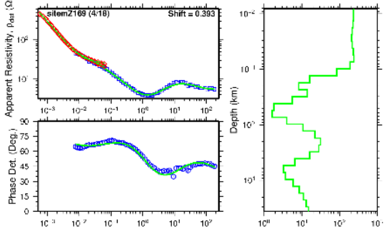

slmt170_o

χ = 1.8471

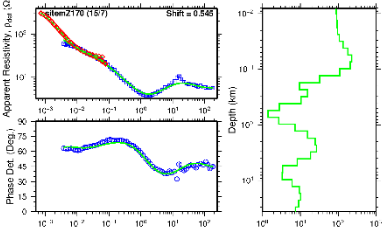

slmt171_o

χ = 2.2698

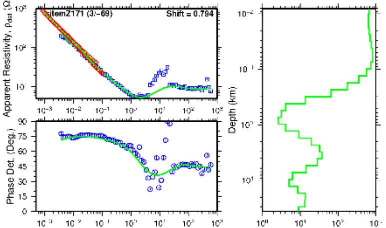

slmt172_o

χ = 1.6321

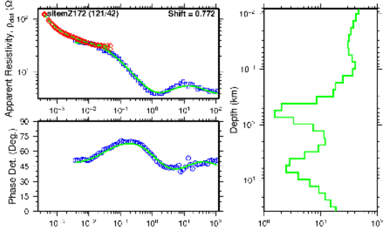

slmt173_o

χ = 2.4675

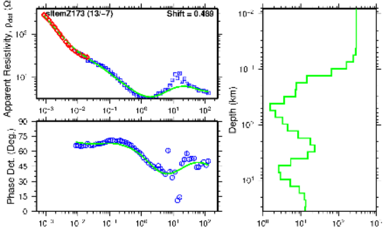

silmt175_o

χ = 4.9694

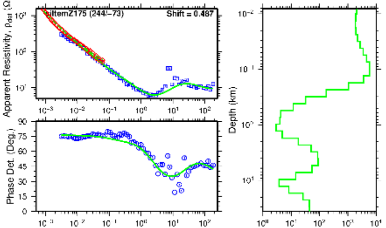

slmt177_o

χ = 1.7378

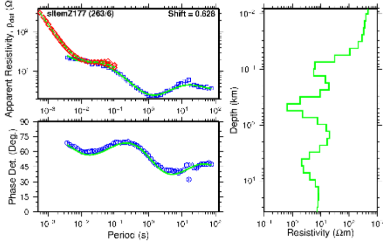

silmt180_o

χ = 2.1814

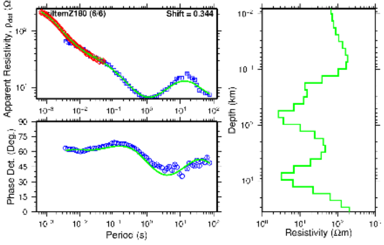

slmt182_o

χ = 1.7485

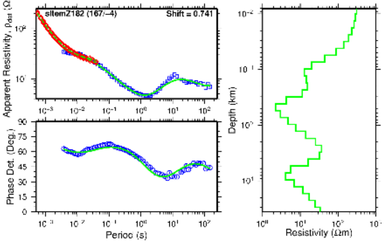

slmt185_o

χ = 1.1263

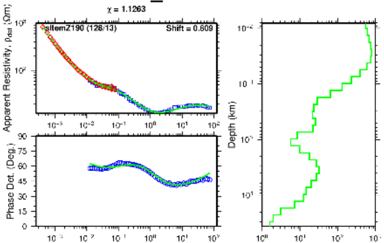

slmt188_o

χ = 1.2343

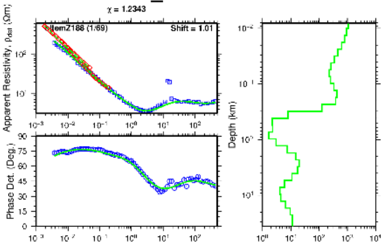

silmt192_o

χ = 1.224

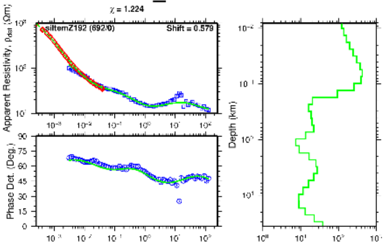

slmt194_o

χ = 1.1166

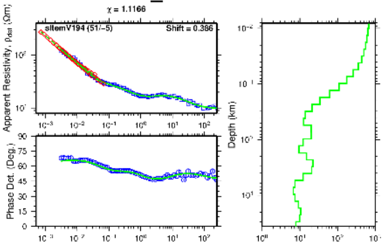

slmt195_o

χ = 1.0631

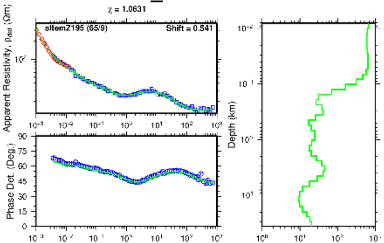

slmt197_o

χ = 1.282

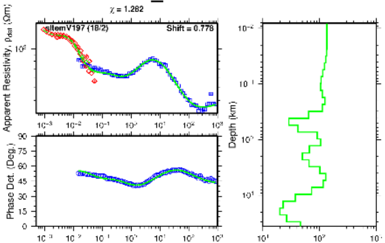

slmt199_o

χ = 1.4138

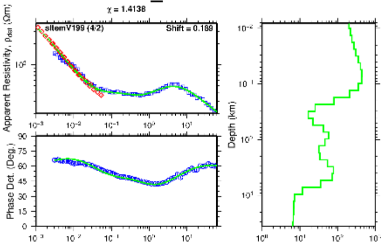

silmt219_o

χ = 2.5219

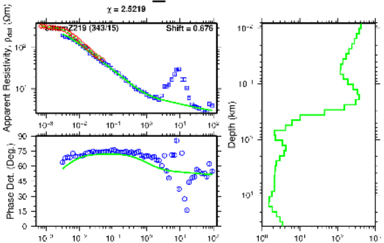

silmt221_o

χ = 1.5353

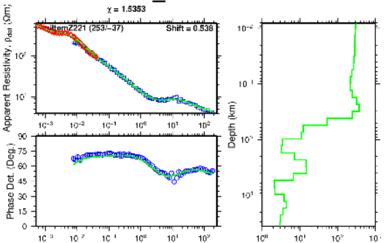

slmt229_o

χ = 2.7516

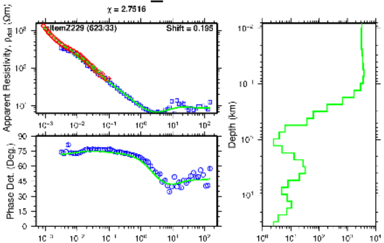

slmt246_o

χ = 2.732

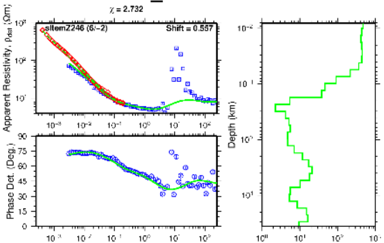

slmt249_o

χ = 1.6772

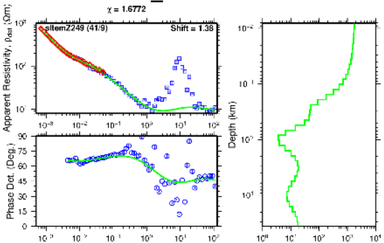

slmt250_o

χ = 1.918

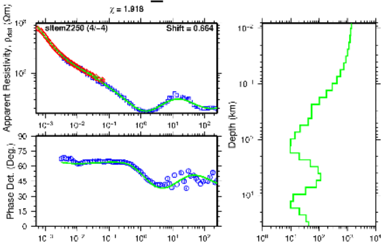

silmt251_o

χ = 1.4328

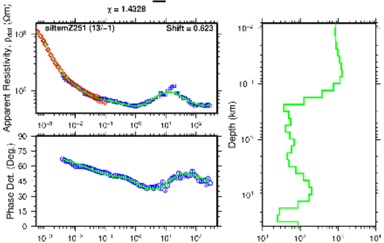

slmt252a_o

χ = 1.3102

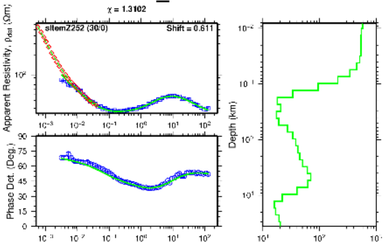

slmt253_o

χ = 0.9691

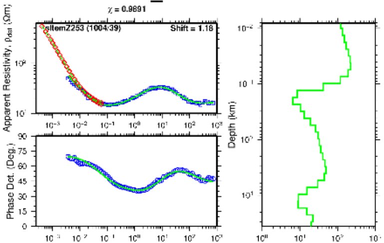

slmt254_o

χ = 1.4408

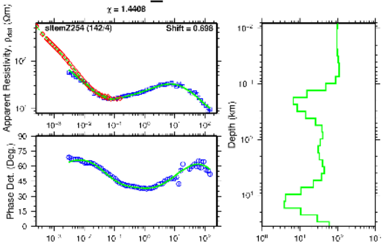

slmt255_o

χ = 1.0562

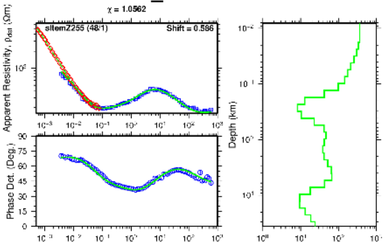

slmt256_o

χ = 0.99114

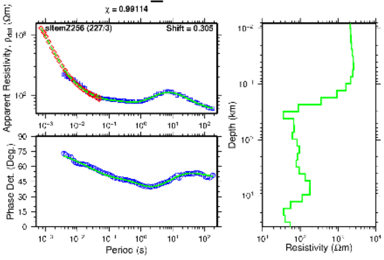

slmt257_o

χ = 1.2179

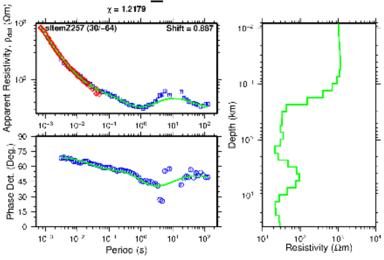

slmt258_o

χ = 1.9913

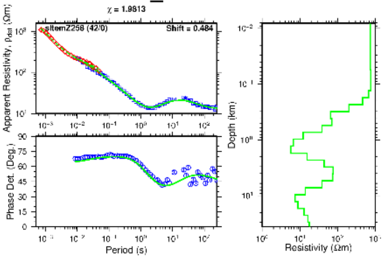

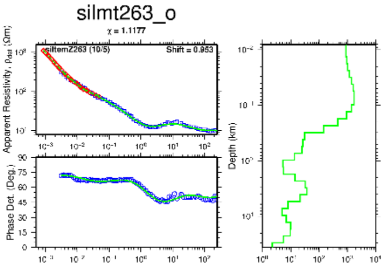
silmt263_o
χ = 1.1177
siltemZ263 (10/5)
Shift = 0.953
Apparent Resistivity, ρdet (Ωm)
Phase Det. (Deg.)
Period (s)
Depth (km)
Resistivity (Ωm)

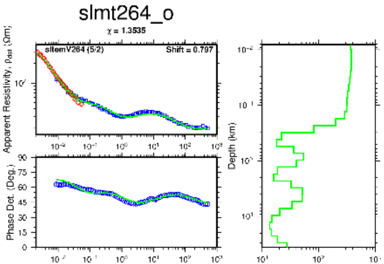
slmt264_o
χ = 1.3535
sltemV264 (5/2)
Shift = 0.797
Apparent Resistivity, ρdet (Ωm)
Phase Det. (Deg.)
Period (s)
Depth (km)
Resistivity (Ωm)

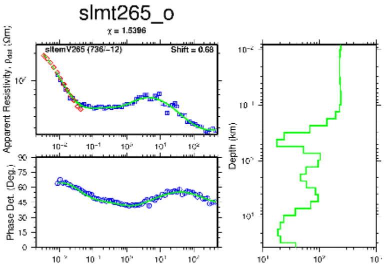
slmt265_o
χ = 1.5396
sltemV265 (736/−12)
Shift = 0.68
Apparent Resistivity, ρdet (Ωm)
Phase Det. (Deg.)
Period (s)
Depth (km)
Resistivity (Ωm)

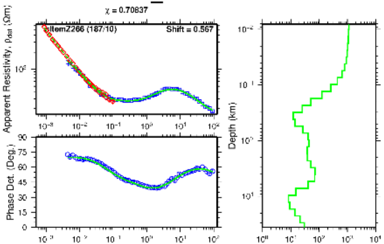
slmt266_o
χ = 0.70837
sltemZ266 (187/10)
Shift = 0.567
Apparent Resistivity, ρdet (Ωm)
Phase Det. (Deg.)
Period (s)
Depth (km)
Resistivity (Ωm)

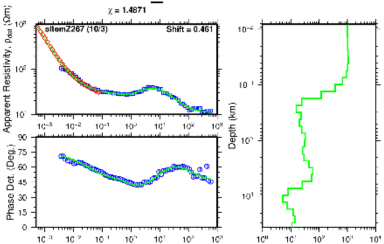
slmt267_o
χ = 1.4871
sltemZ267 (10/3)
Shift = 0.461
Apparent Resistivity, ρdet (Ωm)
Phase Det. (Deg.)
Period (s)
Depth (km)
Resistivity (Ωm)

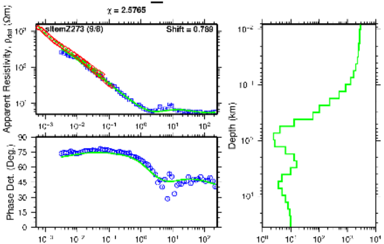
slmt273_o
χ = 2.5765
sltemZ273 (9/8)
Shift = 0.789
Apparent Resistivity, ρdet (Ωm)
Phase Det. (Deg.)
Period (s)
Depth (km)
Resistivity (Ωm)

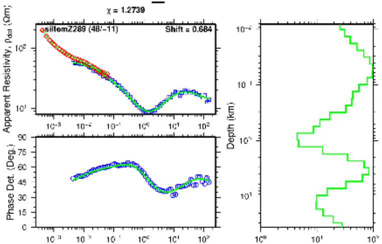
silmt288_o
χ = 1.2739
siltemZ289 (48/−11)
Shift = 0.684
Apparent Resistivity, ρdet (Ωm)
Phase Det. (Deg.)
Period (s)
Depth (km)
Resistivity (Ωm)

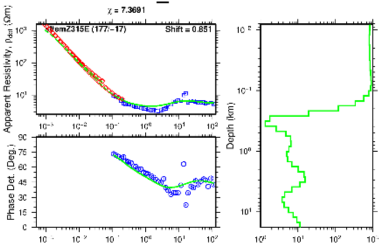
slmt315E_o
χ = 7.3691
sltemZ315E (177/−17)
Shift = 0.851
Apparent Resistivity, ρdet (Ωm)
Phase Det. (Deg.)
Period (s)
Depth (km)
Resistivity (Ωm)

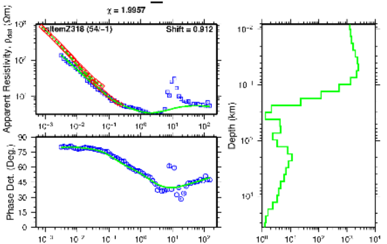
slmt318_o
χ = 1.9957
sltemZ318 (54/−1)
Shift = 0.912
Apparent Resistivity, ρdet (Ωm)
Phase Det. (Deg.)
Period (s)
Depth (km)
Resistivity (Ωm)

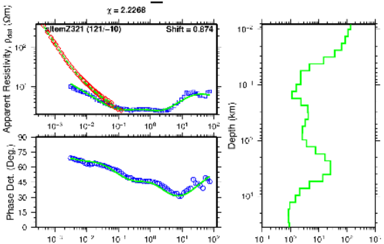
slmt321_o
χ = 2.2268
sltemZ321 (121/−10)
Shift = 0.874
Apparent Resistivity, ρdet (Ωm)
Phase Det. (Deg.)
Period (s)
Depth (km)
Resistivity (Ωm)

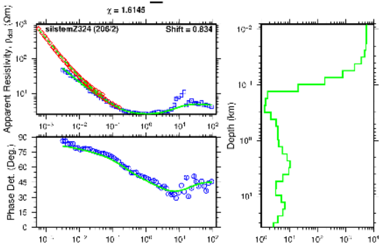
slmt324_o
χ = 1.6145
silstemZ324 (206/2)
Shift = 0.834
Apparent Resistivity, ρdet (Ωm)
Phase Det. (Deg.)
Period (s)
Depth (km)
Resistivity (Ωm)

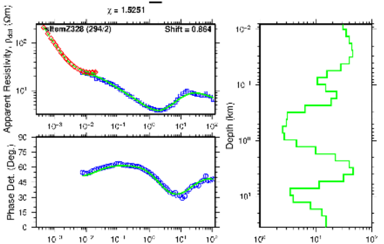
slmt328_o
χ = 1.5251
sltemZ328 (294/2)
Shift = 0.864
Apparent Resistivity, ρdet (Ωm)
Phase Det. (Deg.)
Period (s)
Depth (km)
Resistivity (Ωm)

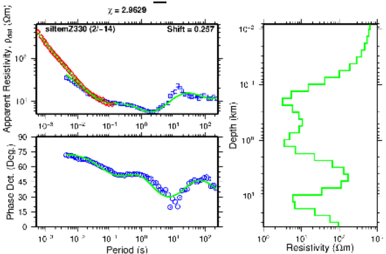
silmt330_o
χ = 2.9629
siltemZ330 (2/−14)
Shift = 0.257
Apparent Resistivity, ρdet (Ωm)
Phase Det. (Deg.)
Period (s)
Depth (km)
Resistivity (Ωm)

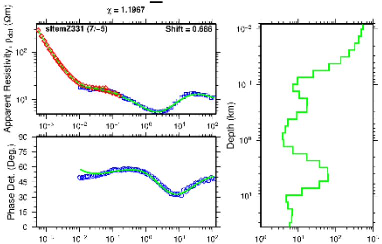
slmt331_o
χ = 1.1967
sltemZ331 (7/−5)
Shift = 0.686
Apparent Resistivity, ρdet (Ωm)
Phase Det. (Deg.)
Period (s)
Depth (km)
Resistivity (Ωm)

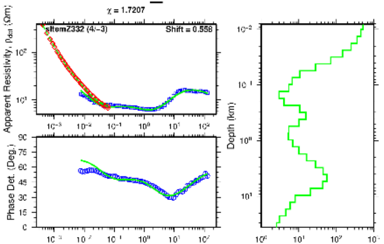
slmt332_o
χ = 1.7207
sltemZ332 (4/−3)
Shift = 0.558
Apparent Resistivity, ρdet (Ωm)
Phase Det. (Deg.)
Period (s)
Depth (km)
Resistivity (Ωm)

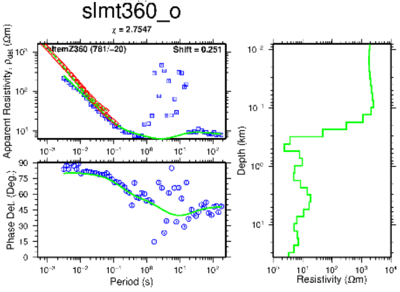
slmt360_o
χ = 2.7547
sltemZ360 (781/−20)
Shift = 0.251
Apparent Resistivity, ρdet (Ωm)
Phase Det. (Deg.)
Period (s)
Depth (km)
Resistivity (Ωm)

## APPENDIX III: 2-D inversion responses

1-D inversion responses for TE-mode, TM-mode and joint TE+TM-mode are presented showing the fit between the apparent resistivity (ohm-m and phase (degrees) of MT sites on each of the profiles considered in this inversion. Solid red/green curves show the response of the inversion model. The black circles are measured MT data points and the number inside the boxes represent the sounding name.

TE−response EW10_4 Profile

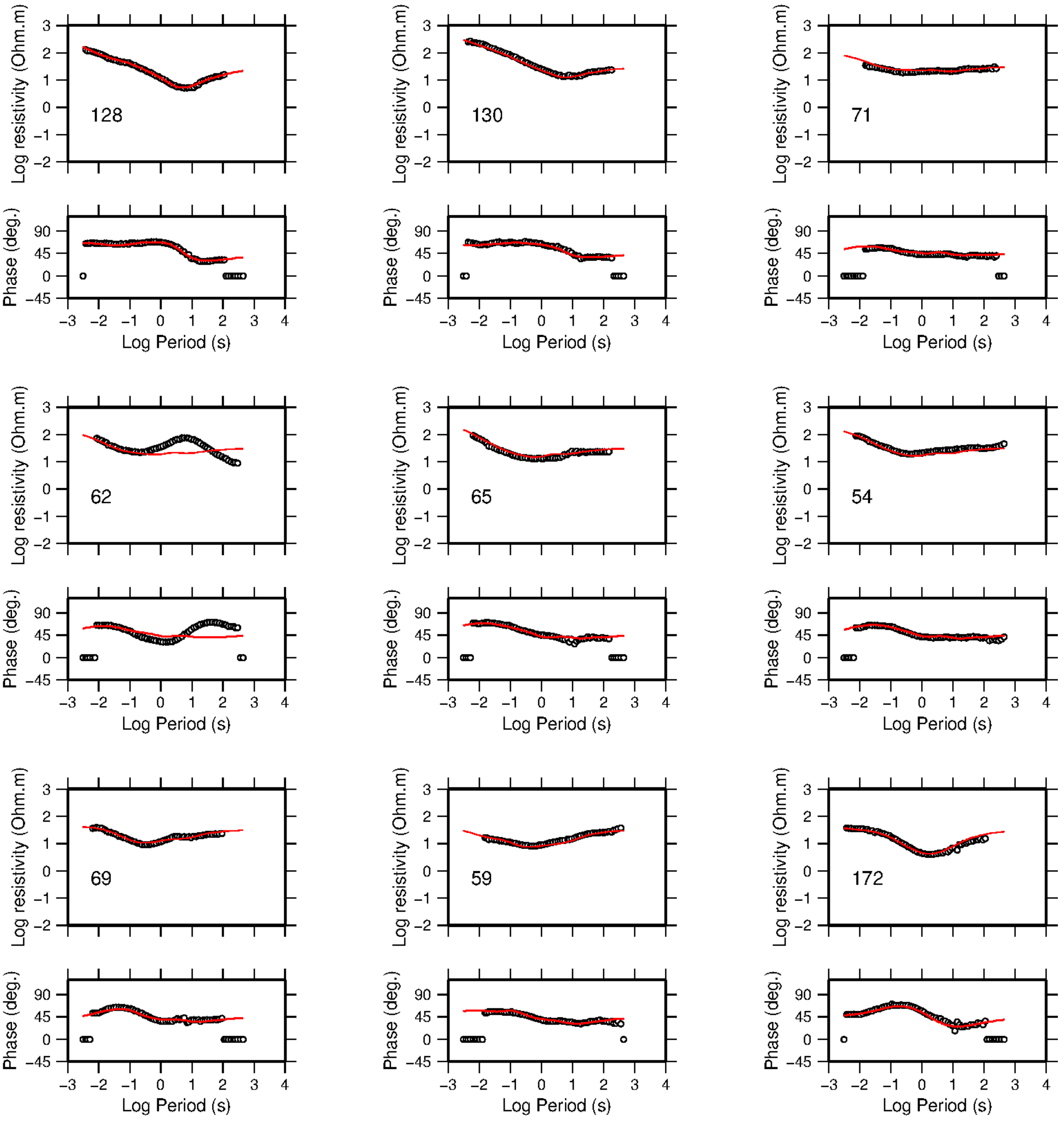

TM MODE−response EW10_4 Profile

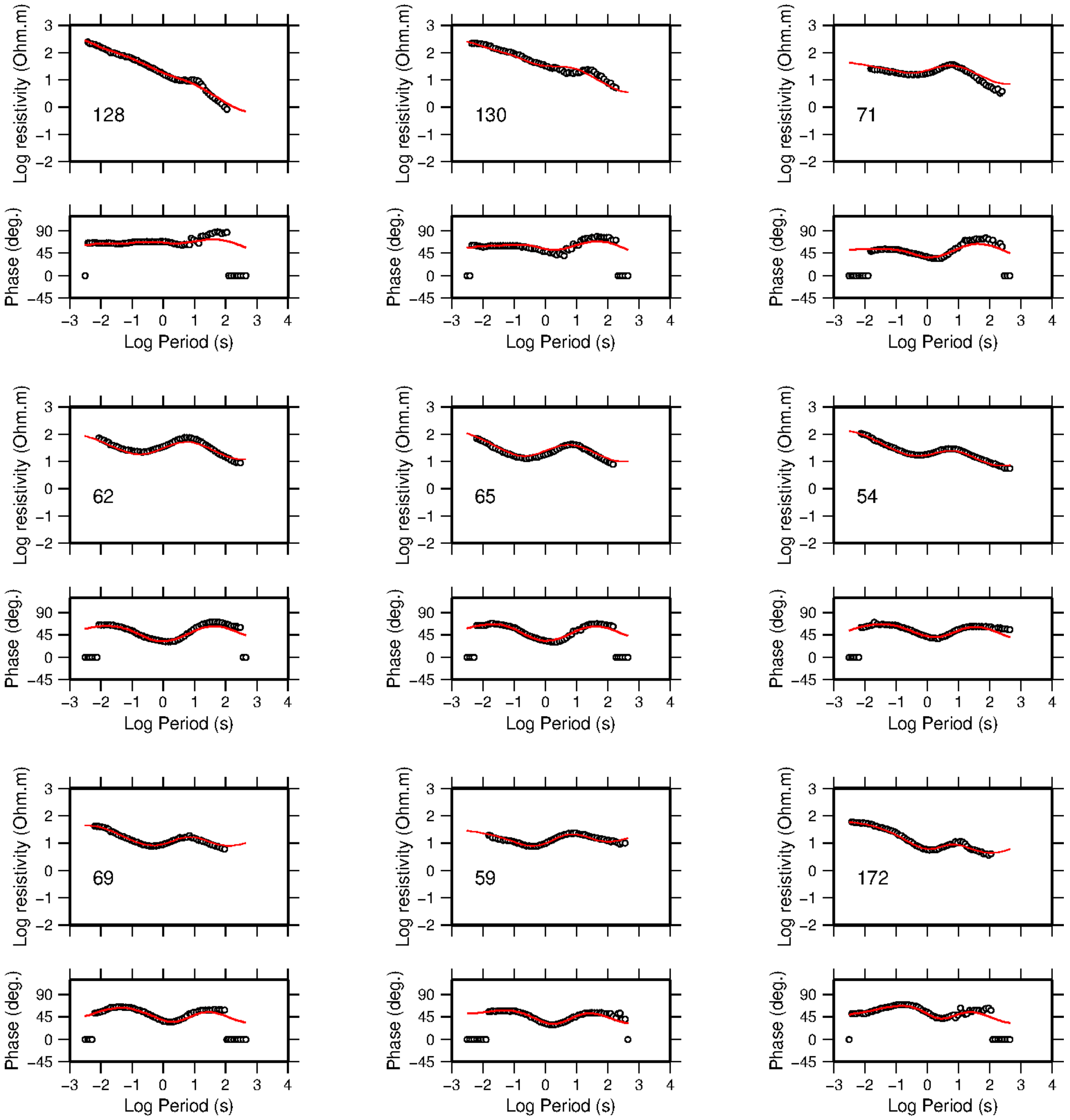

TE−mode in joint TMTE EW10_4 profile

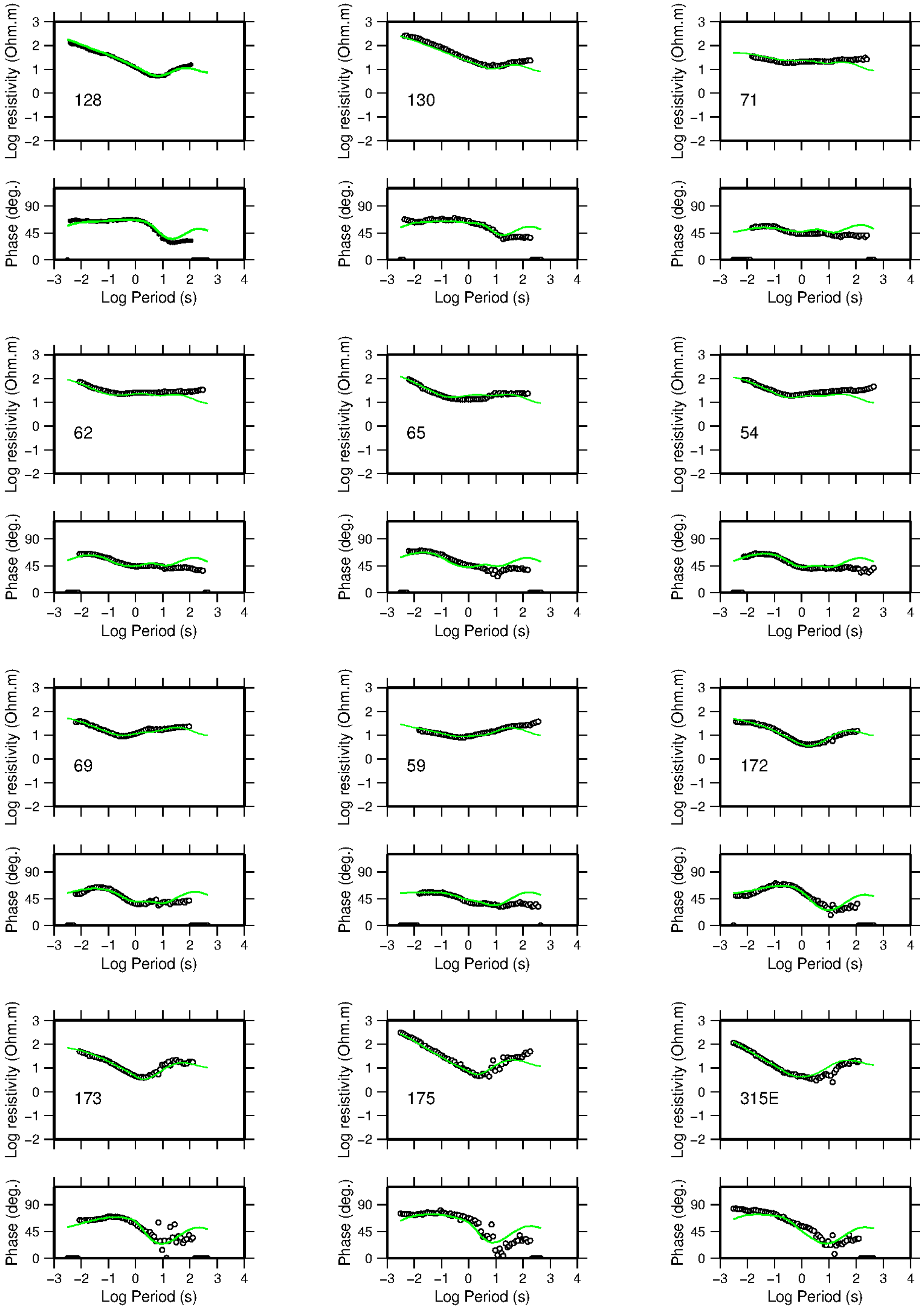

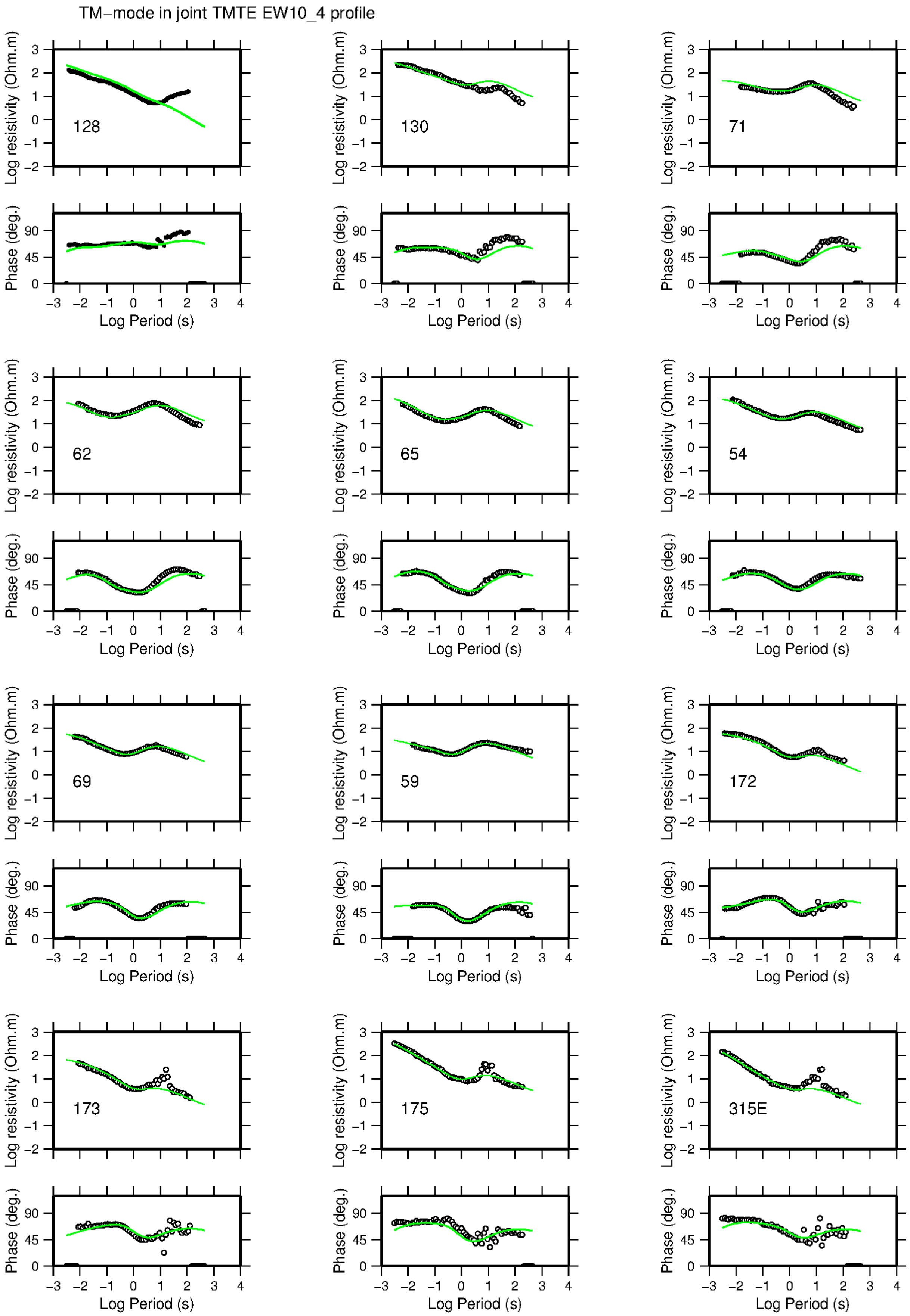
TM−mode in joint TMTE EW10_4 profile
128
130
71
62
65
54
69
59
172
173
175
315E
Log resistivity (Ohm.m)
3
2
1
0
−1
−2
Phase (deg.)
90
45
0
Log Period (s)
−3
−2
−1
0
1
2
3
4

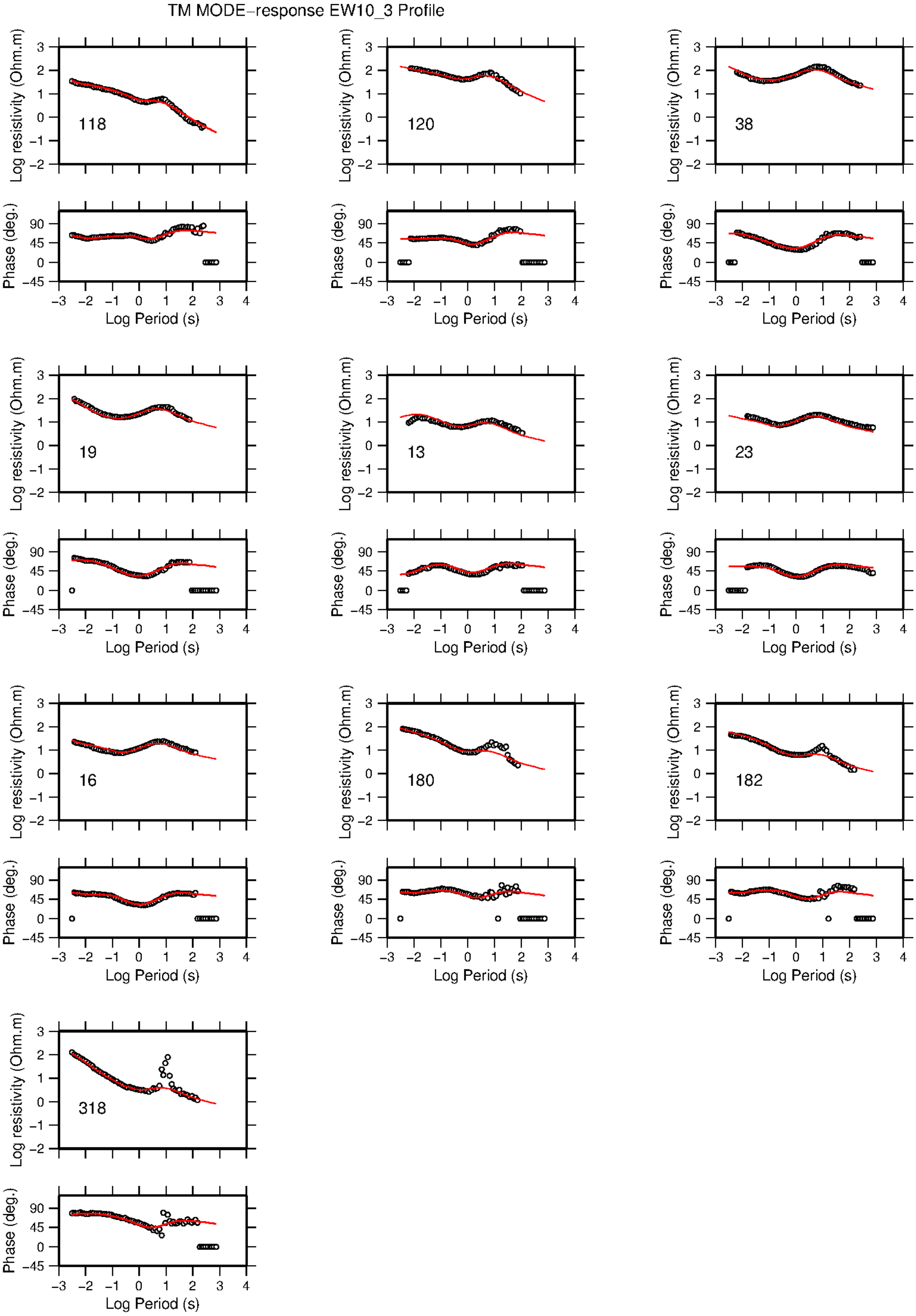
TM MODE−response EW10_3 Profile
Log resistivity (Ohm.m)
Phase (deg.)
Log Period (s)
118
120
38
19
13
23
16
180
182
318
3
2
1
0
−1
−2
90
45
0
−45
−3
−2
−1
0
1
2
3
4

TE−response EW10_3 Profile

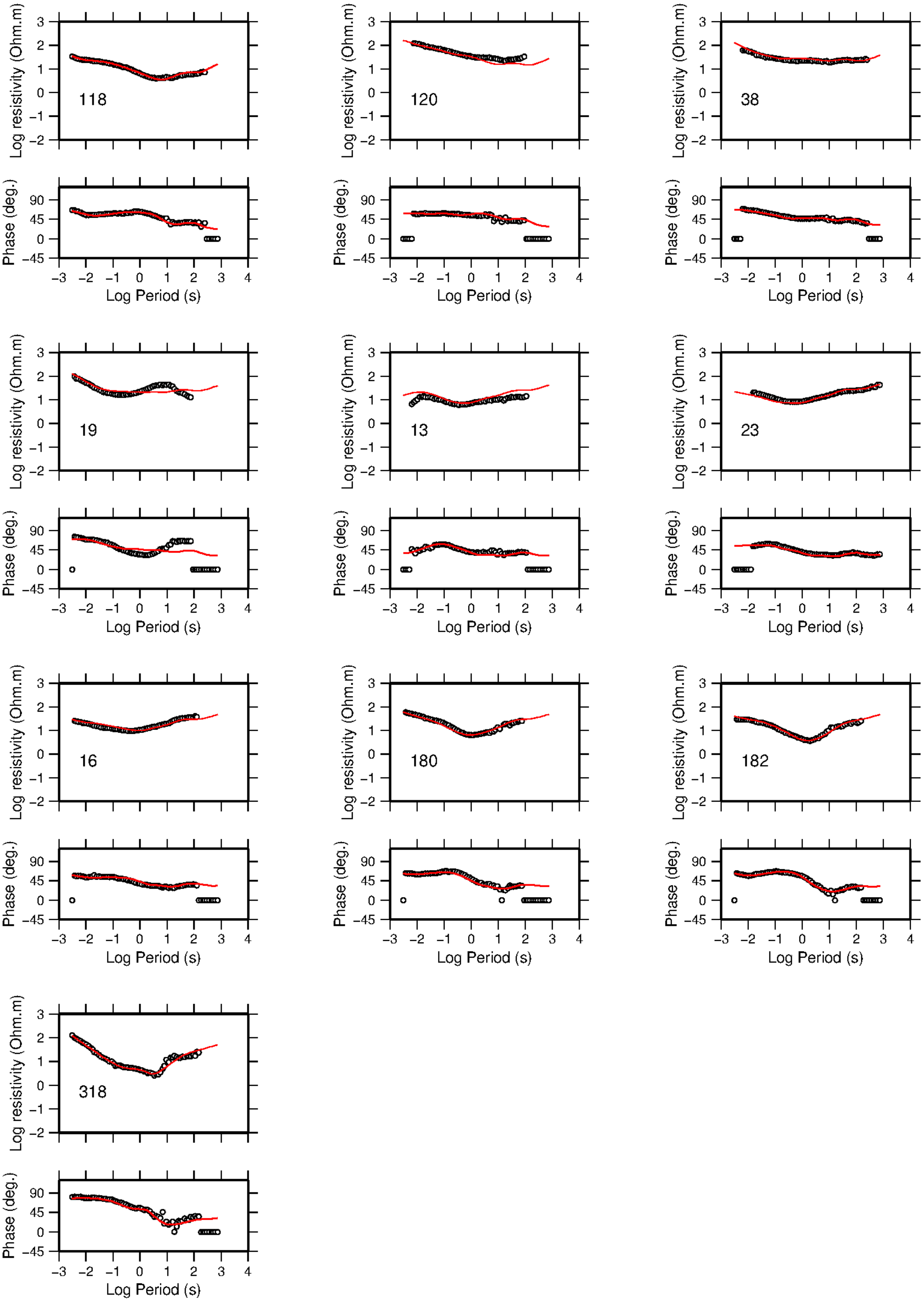

TE−mode in joint TMTE EW10_3 profile

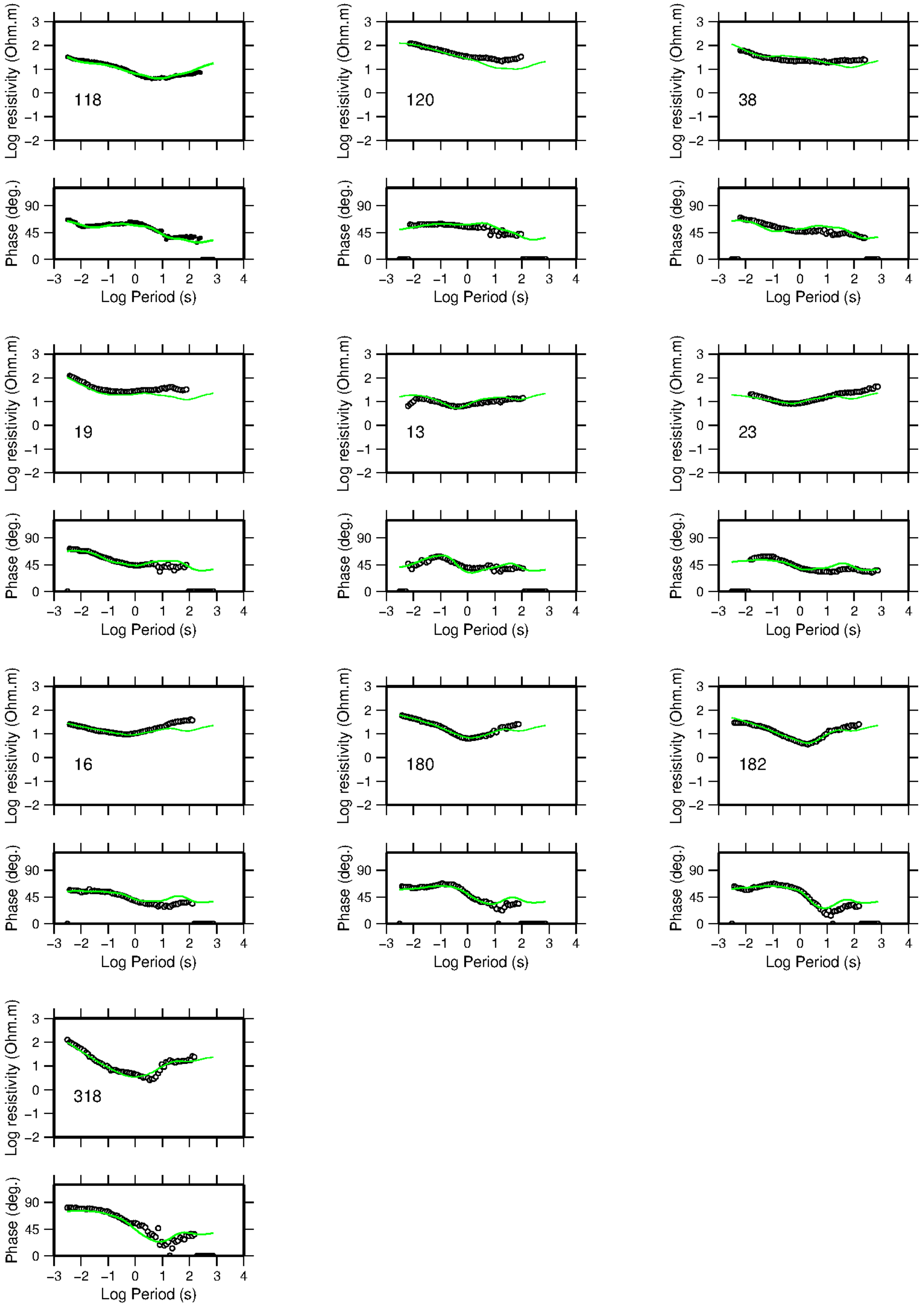

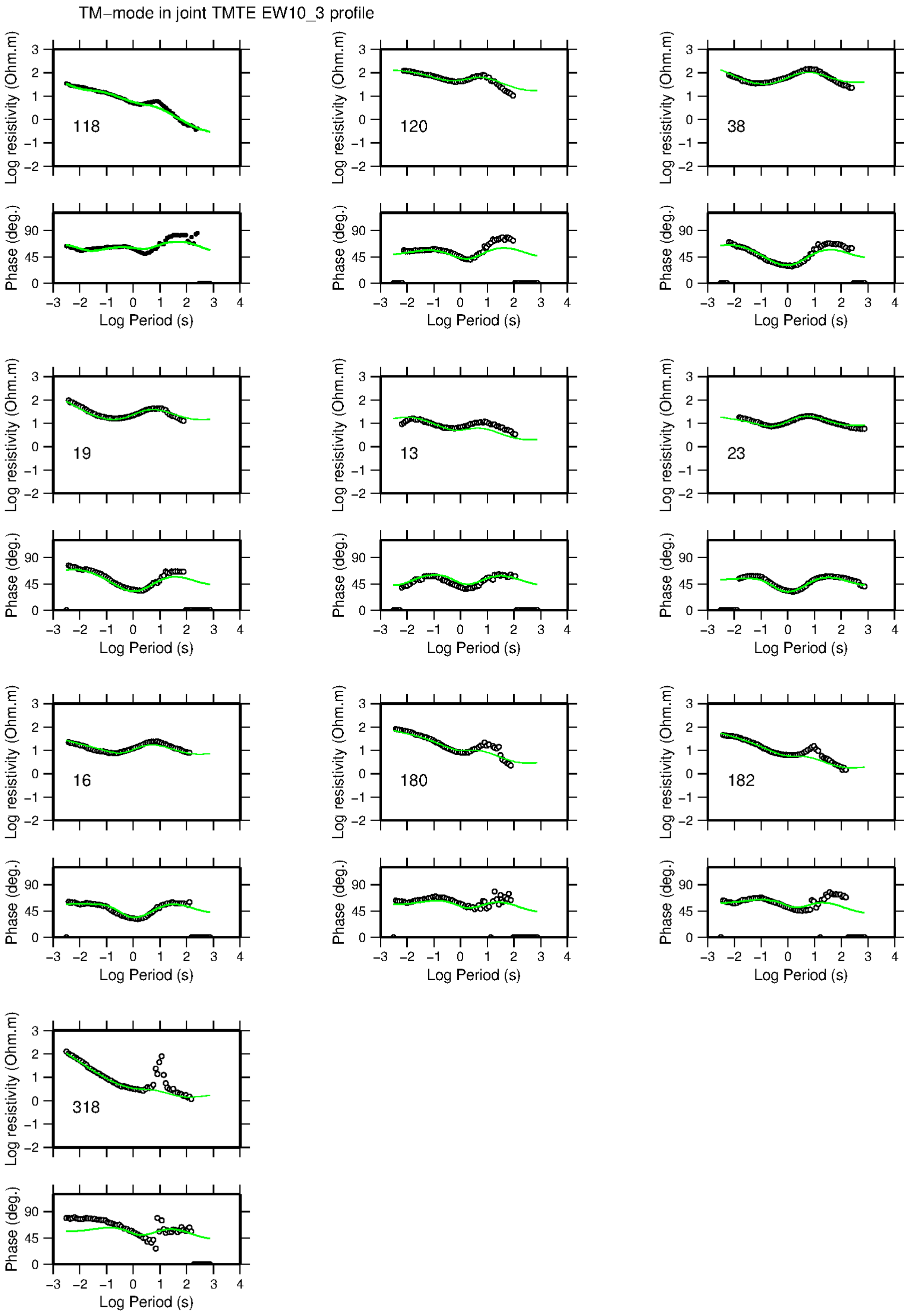
TM−mode in joint TMTE EW10_3 profile
118
120
38
19
13
23
16
180
182
318
Log resistivity (Ohm.m)
3
2
1
0
−1
−2
Phase (deg.)
90
45
0
−3
−2
−1
0
1
2
3
4
Log Period (s)

TE−response EW10_2 Profile

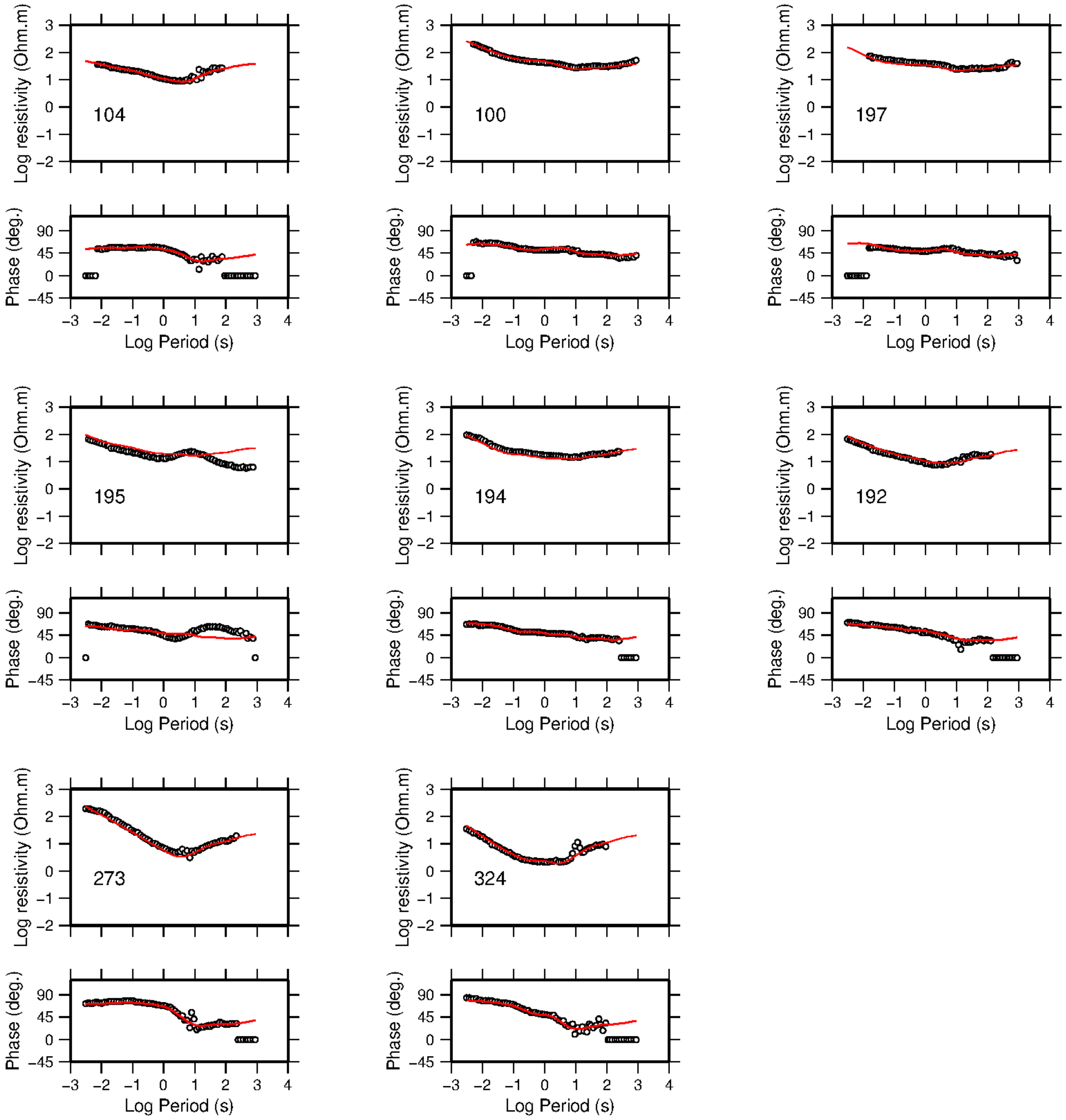

TM MODE−response EW10_2 Profile

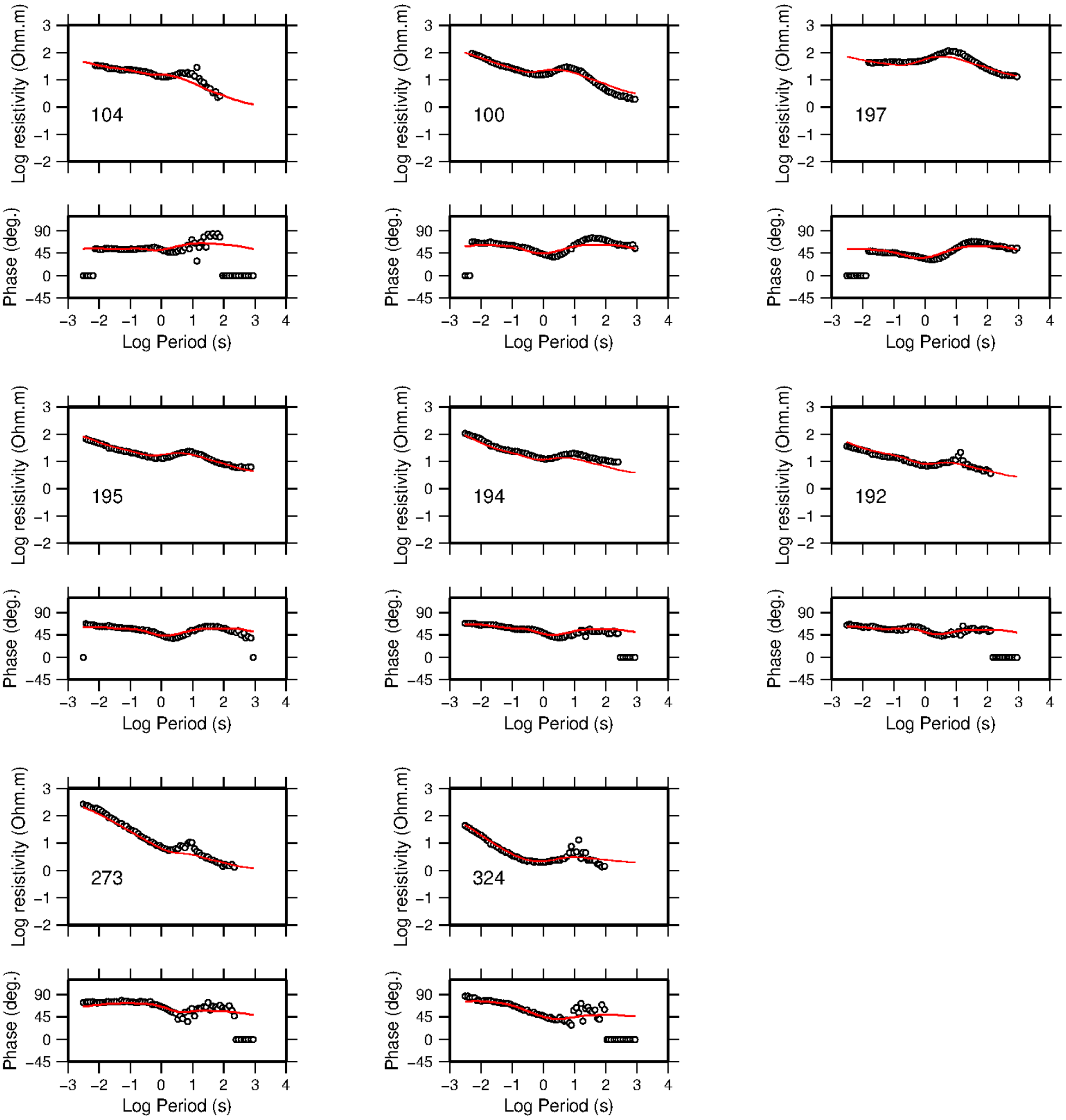

TE−mode in joint TMTE EW10_2 profile

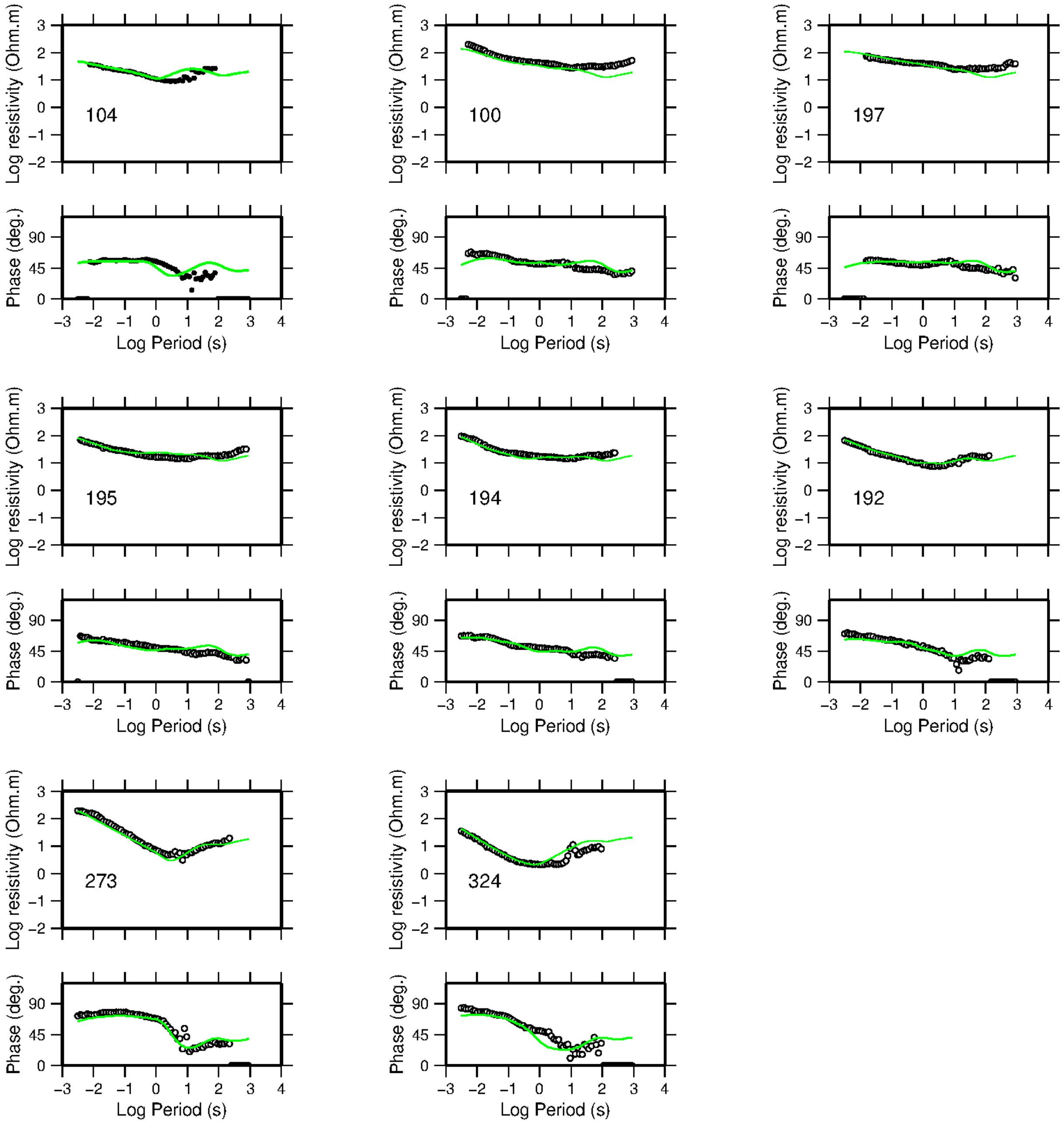

TM−mode in joint TMTE EW10_2 profile

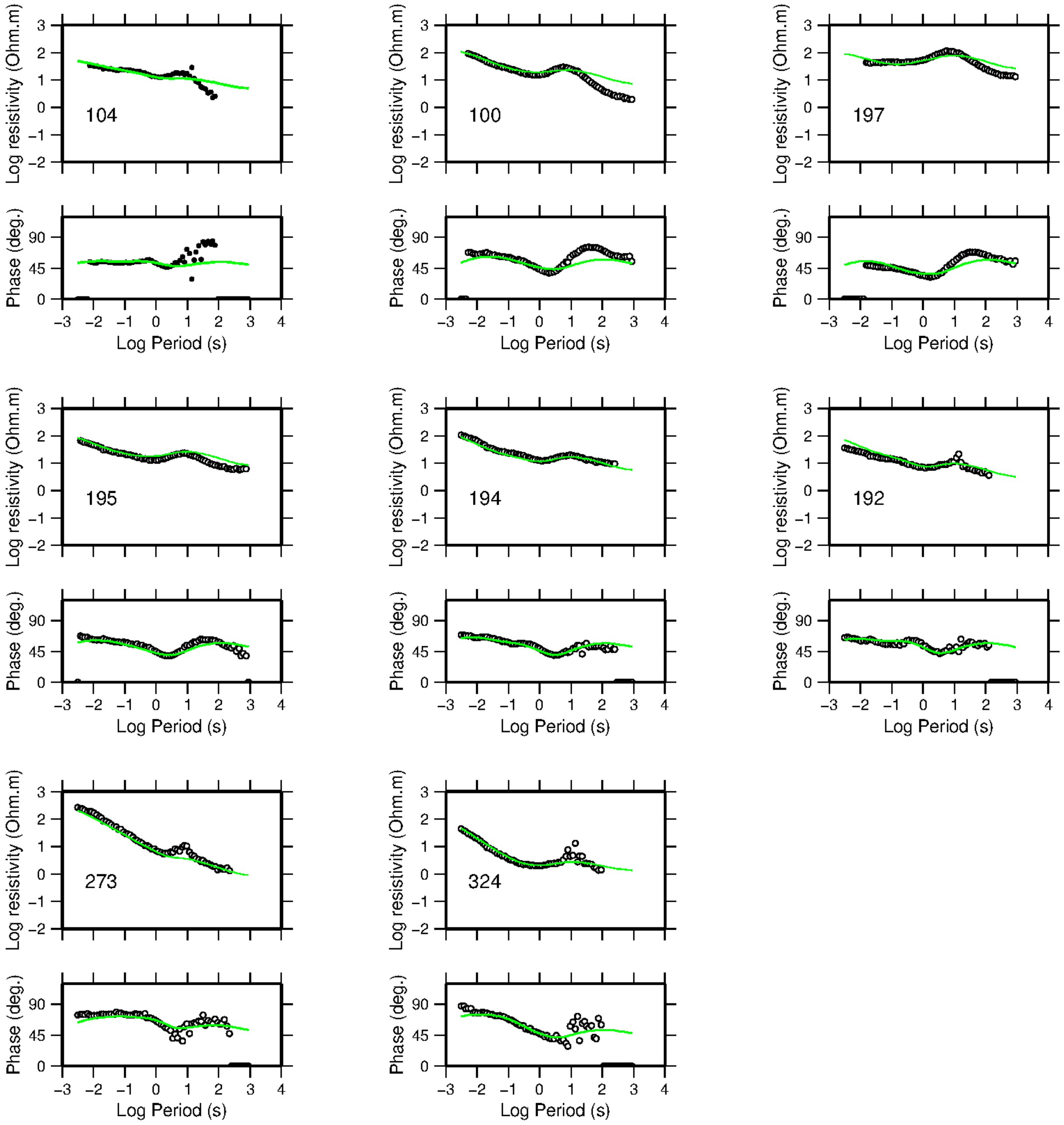

# TE−response EW10_1 Profile

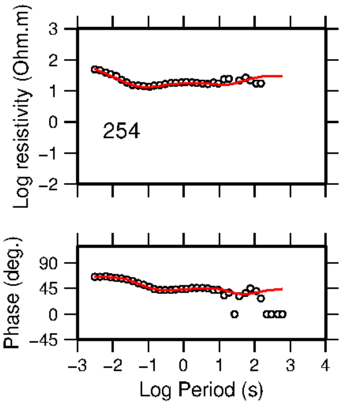

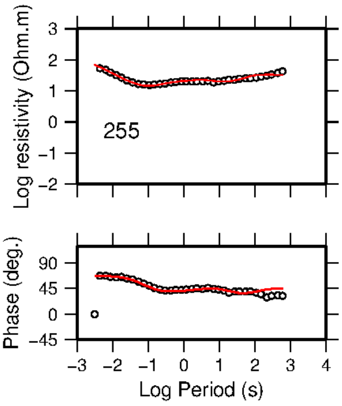

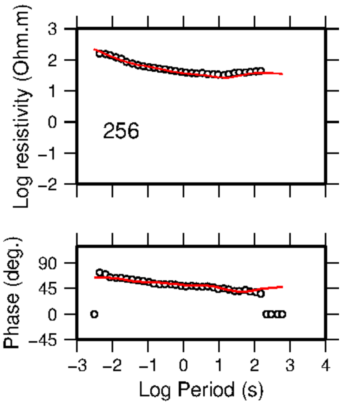

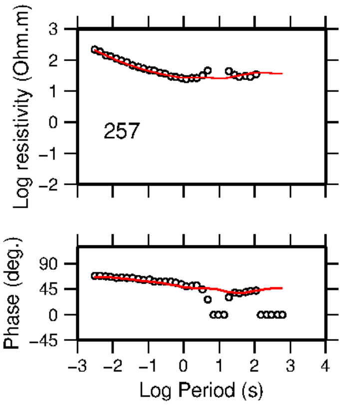

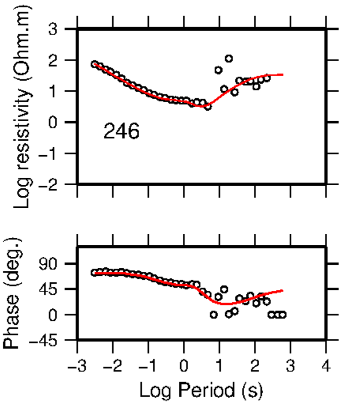

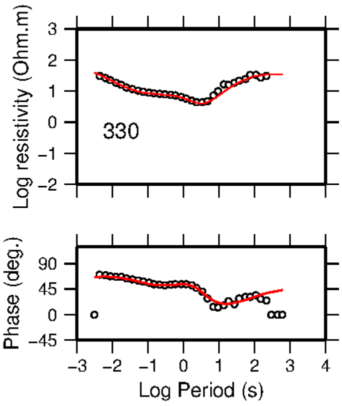

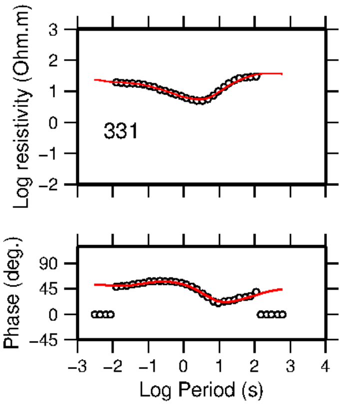

TM MODE−response EW10_1 Profile

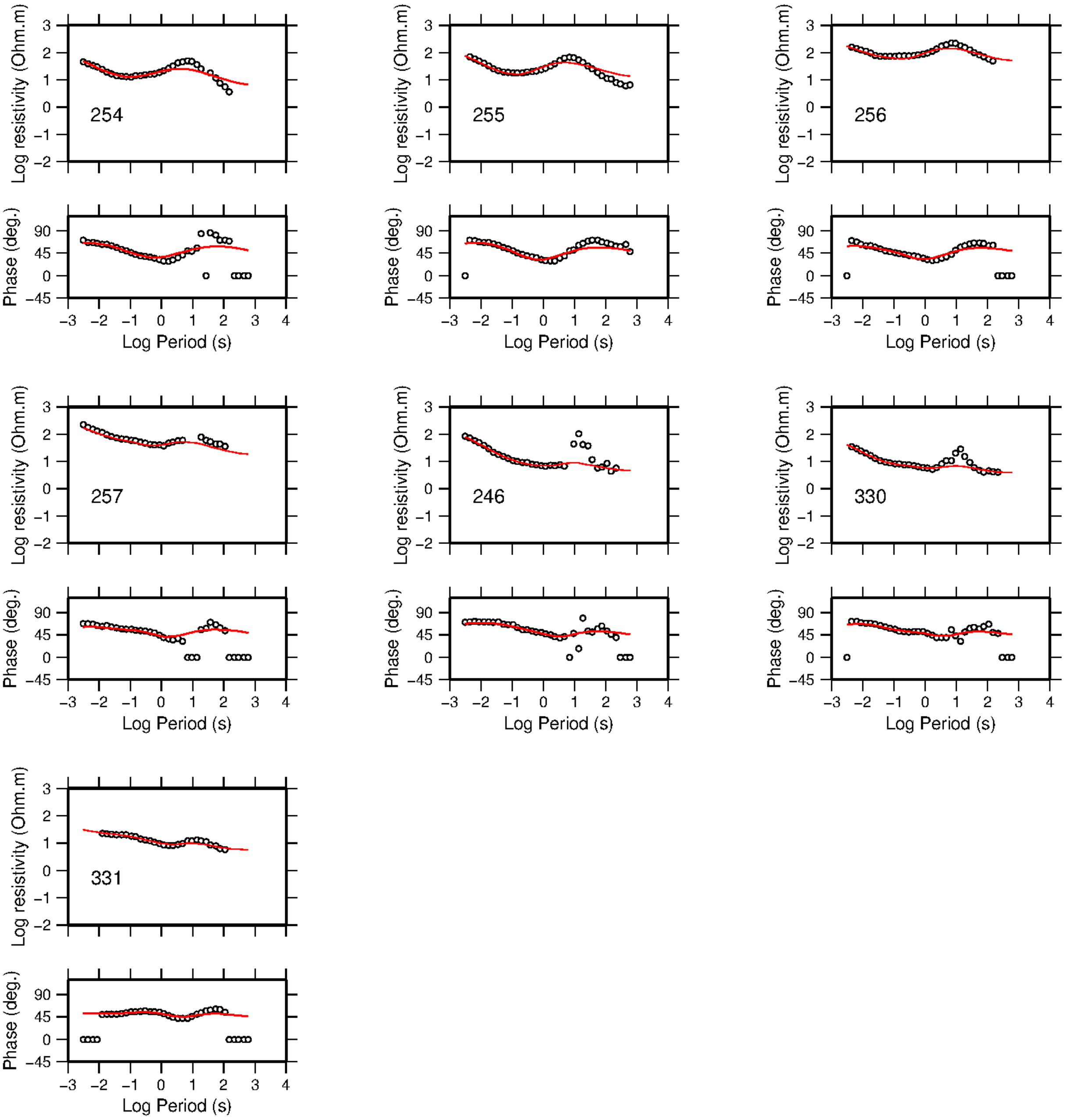

TE−mode in joint TMTE EW10_1 profile

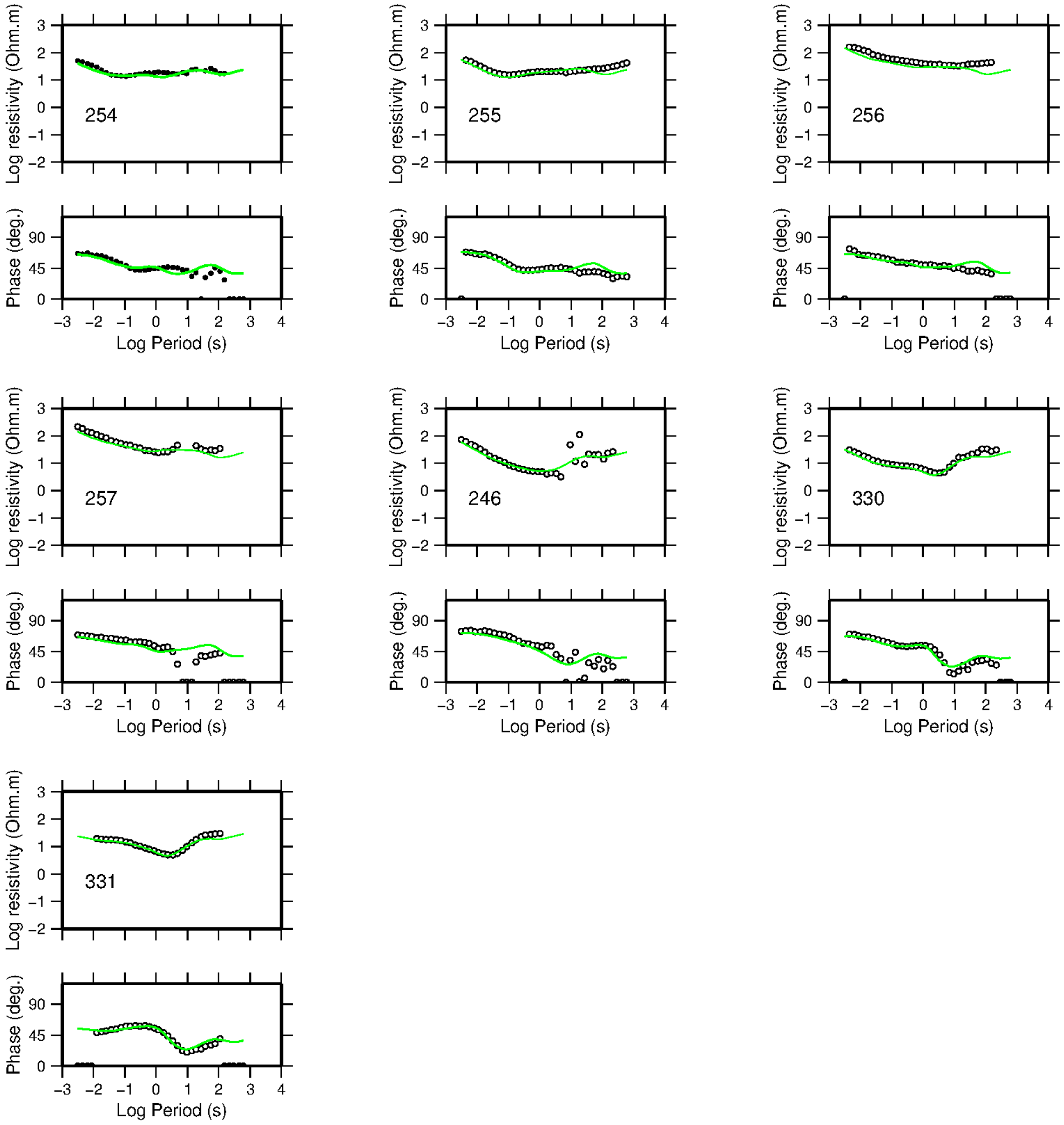

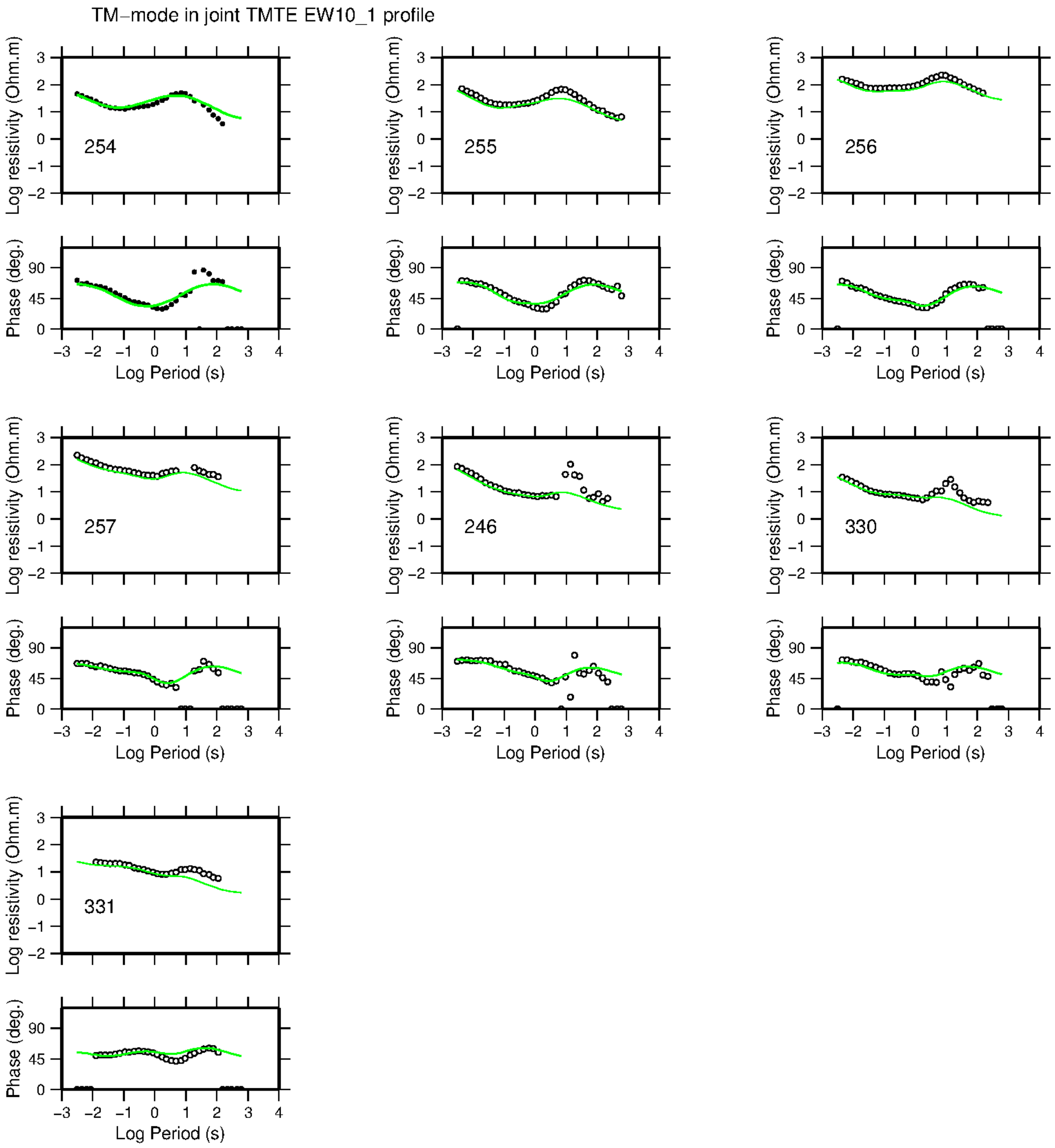
TM−mode in joint TMTE EW10_1 profile
Log resistivity (Ohm.m)
Phase (deg.)
Log Period (s)
254
255
256
257
246
330
331
3
2
1
0
−1
−2
90
45
0
−3
−2
−1
0
1
2
3
4

# APPENDIX IV: 3-D inversion data fit

A data fit for the resampled impedance data for all the inverted soundings presented as apparent resistivity and phase and the calculated response of the final model from the 10 ohm-m homogeneous half-space initial model. The data misfit is defined as the RMS (Root-Mean-Square) of the difference between the measured and calculated values of the off diagonal tensor elements (real and imaginary parts). The RMS misfit for the final model from the 10 ohm-m homogeneous half-space initial model was 1.5.

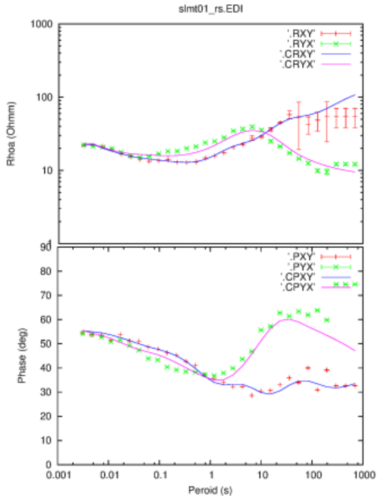
slmt01_rs.EDI

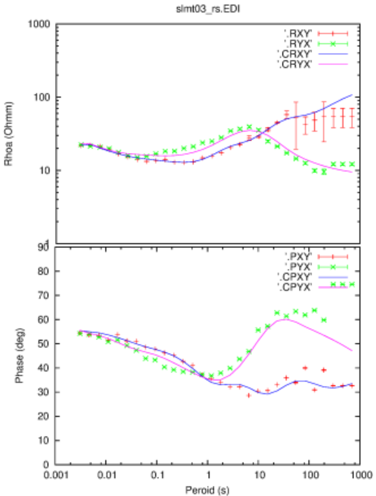
slmt03_rs.EDI

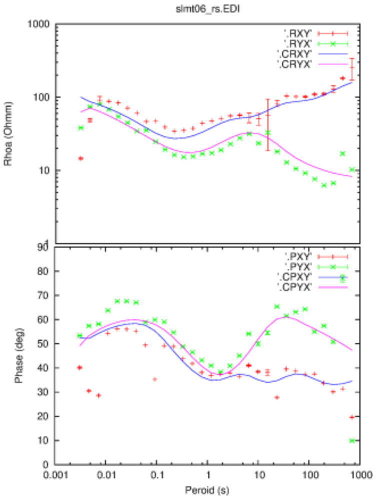
slmt06_rs.EDI

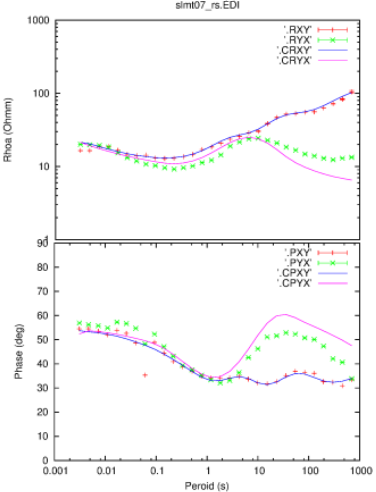
slmt07_rs.EDI

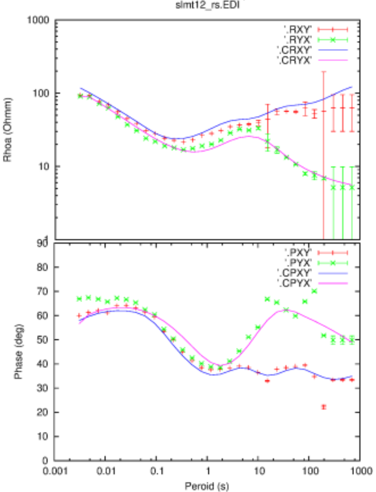
slmt12_rs.EDI

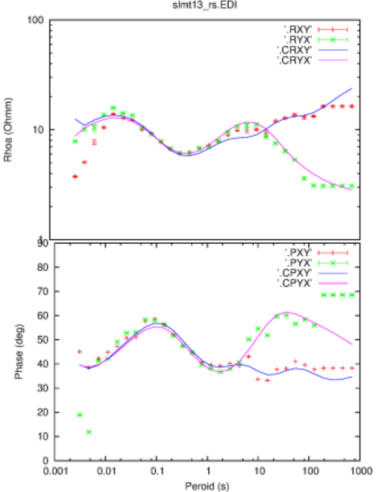
slmt13_rs.EDI

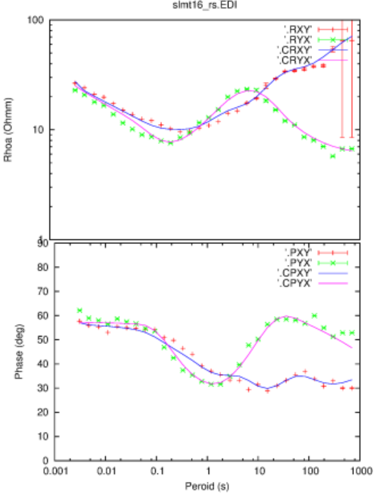
slmt16_rs.EDI

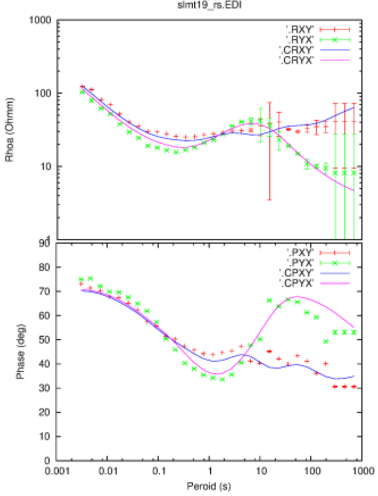
slmt19_rs.EDI

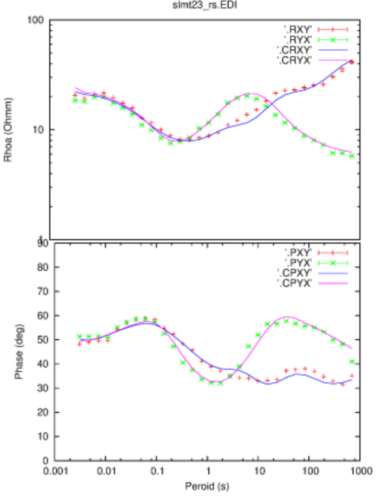
slmt23_rs.EDI

slmt25_rs.EDI

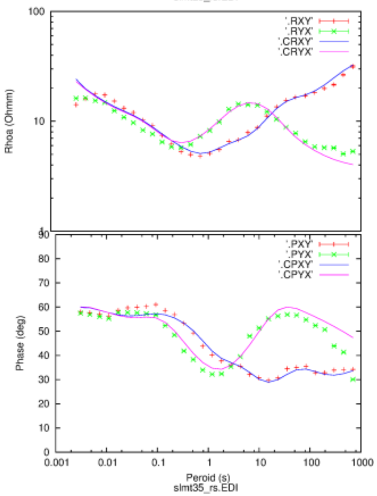

slmt26_rs.EDI

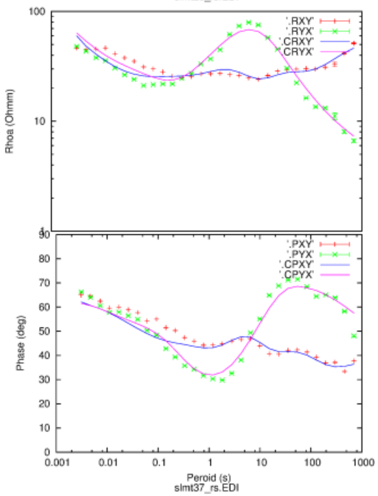

slmt34_rs.EDI

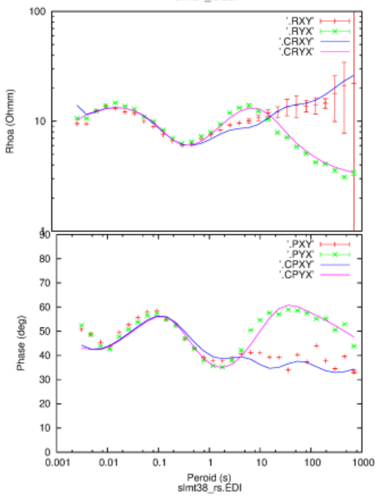

slmt35_rs.EDI

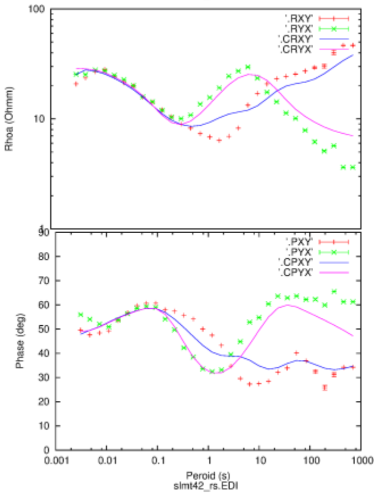

slmt37_rs.EDI

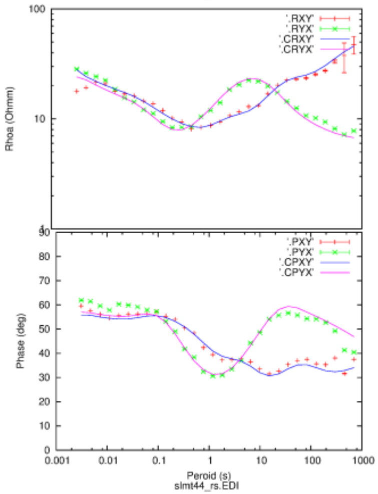

slmt38_rs.EDI

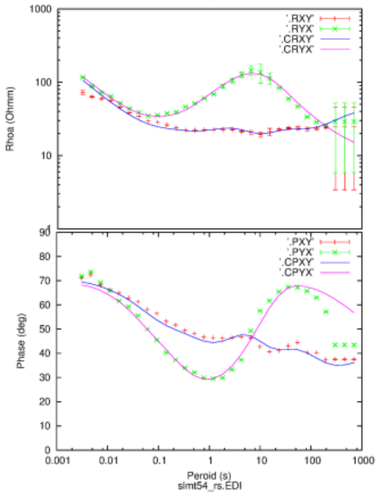

slmt42_rs.EDI

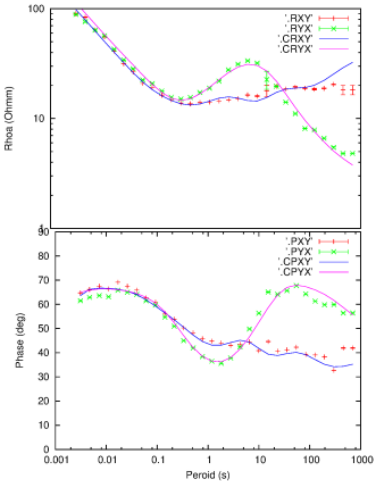

slmt44_rs.EDI

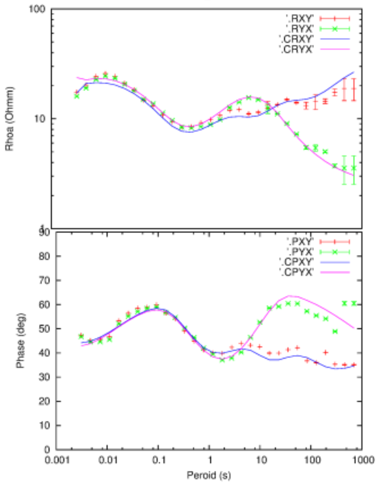

slmt54_rs.EDI

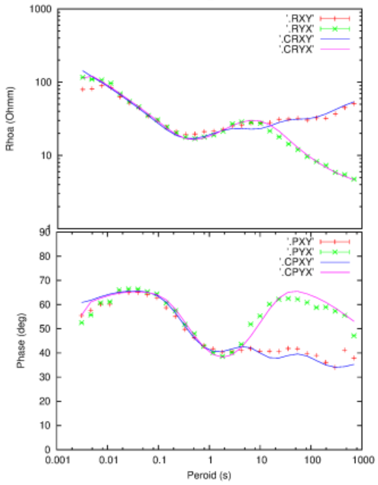

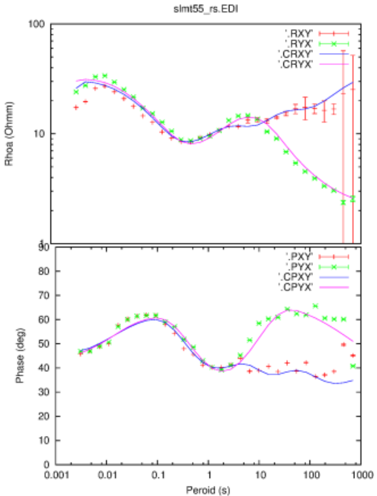
slmt55_rs.EDI
'.RXY'
'.RYX'
'.CRXY'
'.CRYX'
Rhoa (Ohmm)
100
10
1
'.PXY'
'.PYX'
'.CPXY'
'.CPYX'
Phase (deg)
90
80
70
60
50
40
30
20
10
0
0.001
0.01
0.1
1
10
100
1000
Peroid (s)

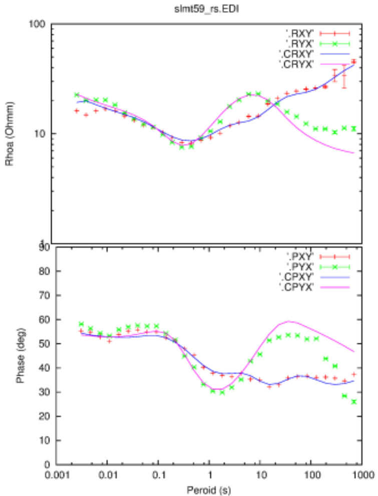
slmt59_rs.EDI
'.RXY'
'.RYX'
'.CRXY'
'.CRYX'
Rhoa (Ohmm)
100
10
1
'.PXY'
'.PYX'
'.CPXY'
'.CPYX'
Phase (deg)
90
80
70
60
50
40
30
20
10
0
0.001
0.01
0.1
1
10
100
1000
Peroid (s)

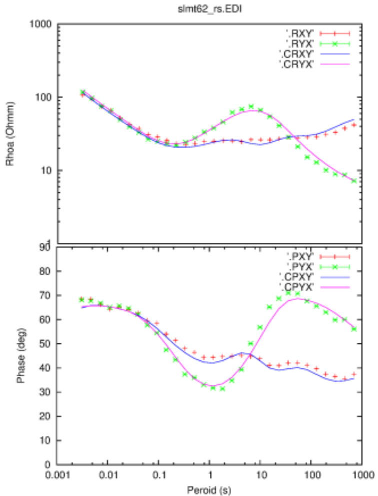
slmt62_rs.EDI
'.RXY'
'.RYX'
'.CRXY'
'.CRYX'
Rhoa (Ohmm)
1000
100
10
1
'.PXY'
'.PYX'
'.CPXY'
'.CPYX'
Phase (deg)
90
80
70
60
50
40
30
20
10
0
0.001
0.01
0.1
1
10
100
1000
Peroid (s)

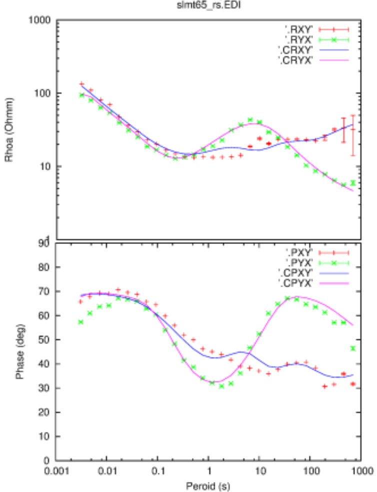
slmt65_rs.EDI
'.RXY'
'.RYX'
'.CRXY'
'.CRYX'
Rhoa (Ohmm)
1000
100
10
1
'.PXY'
'.PYX'
'.CPXY'
'.CPYX'
Phase (deg)
90
80
70
60
50
40
30
20
10
0
0.001
0.01
0.1
1
10
100
1000
Peroid (s)

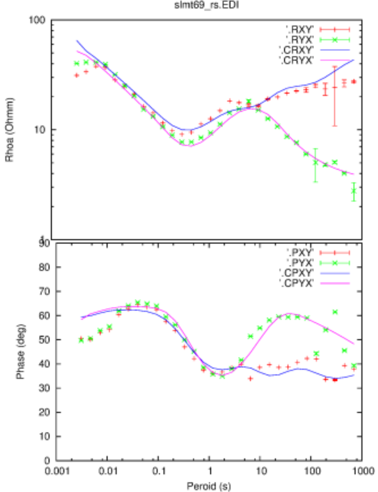
slmt69_rs.EDI
'.RXY'
'.RYX'
'.CRXY'
'.CRYX'
Rhoa (Ohmm)
100
10
1
'.PXY'
'.PYX'
'.CPXY'
'.CPYX'
Phase (deg)
90
80
70
60
50
40
30
20
10
0
0.001
0.01
0.1
1
10
100
1000
Peroid (s)

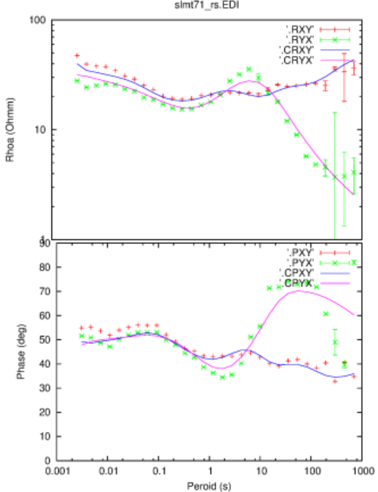
slmt71_rs.EDI
'.RXY'
'.RYX'
'.CRXY'
'.CRYX'
Rhoa (Ohmm)
100
10
1
'.PXY'
'.PYX'
'.CPXY'
'.CPYX'
Phase (deg)
90
80
70
60
50
40
30
20
10
0
0.001
0.01
0.1
1
10
100
1000
Peroid (s)

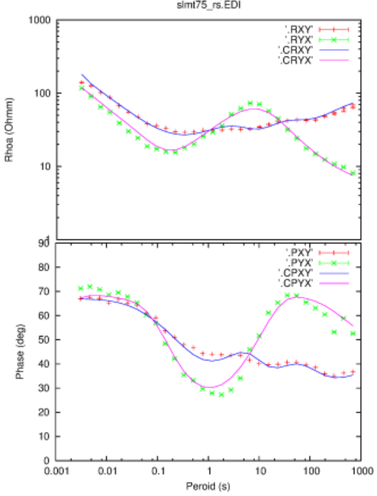
slmt75_rs.EDI
'.RXY'
'.RYX'
'.CRXY'
'.CRYX'
Rhoa (Ohmm)
1000
100
10
1
'.PXY'
'.PYX'
'.CPXY'
'.CPYX'
Phase (deg)
90
80
70
60
50
40
30
20
10
0
0.001
0.01
0.1
1
10
100
1000
Peroid (s)

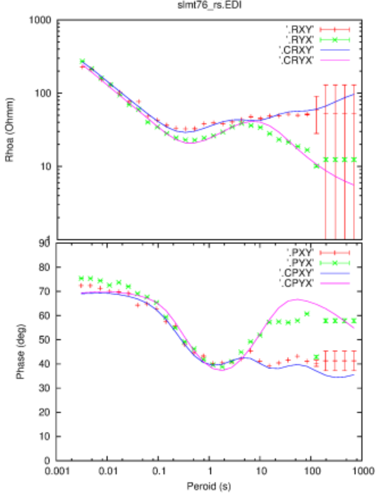
slmt76_rs.EDI
'.RXY'
'.RYX'
'.CRXY'
'.CRYX'
Rhoa (Ohmm)
1000
100
10
1
'.PXY'
'.PYX'
'.CPXY'
'.CPYX'
Phase (deg)
90
80
70
60
50
40
30
20
10
0
0.001
0.01
0.1
1
10
100
1000
Peroid (s)

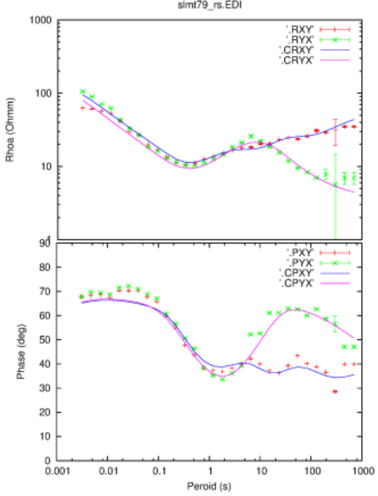
slmt79_rs.EDI
'.RXY'
'.RYX'
'.CRXY'
'.CRYX'
Rhoa (Ohmm)
1000
100
10
1
'.PXY'
'.PYX'
'.CPXY'
'.CPYX'
Phase (deg)
90
80
70
60
50
40
30
20
10
0
0.001
0.01
0.1
1
10
100
1000
Peroid (s)

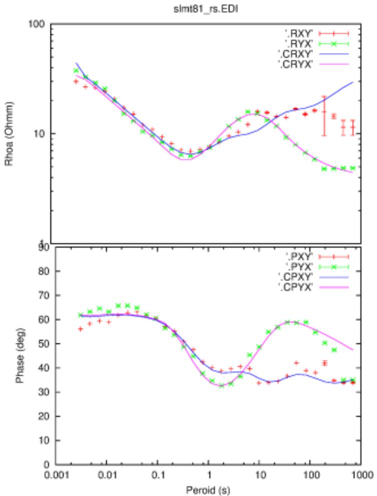
slmt81_rs.EDI
Rhoa (Ohmm)
'.RXY'
'.RYX'
'.CRXY'
'.CRYX'
Phase (deg)
'.PXY'
'.PYX'
'.CPXY'
'.CPYX'
Peroid (s)

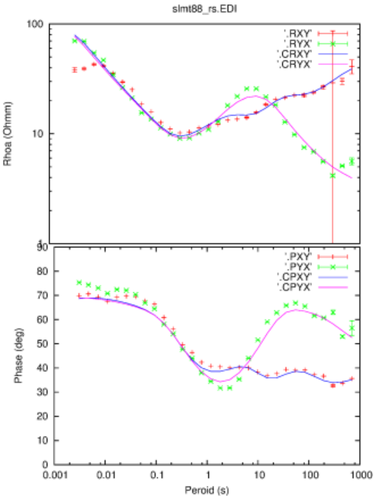
slmt88_rs.EDI
Rhoa (Ohmm)
'.RXY'
'.RYX'
'.CRXY'
'.CRYX'
Phase (deg)
'.PXY'
'.PYX'
'.CPXY'
'.CPYX'
Peroid (s)

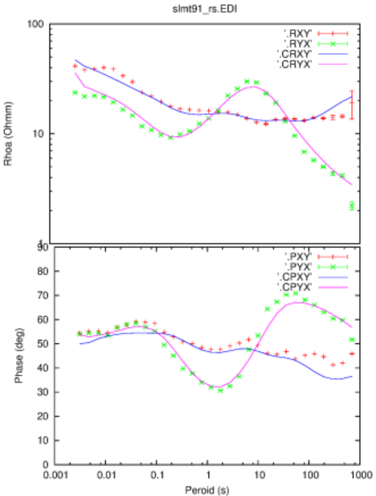
slmt91_rs.EDI
Rhoa (Ohmm)
'.RXY'
'.RYX'
'.CRXY'
'.CRYX'
Phase (deg)
'.PXY'
'.PYX'
'.CPXY'
'.CPYX'
Peroid (s)

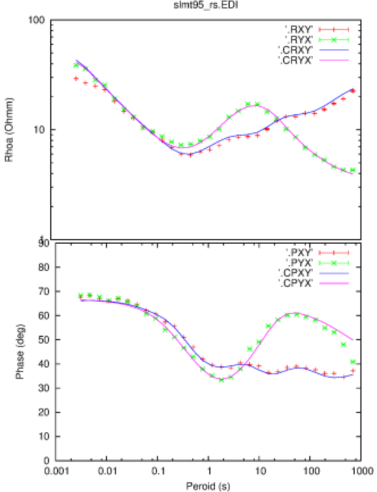
slmt95_rs.EDI
Rhoa (Ohmm)
'.RXY'
'.RYX'
'.CRXY'
'.CRYX'
Phase (deg)
'.PXY'
'.PYX'
'.CPXY'
'.CPYX'
Peroid (s)

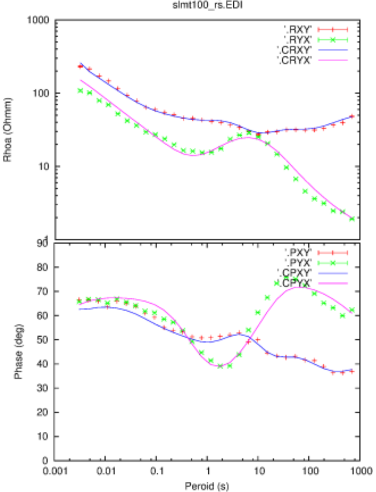
slmt100_rs.EDI
Rhoa (Ohmm)
'.RXY'
'.RYX'
'.CRXY'
'.CRYX'
Phase (deg)
'.PXY'
'.PYX'
'.CPXY'
'.CPYX'
Peroid (s)

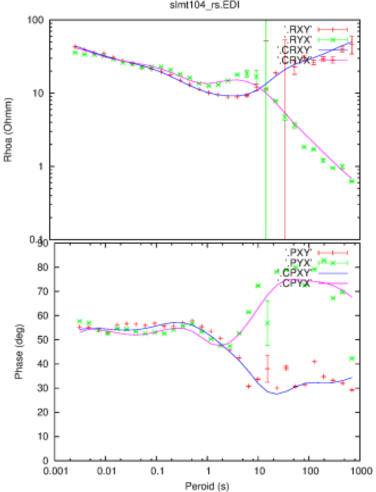
slmt104_rs.EDI
Rhoa (Ohmm)
'.RXY'
'.RYX'
'.CRXY'
'.CRYX'
Phase (deg)
'.PXY'
'.PYX'
'.CPXY'
'.CPYX'
Peroid (s)

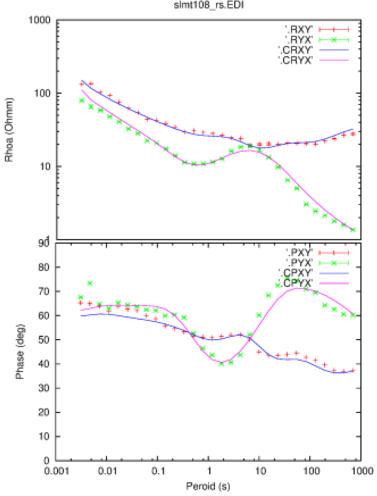
slmt108_rs.EDI
Rhoa (Ohmm)
'.RXY'
'.RYX'
'.CRXY'
'.CRYX'
Phase (deg)
'.PXY'
'.PYX'
'.CPXY'
'.CPYX'
Peroid (s)

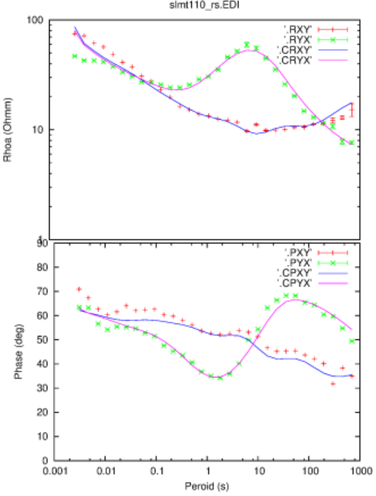
slmt110_rs.EDI
Rhoa (Ohmm)
'.RXY'
'.RYX'
'.CRXY'
'.CRYX'
Phase (deg)
'.PXY'
'.PYX'
'.CPXY'
'.CPYX'
Peroid (s)

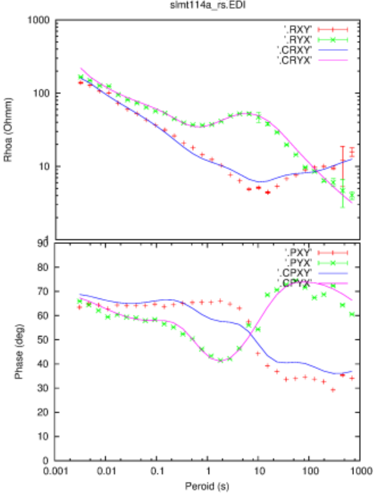
slmt114a_rs.EDI
Rhoa (Ohmm)
'.RXY'
'.RYX'
'.CRXY'
'.CRYX'
Phase (deg)
'.PXY'
'.PYX'
'.CPXY'
'.CPYX'
Peroid (s)

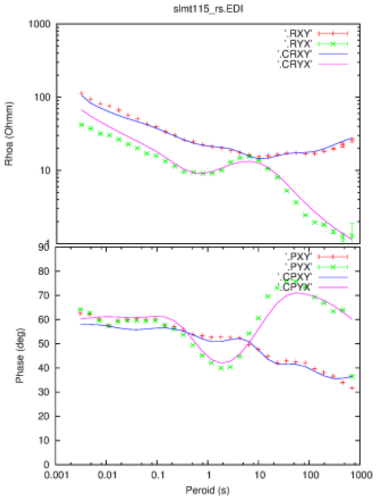
slmt115_rs.EDI
Rhoa (Ohmm)
Phase (deg)
Peroid (s)
'.RXY'
'.RYX'
'.CRXY'
'.CRYX'
'.PXY'
'.PYX'
'.CPXY'
'.CPYX'

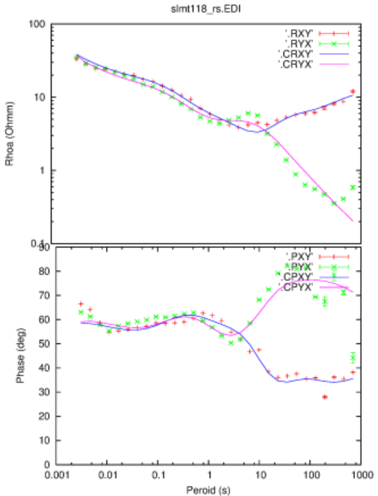
slmt118_rs.EDI
Rhoa (Ohmm)
Phase (deg)
Peroid (s)
'.RXY'
'.RYX'
'.CRXY'
'.CRYX'
'.PXY'
'.PYX'
'.CPXY'
'.CPYX'

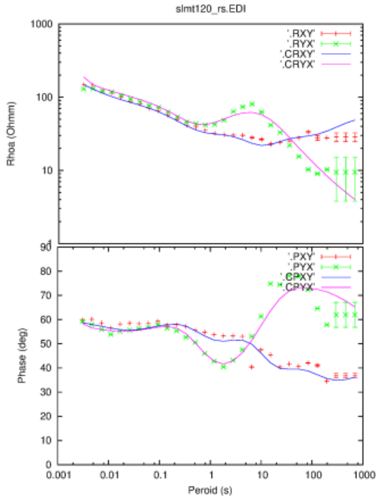
slmt120_rs.EDI
Rhoa (Ohmm)
Phase (deg)
Peroid (s)
'.RXY'
'.RYX'
'.CRXY'
'.CRYX'
'.PXY'
'.PYX'
'.CPXY'
'.CPYX'

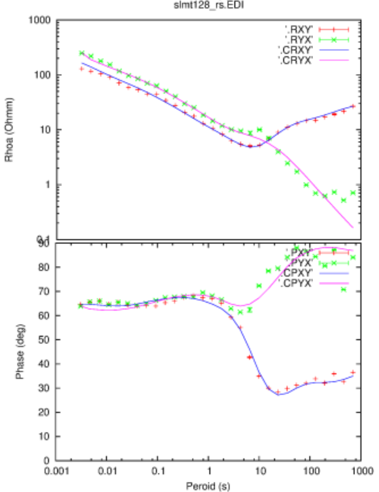
slmt128_rs.EDI
Rhoa (Ohmm)
Phase (deg)
Peroid (s)
'.RXY'
'.RYX'
'.CRXY'
'.CRYX'
'.PXY'
'.PYX'
'.CPXY'
'.CPYX'

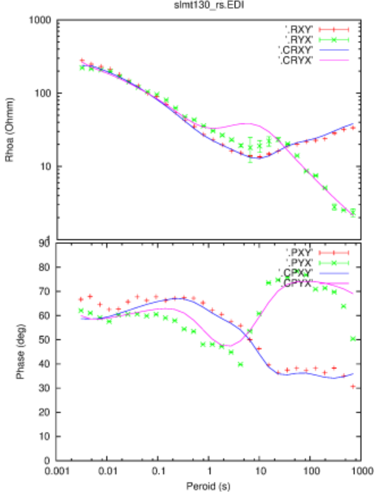
slmt130_rs.EDI
Rhoa (Ohmm)
Phase (deg)
Peroid (s)
'.RXY'
'.RYX'
'.CRXY'
'.CRYX'
'.PXY'
'.PYX'
'.CPXY'
'.CPYX'

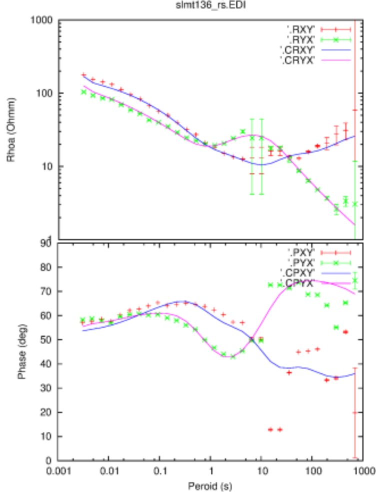
slmt136_rs.EDI
Rhoa (Ohmm)
Phase (deg)
Peroid (s)
'.RXY'
'.RYX'
'.CRXY'
'.CRYX'
'.PXY'
'.PYX'
'.CPXY'
'.CPYX'

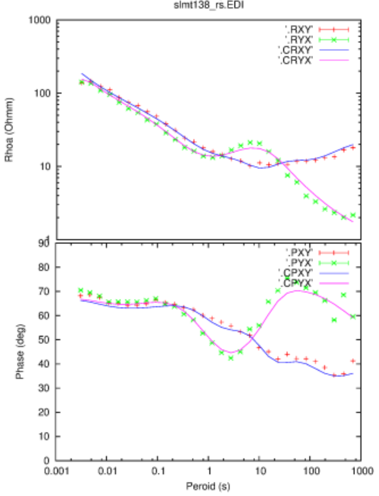
slmt138_rs.EDI
Rhoa (Ohmm)
Phase (deg)
Peroid (s)
'.RXY'
'.RYX'
'.CRXY'
'.CRYX'
'.PXY'
'.PYX'
'.CPXY'
'.CPYX'

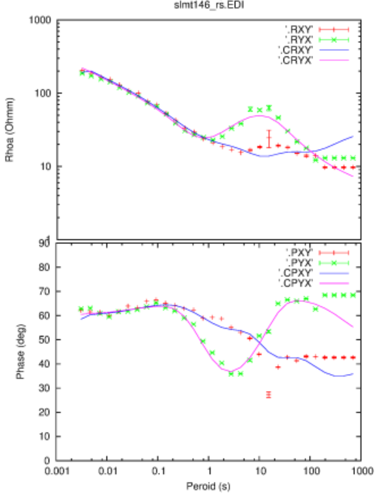
slmt146_rs.EDI
Rhoa (Ohmm)
Phase (deg)
Peroid (s)
'.RXY'
'.RYX'
'.CRXY'
'.CRYX'
'.PXY'
'.PYX'
'.CPXY'
'.CPYX'

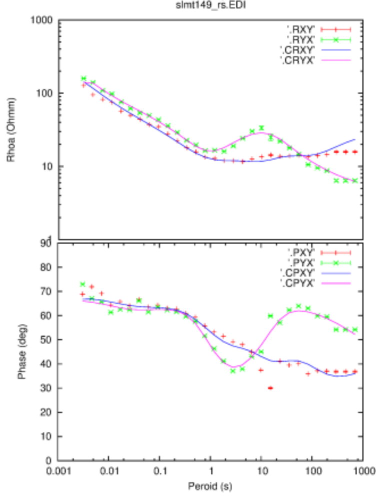
slmt149_rs.EDI
Rhoa (Ohmm)
Phase (deg)
Peroid (s)
'.RXY'
'.RYX'
'.CRXY'
'.CRYX'
'.PXY'
'.PYX'
'.CPXY'
'.CPYX'

slmt153_rs.EDI

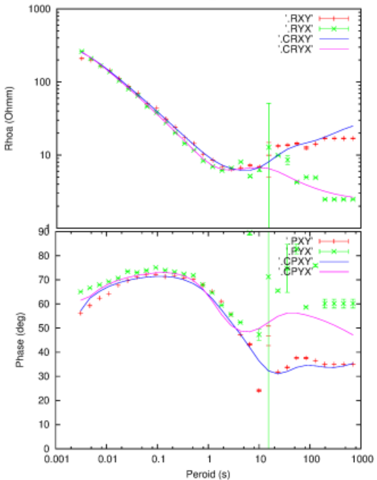

slmt157_rs.EDI

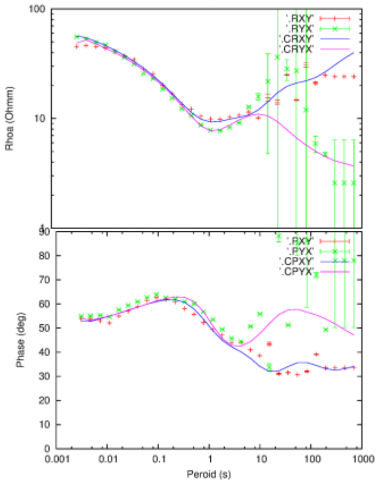

slmt164_rs.EDI

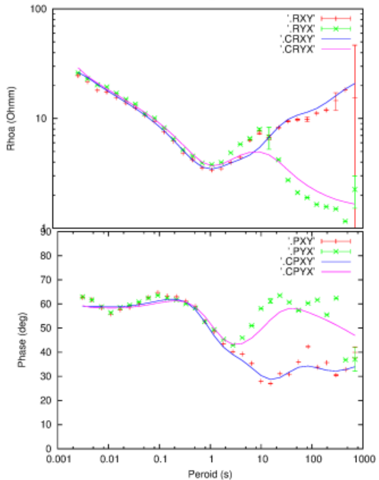

slmt166_rs.EDI

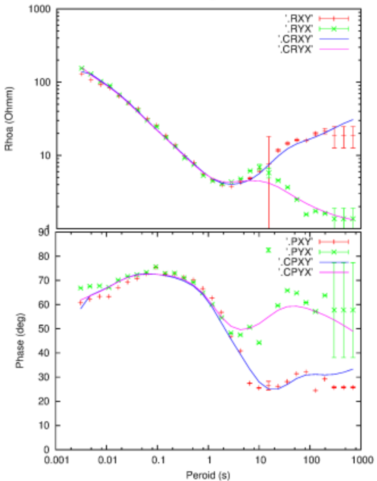

slmt167_rs.EDI

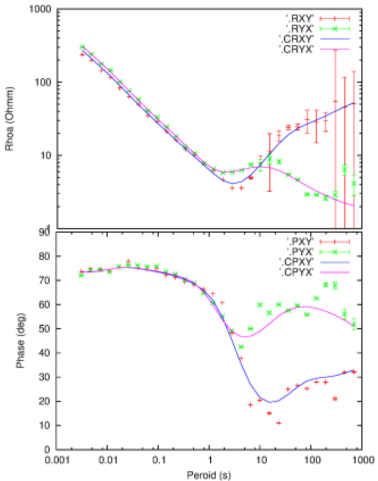

slmt169_rs.EDI

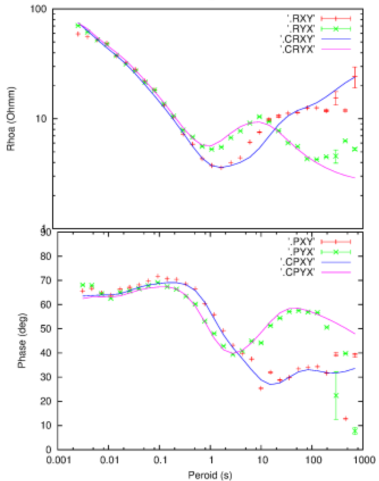

slmt170_rs.EDI

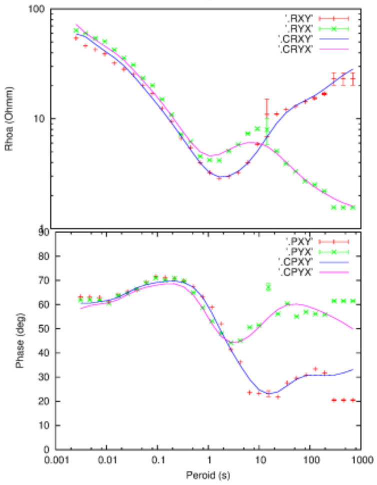

slmt171_rs.EDI

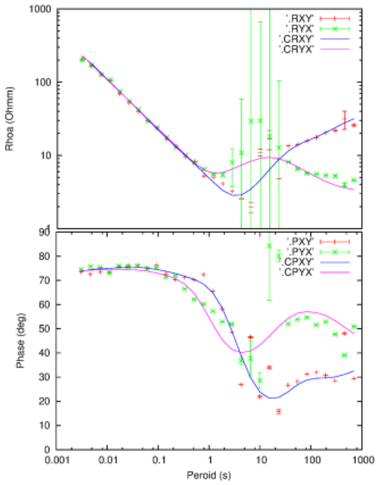

slmt172_rs.EDI

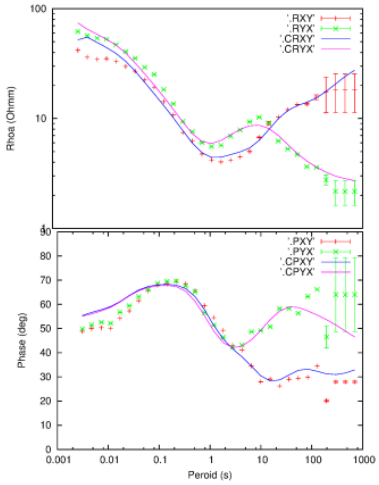

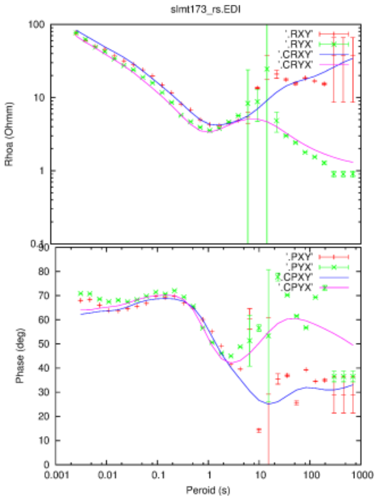
slmt173_rs.EDI
'.RXY'
'.RYX'
'.CRXY'
'.CRYX'
Rhoa (Ohmm)
'.PXY'
'.PYX'
'.CPXY'
'.CPYX'
Phase (deg)
Peroid (s)

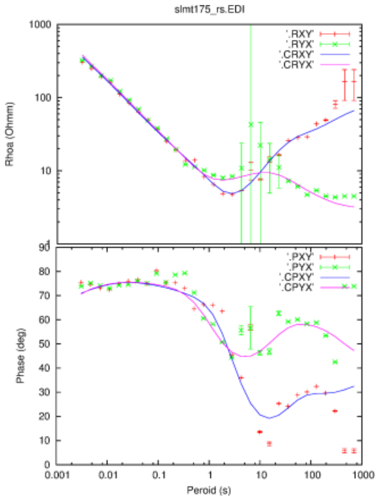
slmt175_rs.EDI
'.RXY'
'.RYX'
'.CRXY'
'.CRYX'
Rhoa (Ohmm)
'.PXY'
'.PYX'
'.CPXY'
'.CPYX'
Phase (deg)
Peroid (s)

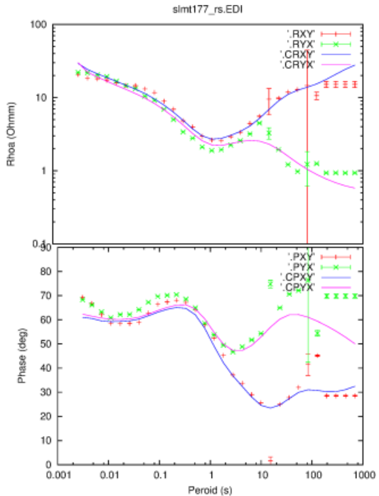
slmt177_rs.EDI
'.RXY'
'.RYX'
'.CRXY'
'.CRYX'
Rhoa (Ohmm)
'.PXY'
'.PYX'
'.CPXY'
'.CPYX'
Phase (deg)
Peroid (s)

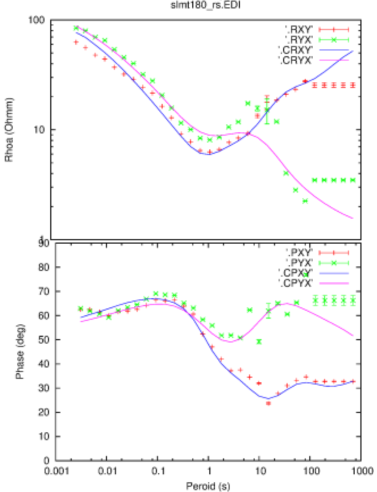
slmt180_rs.EDI
'.RXY'
'.RYX'
'.CRXY'
'.CRYX'
Rhoa (Ohmm)
'.PXY'
'.PYX'
'.CPXY'
'.CPYX'
Phase (deg)
Peroid (s)

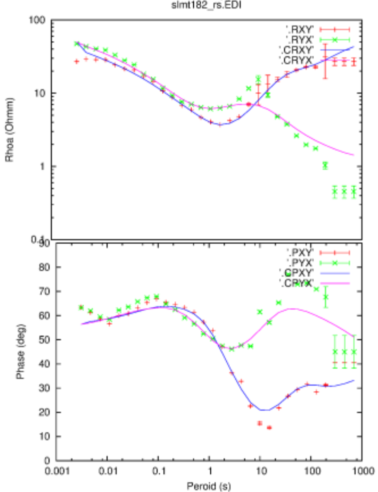
slmt182_rs.EDI
'.RXY'
'.RYX'
'.CRXY'
'.CRYX'
Rhoa (Ohmm)
'.PXY'
'.PYX'
'.CPXY'
'.CPYX'
Phase (deg)
Peroid (s)

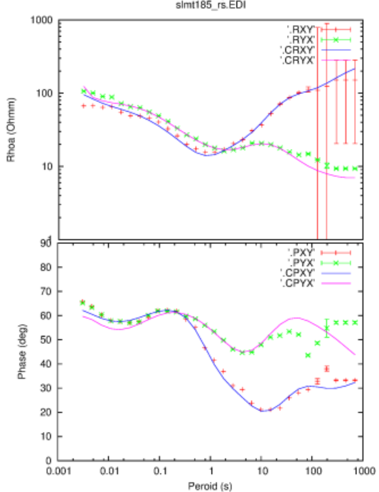
slmt185_rs.EDI
'.RXY'
'.RYX'
'.CRXY'
'.CRYX'
Rhoa (Ohmm)
'.PXY'
'.PYX'
'.CPXY'
'.CPYX'
Phase (deg)
Peroid (s)

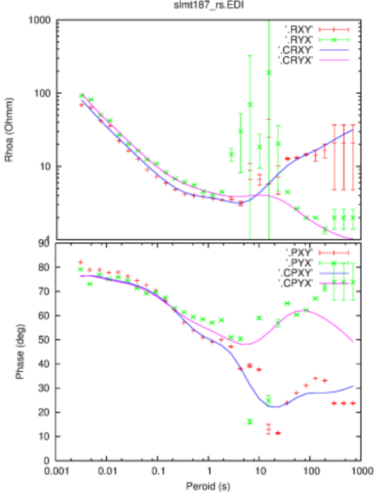
slmt187_rs.EDI
'.RXY'
'.RYX'
'.CRXY'
'.CRYX'
Rhoa (Ohmm)
'.PXY'
'.PYX'
'.CPXY'
'.CPYX'
Phase (deg)
Peroid (s)

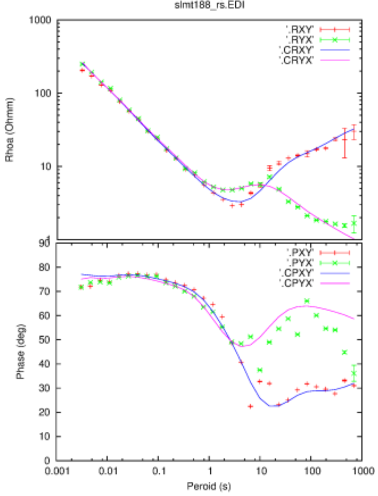
slmt188_rs.EDI
'.RXY'
'.RYX'
'.CRXY'
'.CRYX'
Rhoa (Ohmm)
'.PXY'
'.PYX'
'.CPXY'
'.CPYX'
Phase (deg)
Peroid (s)

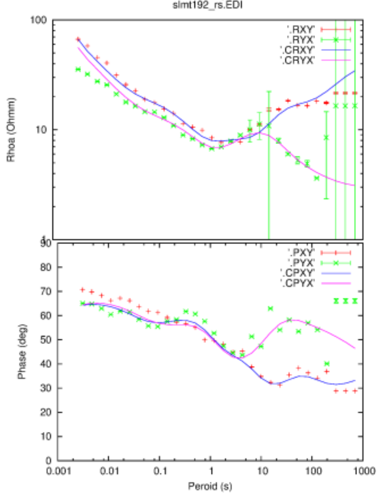
slmt192_rs.EDI
'.RXY'
'.RYX'
'.CRXY'
'.CRYX'
Rhoa (Ohmm)
'.PXY'
'.PYX'
'.CPXY'
'.CPYX'
Phase (deg)
Peroid (s)

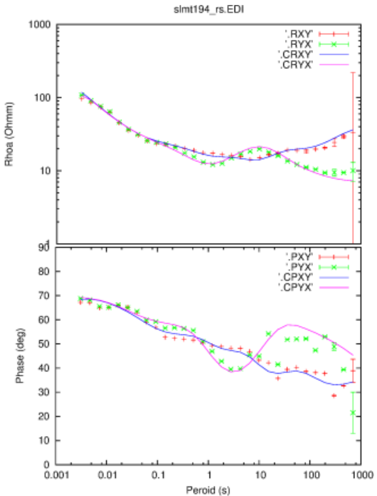
slmt194_rs.EDI

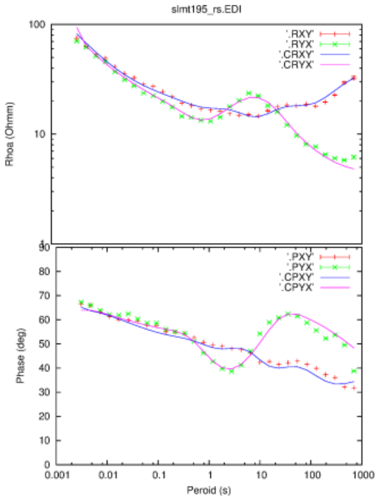
slmt195_rs.EDI

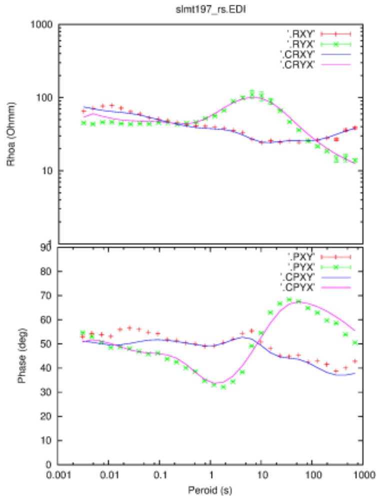
slmt197_rs.EDI

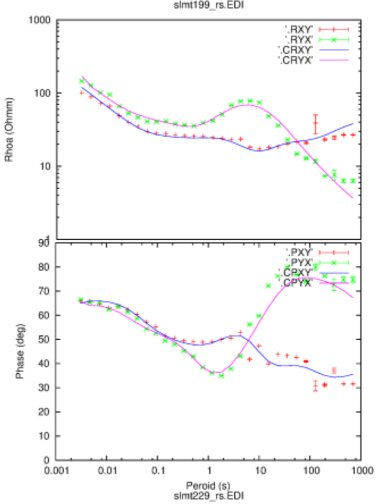
slmt199_rs.EDI

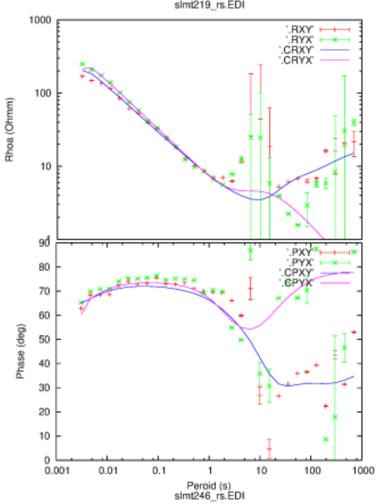
slmt219_rs.EDI

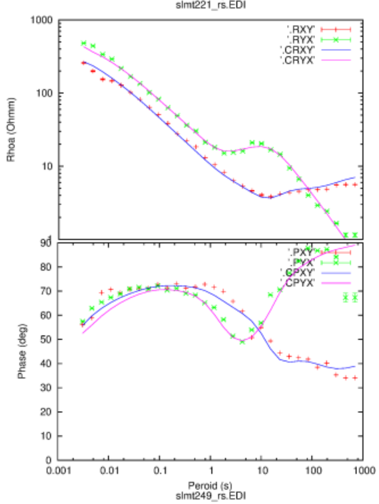
slmt221_rs.EDI

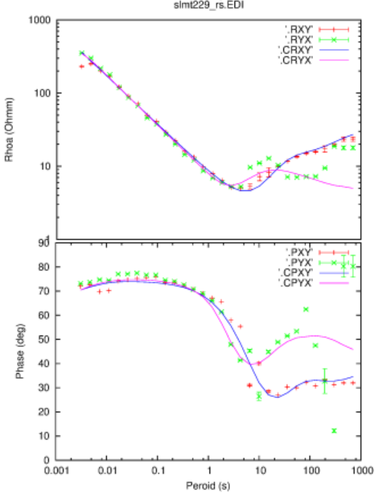
slmt229_rs.EDI

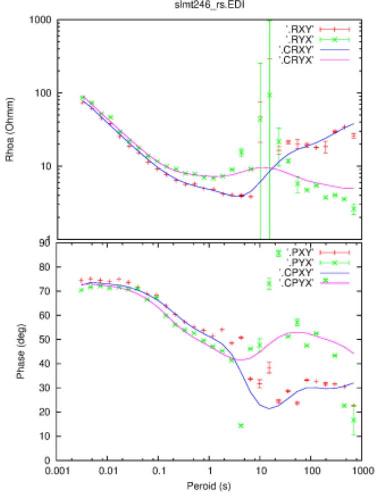
slmt246_rs.EDI

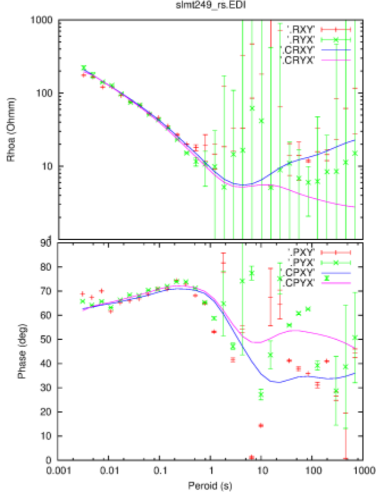
slmt249_rs.EDI

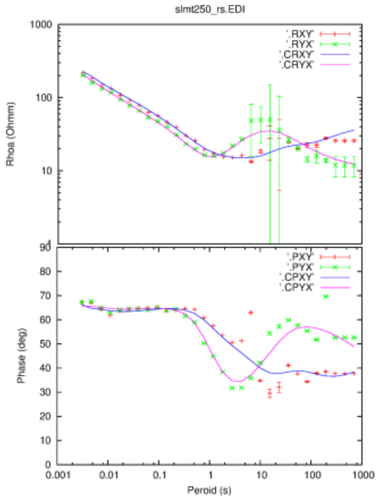
slmt250_rs.EDI
'.RXY'
'.RYX'
'.CRXY'
'.CRYX'
'.PXY'
'.PYX'
'.CPXY'
'.CPYX'
Rhoa (Ohmm)
Phase (deg)
Peroid (s)
0.001
0.01
0.1
1
10
100
1000

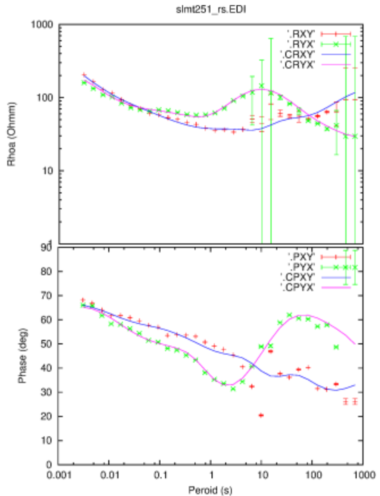
slmt251_rs.EDI
'.RXY'
'.RYX'
'.CRXY'
'.CRYX'
'.PXY'
'.PYX'
'.CPXY'
'.CPYX'
Rhoa (Ohmm)
Phase (deg)
Peroid (s)

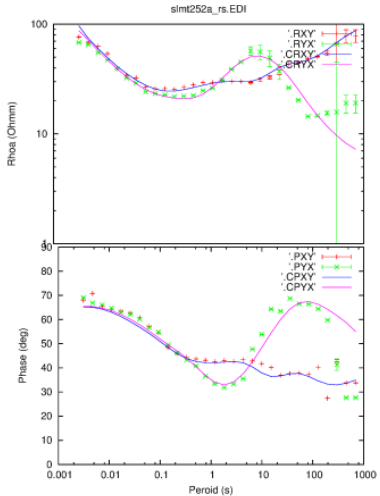
slmt252a_rs.EDI
'.RXY'
'.RYX'
'.CRXY'
'.CRYX'
'.PXY'
'.PYX'
'.CPXY'
'.CPYX'
Rhoa (Ohmm)
Phase (deg)
Peroid (s)

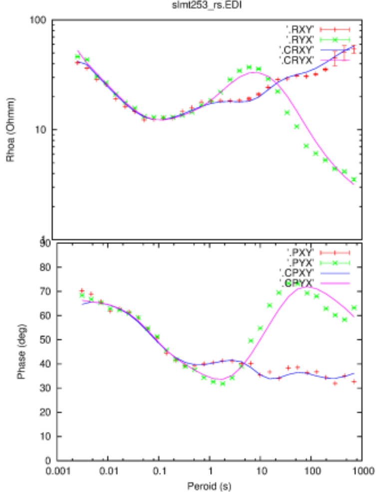
slmt253_rs.EDI
'.RXY'
'.RYX'
'.CRXY'
'.CRYX'
'.PXY'
'.PYX'
'.CPXY'
'.CPYX'
Rhoa (Ohmm)
Phase (deg)
Peroid (s)

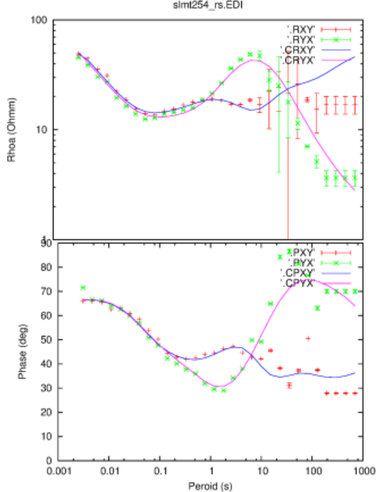
slmt254_rs.EDI
'.RXY'
'.RYX'
'.CRXY'
'.CRYX'
'.PXY'
'.PYX'
'.CPXY'
'.CPYX'
Rhoa (Ohmm)
Phase (deg)
Peroid (s)

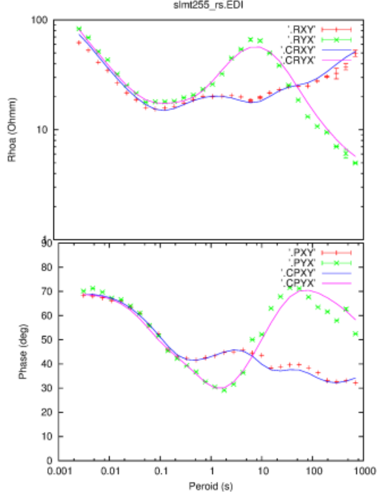
slmt255_rs.EDI
'.RXY'
'.RYX'
'.CRXY'
'.CRYX'
'.PXY'
'.PYX'
'.CPXY'
'.CPYX'
Rhoa (Ohmm)
Phase (deg)
Peroid (s)

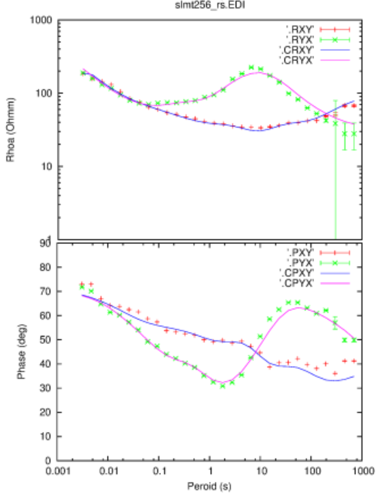
slmt256_rs.EDI
'.RXY'
'.RYX'
'.CRXY'
'.CRYX'
'.PXY'
'.PYX'
'.CPXY'
'.CPYX'
Rhoa (Ohmm)
Phase (deg)
Peroid (s)

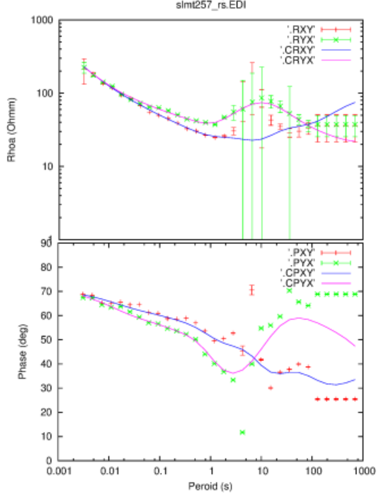
slmt257_rs.EDI
'.RXY'
'.RYX'
'.CRXY'
'.CRYX'
'.PXY'
'.PYX'
'.CPXY'
'.CPYX'
Rhoa (Ohmm)
Phase (deg)
Peroid (s)

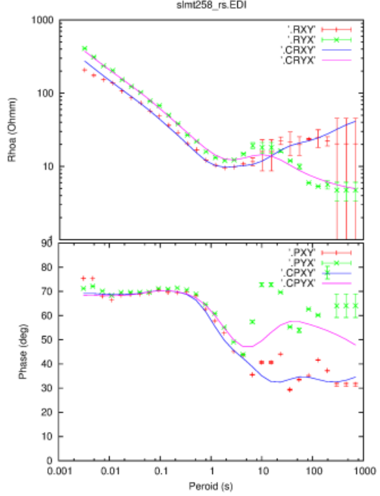
slmt258_rs.EDI
'.RXY'
'.RYX'
'.CRXY'
'.CRYX'
'.PXY'
'.PYX'
'.CPXY'
'.CPYX'
Rhoa (Ohmm)
Phase (deg)
Peroid (s)

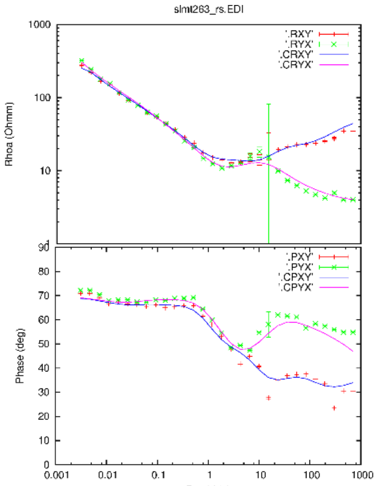
slmt263_rs.EDI
Rhoa (Ohmm)
1000
100
10
1
'.RXY'
'.RYX'
'.CRXY'
'.CRYX'
Phase (deg)
90
80
70
60
50
40
30
20
10
0
'.PXY'
'.PYX'
'.CPXY'
'.CPYX'
0.001
0.01
0.1
1
10
100
1000
Peroid (s)

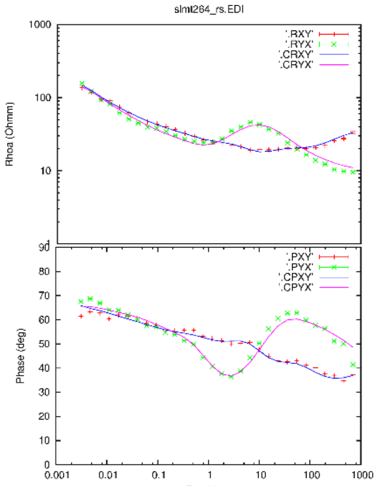
slmt264_rs.EDI
Rhoa (Ohmm)
1000
100
10
1
'.RXY'
'.RYX'
'.CRXY'
'.CRYX'
Phase (deg)
90
80
70
60
50
40
30
20
10
0
'.PXY'
'.PYX'
'.CPXY'
'.CPYX'
0.001
0.01
0.1
1
10
100
1000
Peroid (s)

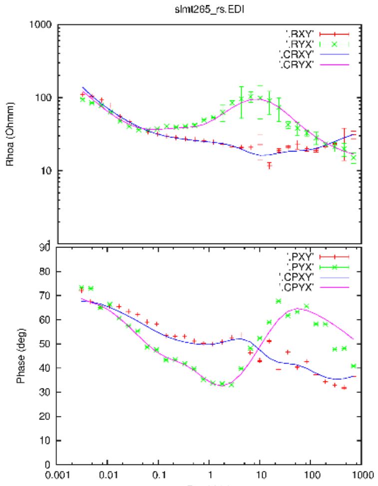
slmt265_rs.EDI
Rhoa (Ohmm)
1000
100
10
1
'.RXY'
'.RYX'
'.CRXY'
'.CRYX'
Phase (deg)
90
80
70
60
50
40
30
20
10
0
'.PXY'
'.PYX'
'.CPXY'
'.CPYX'
0.001
0.01
0.1
1
10
100
1000
Peroid (s)

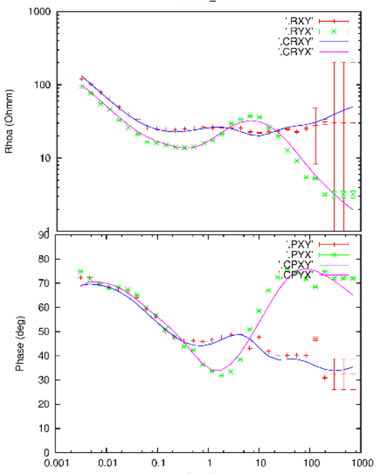
slmt266_rs.EDI
Rhoa (Ohmm)
1000
100
10
1
'.RXY'
'.RYX'
'.CRXY'
'.CRYX'
Phase (deg)
90
80
70
60
50
40
30
20
10
0
'.PXY'
'.PYX'
'.CPXY'
'.CPYX'
0.001
0.01
0.1
1
10
100
1000
Peroid (s)

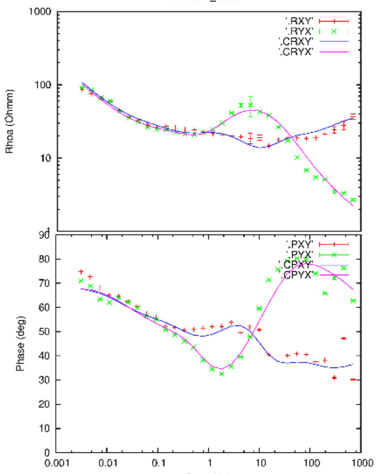
slmt267_rs.EDI
Rhoa (Ohmm)
1000
100
10
1
'.RXY'
'.RYX'
'.CRXY'
'.CRYX'
Phase (deg)
90
80
70
60
50
40
30
20
10
0
'.PXY'
'.PYX'
'.CPXY'
'.CPYX'
0.001
0.01
0.1
1
10
100
1000
Peroid (s)

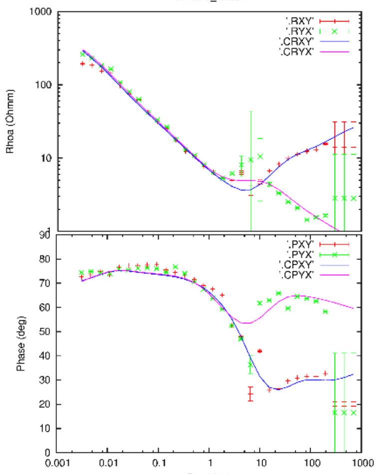
slmt273_rs.EDI
Rhoa (Ohmm)
1000
100
10
1
'.RXY'
'.RYX'
'.CRXY'
'.CRYX'
Phase (deg)
90
80
70
60
50
40
30
20
10
0
'.PXY'
'.PYX'
'.CPXY'
'.CPYX'
0.001
0.01
0.1
1
10
100
1000
Peroid (s)

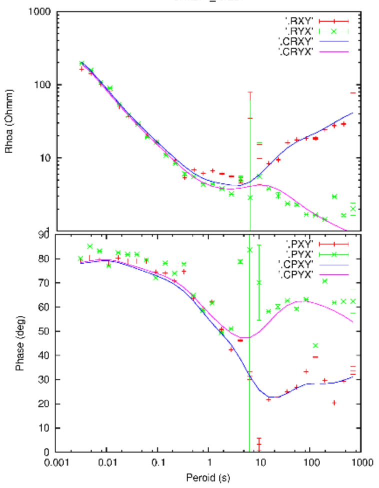
slmt274_rs.EDI
Rhoa (Ohmm)
1000
100
10
1
'.RXY'
'.RYX'
'.CRXY'
'.CRYX'
Phase (deg)
90
80
70
60
50
40
30
20
10
0
'.PXY'
'.PYX'
'.CPXY'
'.CPYX'
0.001
0.01
0.1
1
10
100
1000
Peroid (s)

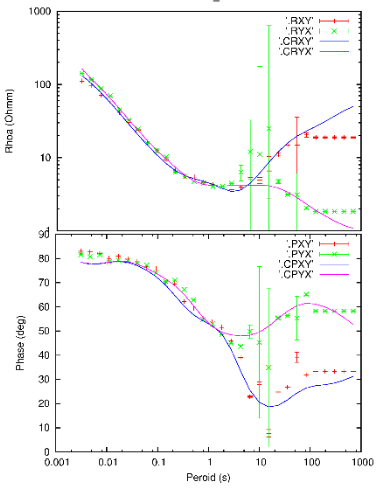
slmt315E_rs.EDI
Rhoa (Ohmm)
1000
100
10
1
'.RXY'
'.RYX'
'.CRXY'
'.CRYX'
Phase (deg)
90
80
70
60
50
40
30
20
10
0
'.PXY'
'.PYX'
'.CPXY'
'.CPYX'
0.001
0.01
0.1
1
10
100
1000
Peroid (s)

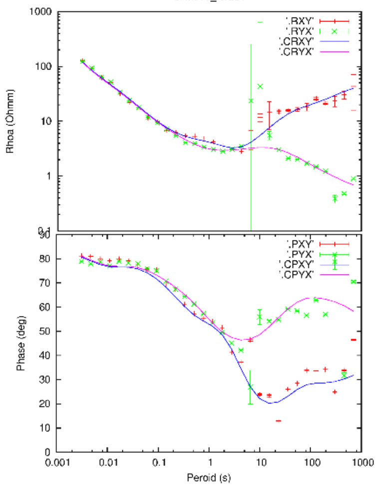
slmt318_rs.EDI
Rhoa (Ohmm)
1000
100
10
1
0.1
'.RXY'
'.RYX'
'.CRXY'
'.CRYX'
Phase (deg)
90
80
70
60
50
40
30
20
10
0
'.PXY'
'.PYX'
'.CPXY'
'.CPYX'
0.001
0.01
0.1
1
10
100
1000
Peroid (s)

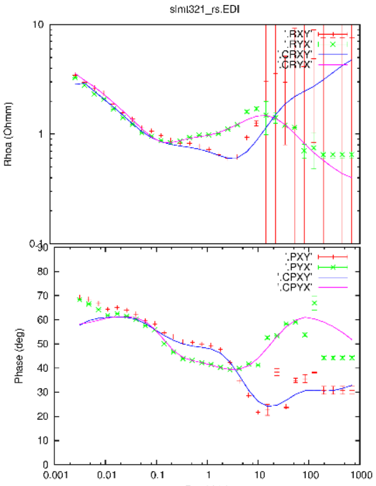
slmt321_rs.EDI
Rhoa (Ohmm)
Phase (deg)
Peroid (s)
'.RXY'
'.RYX'
'.CRXY'
'.CRYX'
'.PXY'
'.PYX'
'.CPXY'
'.CPYX'
0.1
1
10
0
10
20
30
40
50
60
70
80
90
0.001
0.01
0.1
1
10
100
1000

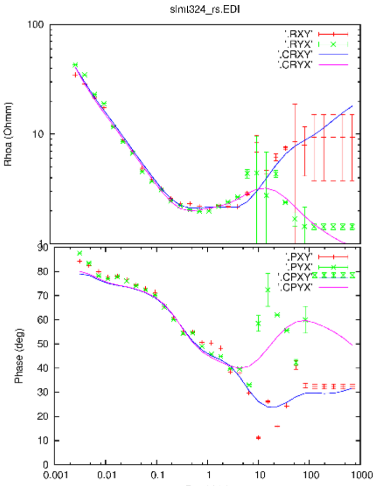
slmt324_rs.EDI
Rhoa (Ohmm)
Phase (deg)
Peroid (s)
'.RXY'
'.RYX'
'.CRXY'
'.CRYX'
'.PXY'
'.PYX'
'.CPXY'
'.CPYX'
1
10
100
0
10
20
30
40
50
60
70
80
90
0.001
0.01
0.1
1
10
100
1000

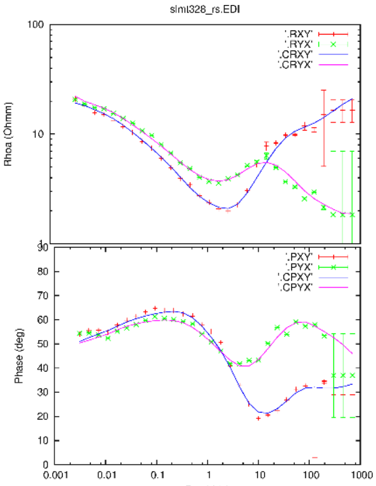
slmt328_rs.EDI
Rhoa (Ohmm)
Phase (deg)
Peroid (s)
'.RXY'
'.RYX'
'.CRXY'
'.CRYX'
'.PXY'
'.PYX'
'.CPXY'
'.CPYX'
1
10
100
0
10
20
30
40
50
60
70
80
90
0.001
0.01
0.1
1
10
100
1000

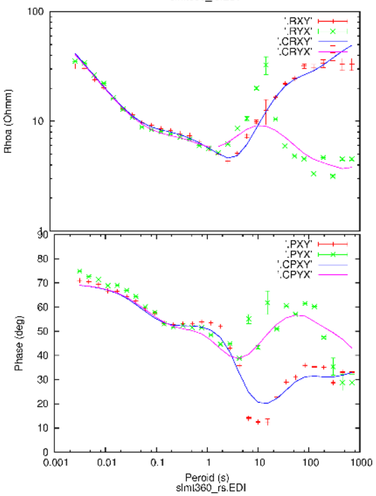
slmt330_rs.EDI
Rhoa (Ohmm)
Phase (deg)
Peroid (s)
'.RXY'
'.RYX'
'.CRXY'
'.CRYX'
'.PXY'
'.PYX'
'.CPXY'
'.CPYX'
1
10
100
0
10
20
30
40
50
60
70
80
90
0.001
0.01
0.1
1
10
100
1000

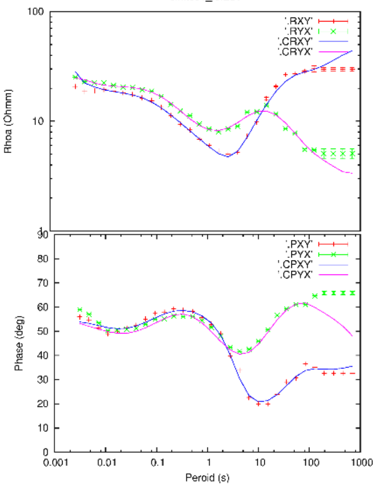
slmt331_rs.EDI
Rhoa (Ohmm)
Phase (deg)
Peroid (s)
'.RXY'
'.RYX'
'.CRXY'
'.CRYX'
'.PXY'
'.PYX'
'.CPXY'
'.CPYX'
1
10
100
0
10
20
30
40
50
60
70
80
90
0.001
0.01
0.1
1
10
100
1000

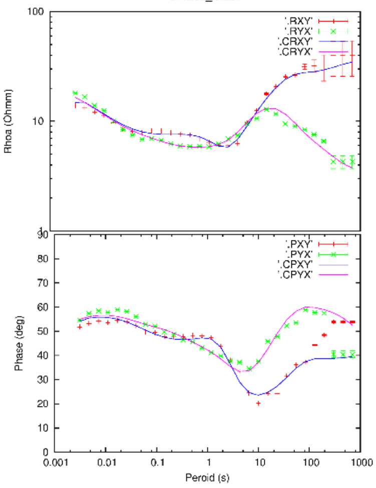
slmt332_rs.EDI
Rhoa (Ohmm)
Phase (deg)
Peroid (s)
'.RXY'
'.RYX'
'.CRXY'
'.CRYX'
'.PXY'
'.PYX'
'.CPXY'
'.CPYX'
1
10
100
0
10
20
30
40
50
60
70
80
90
0.001
0.01
0.1
1
10
100
1000

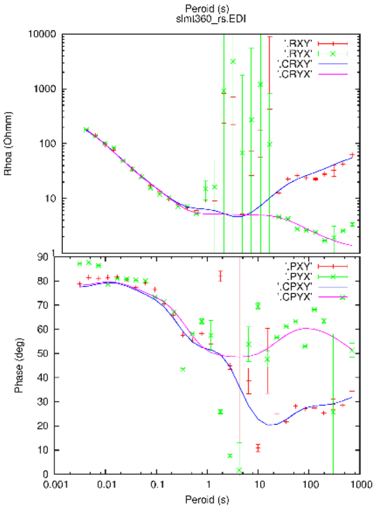
slmt360_rs.EDI
Rhoa (Ohmm)
Phase (deg)
Peroid (s)
'.RXY'
'.RYX'
'.CRXY'
'.CRYX'
'.PXY'
'.PYX'
'.CPXY'
'.CPYX'
1
10
100
1000
10000
0
10
20
30
40
50
60
70
80
90
0.001
0.01
0.1
1
10
100
1000

# APPENDIX V: 3-D iso-resistivity maps

The resistivity models from the 3-D inversion showing smoothed resistivity maps for the 10 ohm-m initial model from the elevation corrected models.

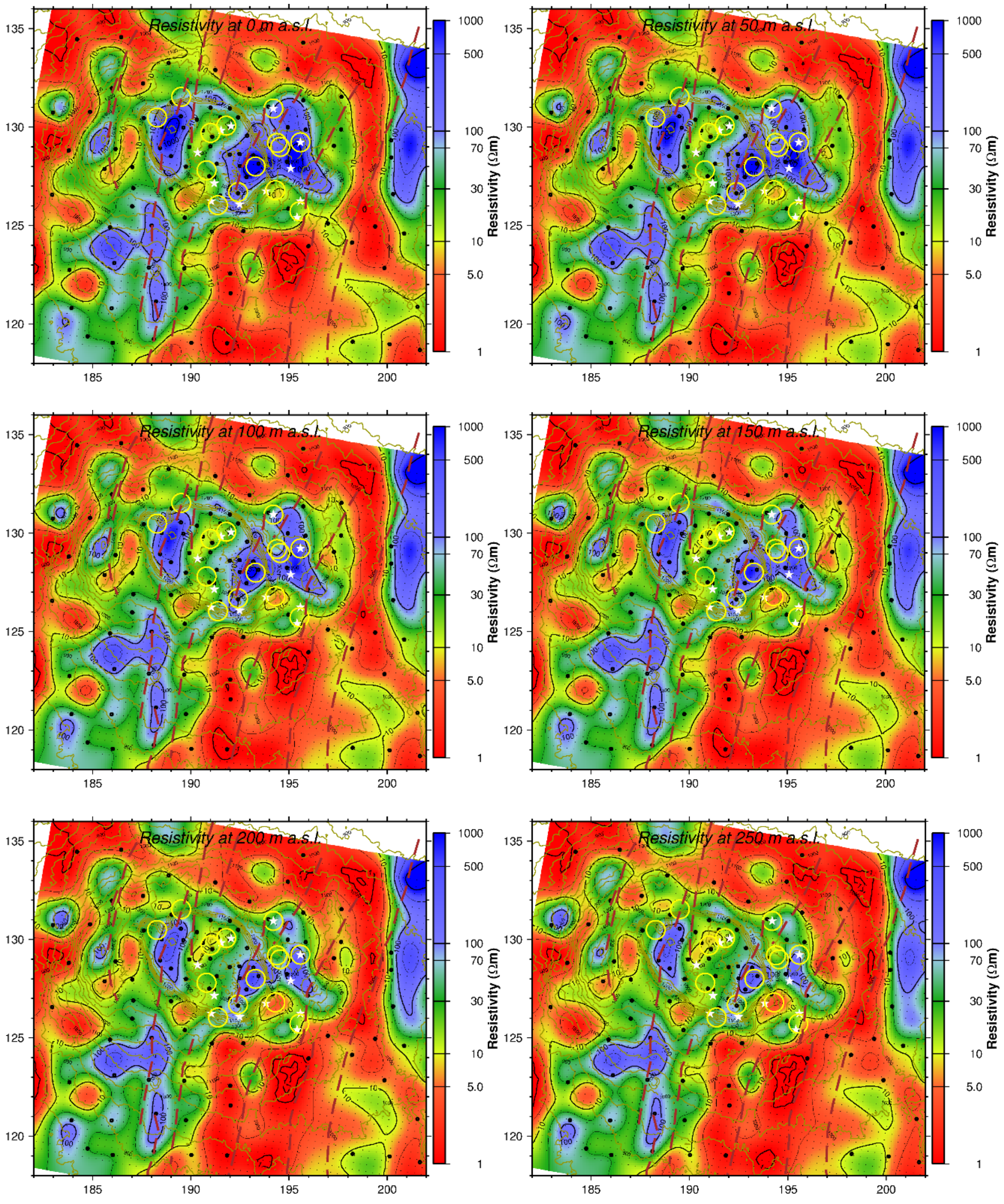

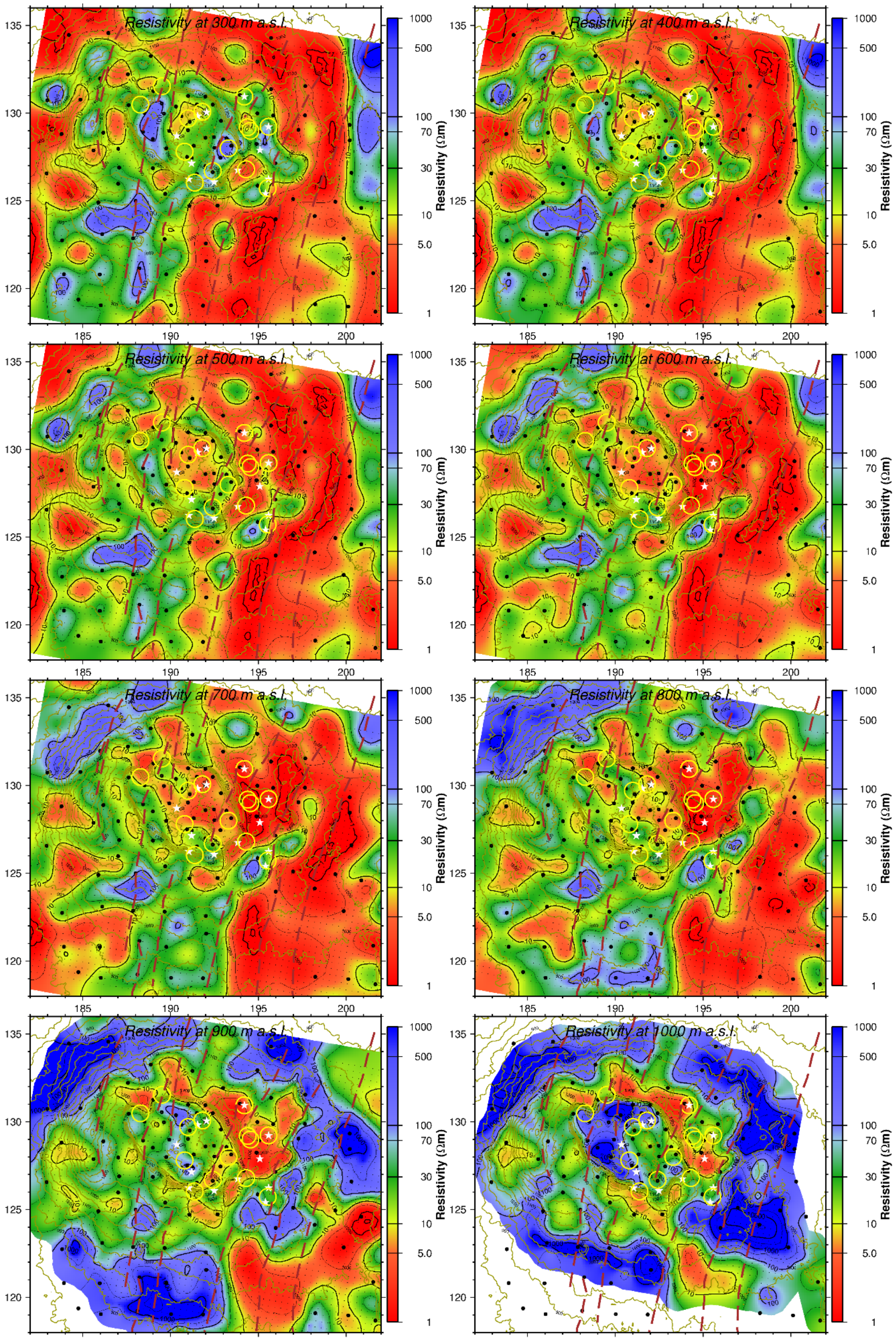
Resistivity at 300 m a.s.l.
Resistivity at 400 m a.s.l.
Resistivity at 500 m a.s.l.
Resistivity at 600 m a.s.l.
Resistivity at 700 m a.s.l.
Resistivity at 800 m a.s.l.
Resistivity at 900 m a.s.l.
Resistivity at 1000 m a.s.l.
135
130
125
120
185
190
195
200
Resistivity (Ωm)
1000
500
100
70
30
10
5.0
1

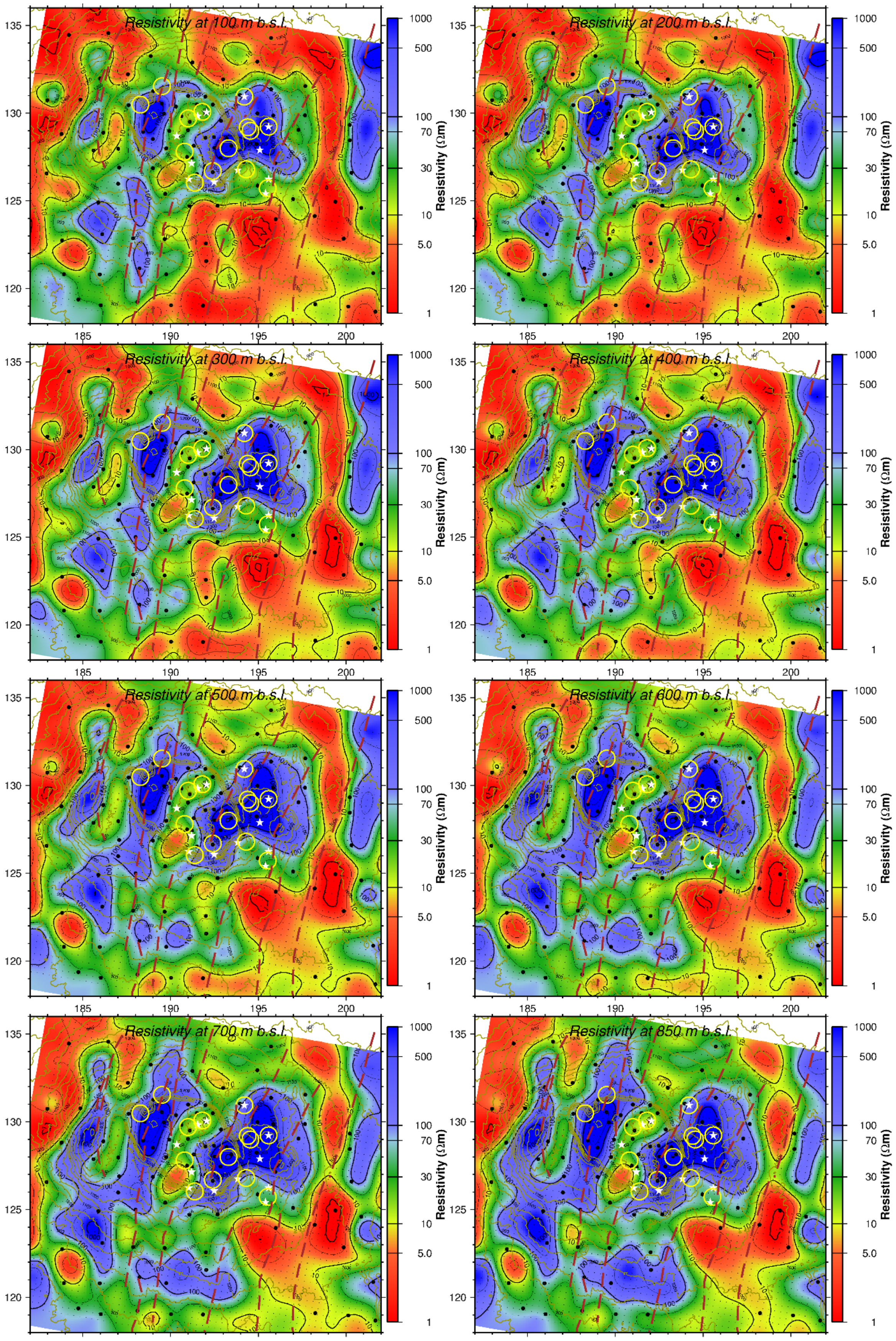
Resistivity at 100 m b.s.l.
Resistivity at 200 m b.s.l.
Resistivity at 300 m b.s.l.
Resistivity at 400 m b.s.l.
Resistivity at 500 m b.s.l.
Resistivity at 600 m b.s.l.
Resistivity at 700 m b.s.l.
Resistivity at 850 m b.s.l.
135
130
125
120
185
190
195
200
Resistivity (Ωm)
1000
500
100
70
30
10
5.0
1

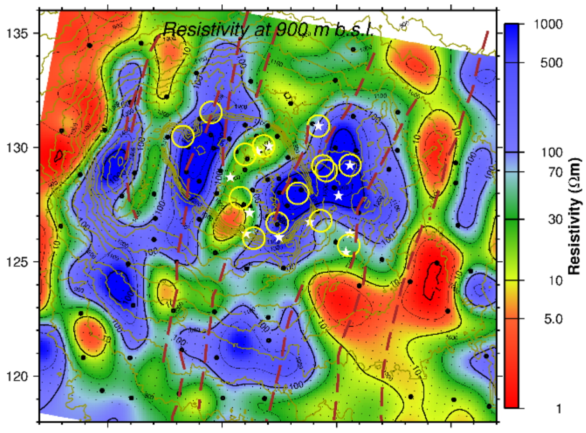
Resistivity at 900 m b.s.l.
135
130
125
120
185
190
195
200
1000
500
100
70
30
10
5.0
1
Resistivity (Ωm)

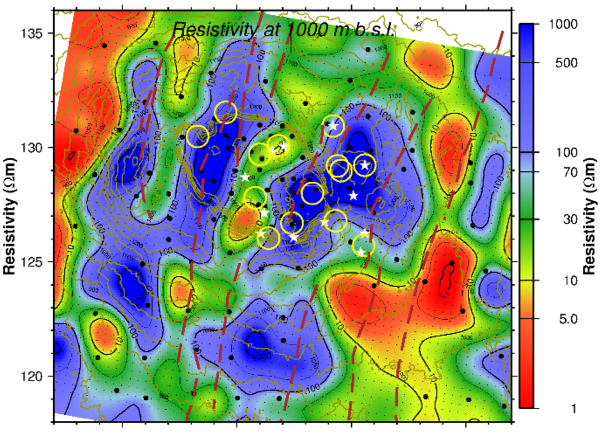
Resistivity at 1000 m b.s.l.
135
130
125
120
185
190
195
200
1000
500
100
70
30
10
5.0
1
Resistivity (Ωm)

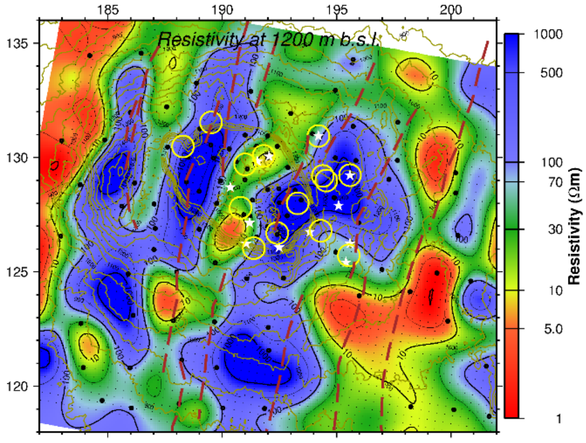
Resistivity at 1200 m b.s.l.
135
130
125
120
185
190
195
200
1000
500
100
70
30
10
5.0
1
Resistivity (Ωm)

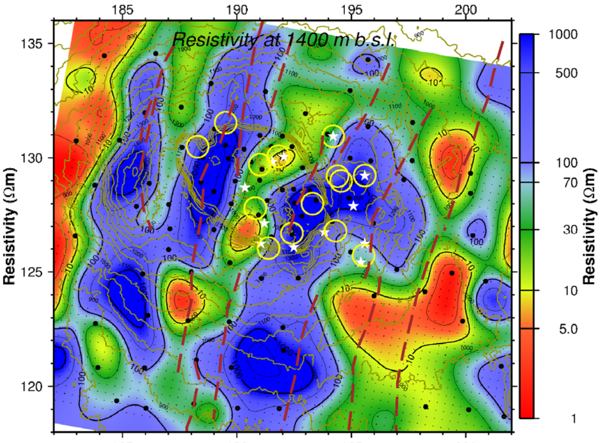
Resistivity at 1400 m b.s.l.
135
130
125
120
185
190
195
200
1000
500
100
70
30
10
5.0
1
Resistivity (Ωm)

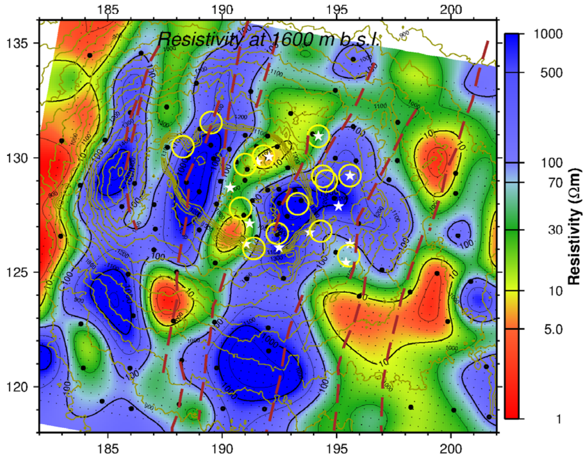
Resistivity at 1600 m b.s.l.
135
130
125
120
185
190
195
200
1000
500
100
70
30
10
5.0
1
Resistivity (Ωm)

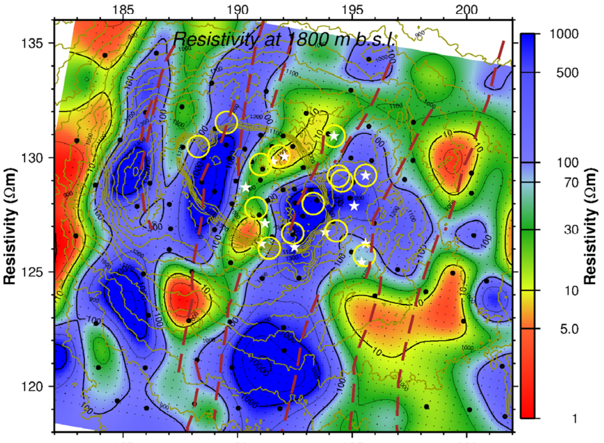
Resistivity at 1800 m b.s.l.
135
130
125
120
185
190
195
200
1000
500
100
70
30
10
5.0
1
Resistivity (Ωm)

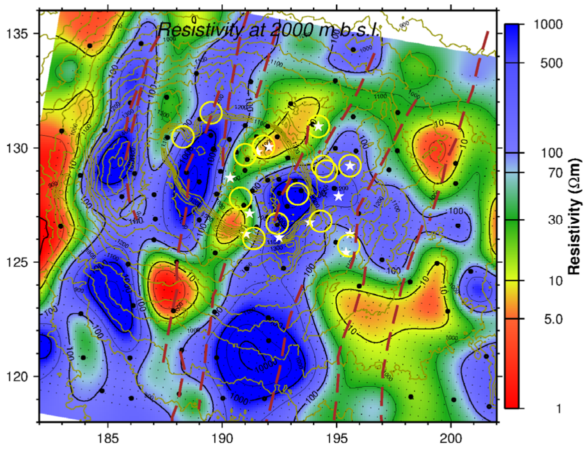
Resistivity at 2000 m b.s.l.
135
130
125
120
185
190
195
200
1000
500
100
70
30
10
5.0
1
Resistivity (Ωm)

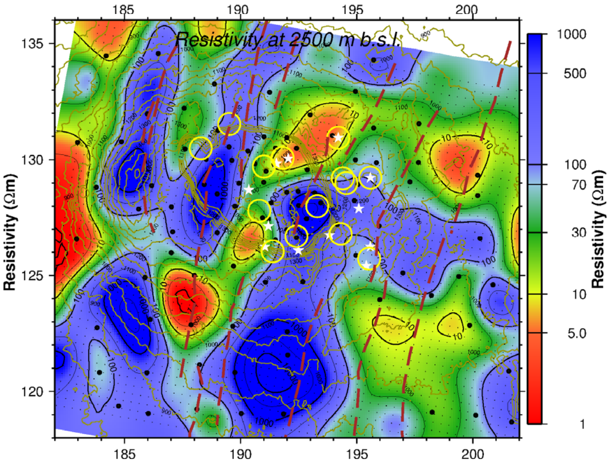
Resistivity at 2500 m b.s.l.
135
130
125
120
185
190
195
200
1000
500
100
70
30
10
5.0
1
Resistivity (Ωm)

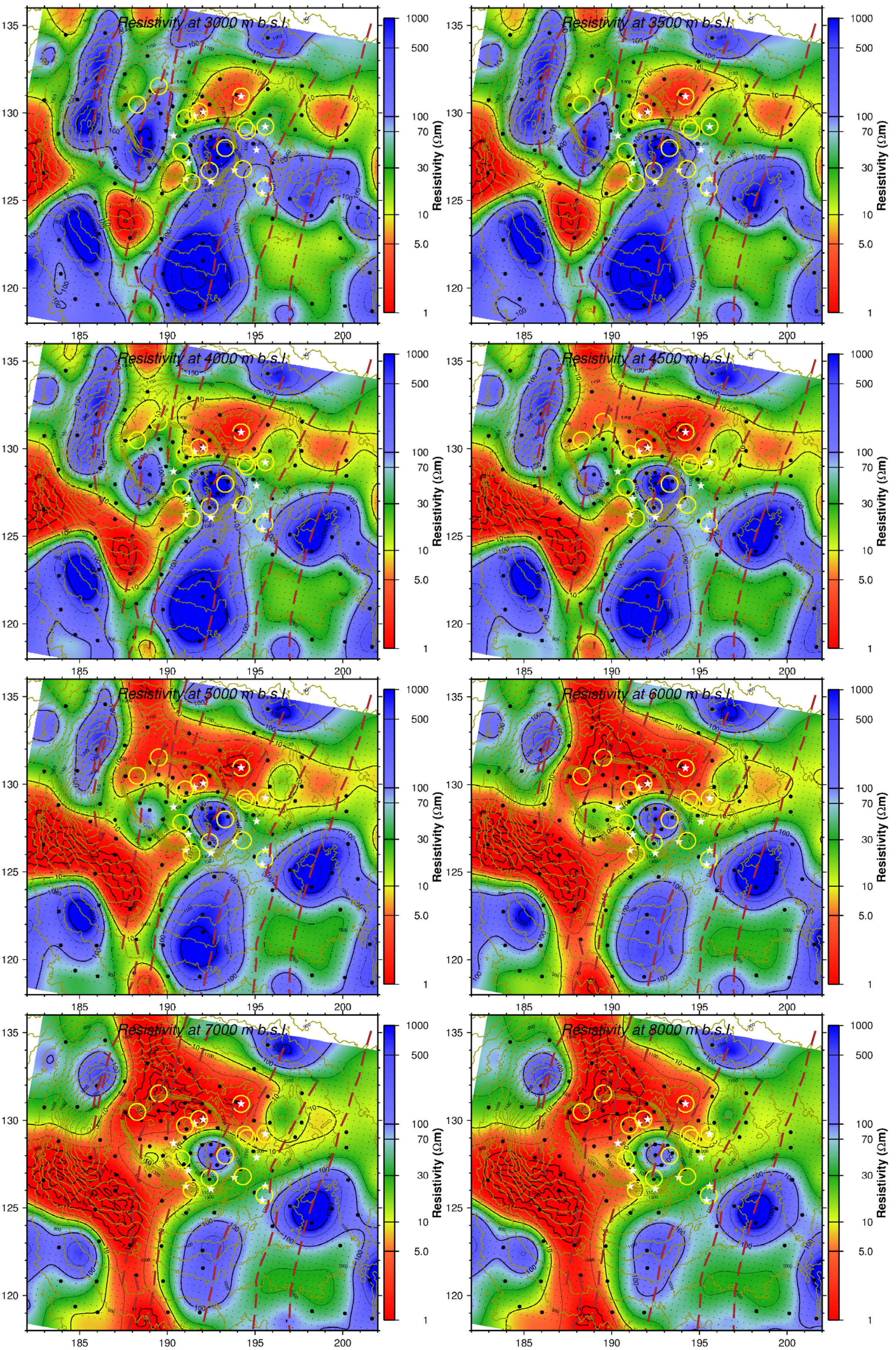
Resistivity at 3000 m b.s.l.
Resistivity at 3500 m b.s.l.
Resistivity at 4000 m b.s.l.
Resistivity at 4500 m b.s.l.
Resistivity at 5000 m b.s.l.
Resistivity at 6000 m b.s.l.
Resistivity at 7000 m b.s.l.
Resistivity at 8000 m b.s.l.
135
130
125
120
185
190
195
200
Resistivity (Ωm)
1000
500
100
70
30
10
5.0
1

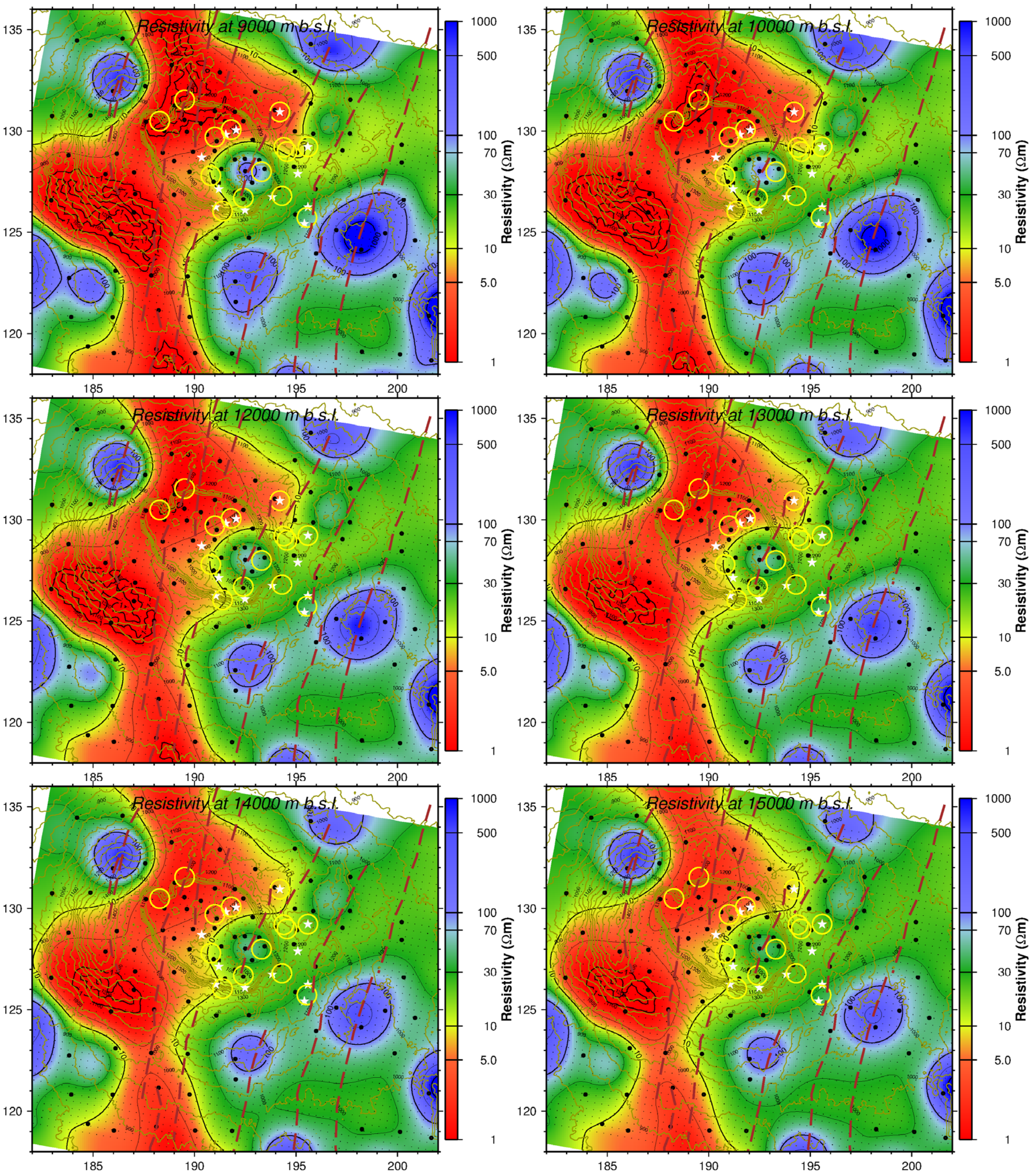
Resistivity at 9000 m b.s.l.
Resistivity at 10000 m b.s.l.
Resistivity at 12000 m b.s.l.
Resistivity at 13000 m b.s.l.
Resistivity at 14000 m b.s.l.
Resistivity at 15000 m b.s.l.
135
130
125
120
185
190
195
200
Resistivity (Ωm)
1000
500
100
70
30
10
5.0
1

# APPENDIX VI: Cross-sections

Smoothed elevation corrected EW and NS lying cross-sections, through the dense part of the model grid, from the 10 ohm-m homogeneous half-space initial model. Their location is given in Figure 8.26.

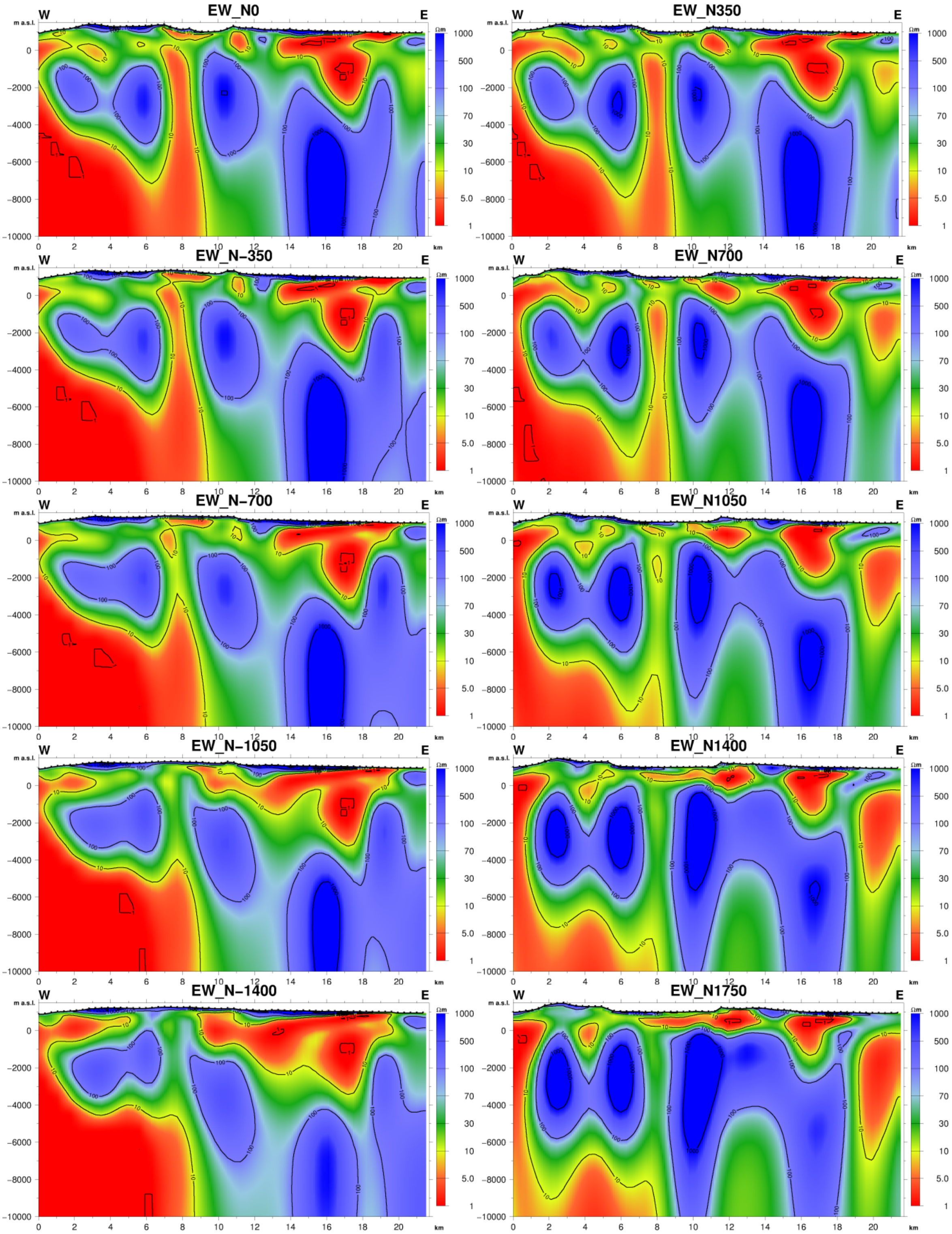

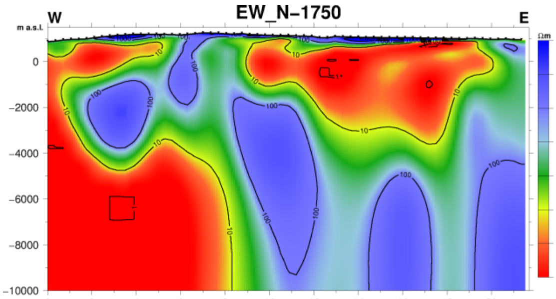
EW_N-1750

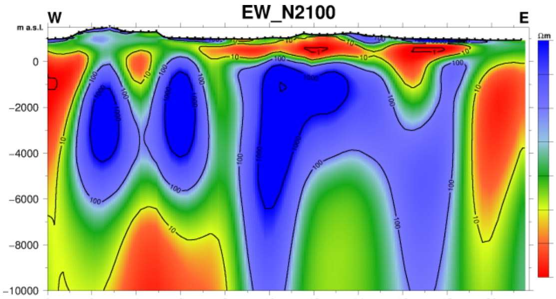
EW_N2100

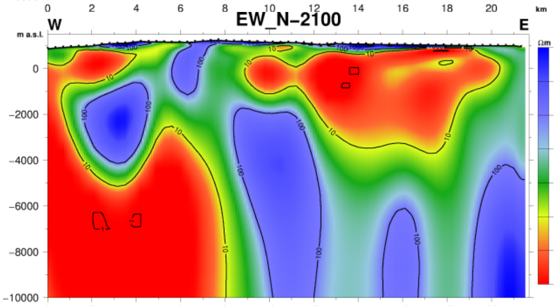
EW_N-2100

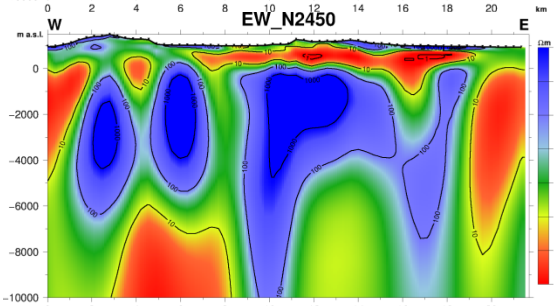
EW_N2450

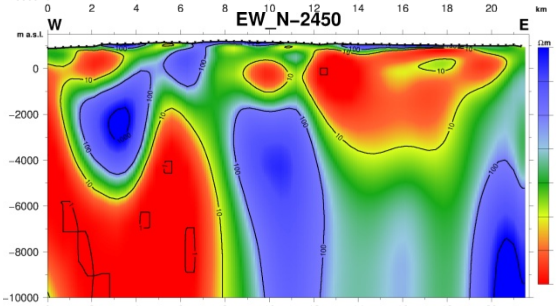
EW_N-2450

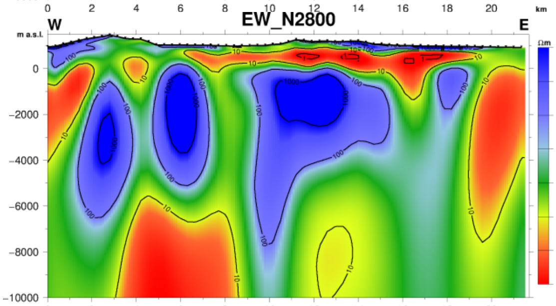
EW_N2800

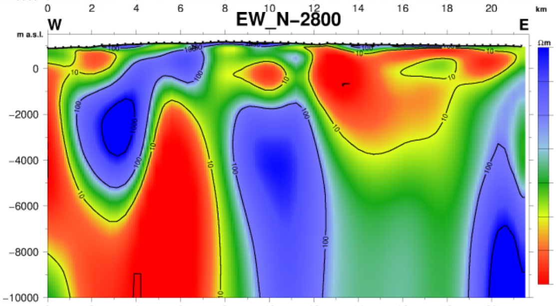
EW_N-2800

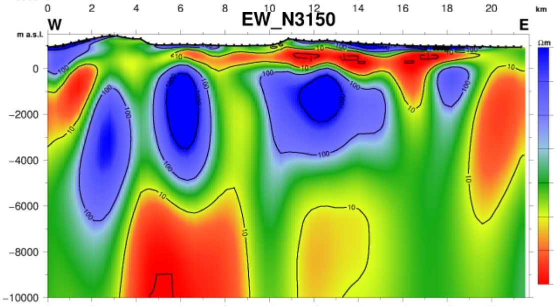
EW_N3150

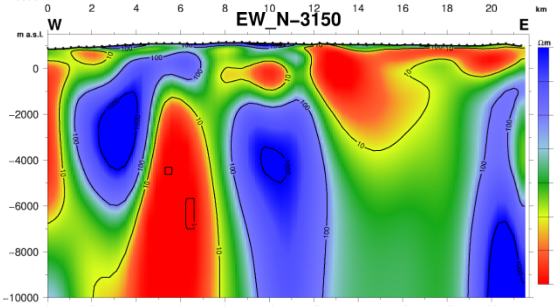
EW_N-3150

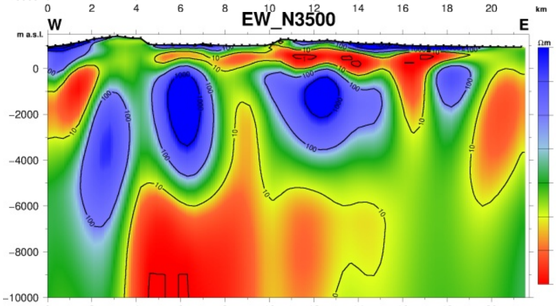
EW_N3500

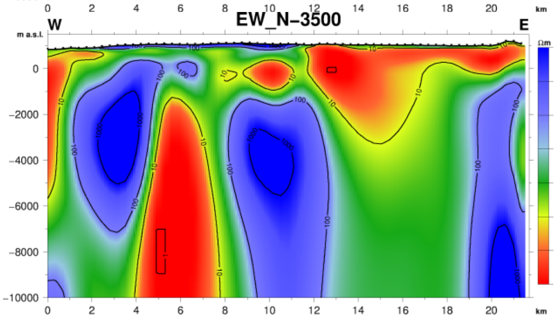
EW_N-3500

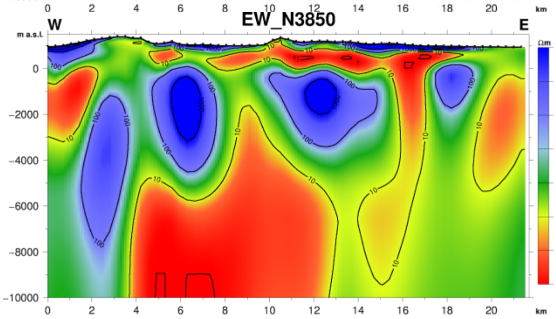
EW_N3850

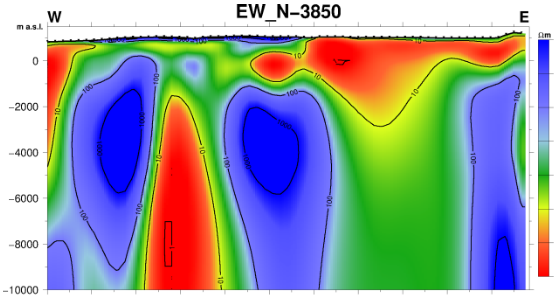
W
EW_N-3850
E
m a.s.l.
0
−2000
−4000
−6000
−8000
−10000
0 2 4 6 8 10 12 14 16 18 20
km
Ωm
1000
500
100
70
30
10
5.0
1

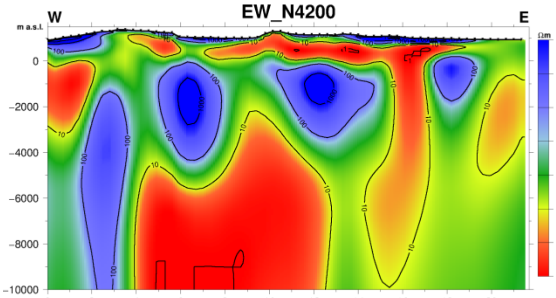
W
EW_N4200
E
m a.s.l.
0
−2000
−4000
−6000
−8000
−10000
0 2 4 6 8 10 12 14 16 18 20
km
Ωm
1000
500
100
70
30
10
5.0
1

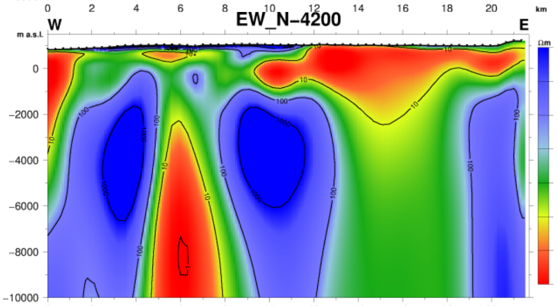
W
EW_N-4200
E
m a.s.l.
0
−2000
−4000
−6000
−8000
−10000
0 2 4 6 8 10 12 14 16 18 20
km
Ωm
1000
500
100
70
30
10
5.0
1

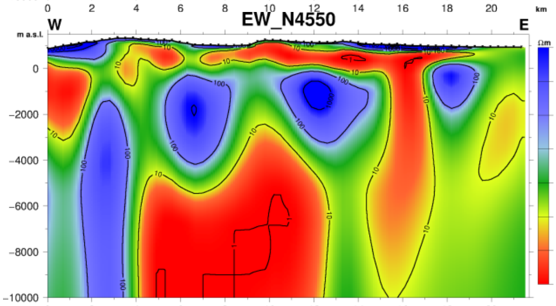
W
EW_N4550
E
m a.s.l.
0
−2000
−4000
−6000
−8000
−10000
0 2 4 6 8 10 12 14 16 18 20
km
Ωm
1000
500
100
70
30
10
5.0
1

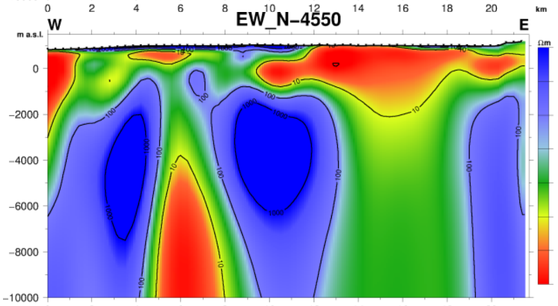
W
EW_N-4550
E
m a.s.l.
0
−2000
−4000
−6000
−8000
−10000
0 2 4 6 8 10 12 14 16 18 20
km
Ωm
1000
500
100
70
30
10
5.0
1

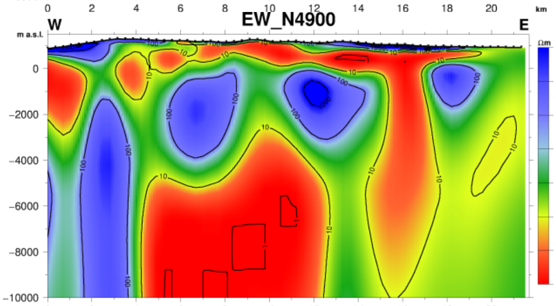
W
EW_N4900
E
m a.s.l.
0
−2000
−4000
−6000
−8000
−10000
0 2 4 6 8 10 12 14 16 18 20
km
Ωm
1000
500
100
70
30
10
5.0
1

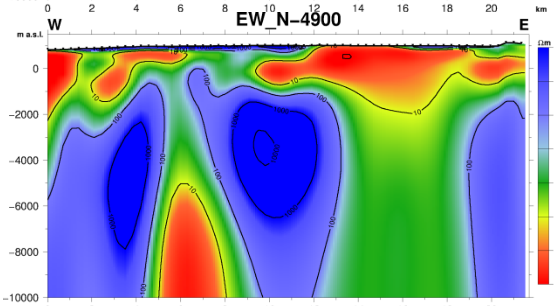
W
EW_N-4900
E
m a.s.l.
0
−2000
−4000
−6000
−8000
−10000
0 2 4 6 8 10 12 14 16 18 20
km
Ωm
1000
500
100
70
30
10
5.0
1

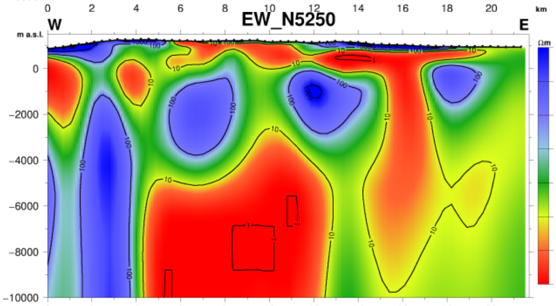
W
EW_N5250
E
m a.s.l.
0
−2000
−4000
−6000
−8000
−10000
0 2 4 6 8 10 12 14 16 18 20
km
Ωm
1000
500
100
70
30
10
5.0
1

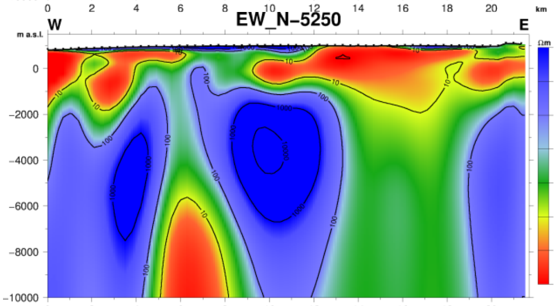
W
EW_N-5250
E
m a.s.l.
0
−2000
−4000
−6000
−8000
−10000
0 2 4 6 8 10 12 14 16 18 20
km
Ωm
1000
500
100
70
30
10
5.0
1

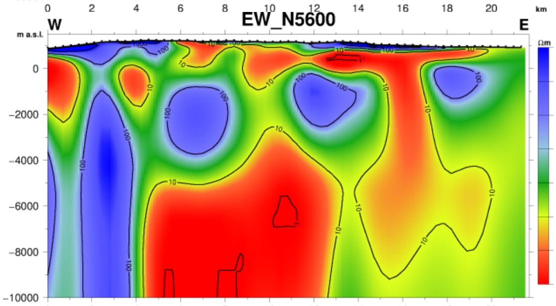
W
EW_N5600
E
m a.s.l.
0
−2000
−4000
−6000
−8000
−10000
0 2 4 6 8 10 12 14 16 18 20
km
Ωm
1000
500
100
70
30
10
5.0
1

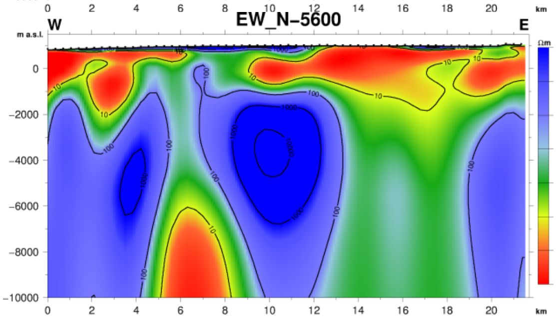
W
EW_N-5600
E
m a.s.l.
0
−2000
−4000
−6000
−8000
−10000
0 2 4 6 8 10 12 14 16 18 20
km
Ωm
1000
500
100
70
30
10
5.0
1

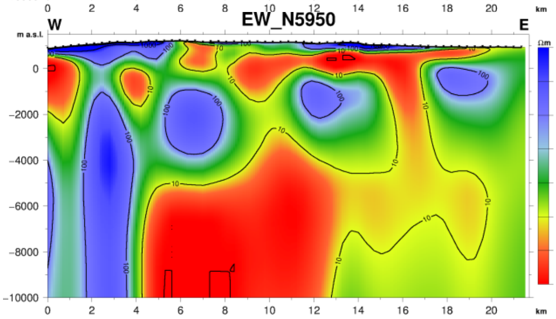
W
EW_N5950
E
m a.s.l.
0
−2000
−4000
−6000
−8000
−10000
0 2 4 6 8 10 12 14 16 18 20
km
Ωm
1000
500
100
70
30
10
5.0
1

EW_N-5950

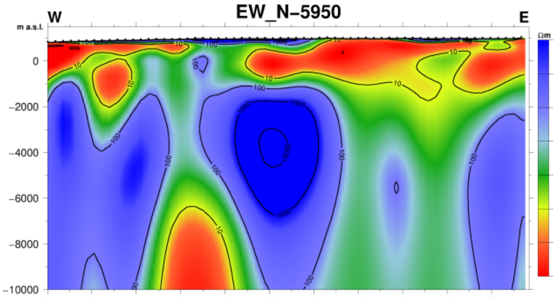

EW_N6300

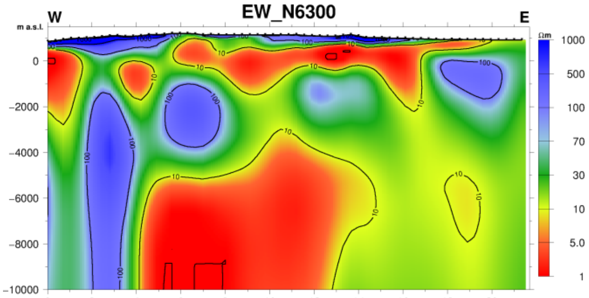

EW_N-6300

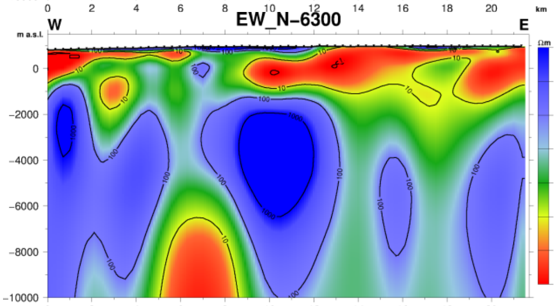

EW_N6650

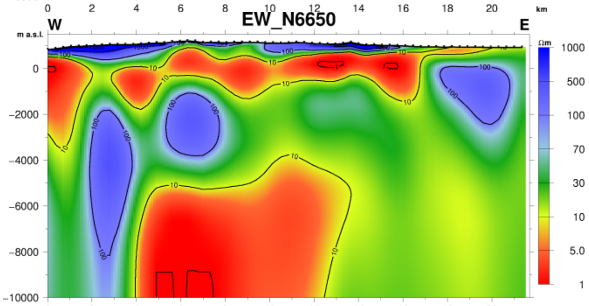

EW_N-6650

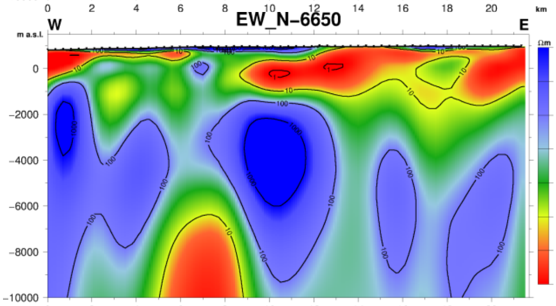

EW_N7000

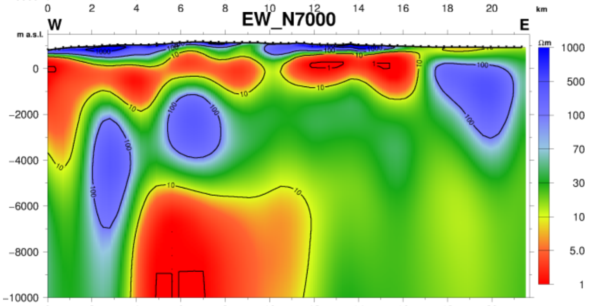

EW_N-7000

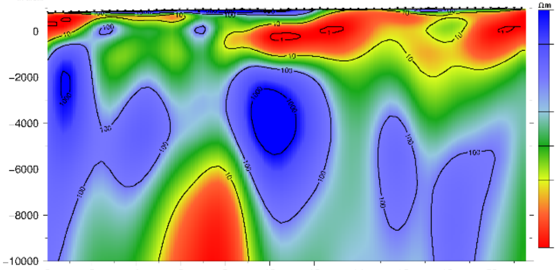

EW_N7350

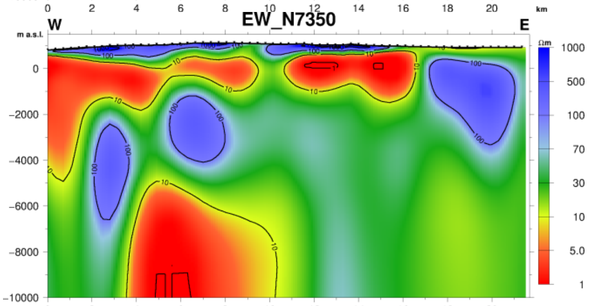

EW_N-7350

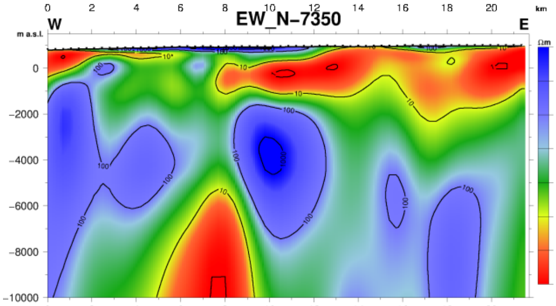

EW_N7700

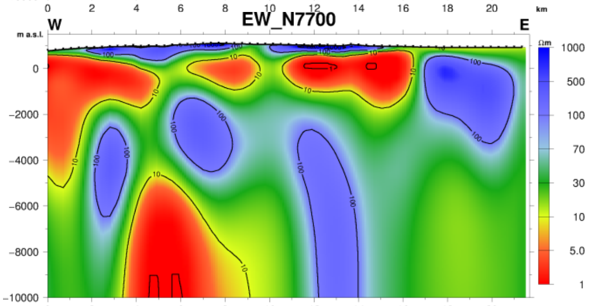

EW_N-7700

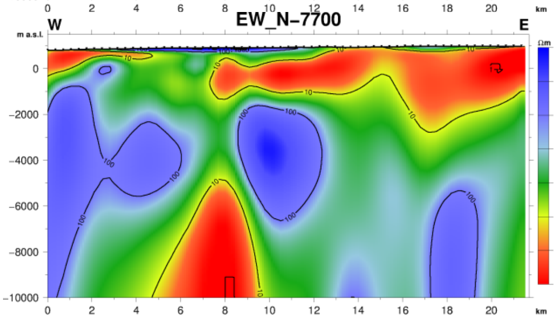

EW_N8050

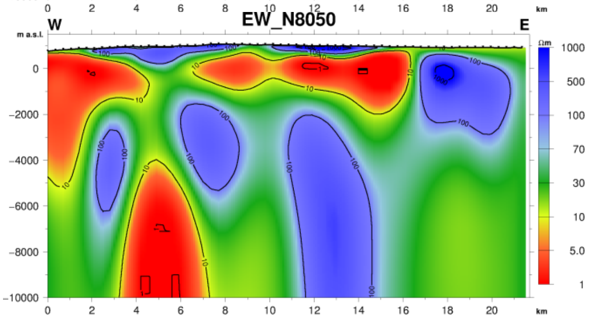

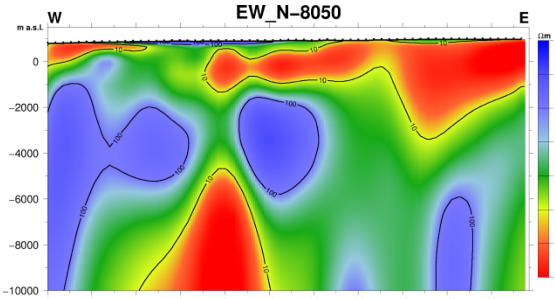

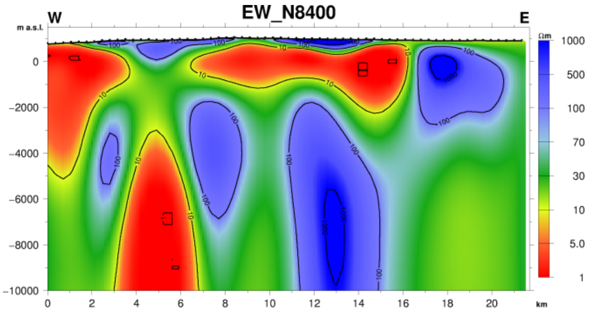

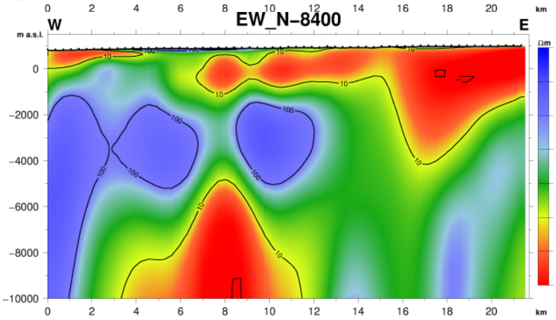

## NS Cross-sections

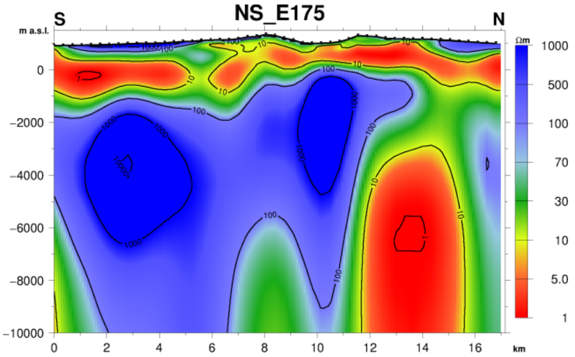

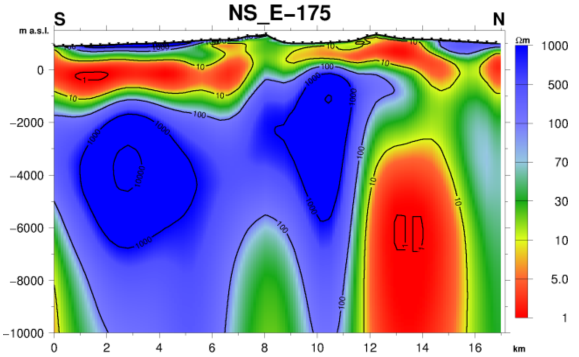

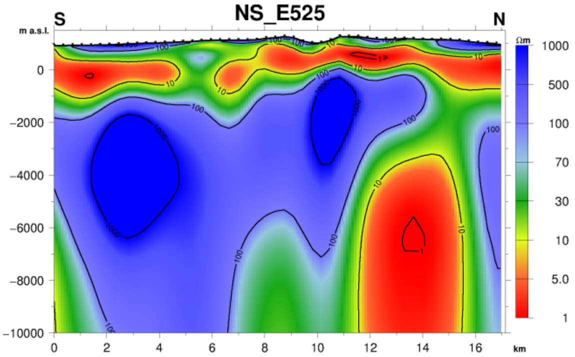

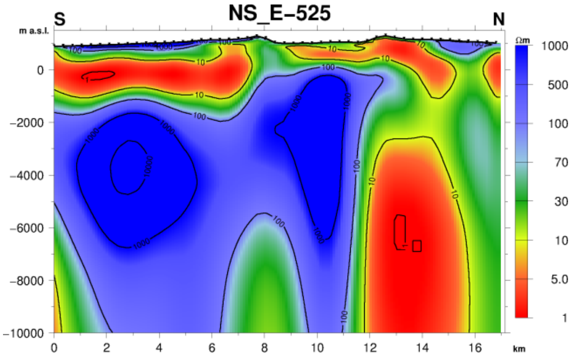

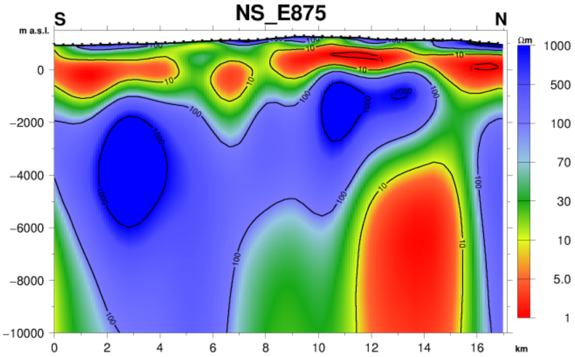

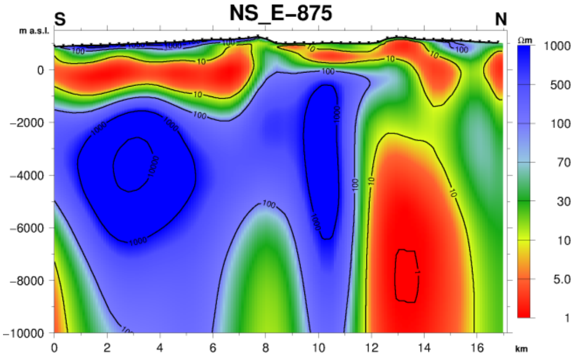

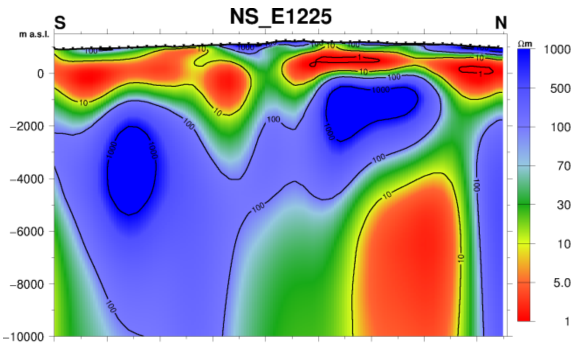
NS_E1225

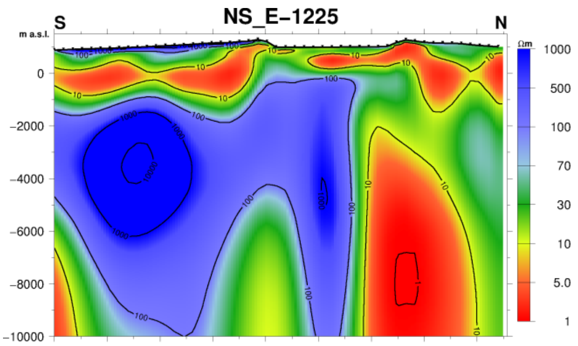
NS_E−1225

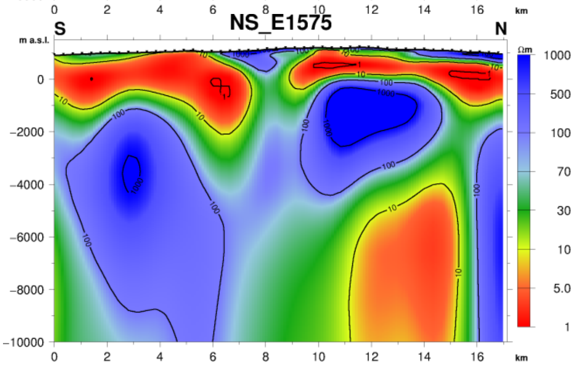
NS_E1575

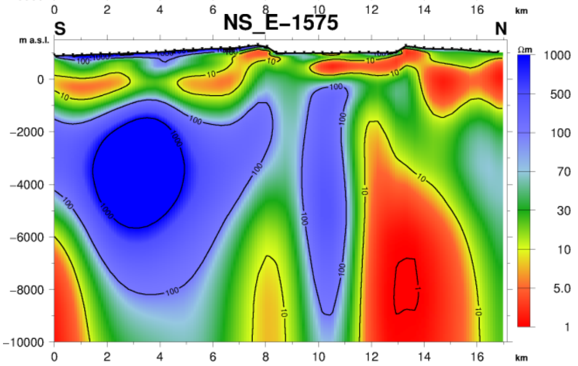
NS_E−1575

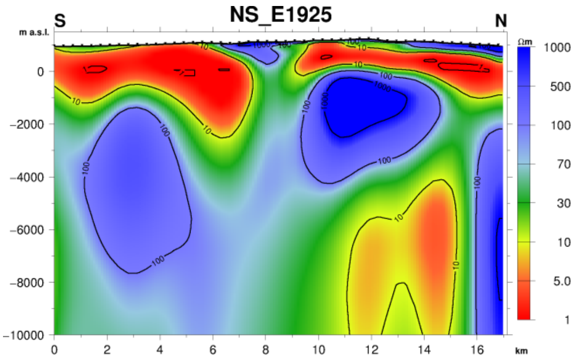
NS_E1925

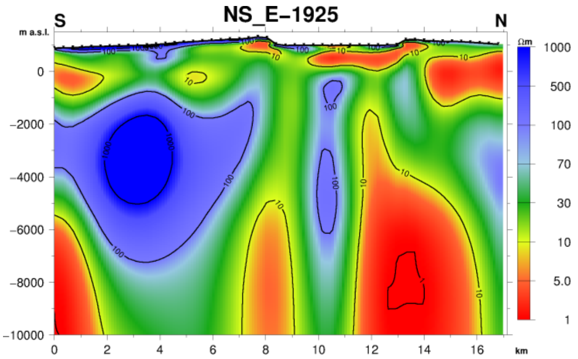
NS_E−1925

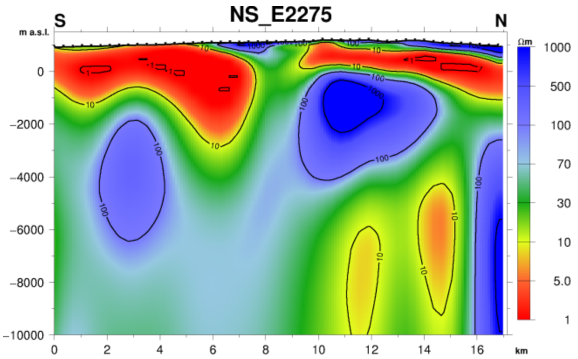
NS_E2275

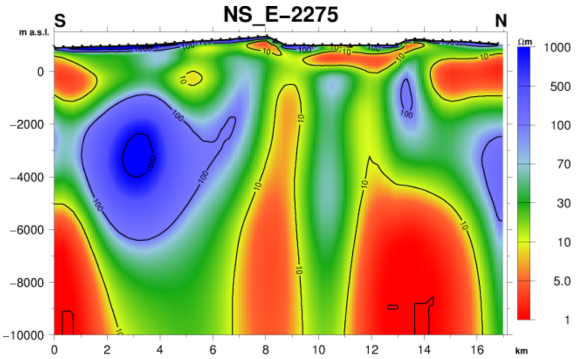
NS_E−2275

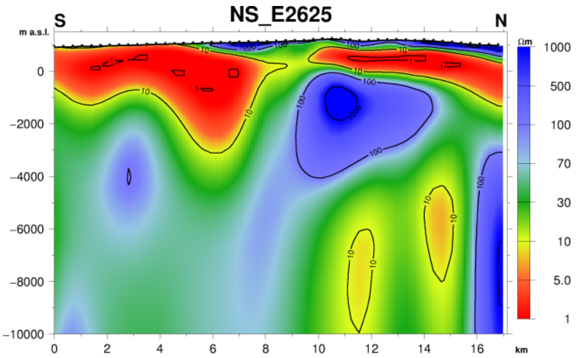
NS_E2625

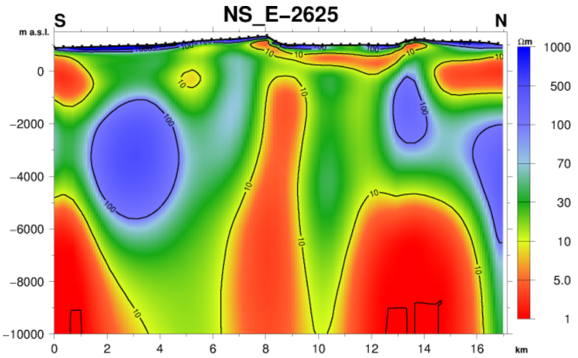
NS_E−2625

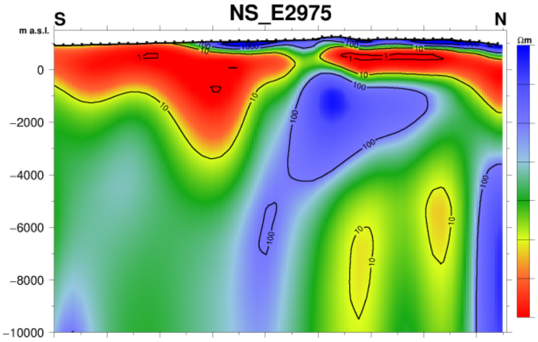
NS_E2975

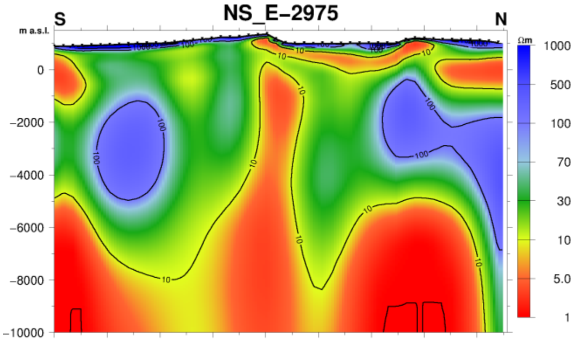
NS_E−2975

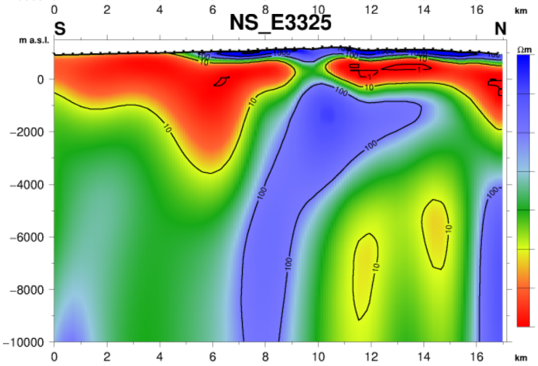
NS_E3325

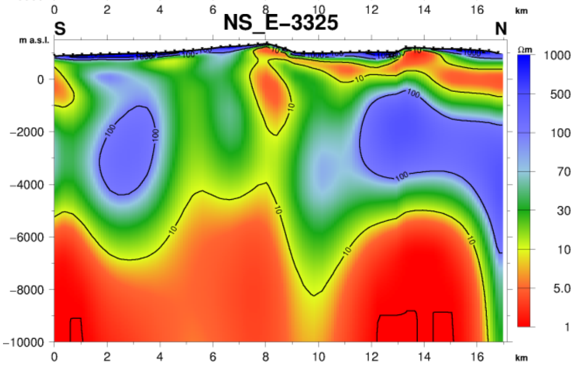
NS_E−3325

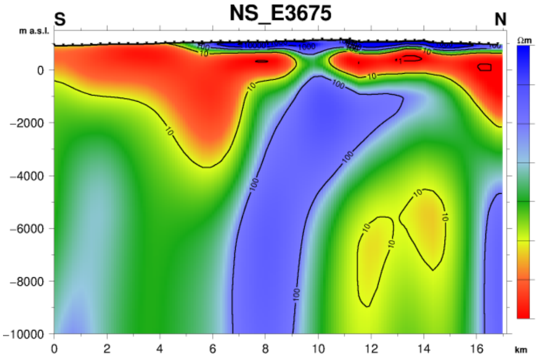
NS_E3675

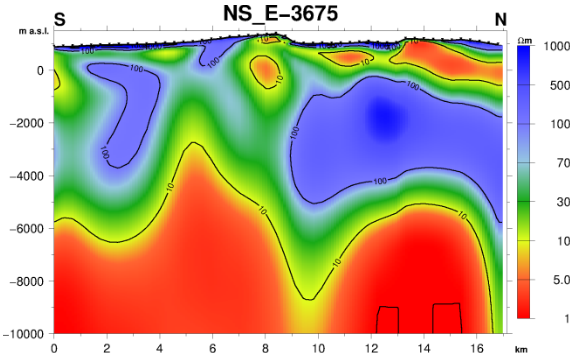
NS_E−3675

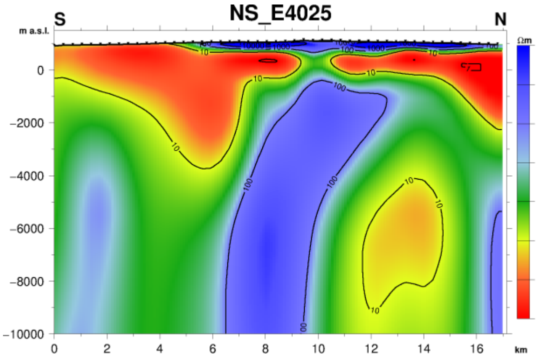
NS_E4025

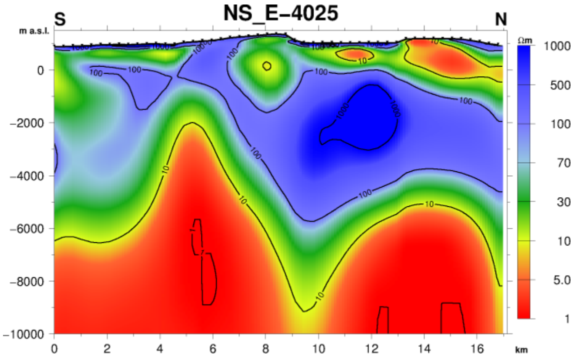
NS_E−4025

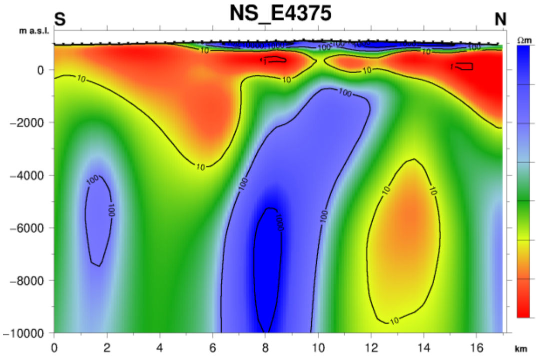
NS_E4375

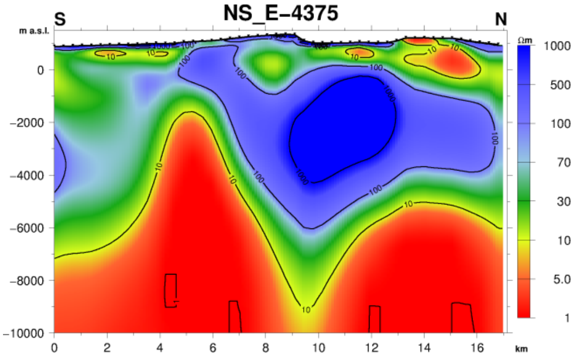
NS_E−4375

NS_E4725

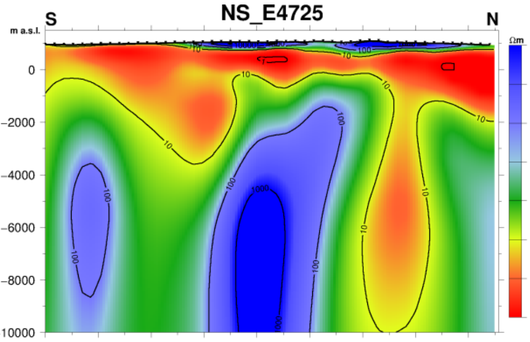

NS_E-4725

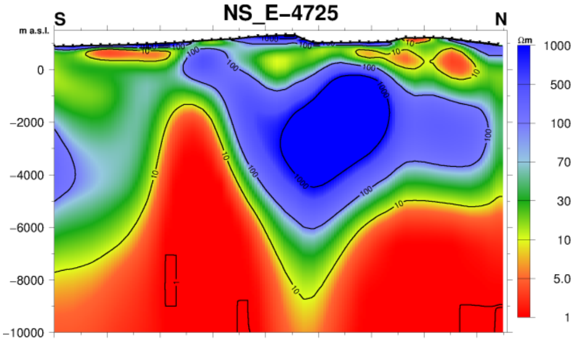

NS_E5075

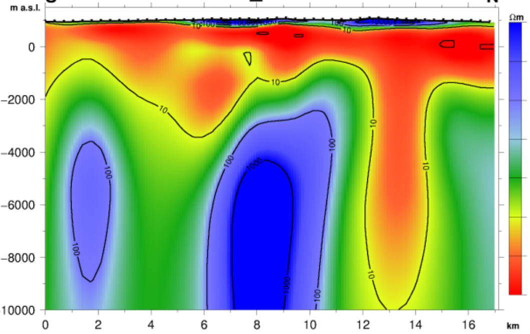

NS_E-5075

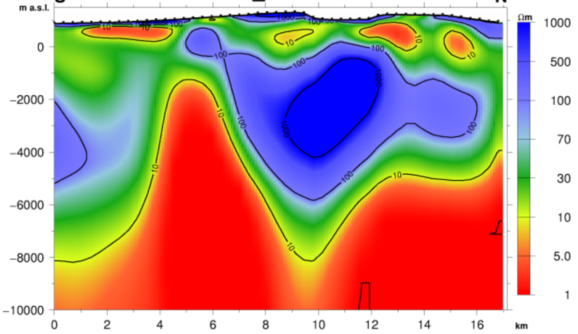

NS_E5425

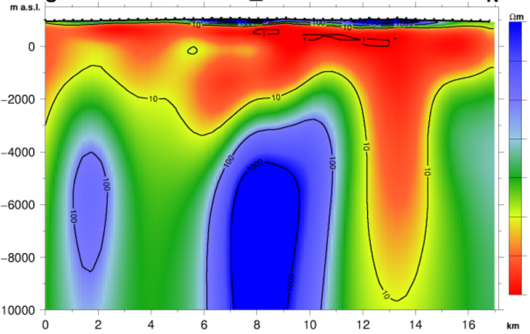

NS_E-5425

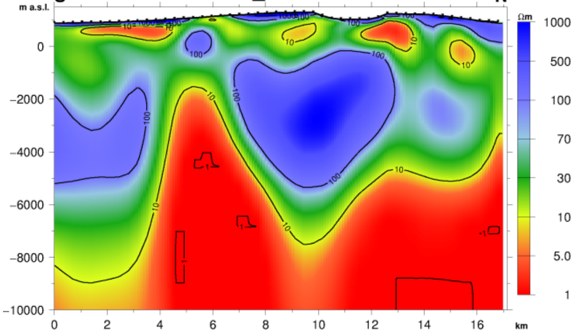

NS_E5775

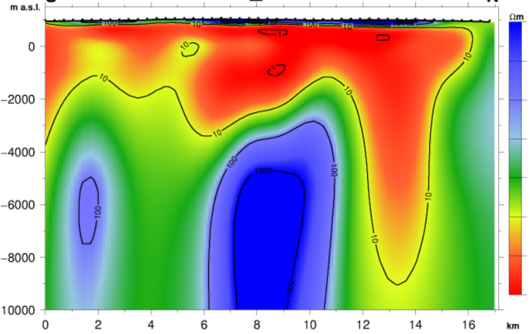

NS_E-5775

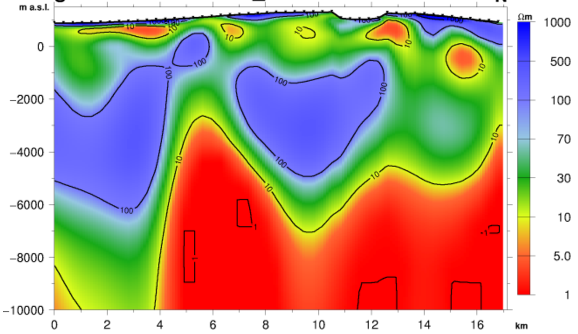

NS_E6125

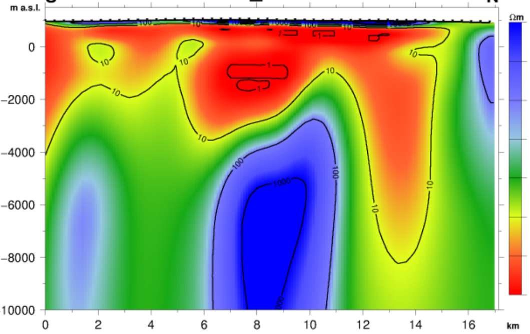

NS_E-6125

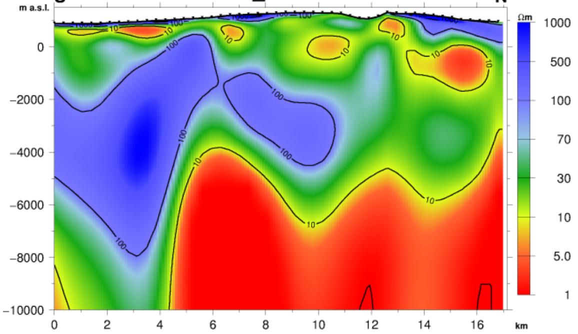

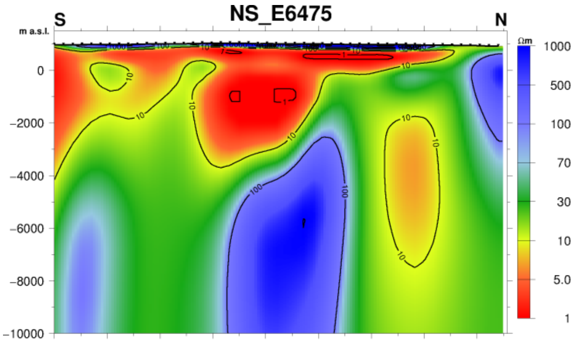
NS_E6475
S
N
m a.s.l.
0
−2000
−4000
−6000
−8000
−10000
0 2 4 6 8 10 12 14 16 km
Ωm
1000 500 100 70 30 10 5.0 1

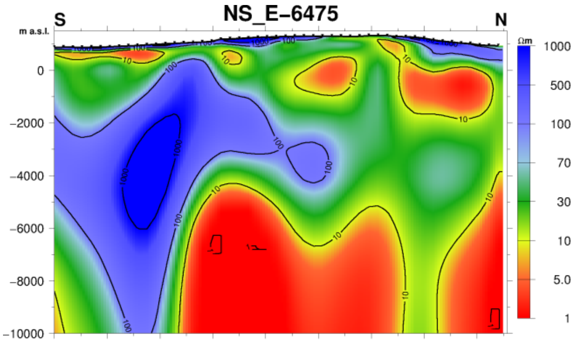
NS_E−6475
S
N
m a.s.l.
0
−2000
−4000
−6000
−8000
−10000
0 2 4 6 8 10 12 14 16 km
Ωm
1000 500 100 70 30 10 5.0 1

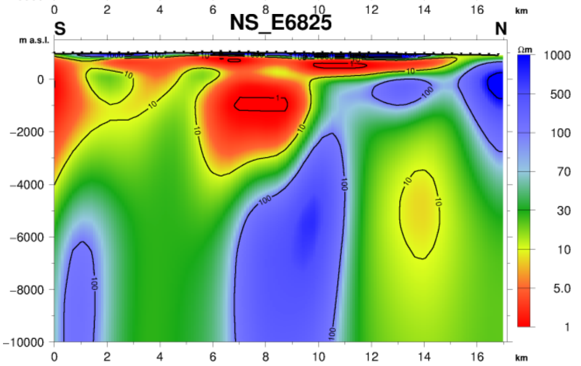
NS_E6825
S
N
m a.s.l.
0
−2000
−4000
−6000
−8000
−10000
0 2 4 6 8 10 12 14 16 km
Ωm
1000 500 100 70 30 10 5.0 1

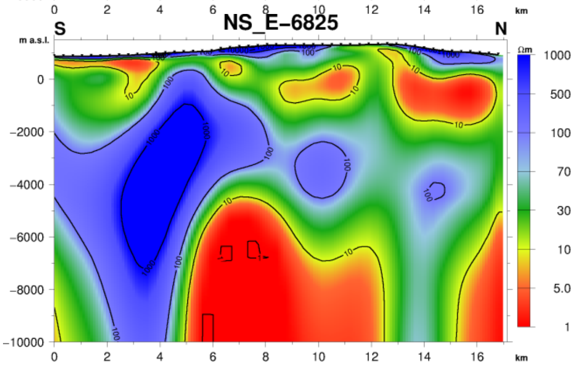
NS_E−6825
S
N
m a.s.l.
0
−2000
−4000
−6000
−8000
−10000
0 2 4 6 8 10 12 14 16 km
Ωm
1000 500 100 70 30 10 5.0 1

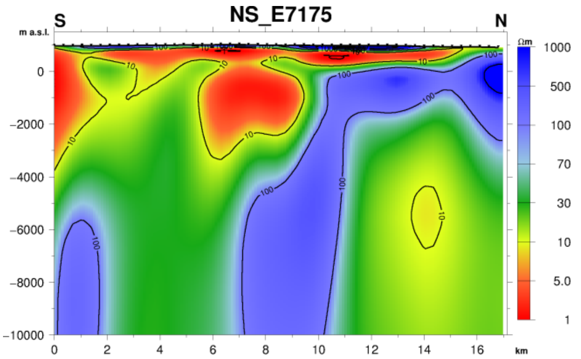
NS_E7175
S
N
m a.s.l.
0
−2000
−4000
−6000
−8000
−10000
0 2 4 6 8 10 12 14 16 km
Ωm
1000 500 100 70 30 10 5.0 1

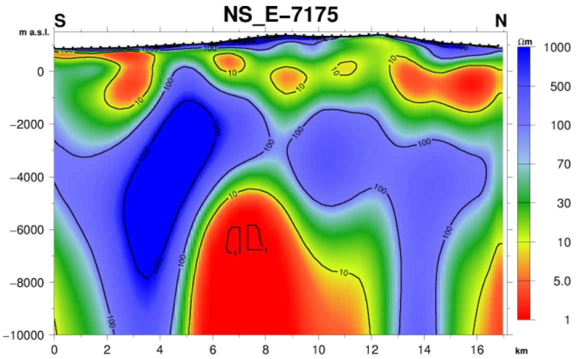
NS_E−7175
S
N
m a.s.l.
0
−2000
−4000
−6000
−8000
−10000
0 2 4 6 8 10 12 14 16 km
Ωm
1000 500 100 70 30 10 5.0 1

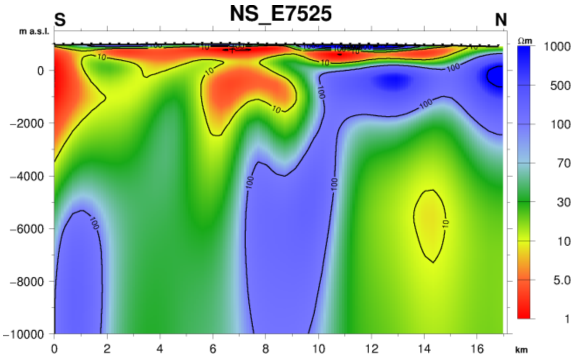
NS_E7525
S
N
m a.s.l.
0
−2000
−4000
−6000
−8000
−10000
0 2 4 6 8 10 12 14 16 km
Ωm
1000 500 100 70 30 10 5.0 1

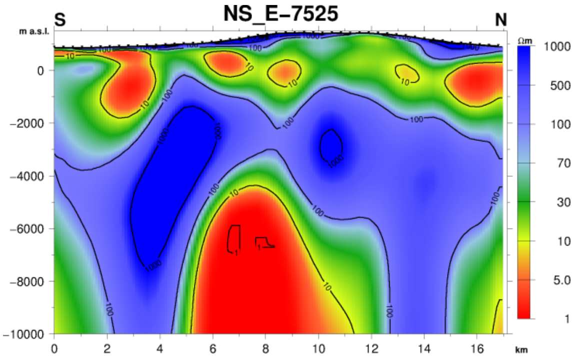
NS_E−7525
S
N
m a.s.l.
0
−2000
−4000
−6000
−8000
−10000
0 2 4 6 8 10 12 14 16 km
Ωm
1000 500 100 70 30 10 5.0 1

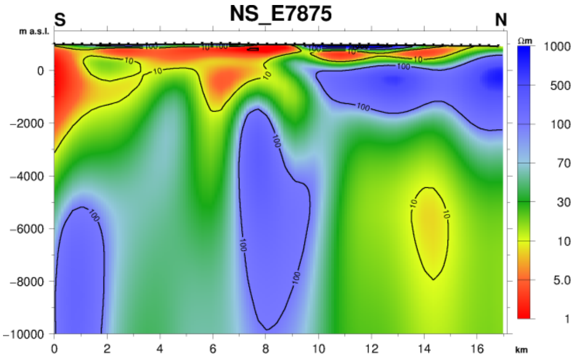
NS_E7875
S
N
m a.s.l.
0
−2000
−4000
−6000
−8000
−10000
0 2 4 6 8 10 12 14 16 km
Ωm
1000 500 100 70 30 10 5.0 1

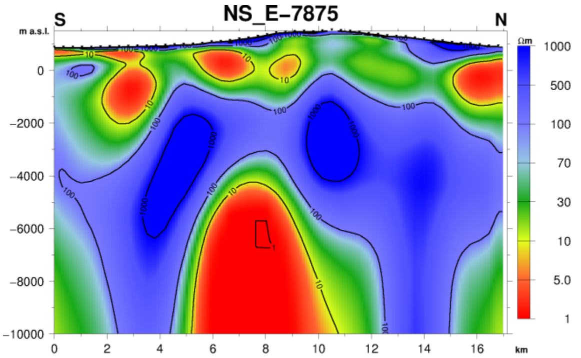
NS_E−7875
S
N
m a.s.l.
0
−2000
−4000
−6000
−8000
−10000
0 2 4 6 8 10 12 14 16 km
Ωm
1000 500 100 70 30 10 5.0 1

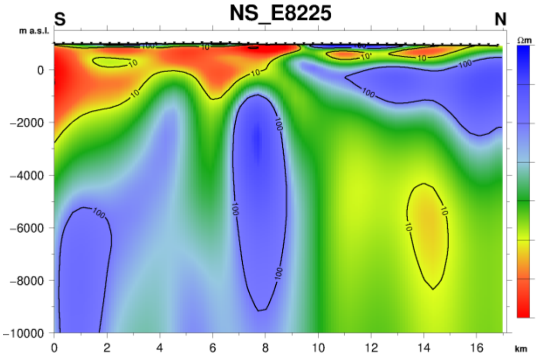
NS_E8225

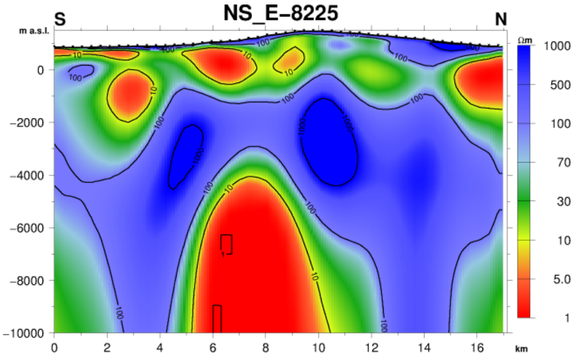
NS_E–8225

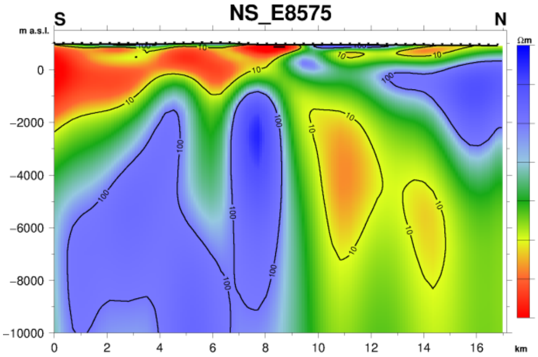
NS_E8575

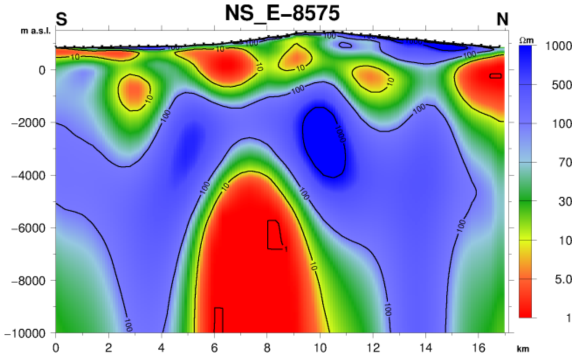
NS_E–8575

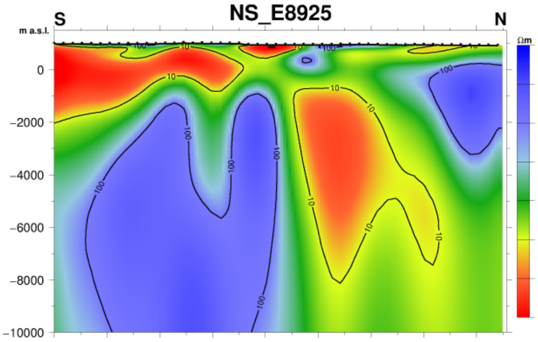
NS_E8925

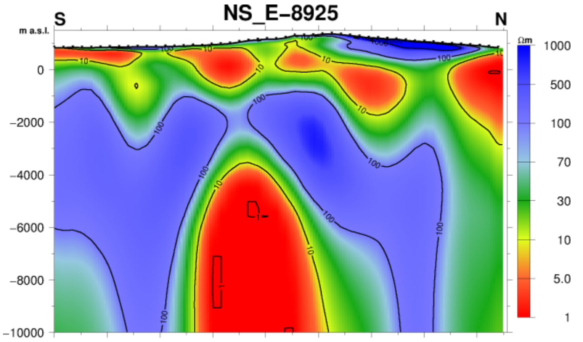
NS_E–8925

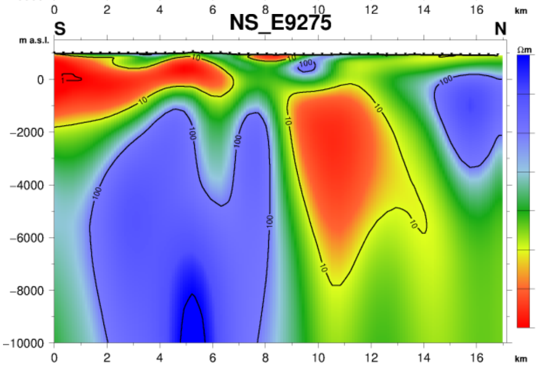
NS_E9275

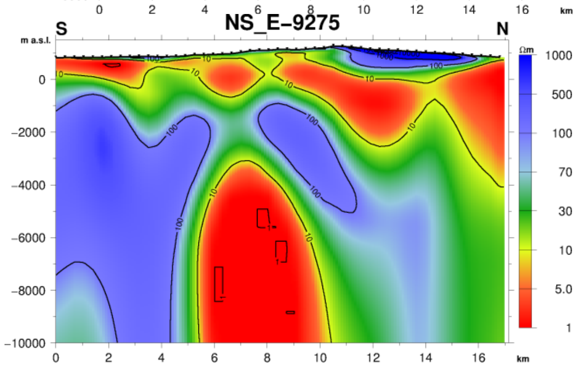
NS_E–9275

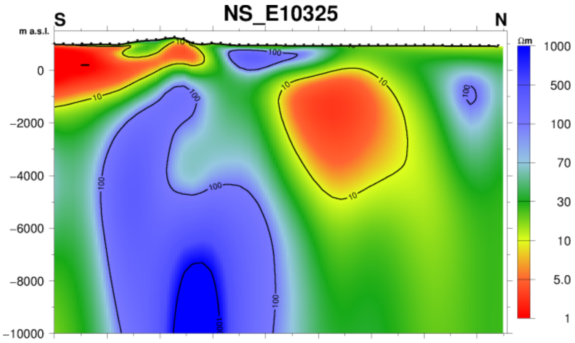
NS_E10325

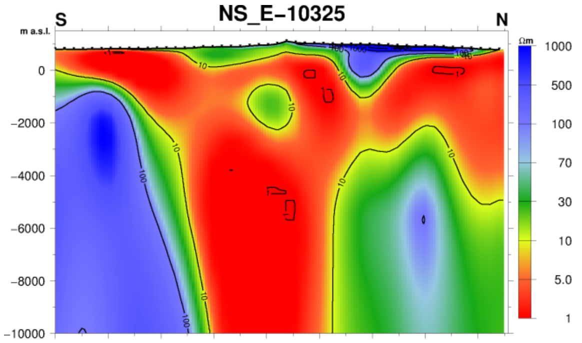
NS_E−10325

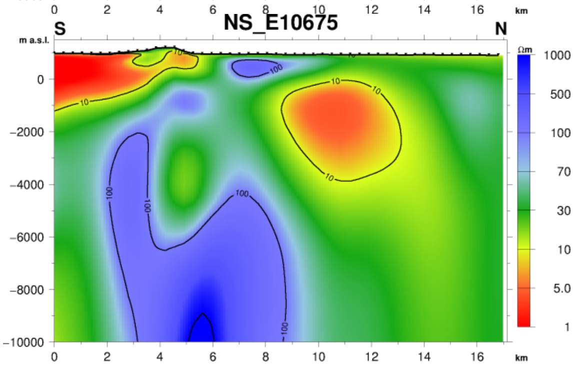
NS_E10675

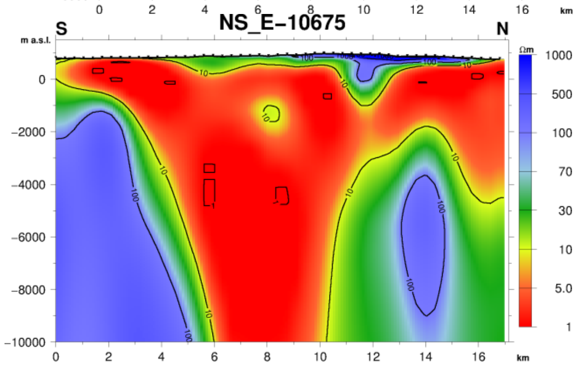
NS_E−10675